Author/s:
Kadinappuli Hewage, Suresh Madushan Sampath

Title:
A comprehensive analysis of the structural alterations occur in CO2- interacted coal: An insight into CO2 sequestration in coal

Date:
2020

Persistent Link:
https://hdl.handle.net/11343/243041

A comprehensive analysis of the structural alterations occur in CO_2-interacted coal: An insight into CO_2 sequestration in coal

Suresh Madushan Sampath Kadinappuli Hewage

0000-0003-3605-4281

Doctor of Philosophy

June 2020

Department of Infrastructure Engineering

The University of Melbourne

Submitted in total fulfilment of the requirements of the degree of Doctor of Philosophy

Page intentionally left blank

Abstract

Human activities from overpopulation to pollution are drastically increasing the global temperature and causing fundamental changes in the Earth. The primary reason for this phenomenon is the greenhouse gas effect that primarily comes from the destruction of the forest cover and conventional energy production. This would cause extreme weather conditions, consequently imperilling the natural habitats, ecosystems and all the Earth's activities. One of the most recent catastrophic event recorded is the Australian bushfire that destroyed over 3048 homes and killed over 1 billion wild animals. Emission of an enormous amount of anthropogenic carbon dioxide (CO_2) has become the primary reason for global warming; so, it is vital to advance towards novel techniques to alleviate the issue. Within a portfolio of options, CO_2 sequestration has gained growing attention – aimed at carbon capture and storage in geological formations. In this context, CO_2 sequestration in coal reservoirs is identified as an effective method, because the process is associated with enhanced coalbed methane (ECBM) extraction – that further offsets the cost of CO_2 storage in coal reservoirs. The successful implementation of the process would certainly lead to a pollution-free world and ultimately a better future, through the mitigation of the greenhouse gas effect.

Although the fundamental physics of CO_2 sequestration have been evolved over several decades, there are some grey areas and unexplored aspects, that need further improvement through investigations. For instance, the injection of CO_2 into coal affects its structural properties, and consequently, the efficiency of the sequestration process as well as the long-term integrity of the reservoir. The coal-CO_2 interaction is a complicated physico-chemical and thermodynamic process that depends on multiple parameters, which in turn makes the evaluations quite challenging. For instance, the unique coalification process and the spatial disposition of maceral/mineral phases and natural cleat system induce a highly-heterogeneous and anisotropic nature in coal, causing spatially sensitive and localized alterations. The CO_2 adsorption-induced coal matrix swelling that consequently modifies the local fracture aperture and therefore the fracture permeability, adversely affects the CO_2 flow behaviour in coal. The CO_2 interaction-induced plasticization effect, change in effective stress and surface energy, swelling/shrinkage-induced micro-cracking, and dissolution of pore-filling minerals may damagingly affect the mechanical competency of the seam. Further, the CO_2 phase change into the supercritical-state, due to high pressure and temperature conditions under *in-situ* environment may exaggerate the interactions causing irreversible and unforeseen modifications in the coal structure. A deep understanding of the structural alterations, in terms of coal hydro-mechanical properties, is thus essential to optimize the process, while minimizing the reservoir damage.

Considering the above aspects, this research aims to comprehensively characterize the alterations in hydraulic and mechanical parameters of CO_2-interacted coal, through a combination of systematic experimental, numerical and statistical analyses, integrated with advanced image analysis techniques and chemical analyses. The study is specifically focused on analysing the fully-coupled CO_2 flow–adsorption–deformation process in coal and investigating the consequent hydro-mechanical modifications occur in coal structure, due to the complex coal-CO_2 interaction.

Initially, the fully-coupled CO_2 diffusion–adsorption–deformation process in a single coal matrix block was modelled, in which the multiple diffusion mechanisms in matrix pore network were simulated using a theoretically-extended diffusion modelling approach, and the consequent CO_2 adsorption-induced matrix swelling was modelled and validated with experimental results. The analysis was then extended on a fractured coal geometry at the coal constituent-scale, through the inclusion of a 3D – discrete fracture matrix (DFM) network, in which the alterations in local fracture aperture and the subsequent fracture permeability were investigated. In general, the results conclude that the CO_2 interaction-induced hydro-mechanical alterations of a fractured coal seam are largely geometry-dependent and highly-localized; thus, should be resolved accurately through a fully-coupled DFM modelling approach. Next, a series of experimental, numerical and statistical studies was conducted to further assess the CO_2-interaction-induced complex mechanical property alterations in coal. The alterations in compressive strength, Young's modulus, brittleness index and dynamic moduli were experimentally investigated, in which the temporal and localized mechanical alterations were specifically analysed in detail. A numerical model was developed to evaluate the free and adsorbed CO_2-induced compressive strength alterations in coal, under both confined and unconfined conditions. The compressive strength was determined with the Mohr-Coulomb failure criterion, where a theoretically-modified cohesion model was derived, by integrating the effective stress change and the surface energy change – caused by CO_2 interaction. Further, a statistical analysis was conducted using advanced soft computing techniques to predict the mechanical property alterations in coal, under different CO_2 interaction conditions. The studies combinedly conclude that CO_2 interaction results in adverse mechanical alterations in coal and the developed numerical and statistical models are capable of accurately simulating/capturing this behaviour. Finally, the conclusions, recommendations for future research and an insight into the field-application of CO_2 sequestration technique were provided based on the results of the combined analyses.

Overall, the outcome of this research is intended to provide knowledge and insight into the productivity and safety of the CO_2 sequestration in coal reservoirs, by conclusively evaluating the CO_2 interaction-induced structural alterations in coal, in terms of its hydro-mechanical properties. The information, results and conclusions given herein can be utilised by researchers to build upon and will be beneficial on reducing the global warming and climate change, through effectively minimising the atmospheric CO_2 level.

Declaration

This is to certify that:

i. The thesis comprises only my original work towards the degree of Doctor of Philosophy, except where indicated in the preface.
ii. Due acknowledgement has been made in the text to all other material or work used.
iii. The thesis is fewer than 100,000 word limit in length, exclusive of tables, maps, bibliographies and appendices.

Suresh Kadinappuli Hewage

June 2020

Preface and publications

This doctoral dissertation presents the research undertaken during the course of my PhD candidature between February 2017 to June 2020. The main body of the dissertation contains 5 peer-reviewed journal publications and 1 submitted manuscript that is currently under review. Further, the most relevant sections extracted from 3 other peer-reviewed journal publications are incorporated in the dissertation. In fact, chapters 4, 7 and 8 include 1 journal publication each and chapter 6 contains 2 journal publications. Chapter 5 consists of a submitted manuscript, that is currently under review. Further, the literature review chapter (i.e. chapter 2) and the insight into the field-application section given in chapter 9 consist of some of the most relevant sections extracted from 3 peer-reviewed journal papers, that are produced during the doctoral candidature. These publications comprise of major parts of their respective chapters that directly result from the work done in this doctoral research. The publication status is listed below.

Peer-reviewed journal publications included in the thesis

1. Sampath K. H. S. M., Perera M. S. A., Matthai S. K., Ranjith P. G., Li D. Y. (2020). *Modelling of fully-coupled CO_2 diffusion and adsorption-induced coal matrix swelling*. Fuel, 262, 116486. https://doi.org/10.1016/j.fuel.2019.116486
2. Sampath K. H. S. M., Perera M. S. A., Matthai S. K., Ranjith P. G. *Discrete fracture matrix modelling of fully-coupled CO_2 flow–deformation process in fractured coal*. Submitted in International Journal of Rock Mechanics and Mining Sciences (under review).
3. Sampath K. H. S. M., Perera M. S. A., Li D.Y., Ranjith P. G., Matthai, S. K. (2019). *Evaluation of the mechanical behaviour of brine+ CO_2 saturated brown coal under mono-cyclic uni-axial compression*. Engineering Geology, 263, 105312. https://doi.org/10.1016/j.enggeo.2019.105312
4. Sampath K. H. S. M., Perera M. S. A., Li D. Y., Ranjith P. G., Matthai S. K. (2019). *Characterization of dynamic mechanical alterations of supercritical CO_2-interacted coal through gamma-ray attenuation, ultrasonic and X-ray computed tomography techniques*. Journal of Petroleum Science and Engineering, 174, 268-280. https://doi.org/10.1016/j.petrol.2018.11.044
5. Perera M. S. A., Sampath K. H. S. M., (2019). *Modelling of free and adsorbed CO_2-induced mechanical property alterations in coal*. International Journal of Coal Geology, 217, 103348. https://doi.org/10.1016/j.coal.2019.103348

6. Sampath K. H. S. M., Perera M. S. A., Ranjith P. G., Matthai S. K., Tao X., Wu B. K. (2019). *Application of neural networks and fuzzy systems for the intelligent prediction of CO_2-induced strength alteration of coal*. Measurement (London. Print), 135, 47-60. https://doi.org/10.1016/j.measurement.2018.11.031

Peer-reviewed journal publications partly included in the thesis

1. Sampath K. H. S. M., Perera M. S. A., Ranjith P. G., Matthai S. K., Rathnaweera T., Zhang G., Tao X. (2017). *CH_4-CO_2 gas exchange and supercritical CO_2 based hydraulic fracturing as CBM production-accelerating techniques: A review*. Journal of CO_2 Utilization, 22, 212-230. https://doi.org/10.1016/j.jcou.2017.10.004
2. Sampath K. H. S. M., Perera M. S. A., Ranjith P. G., Matthai S. K. (2019). *CO_2 interaction-induced mechanical characteristics alterations in coal: A review*. International journal of coal geology, 204, 113-129. https://doi.org/10.1016/j.coal.2019.02.004
3. Sampath K. H. S. M., Perera M. S. A., Elsworth D., Ranjith P. G., Matthai S. K., Rathnaweera T., Zhang G. (2019). *Effect of coal maturity on CO_2-based hydraulic fracturing process in coal seam gas reservoirs*. Fuel, 236, 179-189. https://doi.org/10.1016/j.fuel.2018.08.150

In terms of the contributions of the authors towards the above journal publications, I have contributed more than 50% in each publication, being the primary author. I have involved in all stages of the work, including concept, initiation, methodology, experimental analysis, numerical and statistical modelling, data analysis, discussion, writing and presentation, and subsequent editing in response to co-authors' and editors' reviews. The co-authors, being the doctoral supervisors and other collaborators have contributed towards the publications by providing their expert knowledge, valuable insights and ideas to ensure quality output. Moreover, they have contributed in reviewing and editing the written material, providing comments and feedback to improve the quality, quantity and the clarity of the manuscripts. All the publications in the main dissertation body are provided in the ‘author-accepted’ version. A detailed description of the publication status and dates, the candidate’s contributions and co-authors in each publication are listed in the following table.

Thesis chapter	Publication title	Publication status and date of acceptance	Nature and % of the candidate's contribution	Co-author name(s)
2	CH_4-CO_2 gas exchange and supercritical CO_2 based hydraulic fracturing as CBM production-accelerating techniques: A review	Published in **Journal of CO_2 utilization** (05/10/2017)	Concept, literature review, discussion, writing and presentation • Contribution: **85%**	• M.S.A. Perera • S.K. Matthai • P.G. Ranjith • T. Ratnaweera • X. Tao • G. Zhang
2	CO_2 interaction-induced mechanical characteristics alterations in coal: A review	Published in **International journal of coal geology** (14/02/2019)	Concept, literature review, discussion, writing and presentation • Contribution: **85%**	• M.S.A. Perera • S.K. Matthai • P.G. Ranjith
4	Modelling of fully-coupled CO_2 diffusion and adsorption-induced coal matrix swelling	Published in **Fuel** (22/10/2019)	Concept, methodology, experimental analysis, modelling, discussion, writing and presentation • Contribution: **80%**	• M.S.A. Perera • S.K. Matthai • P.G. Ranjith • Li Dong-yin
5	Discrete fracture matrix modelling of fully-coupled CO_2 flow – deformation process in fractured coal	Under review	Concept, methodology, modelling, discussion, writing and presentation • Contribution: **80%**	• M.S.A. Perera • S.K. Matthai • P.G. Ranjith
6	Evaluation of the mechanical behaviour of brine+ CO_2 saturated brown coal under mono-cyclic uni-axial compression	Published in **Engineering Geology** (25/09/2019)	Concept, methodology, experimental analysis, discussion, writing and presentation • Contribution: **85%**	• M.S.A. Perera • S.K. Matthai • P.G. Ranjith • Li Dong-yin
6	Characterization of dynamic mechanical alterations of	Published in **Journal of Petroleum**	Concept, methodology, experimental	• M.S.A. Perera • S.K. Matthai

	supercritical CO_2-interacted coal through gamma-ray attenuation, ultrasonic and X-ray computed tomography techniques	**Science and Engineering** (17/11/2018)	analysis, discussion, writing and presentation • Contribution: **85%**	• P.G. Ranjith • Li Dong-yin
7	Modelling of free and adsorbed CO_2-induced mechanical property alterations in coal	Published in **International journal of coal geology** (19/11/2019)	Concept, modelling, discussion, writing and presentation • Contribution: **75%**	• M.S.A. Perera
8	Application of neural networks and fuzzy systems for the intelligent prediction of CO_2-induced strength alteration of coal	Published in **Measurement** (09/11/2018)	Concept, methodology, modelling, discussion, writing and presentation • Contribution: **85%**	• M.S.A. Perera • S.K. Matthai • P.G. Ranjith • X. Tao • B. Wu
9	Effect of coal maturity on CO_2-based hydraulic fracturing process in coal seam gas reservoirs	Published in **Fuel** (30/08/2018)	Concept, methodology, experimental analysis, discussion, writing and presentation • Contribution: **85%**	• M.S.A. Perera • S.K. Matthai • P.G. Ranjith • D. Elsworth • T. Ratnaweera • G. Zhang

In addition to the above-mentioned publications included within the thesis, two peer-reviewed conference publications have been produced with the findings of the research. The details are given below. However, they do not make a part of the thesis, due to the conciseness of the dissertation. Moreover, a scholarship and few awards have been received during the candidature, in recognition of the research findings.

Peer-reviewed conference publications

1. Sampath K. H. S. M., Perera M. S. A., Ranjith P. G., Matthai S. K. (2018). *Evaluation of Superiority of Liquid CO_2 as a Non-Aqueous Fracturing Fluid for Coal Seam Gas Extraction*. In 52nd US Rock Mechanics/Geomechanics Symposium. American Rock Mechanics Association, June 2018, Washington, USA.

2. Sampath, K. H. S. M., Perera, M. S. A., Ranjith, P. G., & Matthai, S. K. (2018). *Investigation of the mechanical behaviour of brine saturated brown coal under uni-axial compression*. In Deep Rock Mechanics: From Research to Engineering: Proceedings of the International Conference on Geo-Mechanics, Geo-Energy and Geo-Resources, September 2018, Chengdu, PR China.

Scholarships and awards received during the doctoral candidature

1. "**George Lansell Memorial Scholarship**" awarded by Melbourne School of Engineering, University of Melbourne – 2019.
2. "**Best Presentation Award (Storage)**" awarded at the PCC Research Snapshot organized by Peter Cook Centre for Carbon Capture and Storage Research, University of Melbourne, 4th December 2019.
3. "**Best research presentation award**" awarded at the International postgraduate summer school, North-eastern University, China, 9th – 16th August 2019.

Research collaborations

Some of the work towards the dissertation was conducted in collaboration with several other researchers in different institutes around the globe, who provided their expert knowledge and support on various aspects. The main research collaborators include: Prof. Derek Elsworth from Pennsylvania State University, USA, Dr. Irina Sin from MINES ParisTech, France, Prof. Xu Tao from Northeastern University, China, Prof. Li Dong-Yin from Henan Polytechnic University, China, Dr Bailin Wu from CSIRO, Australia and, Dr Anton Maksimenko from imaging and medical beamline (IMBL) Synchrotron, Australia. The research collaborations include supplying required material, providing invaluable assistance when conducting analyses and giving perspective comments on manuscripts that guided the research to a quality output.

Finally, this research would not have been possible without the support and the funding provided by the University of Melbourne, and all the other supports provided by various research institutes, platforms and facilities. In fact, most of the experimental analyses were carried out in the deep earth engineering research laboratory (DEERL) in Monash University, and micro-CT imaging experiments were done in the Australian synchrotron IMBL facility. Further, the other imaging and chemical analyses were conducted in Bio21 institute, material characterisation and fabrication platform (MCFP), TrACEES platform, clean energy lab and petrophysics lab in the University of Melbourne. The analysis of large data sets and numerical simulations were carried out in high-performing computing facilities such as *MASSIVE* supercomputing cluster, *Nectar* and *Spartan*.

Acknowledgement

This doctoral research would not have been possible without the enthusiastic support and the supervision of the primary supervisor Dr. Samintha Perera. Thank you for the guidance, unconditional support and inspiration all through my candidature that pushed me to excel and to a rewarding research life. Your mentorship, the friendly atmosphere, motivations and all the encouragement have made me confident and stronger to face all the challenges encountered throughout these years.

Also, I would like to thank my secondary supervisor, Prof. Stephan Matthai, for always offering me valued ideas and directions along the way, guiding to a quality research. Your expert knowledge and the deep understanding of the field helped to a great extent to shape this research. Moreover, my sincere gratitude goes to my external supervisor Prof. Ranjith Pathegama from Monash University, for unconditionally allowing me to use all the research facilities in Monash University. The perspective comments, invaluable assistance and insights often provided by him were beneficial to improve the quality of the research.

Next, I would like to acknowledge all the research facilities/platforms in the University of Melbourne that provided their support on every aspect to make this research study a success. Further, I would like to extend my gratitude towards the Civil Engineering technical staff in Monash University, mainly Mr Michael Leach, Mr Zoltan Csaki and Mr Sarvan Mani, and Dr Anton Maksimenko from Australian synchrotron imaging and medical beamline (IMBL) facility for assisting me on my experimental analyses.

My gratitude also goes to my research colleagues, and my friends who kept me company throughout these years. The joyful moments spent with you have helped me further grow and often lent a helping hand to overcome all my hard times. This journey would not have been the same without you.

Importantly, it would never be possible to complete this journey without the love and the limitless support of my beloved parents, Piyasena and Yasanthi, my loving brother and sister Dr. Sampath Hewage and Dr. Iranthi Nadeesha, who made everything perfect and so comfortable. Finally, my most heartfelt gratitude goes to my dearest loving partner, Keshini, for always being with me in all the ups and downs, believing in me on every step of the way and making me smile even on the rainiest of days.

Table of contents

Abstract .... **i**

Declaration .... **iii**

Preface and publications .... **iv**

Acknowledgement .... **ix**

Table of contents .... **x**

List of figures .... **xiii**

List of tables .... **xx**

1 Introduction **2**

1.1 Research background 2
1.2 Research gaps 4
1.3 Research objectives 5
1.4 Thesis outline 6

2 Literature review **12**

2.1 Chapter overview and structure 12
2.2 CO_2 sequestration process and the associated structural alterations in coal 13
2.2.1 CO_2 interaction-induced structural alterations in coal (Sampath et al., 2017) 13
2.2.2 Fully-coupled CO_2 flow–adsorption–coal deformation process 15
2.2.3 Discrete fracture matrix (DFM) modelling approach to model the fully-coupled process 18
2.3 CO_2-induced mechanical property alterations in coal (Sampath et al., 2019) 19
2.3.1 Influential parameters for the mechanical alterations 19
2.3.2 Causative factors for the CO_2 interaction-induced strength alterations 23
2.4 Chapter summary 26

3 Experimental procedures **28**

3.1 Chapter overview and structure 28
3.2 Sample preparation 29
3.2.1 Sample acquisition 29
3.2.2 Sample coring, cutting and grinding 31
3.2.3 CO_2 + water/brine saturation of coal 32
3.3 Sample characterisation 33
3.3.1 Scanning electron microscope - energy dispersive spectrometry (SEM-EDS) analysis 33
3.3.2 X-ray diffraction (XRD) analysis 33
3.3.3 Fourier-transform infrared spectroscopy (FT-IR) 34
3.3.4 Micro-computed tomography (Micro-CT) 35
3.4 Primary experimental analyses 37
3.4.1 CO_2 diffusion experiment 37
3.4.2 CO_2 adsorption-induced coal swelling experiments 37
3.4.3 Unconfined compressive strength (UCS) analysis 38

3.4.4 ARAMIS analysis 38
3.4.5 Gamma-density test 39
3.4.6 Ultrasonic wave measurement 39
3.5 Chapter summary 40

4 Evaluation of CO_2 flow behaviour, adsorption and the mechanical deformation of coal matrix 43

4.1 Chapter overview and structure 43
4.2 Journal paper: CO_2 diffusion and adsorption-induced swelling of coal matrix 44
4.2.1 Introduction 45
4.2.2 The theoretical approach of CO_2 diffusion and adsorption-induced coal matrix swelling 47
4.2.3 Experimental analysis 54
4.2.4 Boundary/initial conditions and model parameters 56
4.2.5 Results and discussion 59
4.2.6 Summary and recommendations 68
4.2.7 Conclusions 69
4.3 Chapter summary 74

5 Evaluation of fully-coupled CO_2 flow behaviour, adsorption and the mechanical deformation of fractured coal seams 76

5.1 Chapter overview and structure 76
5.2 Discrete fracture matrix (DFM) modelling of CO_2 flow – deformation process in fractured coal: Single-phase flow 78
5.2.1 Introduction 79
5.2.2 The Discrete fracture matrix (DFM) modelling approach 81
5.2.3 Theoretical approach for the hydro-mechanical model 81
5.2.4 Model validation 87
5.2.5 Simulation of a complex DFM model 90
5.2.6 Conclusions 101
5.3 Discrete fracture matrix (DFM) modelling of CO_2 flow – deformation process in fractured coal: Two-phase flow 105
5.3.1 Introduction 105
5.3.2 Theoretical approach for the hydro-mechanical model 105
5.3.3 Model geometry and simulation procedure 111
5.3.4 Modelling results 113
5.3.5 Conclusions 118
5.4 Chapter summary 119

6 Experimental analysis of static and dynamic mechanical property alterations in CO_2-interacted coal 122

6.1 Chapter overview and structure 122
6.2 Journal paper: Static mechanical property alterations in CO_2-interacted coal 124
6.2.1 Introduction 125
6.2.2 Experimental procedure 127
6.2.3 Results and discussion 131
6.2.4 Conclusions 145

6.3 Journal paper: Dynamic mechanical property alterations in CO_2-interacted coal......... 148
6.3.1 Introduction....... 149
6.3.2 Experimental procedure....... 151
6.3.3 Results and discussion....... 155
6.3.4 Conclusions....... 169
6.4 Chapter summary....... 172

7 Numerical analysis of free and adsorbed CO_2-induced mechanical property alterations in coal....... 174

7.1 Chapter overview and structure....... 174
7.2 Journal paper: Free and adsorbed CO_2-induced mechanical alterations in coal....... 175
7.2.1 Introduction....... 176
7.2.2 The theoretical approach of modelling the coal strength alterations....... 177
7.2.3 Simulation procedure to model the mechanical property alterations....... 185
7.2.4 Validation of the model with experimental results....... 186
7.2.5 Model performance-based sensitivity analysis....... 196
7.2.6 Conclusions....... 200
7.3 Chapter summary....... 203

8 Statistical analysis with machine learning techniques to predict the CO_2-induced mechanical property alterations in coal....... 205

8.1 Chapter overview and structure....... 205
8.2 Journal paper: Intelligent prediction of CO_2-induced mechanical property alterations in coal 206
8.2.1 Introduction....... 207
8.2.2 Experimental methodology....... 209
8.2.3 Selection of input parameters....... 210
8.2.4 Multivariate Regression Analysis (MRA)....... 212
8.2.5 Artificial Neural Network (ANN)....... 213
8.2.6 Adaptive neuro-fuzzy inference system (ANFIS)....... 216
8.2.7 Results and Discussion....... 219
8.2.8 Conclusions....... 228
8.3 Chapter summary....... 232

9 Conclusions, suggestions for future research and insight into field-applications 235

9.1 Conclusions....... 236
9.1.1 Conclusions drawn from objective 1 of the research....... 236
9.1.2 Conclusions drawn from objective 2 of the research....... 238
9.2 Suggestions for future research....... 242
9.2.1 Suggestions for extending the work carried out in objective 1 of the research....... 242
9.2.2 Suggestions for extending the work carried out in objective 2 of the research....... 243
9.3 An insight into the field-application of the CO_2 sequestration technique....... 245

Reference....... 249

List of figures

Figure 1-1 – Composition of a typical coal mass (modified after Sampath et al. (2019)). 3

Figure 1-2 - Brief illustration of the thesis outline. 6

Figure 2-1 – Variation of a) matrix swelling and, b) permeability with increasing gas pore pressure: comparison between N_2 and CO_2 (modified after Pini et al. (2009)). 14

Figure 2-2 –Illustration of the fully-coupled hydro-mechanical process used in the numerical simulations. 17

Figure 2-3 – Illustration of the meshing of a) mixed dimensional/hybrid DFM model and, b) equi-dimensional DFM model. Note that although equi-dimensional DFM modelling approach is straight forward, the complex mesh requires large computational power for the simulation. 19

Figure 2-4 – Variation of strength and Young's modulus of a) Australian black coal and, b) Indian coal with CO_2 saturation time (modified after a) Masoudian et al. (2014), b) Bagga et al. (2015)) 21

Figure 2-5 – Comparison of UCS reduction in bituminous coal and Lignite (modified after Ranjith and Perera (2012)) 22

Figure 3-1 – Schematic diagram of the utilization of sample preparation, characterization and experimental analyses in each chapter. 28

Figure 3-2 – Acquisition of coal samples as blocks and double sealed with polyethylene-films until the sample preparation to prevent the moisture loss during transportation and storage. 30

Figure 3-3 – Machines used for the sample preparation process: a) coring machine, b) cutting machine and, c) grinding machine. 31

Figure 3-4 – a) Vacuum chamber used to conduct water saturation and, b) reaction chamber used to conduct pure CO_2, water+CO_2 and brine+CO_2 saturations. 32

Figure 3-5 – a) OXFORD INCA instrument used for SEM-EDS analysis and, b) typical SEM-EDS results indicating the elemental composition of a representative sample. 33

Figure 3-6 – a) D8 advance diffractometer used for X-ray diffraction (XRD) analysis and, b) typical XRD results showing the mineral composition of a representative specimen. 34

Figure 3-7 – Experimental procedure for FT-IR analysis. 35

Figure 3-8 – a) Australian Synchrotron IMBL facility used for full-scale micro-CT analyses and, b) schematic diagram of monochromatic X-ray beam transmitting through a sample (modified after Stevenson et al. (2012)). 36

Figure 3-9 – Experimental setup adopted to conduct the CO_2 diffusion and swelling experiments. 37

Figure 3-10 – a) UCS testing machine and the ARAMIS equipment and, b) prepared core sample for UCS and ARAMIS testing. 38

Figure 3-11 – Density measurement of the core sample using the multi-sensor core logger. 39

Figure 4-1 - a) Micro-CT image-based 3D-reconstruction of a coal section indicating face cleats, butt cleats and coal matrix blocks (Jing et al., 2016) and, b) representative approximation of coal structure. 46

Figure 4-2 – Variation of Knudsen number with pore pressure for different pore sizes, highlighting the dominant flow mechanism ranges. 51

Figure 4-3 – Schematic diagram of the experimental setup used for the CO_2 diffusion and adsorption-induced swelling experiments. 55

Figure 4-4 – Geometry and boundary conditions of the modelled cubical block. 57

Figure 4-5 – The piecewise function adopted to specify the boundary gas pressure on the model. 57

Figure 4-6 – a) Pore size distribution data used to determine the connected porosity and equivalent pore radius *(refer Eq. 4-32)* (Zhou et al., 2017) and, b) current experimental diffusion data fitted with the analytical model to obtain the CO_2 diffusion coefficient of the particular coal type. 59

Figure 4-7 – Model validation with experimental data: Fitting the volumetric strain vs. CO_2 pore pressure with a) Day et al. (2008)'s data and, b) Pini et al. (2009)'s data, and c) fitting the volumetric strain vs. CO_2 interaction time with current experimental data. 61

Figure 4-8 – Simulation results showing the spatial and temporal distribution of CO_2 diffusion-induced pore pressure in the coal matrix. 62

Figure 4-9 – a) Variation of the adsorbed amount of CO_2 in the coal matrix with the normalized average pore pressure for different CO_2 boundary pressures and, b) variation of the maximum adsorbed amount of CO_2 with the applied boundary pressure (i.e. equilibrium pressure). 63

Figure 4-10 – Simulation results showing the sensitivity of the model to the Langmuir sorption constant (VL) and the Langmuir volumetric strain constant (εL). 65

Figure 4-11 – a) Variation of the total flow conductance with pore pressure for different pore sizes and, b) change in the total flow conductance (compared to 182 nm pore size) with pore size for different pore pressures. Note: internal graph in figure b further illustrates the change in the total flow conductance (compared to 182 nm pore size) with pore pressure for different pore sizes. 67

Figure 4-12 – Contribution share of each transport mechanism with pore pressure: a) Slip flow contribution and, b) Knudsen diffusion contribution to the total flow conductance. 68

Figure 5-1 – Schematic of cross-coupling relationships among gas flow in fractures, diffusion in matrix and coal deformation. 82

Figure 5-2 – a) The flow model within the fracture and matrix domains, indicating both longitudinal and transverse flows and the corresponding pressure terms and, b) definition of the mechanical system of the fractured medium as analogous to a linear spring-closure system. 87

Figure 5-3 – The single-fractured DFM geometric model utilized for the validation; developed after Siriwardane et al. (2009). 89

Figure 5-4 – Variation of permeability ratio with CO_2 interaction time: Modelling results fitted to experimental data from Siriwardane et al. (2009). 90

Figure 5-5 – Extruded and re-scaled 3D-geometric model developed based on the stochastically simplified and reconstructed DFM model from Jing et al. (2016). 92

Figure 5-6 – a) Geometric model, indicating the meshing, boundary pressures and the location of CO_2 injection and, b) plan view of the geometry, indicating the points of interest used to analyse spatial variations in simulation variables. 92

Figure 5-7 – Temporal and spatial variation of CO_2 pore pressure development in the coal mass. 93

Figure 5-8 – Variation of a) fracture pressure and, b) matrix pressure with CO_2 interaction time. 94

Figure 5-9 – a) Variation of the adsorbed mass of CO_2 in a selected coal matrix block with CO_2 interaction time and with average CO_2 pore pressure and, b) variation of the volumetric strain of a selected coal matrix block with CO_2 interaction time and with average CO_2 pore pressure. Note that the strain results are plotted together for cases both with- and without-swelling, for direct comparison. 96

Figure 5-10 – Spatial variation of fracture aperture: a) before CO_2 injection (at 0 s) and, b) after full pressure equilibration (at 150000 s). 98

Figure 5-11 – Temporal variation of fracture aperture both with- and without-swelling. 98

Figure 5-12 – Variation of fracture aperture with average pore pressure in the bounding coal matrix. 99

Figure 5-13 – Temporal variation of fracture permeability ratio with- and without-swelling conditions. 99

Figure 5-14 – Spatial variation of normal contact pressure: a) before CO_2 injection (at 0 s) and, b) after full pressure equilibration (at 150000 s), indicating the locations of fully-closed fractures. 100

Figure 5-15 – Variation of maximum contact pressure with CO_2 interaction time, within a fully-closed fracture. 101

Figure 5-16 – The relative permeability curves of water and gas, considering X model and viscous coupling model. 108

Figure 5-17 - Geometric model, indicating the meshing, boundary pressures and displacement, the CO_2 injection and, the points of interest used to analyse the spatial variations. 113

Figure 5-18– Comparison of analytical and numerical results between the range of initial and irreducible water saturation: a) relative permeabilities and, b) capillary pressure curve. 114

Figure 5-19 – a) Variation of water and gas saturations with the fracture gas pressure and, b) variation of matrix pore pressure at two points of interest with CO_2 interaction time. 115

Figure 5-20 – Variation of adsorbed amount of CO_2 with CO_2 interaction time and matrix pore pressure. 116

Figure 5-21 – Variation of volumetric swelling at two points of interest with CO_2 interaction time. 116

Figure 5-22 – Variation of fracture aperture at two points of interest with a) CO_2 interaction time and, b) average pore pressure of bounding matrices of the corresponding fracture. 117

Figure 5-23 – Variation of fracture permeability ratio at two points of interest with CO_2 interaction time. 118

Figure 6-1 – Geo-graphical location of the Loy-Yang mine, Victoria, Australia (Holdgate et al., 2014). 127

Figure 6-2 - Schematic diagram of the high pressure/temperature reaction chamber system used for the simultaneous brine+CO_2 saturation. 129

Figure 6-3 – a) Complete experimental setup used for coal UCS testing and, b) a typical ARAMIS strain colour map that shows the four cross-sections and three longitudinal-sections used to compute average lateral and axial strains of samples. 130

Figure 6-4 - SEM-EDS graph, showing the chemical elemental composition of the coal sample. 132

Figure 6-5 - Determination of a) Young's modulus *(refer Eq. 6-2)* and, b) brittleness index *(refer Eq. 6-3)*. 132

Figure 6-6 - Variation of average UCS and the reduction of UCS (compared to natural condition) with different saturation conditions. Note: Equal saturation time of 45 days was used at each condition. 133

Figure 6-7 - Variation of average Young's modulus (E) and reduction of Young's modulus (compared to natural condition) with different saturation conditions. Note: Equal saturation time of 45 days was used at each condition. 135

Figure 6-8 - Variation of average brittleness index (BI) and the reduction of BI (compared to natural condition) with different saturation conditions. Note: Equal saturation time of 45 days was used at each condition. 136

Figure 6-9 – Variation of a) average UCS and, b) average Young's modulus with saturation time for different saturation conditions. 137

Figure 6-10 - Strain distribution colour maps of representative specimens from each saturation condition: a) natural (as-received) sample, b) water saturated sample, c) water+CO_2 interacted sample, d) 10% brine+CO_2 interacted sample and, e) 20% brine+CO_2 interacted sample. 138

Figure 6-11 - Variation of volumetric strain vs axial stress of representative samples at each saturation condition. 139

Figure 6-12 – The workflow adopted for the qualitative and quantitative analysis of micro-CT data. 140

Figure 6-13 - Micro-CT image-based 3D-reconstruction of the failed samples, indicating the failure patterns and induced fracture networks of; a) natural (as-received) sample, b) water+CO_2 interacted sample, c) 10% brine+CO_2 interacted sample and, d) 20% brine+CO_2 interacted sample. 142

Figure 6-14 - Variation of fracture fraction with different saturation conditions. Note: The fracture fractions were calculated based on micro-CT 3D-reconstructed data of representative samples at failure *(refer Figure 6-13)*. 142

Figure 6-15 - FT-IR spectrums of the brown coal samples before and after S-CO_2 interaction for 45 days, highlighting the alterations in peak intensities of different functional groups... 144

Figure 6-16 - XRD results, indicating the mineral composition of the coal type used for the analyses. Note that the predominant mineral type detected is Kaolinite. 152

Figure 6-17 – a) Natural coal sample, indicating the mineral layering at a preferential orientation, b) a representative ortho-slice and the measured radial orientations with respect to the mineral layering and, c) 3D-reconstructed image of natural coal sample, indicating the coal mass (black), spatial distribution of mineral phase (white) and natural fractures (blue). 152

Figure 6-18 - Data measured orientations and points in core sample: a) axial, b) parallel to mineral layering plane ($0o - 180o$), c) on angle to mineral layering plane ($45o - 225o$), d) perpendicular to mineral layering plane ($90o - 270o$) and, e) on angle to mineral layering plane ($135o - 315o$). 152

Figure 6-19 - Schematic diagram of the reaction chamber used for the coal-S-CO_2 treatment. 153

Figure 6-20 - Schematic diagram of the gamma-ray attenuation system *(not to scale)* and the measured orientations of the core specimen. 154

Figure 6-21 - Measurement of ultrasonic wave velocities at: a) axial direction and, b) pre-defined radial orientations of the core specimen *(not to scale)*. 154

Figure 6-22 - Visualization of full-scale core specimens: a) natural core specimen, indicating the mineral layering and pre-defined orientations. 3D-reconstructed full-scale specimen: b) at natural conditions, c) after 14 days of S-CO_2 interaction and, d) after 45 days of S-CO_2 interaction. Note that the fracture network and coal mass are segmented in green and black colours, respectively, for the visualization. 156

Figure 6-23 – Quantification of induced fracture network: a) variation of fracture fraction with S-CO_2 interaction time and, b) variation of cumulative fracture volume with the angle to mineral layer. 157

Figure 6-24 – Variation of gamma-density at radial orientations. 158

Figure 6-25 – Variation of a) P wave velocities and, b) S wave velocities with angle to mineral layering. 161

Figure 6-26 – Variation of axial: a) P and S wave delay times and, b) P and S wave velocities with S-CO_2 interaction time. 161

Figure 6-27 – Variation of radially measured P and S wave delay times and velocities. 162

Figure 6-28 – Variation of axially measured dynamic strength parameters with S-CO_2 interaction time. 166

Figure 6-29 – Variation of radially measured dynamic strength parameters. 167

Figure 7-1 – Effect of free and adsorbed gas phases on the alteration of compressive strength of CO_2-interacted coal based on the Mohr-Coulomb failure criterion. 184

Figure 7-2 – Complete simulation procedure to model the mechanical property alterations. 186

Figure 7-3 – Geometry and the boundary conditions for the confined-stress condition. 187

Figure 7-4 – Variation of natural coal strength with confining pressure (fitted with the data from Masoudian et al. (2014)). 188

Figure 7-5 – Temporal and spatial distribution of CO_2 pore pressure and the consequent swelling deformation of the sample, under confined-stress condition – simulated at $Pb = PCO2$= 5.5 MPa. 189

Figure 7-6 – Simulation results under confined-stress condition: a) variation of average pore pressure and, b) variation of volumetric strain with CO_2 interaction time. c) variation of porosity, d) variation of permeability, e) change in adsorption-induced surface energy ($\Delta\gamma$) *(refer Eq. 7-32)* and, f) variation of cohesion *(refer Eq. 7-35)* with the CO_2 pore pressure – simulated at $Pb = PCO2$= 5.5 MPa. 190

Figure 7-7 – The experimental data fitted with the Langmuir-type model, illustrating the change in the Young's modulus with the CO_2 pore pressure *(refer Eq. 7-36)* (modified after Masoudian et al. (2014)). 191

Figure 7-8 – Comparison of strength variation between natural and CO_2-interacted coal, which indicates the effect of confining pressure and CO_2 injection pressure on the strength alteration (fitted with the data from Masoudian et al. (2014)). 192

Figure 7-9 - Modelled stress-strain curves for selected confining pressures that depict the variation of Young's modulus and compressive strength. 192

Figure 7-10 – Geometry and the boundary conditions for the unconfined-stress condition. 193

Figure 7-11 – Temporal and spatial distribution of CO_2 pore pressure and the consequent swelling deformation of the sample, under unconfined-stress condition. 195

Figure 7-12 – a) Variation of cohesion with CO_2 interaction pressure *(refer Eq.7-40)* and, b) the experimental data fitted with the Langmuir-type model, illustrating the change in the Young's modulus with the CO_2 interaction pressure *(refer Eq. 7-36)* (modified after Perera et al. (2013)) 195

Figure 7-13 – a) Variation of UCS with CO_2 interaction pressure (fitted with the data from Perera et al. (2013)) and, b) modelled stress-strain curves that depict the variation of Young's modulus and compressive strength at different CO_2 interaction pressures. 196

Figure 7-14 – Variation of a) cohesion and, b) peak compressive strength with CO_2 pore pressure, for different Biot's coefficient values (Note: $Pb = 25\ MPa$). 197

Figure 7-15 – Sensitivity analysis based on Langmuir constants: Variation of a) volumetric strain and b) peak compressive strength for different εL values. Variation of c) adsorbed amount of CO_2 and d) peak compressive strength for different VL values. Variation of e) Young's modulus and f) peak compressive strength for different EL values. (Note: $Pb = 25\ MPa$). 199

Figure 8-1 - Strength results from the current experimental study: a) variation of UCS with CO_2 interaction time and, b) reduction of UCS with CO_2 interaction time. 210

Figure 8-2 - Relationship between natural coal strength and fixed carbon content (developed with data from (Bagga et al., 2015; Perera; Perera et al., 2011b; Perera et al., 2013; Ranathunga et al., 2016a; Ranathunga et al., 2016b; Viete and Ranjith, 2006; Vishal et al., 2015)). 211

Figure 8-3 - Network architecture of ANN structure with feed-forward back-propagation network. 214

Figure 8-4 - Network architecture of ANFIS with m inputs and one output, equivalent to Sugeno-type fuzzy inference structure. 218

Figure 8-5 - The correlation between L-MRA predicted UCS values and the measured UCS values at a) training stage and, b) testing stage.. 220

Figure 8-6 - The correlation between NL-MRA predicted UCS values and the measured UCS values at a) training stage and, b) testing stage.. 220

Figure 8-7 - Validation curve for the ANN model. 221

Figure 8-8 - The correlation between ANN predicted UCS values and the measured UCS values at a) training stage and, b) testing stage.. 221

Figure 8-9 - Training error minimization in the ANFIS model. 222

Figure 8-10 - The correlation between ANFIS predicted UCS values and the measured UCS values at a) training stage and, b) testing stage.. 222

Figure 8-11 – a) Measured UCS and predicted UCS by L-MRA, NL-MRA, ANN and ANFIS models for the tested 15 data sets and, b) residual error of L-MRA, NL-MRA, ANN and ANFIS predicted UCS values for the tested 15 data sets.. 223

Figure 8-12 – a) ANN and ANFIS predicted results fitted with the experimental data from current study and, b) variation of coal UCS due to long-term CO_2 interaction, forecasted with ANN and ANFIS models. 227

List of tables

Table 3-1 – Typical characteristics of coal types used in the study (Li et al., 2012; Sampath et al., 2018; Zhang et al., 2014) 30

Table 3-2 – Specifications and imaging parameters of the micro-CT analyses. 36

Table 4-1 – Proximate analysis results. 54

Table 4-2 - The coal properties and modelling parameters used for the numerical simulation. 58

Table 4-3 – Geometric and modelling parameters used for the validation-models. 60

Table 4-4 – Simulation strategy of varying the Langmuir sorption constant (VL) and the Langmuir volumetric strain constant (εL), and the simulation results. 64

Table 5-1 – Parameters used for validation. 88

Table 5-2 – Parameters used in the model. 112

Table 6-1 - Typical characteristics of the Latrobe Valley brown coal (Sakaguchi et al., 2008). 127

Table 6-2 - Sample testing conditions and saturation time. 128

Table 6-3 - Imaging parameters and specification of the micro-CT analysis. 130

Table 6-4 - Proximate analysis results of the used coal type 151

Table 6-5 - Results of radially measured gamma-densities at three S-CO_2 interaction periods. 158

Table 6-6 - Axially and radially measured P and S wave delay times at three S-CO_2 interaction periods. 162

Table 6-7 - Computed axial and radial P and S wave velocities at three S-CO_2 interaction periods. 163

Table 6-8 – Results of the dynamic strength parameters at three stages of the experiment and the strength reductions with respect to the natural condition. 168

Table 7-1 – Parameters used for validation of the model under confined-stress condition. 187

Table 7-2 –Parameters used for validation of the model under unconfined-stress condition. 194

Table 8-1 - Ranges of the parameters used for regression analysis and machine learning techniques. 212

Table 8-2 - Model parameters and the network architecture of the ANN model. 216

Table 8-3 - Model parameters and the network architecture of the ANFIS model. 218

Table 8-4 - Statistical information of L-MRA 219

Table 8-5 - Testing data set with measured UCS values and predicted UCS values by L-MRA, NL-MRA, ANN and ANFIS models. 224

Table 8-6 - Statistical parameters used to assess the prediction performance of models 226

Page intentionally left blank

Part 1:

Introduction,

literature review,

experimental procedures

(Chapters 1, 2 and 3)

CHAPTER 1

Introduction

1 Introduction

1.1 Research background

The rapid growth in population and the recent industrial revolution have become the two primary drivers of global warming, due to the enormous amount of anthropogenic CO_2 continuously escaped to the atmosphere. The increment of atmospheric CO_2 level is mostly fuelled by human activities that primarily comes from vast destruction of forests and energy production from burning fossil fuels such as natural gas, oil, coal, etc. At the current rate of growth, the CO_2 level will reach the 500 ppm mark within next 50 years, consequently putting the Earth on track to hit a temperature boost of 2 ºC (IPCC, 2014). This, in turn, would cause extreme weather conditions and rise of sea level, possibly endangering the ecosystems and the global food supply, that imperil the Earth's activities in every possible aspect. Controlling the global climate change by mitigating the atmospheric CO_2 level has thus become a major concern of all the relevant parties.

Within a portfolio of options that aid in stabilising the anthropogenic CO_2 level, CO_2 sequestration in geological formations has been identified as a technically feasible and a safe option. The intention is to minimize the CO_2 emissions from reaching the atmosphere by capturing and systemically diverting them to a safer storage for a significant geological period. The method seems viable – for example, the Statoil petroleum company in Norway has successfully stored approximately 11 million tons of CO_2 in Sleipner gas field, between 1996 and 2008 (Van Alphen et al., 2009). According to the predictions of the International Energy Agency (IEA), approximately 94 Gt are to be sequestrated altogether from 2013 to 2050, in which the resultant percentage contribution of CO_2 sequestration to lower the atmospheric CO_2 level will reach about 12% of the total emission-reduction by 2050 (IEA, 2016). The statistics and the previous work confirm the competency of the technique; however, much work still remains in understanding the engineering and scientific underpinnings to improve the feasibility and to achieve the full potential of the sequestration process. The major challenge associated with the CO_2 sequestration is the maximization of the CO_2 storage quantity in a particular geological reservoir, while ensuring that the stored CO_2 remains entrapped safely for a significant geological period. Therefore, it is crucial to investigate the techniques of storing CO_2 in large quantities while avoiding CO_2 outbursts and back migration – for a safer and effective CO_2 sequestration process.

The potential geological formations for CO_2 sequestration include mature oil and natural gas reservoirs, oil/gas-rich shale formations, basalt formations, un-mineable coal seams, etc. Among these multiple geological mediums, coal seams have proven to be a better option, because the sequestration process can be often coupled with enhanced coalbed methane (ECBM) recovery – that further offsets the sequestration cost. Coal seams as better receptors for CO_2 have large pore surface areas – thus able to adsorb significant quantities of CO_2. Further, the superior adsorption capacity of CO_2 on to coal matrix concomitantly boosts the sweep efficiency of in-built methane, enhancing the CBM production. Previous studies show that one CH_4 molecule may be replaced by two CO_2 molecules during the gas exchange process, confirming the fact that coal seams act as net carbon sinks throughout the process.

Despite its advantages, the CO_2 sequestration in coal seams triggers numerous structural alterations due to intricate physico-chemical interactions occur between coal and CO_2, which in turn adversely affect the productivity of the sequestration process and the coal seam integrity in general. For instance, a typical coal mass comprises of maceral and mineral phases, an orthogonal micro-scale cleat system and a nano-scale pore network *(see Figure 1-1)*, in which the spatial disposition of each component causes heterogeneous and localized alterations, upon CO_2 interaction.

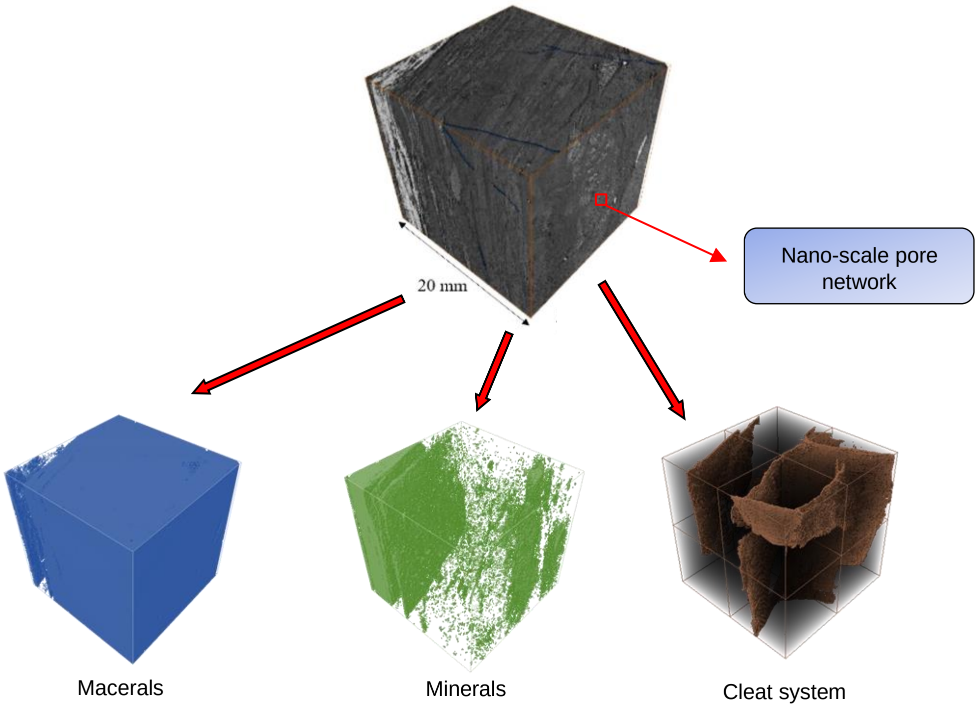

Figure 1-1 – Composition of a typical coal mass (modified after Sampath et al. (2019)).

Since the pressure and ground temperature increase with the depth, the pressure/temperature values of a typical coal reservoir are greater than the critical values of CO_2 (i.e. pressure - 7.38 MPa and temperature – 31.1 ^{0}C), under *in-situ* reservoir conditions. This, in turn, converts CO_2 into its supercritical-state, triggering complex physical and chemical interactions that adversely affect the coal structure. The CO_2 adsorption-induced swelling of coal matrices unfavourably affects the stress-dependent local fracture aperture and subsequently the fracture permeability, rendering considerable flow modifications in the seam. This can hinder the efficiency of the sequestration process by declining the long-term CO_2 injectivity into the seam. Moreover, the adsorption-induced plasticization of the coal's polymer structure converts the glassy-like coal structure to a rubbery material, imperilling the mechanical competency of the seam. The degradation of mechanical integrity may pose a massive threat of CO_2 leakage into the atmosphere, causing sequestration efforts risky. Hence, the analysis of CO_2 interaction-induced coal structural alterations has become critical in the context of CO_2 sequestration in coal seams.

1.2 Research gaps

Identification of research gaps is important in defining the objectives and the scope of the research project. Even though many studies are carried out on evaluating the CO_2 interaction-induced alterations in coal's structure, there exist significant margins and gaps for improvement in the knowledge; thus, should be addressed adequately. For instance, the complex CO_2 diffusion process in nano-scale coal pores and the CO_2 adsorption-induced coal matrix swelling should be further examined, in order to assess complex flow mechanisms and mechanical alterations occur in coal matrices. Although the fully-coupled processes during CO_2 sequestration are often simulated in single- or multi-continuum models, the effect of fracture network is quite dominant in coal – that requires a discrete fracture matrix (DFM) modelling approach to simulate the localized hydro-mechanical alterations and the flow modifications occur in fractured coal seams. Hence, it is important to conduct coupled simulations under *in-situ* reservoir conditions by incorporating the attributes of the coals' natural fracture network in the model geometries.

Further, since the mechanical degradation in CO_2-interacted coal is an extremely complicated process, which is dependent on multiple parameters and specific to the coal rank, more systematic experimental analyses are required to evaluate mechanical property alterations of different coal ranks under different reservoir conditions and CO_2 interaction environments. The experiments should be focused on analysing the effects of CO_2 interaction time, the combined effect of pore fluid+CO_2 interaction on coal mechanical properties and the localized damages induced by CO_2 interaction in heterogeneous coal mass. However, only the experimental analyses are not adequate to understand the general alteration trends. Therefore, more numerical and statistical studies, combined/validated with experimental analyses have to be conducted to understand the underlying physics and to precisely predict the strength alterations of coal, under a certain coal-CO_2 interaction condition. These evaluations should be aimed at evaluating the influence of specific reservoir properties on the overall hydro-mechanical alterations. These gaps should be effectively addressed for an in-depth understanding of the complex process – which is the motivation of the current research project.

1.3 Research objectives

The research objectives are defined based on the current state of available research, preceding information and the identified research gaps. The main objective of the research is to provide new insights into CO_2 sequestration in coal seams by comprehensively analysing the structural alterations occur in CO_2-interacted coal, in terms of its hydraulic and mechanical properties. This is achieved through the following sub-objectives:

1. Evaluate the alterations in CO_2 flow characteristics and the coal structure, induced upon the CO_2 injection into deep coal seams. This is done: i) by analysing multiple diffusion mechanisms in nano-scale pores and the CO_2 adsorption-induced deformation of coal matrix and then, ii) by developing a fully-coupled discrete fracture matrix (DFM) model to extend the hydro-mechanical alteration analysis to a fractured coal geometry.

2. Evaluate the CO_2-induced mechanical property alterations in coal: i) by conducting experimental analyses in the sense of static and dynamic mechanical testings, ii) by developing a fully-coupled numerical model to analyse the effect of the free and the adsorbed CO_2 on the alterations of mechanical properties and, iii) by developing statistical models with machine learning techniques to intelligently predict the alterations, using the experimental data.

If the detailed methodology of the doctoral research is considered, the complex coal structural alterations induced by CO_2 interaction are comprehensively evaluated, in terms of hydraulic and mechanical properties, through a series of advanced experiments, integrated with numerical and statistical modelling. The fully-coupled CO_2 flow–adsorption–deformation process in a single coal matrix block is modelled initially, and then the analysis is extended on a complex fracture geometry that represents an actual coal structure. Furthermore, the CO_2 interaction-induced mechanical property changes are experimentally evaluated with respect to static and dynamic mechanical properties. The effect of the free and the adsorbed CO_2 on the strength modifications of coal is modelled by developing a theoretically-extended cohesion model and validated with experimental results under both confined and unconfined conditions. Also, the experimental data are used to develop statistical models using soft computing techniques, in which the trained machine learning techniques are used to intelligently predict the CO_2-induced coal mechanical alterations. The main experimental program is backed up with a number of advanced imaging techniques and chemical analyses, including micro-CT, SEM/EDS, XRD and FT-IR analyses, where the alterations in coal chemical composition, maceral/mineral phases and natural cleat system are detailly analysed and used to interpret the primarily observed structural alterations. Conclusions, suggestions for future research and insight into field-applications are provided based on the research outcomes, in order to ensure an effective and safer CO_2 sequestration process in coal seams.

1.4 Thesis outline

This doctoral thesis is divided into 4 parts/9 chapters, including this introductory chapter. Part 1 provides an introduction to the research, parts 2 and 3 present the major research work based on the defined two research objectives, and part 4 provides the concluding remarks. Most of the chapters comprise of peer-reviewed journal publications, and where appropriate, chapter overviews, additional analyses, connective descriptions, summaries and conclusions are provided, complementing the published work. The summary of the thesis outline is illustrated in Figure 1-2, that conveys a general idea about the thesis structure.

Part 1: Introduction, literature review and experimental procedures

- **Chapter 1:** Introduction
- **Chapter 2:** Literature review
- **Chapter 3:** Experimental procedures

Part 2: Evaluation of CO_2 flow behaviour and the subsequent alterations in coal structure

- **Chapter 4:** Evaluation of CO_2 flow behaviour, adsorption and the mechanical deformation of coal matrix
- **Chapter 5:** Evaluation of fully-coupled CO_2 flow behaviour, adsorption and the mechanical deformation of fractured coal seams

Part 3: Evaluation of CO_2 interaction-induced mechanical property alterations in coal

- **Chapter 6:** Experimental analysis of static and dynamic mechanical property alterations in CO_2-interacted coal
- **Chapter 7:** Numerical analysis of free and adsorbed CO_2-induced mechanical property alterations in coal
- **Chapter 8:** Statistical analysis with machine learning techniques to predict the CO_2-induced mechanical property alterations in coal

Part 4: Concluding remarks

- **Chapter 9:** Conclusions, suggestions for future research and insight into field-applications

Figure 1-2 - Brief illustration of the thesis outline.

A detailed description of the content of each chapter is given below.

- **Chapter 1** provides the introduction to the research that includes the research background, research gaps, research objectives and the thesis outline. It presents an overview of the research by explaining the significance of the study, identified research gaps and a summary of how the research study was carried out. Further, the main and the sub-objectives of the research are defined, and a detailed description of the thesis outline is provided.

- **Chapter 2** consists of the state-of-the-art literature review, in which most pertinent previous studies are comprehensively reviewed to identify the research gaps and to gain the knowledge on the respective study areas. The complete review includes two major sections. The first section explains the previous understanding of CO_2 diffusion, adsorption and the deformation process and the consequent hydro-mechanical alterations occur in CO_2-interacted coal. Moreover, the section discusses the DFM modelling approach for simulating this fully-coupled process in fractured coal reservoirs. The second section elaborates the CO_2-induced mechanical modifications in coal, that deeply discusses the effect of several influential parameters on the coal strength such as stress-state, CO_2 pore pressure, CO_2 interaction time and coal seam characteristics. Both sections are partly covered with some of the most relevant segments extracted from two journal review papers, published in Journal of CO_2 Utilization (Q1 journal with impact factor of 5.19) and International journal of coal geology (Q1 journal with impact factor of 5.33). The corresponding bibliography is as follows.

  - Sampath K. H. S. M., Perera M. S. A., Ranjith P. G., Matthai S. K., Rathnaweera T., Zhang G., Tao X. (2017). *CH_4-CO_2 gas exchange and supercritical CO_2 based hydraulic fracturing as CBM production-accelerating techniques: A review*. Journal of CO_2 Utilization, 22, 212-230.

  - Sampath K. H. S. M., Perera M. S. A., Ranjith P. G., Matthai S. K. (2019). *CO_2 interaction-induced mechanical characteristics alterations in coal: A review*. International journal of coal geology, 204, 113-129.

  Furthermore, relevant connective sections are added to fill the uncovered sections, to integrate the work and to maintain the dissertation flow.

- **Chapter 3** presents the experimental procedures that include material, sample preparation, instrumentation and the analysing methods adopted in the entire study. Even though most of these details are described in their respective chapters, all the methods and techniques are generally summarised in this chapter. Depending on the nature of each experiment, systematic procedures were adopted for the sample acquisition and preparation processes such as sample coring, cutting and grinding. Detailed descriptions of each of these processes are provided in the first section. Then the physical and chemical characterisation methods of samples are described, including analysing parameters, instruments and relevant research facilities. Final section elaborates the primary experimental procedures carried out in each specific study to complete the research that includes descriptions of experimental setups, experimental conditions and data acquisition methods.

- **Chapter 4** belongs to part 2 of the dissertation and provides a numerical study of modelling the fully-coupled gas diffusion–adsorption–swelling process in a single coal matrix block. One of the major drawbacks associated in CO_2 sequestration process is the sorption-induced matrix swelling that hinders the CO_2 injectivity into the coal reservoir. Since the complete process is quite complicated that involves multi-physics couplings, a single matrix was initially modelled to analyse the diffusion, adsorption and the swelling process comprehensively, in which the simulations were validated with appropriate experimental data. The simulation procedure, validation, results and conclusions are presented in this chapter. The entire chapter is primarily covered by a journal paper, published in Fuel (Q1 journal with impact factor of 5.13). The details are as follows.
    - Sampath K. H. S. M., Perera M. S. A., Matthai S. K., Ranjith P. G., Li D. Y. (2020). *Modelling of fully-coupled CO_2 diffusion and adsorption-induced coal matrix swelling*. Fuel, 262, 116486.

- **Chapter 5** provides an extension to chapter 4, in which a modelling study of CO_2 flow behaviour, adsorption and the coal deformation is explained, by considering multiple matrix block interactions. Since the natural cleat system has a dominating impact on the flow behaviour, a fully-coupled DFM modelling approach was adopted in this study to simulate the hydro-mechanical alterations in fractured coal seams. The chapter comprises of two sections dedicated to single-phase and two-phase flow behaviours, where the single-phase modelling section is covered with a manuscript submitted to a peer-reviewed journal and the two-phase modelling is presented as a regular thesis section. The details of the submitted manuscript are as follows.
    - Sampath K. H. S. M., Perera M. S. A., Matthai S. K., Ranjith P. G. *Discrete fracture matrix modelling of fully-coupled CO_2 flow–deformation process in fractured coal*. Submitted in International Journal of Rock Mechanics and Mining Sciences (under review).

- **Chapter 6** belongs to part 3 of the dissertation and provides experimental results of CO_2-induced mechanical modifications in coal at the supercritical-phase of CO_2 – that mimics the *in-situ* reservoir conditions. The chapter consists of two sections that describe the static and dynamic mechanical property alterations, using UCS technique and ultrasonic wave measurement, respectively. The two sections comprehensively discuss 1) the effect of pore fluid+CO_2 saturation and the effect of CO_2 interaction time on static mechanical properties and, 2) effect of the spatial distribution of mineral/maceral phases and natural cleat system on the localized dynamic mechanical property alterations. The two sections are covered with two journal papers published in Engineering Geology (Q1 journal with impact factor of 3.91) and Journal of Petroleum Science and Engineering (Q1 journal with impact factor of 2.89). The corresponding bibliography is as follows.

- Sampath K. H. S. M., Perera M. S. A., Li D.Y., Ranjith P. G., Matthai, S. K. (2019). *Evaluation of the mechanical behaviour of brine+ CO_2 saturated brown coal under mono-cyclic uni-axial compression*. Engineering Geology, 263, 105312.
- Sampath K. H. S. M., Perera M. S. A., Li D. Y., Ranjith P. G., Matthai S. K. (2019). *Characterization of dynamic mechanical alterations of supercritical CO_2-interacted coal through gamma-ray attenuation, ultrasonic and X-ray computed tomography techniques*. Journal of Petroleum Science and Engineering, 174, 268-280.

- **Chapter 7** presents a numerical study of the CO_2-induced mechanical modifications in coal. The model results of the combined effect of the free CO_2 and the adsorbed CO_2 on the change in coal compressive strength is presented in this chapter, in which the results are validated with experimental data, under both confined and unconfined stress conditions. A theoretically-extended cohesion model is introduced to define the failure of CO_2-interacted coal, using the Mohr-Coulomb failure criterion. This chapter is primarily covered by one journal paper published in International journal of coal geology (Q1 journal with impact factor of 5.33), as mentioned below.
  - Perera M. S. A., Sampath K. H. S. M., (2019). *Modelling of free and adsorbed CO_2-induced mechanical property alterations in coal*. International Journal of Coal Geology, 217, 103348.

- **Chapter 8** explains a statistical modelling study, in which two machine learning techniques are adopted to predict the CO_2-induced strength modifications in coal, under different coal-CO_2 interaction conditions. Further, a comparison of the performance of machine learning techniques with traditional regression analyses is presented to confirm the models' accuracy and reliability. Also, the chapter includes a model fitting with current experimental data and predicting the long-term strength alterations in CO_2-interacted coal, using the trained models. One journal paper covers the entire chapter published in Measurement (Q2 journal with impact factor of 2.79), as mentioned below.
  - Sampath K. H. S. M., Perera M. S. A., Ranjith P. G., Matthai S. K., Tao X., Wu B. K. (2019). *Application of neural networks and fuzzy systems for the intelligent*

prediction of CO_2-induced strength alteration of coal. Measurement (London. Print), 135, 47-60.

- **Chapter 9** presents the concluding remarks and the recommendations for future work based on the research work done. Further, an insight into the field-application of CO_2 sequestration technique is provided referring to some of the extended experimental work done during the doctoral research. The particular sub-section is referred to a peer-reviewed journal paper, published in Fuel (Q1 journal with impact factor of 5.13) during the candidature. The corresponding publication details are as follows.
    - Sampath K. H. S. M., Perera M. S. A., Elsworth D., Ranjith P. G., Matthai S. K., Rathnaweera T., Zhang G. (2019). *Effect of coal maturity on CO_2-based hydraulic fracturing process in coal seam gas reservoirs*. Fuel, 236, 179-189.

CHAPTER 2

Literature review

2 Literature review

2.1 Chapter overview and structure

This chapter presents the comprehensive state-of-the-art literature review carried out with the pertinent previous research work to identify the potential research gaps and to obtain a comprehensive knowledge of the subject areas. The chapter consists of two main sections that cover the previous understandings of the entire research topic.

Section 2.2 provides a detailed discussion on the most relevant experimental (lab- and field- scale) and numerical work on coal-CO_2 interaction and how it generally affects the coal structure, in terms of the alterations in hydraulic and mechanical characteristics, and ultimately how it affects the productivity of the CO_2 sequestration process. Moreover, related to chapters 4 and 5, the section further discusses the 1) CO_2 flow behaviour in coal – including fracture flow behaviour and matrix diffusion, 2) the adsorption process – including theories and influential parameters, 3) the matrix swelling process and how it affects the local fracture aperture and then the permeability, 4) the importance of studying the fully-coupled gas flow–adsorption–deformation process, and 5) a review on the DFM modelling approach. Section 2.3 is related to chapters 6, 7 and 8 that expansively discusses the CO_2 interaction-induced mechanical modifications in coal. It provides a detailed discussion on the influential parameters of the mechanical degradation process, such as the stress-state, the CO_2 adsorption pressure and phase, the CO_2 interaction time and the coal seam characteristics. Moreover, it explains the causative factors that could be the reason for the overall alterations in mechanical strength, such as CO_2-induced plasticization of coal polymer structure, CO_2 adsorption-induced surface energy reduction, micro-cracks formation due to swelling and shrinkage, and mineral dissolution.

The two sections are covered with parts, extracted from two review papers published in Journal of CO_2 Utilization (Q1 journal with impact factor of 5.19) and International journal of coal geology (Q1 journal with impact factor of 5.33) during the doctoral research, as mentioned below.

- Sampath K. H. S. M., Perera M. S. A., Ranjith P. G., Matthai S. K., Rathnaweera T., Zhang G., Tao X. (2017). *CH_4-CO_2 gas exchange and supercritical CO_2 based hydraulic fracturing as CBM production-accelerating techniques: A review*. Journal of CO_2 Utilization, 22, 212-230.

- Sampath K. H. S. M., Perera M. S. A., Ranjith P. G., Matthai S. K. (2019). *CO_2 interaction-induced mechanical characteristics alterations in coal: A review*. International journal of coal geology, 204, 113-129.

2.2 CO_2 sequestration process and the associated structural alterations in coal

The CO_2 sequestration involves capturing and injecting vast quantities of CO_2 into coal reservoirs to safely storing them for a significant geological period. In the complete CO_2 sequestration process, the CO_2 is separated from flue-gas in firing plants, then injected into a seam that acts as a porous media. The injected CO_2 then flows through fractures, diffuses and adsorbs on to potential adsorption sites of the coal matrices (Ertekin, 1995). A number of questions should be resolved to ensure a productive and safer sequestration process: 1) the quantity of CO_2 that can be successfully injected to the candidate coal seam, 2) the time taken for the complete injection process, 3) the parameters that affect the injection process, 4) the alterations and the modifications of the reservoir, upon CO_2 injection, and 5) how it affects the reservoir integrity and the long-term sequestration process. These questions are often answered by conducting lab experiments and field-scale studies and by developing analytical/numerical models under particular *in-situ* conditions (Ozdemir, 2009).

Following sub-sections specifically discusses the coal-CO_2 interactions occur upon the CO_2 injection into the coal seam, subsequent alterations occur in the coal structure and how the complex process is analysed experimentally and numerically – by considering the underlying fully-coupled multi-physics and theories.

2.2.1 CO_2 interaction-induced structural alterations in coal (Sampath et al., 2017)

There exist three CO_2 storage mechanisms in coal: 1) structural- and stratigraphic-trapping as free gas phase in pores, 2) hydrodynamic-trapping as dissolved gas phase in coal seam water, and 3) adsorption-trapping as adsorbed gas phase in the coal matrix. Among these three mechanisms, the CO_2 adsorption on to coal matrix is more dominant due to large pore surface area in coal and the higher adsorption capacity of CO_2 (He et al., 2013). However, due to large sensitivity and the reactivity of the material, the coal-CO_2 interaction causes a number of physico-chemical interactions and consequently modifies the coal structure.

According to Goodman et al. (2005), the principal interaction between coal and CO_2 is physical adsorption that changes the coal macro-molecular structure, resulting in coal plasticization and matrix swelling. Larsen (2004) revealed that the CO_2 adsorption could swell the coal by up to 4% of its original volume, triggering substantial structural alterations. Moreover, the magnitude of the CO_2-induced coal matrix swelling is quite significant when compared to the other relatively non-reactive gases, such as He, N_2 and CH_4 *(see Figure 2-1 (a)).*

The CO_2 interaction-induced matrix swelling changes the 3D-anisotropic features of coal, such as fracture attributes, fracture permeability, coal porosity, mechanical parameters, etc. The fracture permeability is one of the most influential parameters in CO_2 sequestration, as it governs the CO_2 flow behaviour in coal and therefore, the CO_2 injectivity into the seam. However, many researchers have observed that CO_2 interaction-induced matrix swelling significantly reduces the fracture permeability due to fracture closure. The alterations in the coal cleat system due to CO_2 interaction has been visualized by Zhang et al. (2016) using micro-CT imaging technique under *in-situ* reservoir condition. The direct comparison of CT images before and after the CO_2 interaction confirms that most of the natural cleats have been disappeared or their apertures have been reduced due to matrix swelling under confined condition. It, in turn, adversely affects the fracture permeability, because the permeability is a direct function of fracture aperture and fracture connectivity. For instance, Botnen et al. (2009) showed that the matrix swelling might diminish the permeability of Lignite by a factor of 10 from its original value. Further, Figure 2-1 (b) compares the permeability variation with pore pressure between N_2 and CO_2, that confirms the adverse effect of CO_2 interaction on the coal permeability. This reduction in coal permeability hinders the CO_2 injectivity into the coal seam and consequently hampers the productivity of the CO_2 sequestration process. For an example, a significant reduction in CO_2 injectivity was experienced in the Fruitland Coal Fairway sequestration project, in which a reported drop from initial 7.08×10^4 m^3/day to 1.42×10^4 m^3/day was experienced only after a year of CO_2 injection (Oudinot et al., 2011).

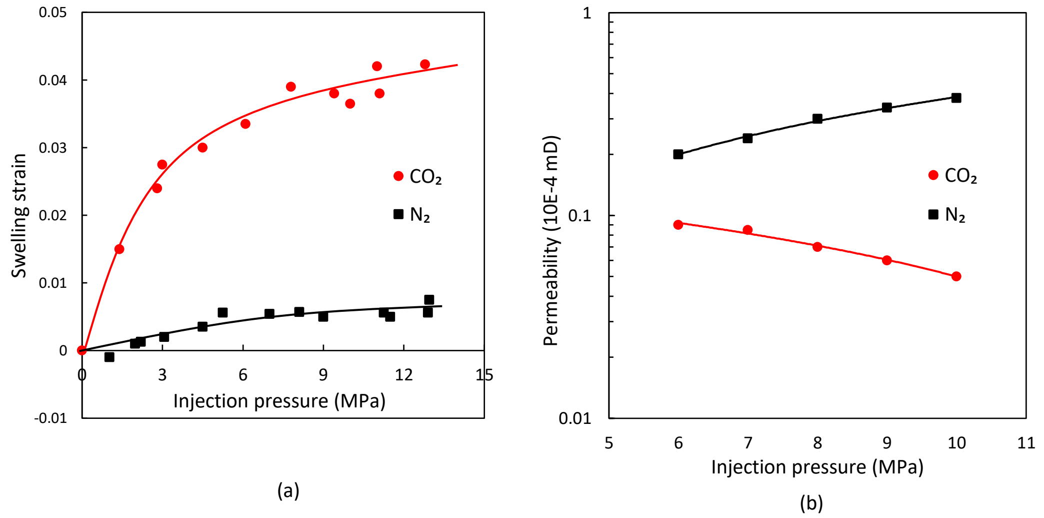

Figure 2-1 – Variation of a) matrix swelling and, b) permeability with increasing gas pore pressure: comparison between N_2 and CO_2 (modified after Pini et al. (2009)).

Except for the swelling-induced fracture permeability variations, several other structural alterations are reported by many scholars. For instance, the CO_2 interaction reduces the coal surface energy and consequently the mechanical properties such as, peak strength, cohesion, dynamic moduli, etc. (Meng and Qiu, 2018; Perera et al., 2013; Ranathunga et al., 2016; Ranjith and Perera, 2012). This is further discussed in section 2.3. CO_2 adsorption alters the coal macro-molecular structure, converting glassy-like coal structure to a rubbery material. It induces a plasticization effect in coal resulting in the matrix swelling (Gathitu et al., 2009; Masoudian et al., 2014). The CO_2 interaction under unconfined and confined conditions induce micro-cracks in coal due to free- and differential-swelling, that possibly changes the fracture characteristics and therefore the CO_2 flow behaviour in coal (Zhang et al., 2016). Moreover, according to Eq. 2-1, the carbonic acid formation due to CO_2 dissolution in pore fluids reduces the pH value of the respective pore fluid, resulting in an acidic environment and concomitantly dissolving the minerals such as Calcite, Dolomite, Kaolinite, etc. (Farquhar et al., 2015). The partial dissolution of the pore-filling minerals may alter the pore connectivity and the absolute porosity of coal (Zhang et al., 2018). Although, carbonic acid is unstable, it has enough time to degrade the surface, affecting the physical properties of coal. This itself forms a future problem to investigate.

$$CO_2 + H_2O \leftrightarrow H_2CO_3 \leftrightarrow H^+ + HCO_3^- \qquad \text{…………… [2-1]}$$

It is evident that the coal-CO_2 interaction causes severe structural alterations in every component of coal; thus, should be further investigated in detail. Although the results are well-observable experimentally, most of the alterations are specific to the coal type being tested and the corresponding experimental conditions. The next important step is to identify the underlying physics and the theories behind the alterations and implement them in numerical models to further simulate/analyse them accurately. The following sub-section discusses the implementation of numerical simulations, in which the fully-coupled CO_2 flow–adsorption–coal deformation process is elaborated comprehensively, relating to their underlying theories.

2.2.2 Fully-coupled CO_2 flow–adsorption–coal deformation process

The entire fully-coupled process involves the CO_2 flow through the coal fractures, diffusion into the coal matrices, adsorption and the resultant matrix swelling that changes the fracture aperture and the permeability. Implementing this whole process in a numerical model by mimicking the *in-situ* reservoir conditions requires several theoretical formulations and stress/displacement definitions at relevant domains and boundaries. A typical coal structure comprises of a natural cleat system built with face and butt cleats, where the coal matrices are formed along with the fracture network. During CO_2 sequestration, the cleat system controls the coal permeability, while the more intact matrices govern the CO_2 diffusion process and the adsorption process, and serve as potential sites for gas sequestration (Shi and Durucan, 2005). Theoretically, the coal structure can be approximated to a bundle of matchstick-geometry, that contains void spaces as fractures and separated homogenous blocks as coal matrices (Ma et al., 2011). The fully-coupled hydro-mechanical process adopted in numerical simulations consists of numerous theories and approximations defined for each process. Based on the previous modelling studies, the following theories have been incorporated in the current study to model the entire process.

- The CO_2 flow through the fractures is modelled with Darcy law (Darcy, 1856), by considering the longitudinal free and dissolved gas flows in the fracture domain.
- The diffusion in matrix domain is modelled with Fick's second law (Crank, 1979), by considering both effects of the free and the adsorbed gas (Saghafi et al., 2007). Moreover, the compound diffusion mechanisms in coal pores are further modelled using a theoretically-extended diffusion approach (Wu et al., 2016).
- The flux and the pressure continuities are preserved at the fracture-matrix interfaces to facilitate the fluid transfer between fracture and matrix domains.
- The CO_2 adsorption and the sorption-induced matrix swelling are modelled using Langmuir-type equations with appropriate coal-specific Langmuir-parameters (Harpalani and Schraufnagel, 1990; Langmuir, 1997).
- The coal matrix deformation is modelled with a Navier-type equation defined for linear poro-elastic material, with the inclusion of the sorption-induced stress and the pore pressure as external body forces (Cui and Bustin, 2005; Harpalani and Schraufnagel, 1990).
- The fracture permeability is defined as a function of local fracture aperture, assuming that a particular fracture is formed with two parallel walls of the corresponding bounding matrices (Witherspoon et al., 1980)
- Assuming that the deformed-fracture follows an elastic behaviour of a spring, the fracture stiffness is included with the constitutive relation of Hooke's law (Lepillier et al., 2019).
- Fracture fluid pressure is applied as a surface pressure at fracture-matrix interfaces to model realistic flow behaviours.
- Frictional interfaces and contact pairs are defined with Coulomb friction theory (Coulomb, 1773) and no-penetration rule (Agheshlui et al., 2018), respectively, where the two fracture surfaces are likely to get in contact during the deformation.
- Appropriate displacement and stress boundary conditions are applied in the geometry, mimicking the reservoir conditions.

The fully-coupled process is further illustrated in Figure 2-2 with their respective governing equations. The modelling procedure is further explained in chapters 4 and 5. It is evident that the entire procedure is quite complicated, in which the hydraulic and mechanical problems and the modelling parameter are inter-dependent on each other, that makes the process fully-coupled. Hence, an organized, methodical simulation approach is required to model the process accurately.

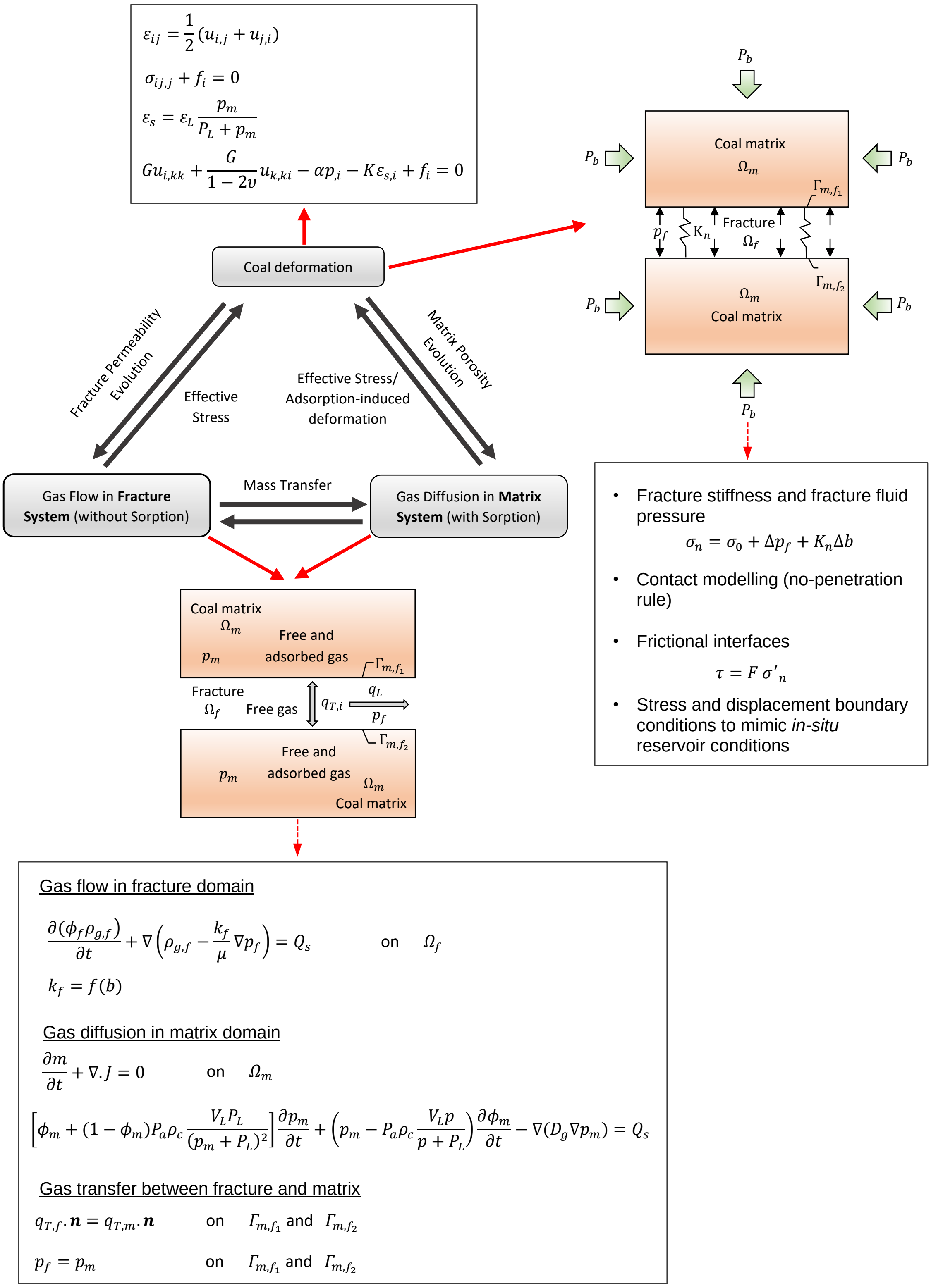

Figure 2-2 –Illustration of the fully-coupled hydro-mechanical process used in the numerical simulations.

2.2.3 Discrete fracture matrix (DFM) modelling approach to model the fully-coupled process

A number of modelling approaches are adopted in previous studies to model the gas flow–reservoir deformation in fractured geological mediums. The selection of the approach depends on the coupled-physics, geometry, accuracy and computational power. The fundamental choice is whether to represent the fracture network explicitly in the geometry or represent them implicitly with a suitable continuum model. There exist several modelling approaches with different accuracy and computational cost. For instance, 1) single-continuum models represent fractures by adopting the reservoir permeability. This method is straight forward and requires a low-level of computational complexity. 2) multi-continuum models are sets of methods that denote the fractured reservoir with many superimposed media, having specific constitutive laws and conservation equations. It is possible to separately represent the different domains using continuous variables and parameters (Arbogast et al., 1990). 3) discrete fracture network (DFN) models represent the fractures explicitly in geometry; however, they disregard the flow in the host medium (i.e. matrix). The flow is assumed to occur only in fractures, which is represented by a lattice. 4) discrete fracture matrix (DFM) models also characterize the fractures explicitly and assume the flow occurs in fractures as well as in matrix (Berre et al., 2019). The models consist of two domains – each for fractures and matrices, and the governing equations are defined in each domain by considering the transverse flow at fracture-matrix interfaces.

Since the effect of the fracture network is quite dominant in coal, the fracture network has to be explicitly represented in the geometry to evaluate localized spatial alterations (Berre et al., 2019). Further, the CO_2 interaction in the coal matrix has also to be considered as it governs the CO_2 diffusion, adsorption and matrix swelling. Attaining all these requirements, the DFM modelling approach is used in the current study as it treats fractures and matrices as separate objects and has provision to model the fully-coupled process explained in section 2.2.2. In the context of DFM modelling, there exist two basic approaches: 1) hybrid or mixed-dimensional models, in which the fractures are characterized by lower-dimensional elements compared to the matrices. In the flow equation discretization, fracture surfaces may be extended into equi-dimensional cells by virtually extending them perpendicular to the respective fracture surfaces. This method is well-suited for modelling complex fracture geometries, as it reduces the meshing complexity at narrow regions (Agheshlui et al., 2018). 2) equi-dimensional models represent both fractures and matrices with same order elements thus, quite straight forward, but require a massive computational power due to the finer meshes generated at narrow regions. *(see Figure 2-3)*. Since the current study involves multi-physics, including hydro-mechanical coupling, time- and stress-dependent fracture aperture variation, contact modelling, etc., adopting the latter approach is more appropriate, regardless of the large computational power. Therefore, the equi-dimensional DFM modelling approach is used in the current study to model the fully-coupled hydro-mechanical alterations, where the separate domains are defined for fractures and matrices (Tunc et al., 2012), and local fracture aperture is directly calculated from the deformed geometry in each time step – as the orthogonal distance between the bounding matrices of the corresponding fracture.

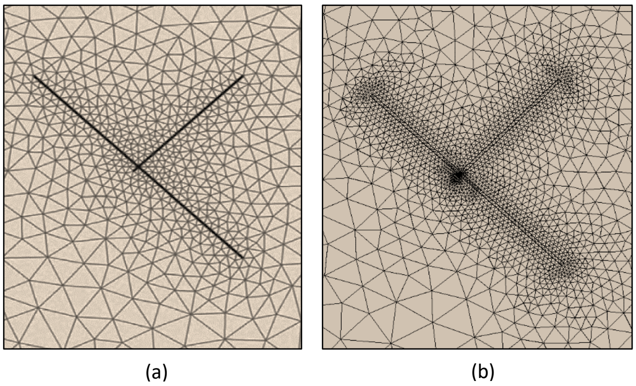

Figure 2-3 – Illustration of the meshing of a) mixed dimensional/hybrid DFM model and, b) equi-dimensional DFM model. Note that although equi-dimensional DFM modelling approach is straight forward, the complex mesh requires large computational power for the simulation.

2.3 CO_2-induced mechanical property alterations in coal (Sampath et al., 2019)

Coal seams' mechanical properties are directly related with the safety of the CO_2 sequestration process, and thus, it is essential to conduct an in-depth investigation on how coal-CO_2 interaction alters the mechanical competency of coal, in terms of widely used mechanical parameters, including compressive strength, Young’s modulus, brittleness index, etc. There are several studies available in the literature, confirming that CO_2 interaction adversely affects reservoir integrity due to mechanical degradation. They have shown that the process is quite complex and depends on many influential parameters. This section covers the effect of numerous influential parameters that cause the mechanical modifications in coal. All these aspects are discussed comprehensively by referring to the previous lab- and field-scale experimental studies and imaging studies that qualitatively and quantitatively analysed the alterations in the complex coal structure.

2.3.1 Influential parameters for the mechanical alterations

The interest in understanding the CO_2 adsorption-induced coal mechanical alteration emerged in the 1980s when many researchers started conducting studies on CO_2-treated coal (Ateş, 1987; Ates and Barron, 1988; Czapliński and Hołda, 1982; Gustkiewicz, 1985; Hiramatsu et al., 1983; Holda, 1986; Jackson, 1984; Vinokurova et al., 1988). Czapliński and Hołda (1982) used a ram-loading setup and a dynamometer to conduct crushing experiments on 4 mm coal cubes. Their results indicated that the extracted coal amount by crushing was high in the case of CO_2-treated coal, and the crushing resistance was reduced by 44% due to CO_2 adsorption. Holda (1986) extended the study by introducing CH_4 into the system, in which a greater strength reduction was observed in CO_2-interacted coal than that of CH_4- and air-interacted coal. Viete and Ranjith (2006) carried out the first UCS experiments on 54 mm × 108 mm core specimens, treated with CO_2 at a pressure of 1.5 MPa for 72 h and observed a decrease of uni-axial compressive strength (UCS) by 13% and Young's modulus by 26% in the CO_2-saturated samples. The studies prove that the evaluation of CO_2 interaction-induced coal mechanical behaviour runs back to many decades and have been continuously improved over time to provide more accurate and reliable results. The following sub-sections comprehensively evaluate the effect of several influential parameters on the CO_2 interaction-induced coal strength alterations.

2.3.1.1 Effect of confining stress

Although a substantial strength reduction was observed on coal tested under uni-axial condition, a number of studies revealed that the reduction of coal stiffness, tested under tri-axial condition is comparatively smaller. For instance, Viete and Ranjith (2006) conducted mechanical experiments on CO_2-saturated Australian brown coal samples, under uni-axial and tri-axial conditions. They observed a 13% strength reduction under uni-axial condition, but only a 0.43% reduction under tri-axial condition. Similarly, Ranathunga et al. (2016) observed a 21.25% UCS reduction in CO_2-saturated Australian brown coal and only a 10.17% strength reduction in the same coal rank, tested under tri-axial condition. The comparatively lesser strength reduction under confined condition can be explained in terms of mechanical strengthening effect and reduced CO_2 adsorption potential, under elevated *in-situ* stresses. As explained by Gentzis et al. (2007), Hoek-Brown criterion better represents the coal strength and well-explains the material strengthening effect with increasing confining pressure, which can make the material stronger and hard to fail.

2.3.1.2 Effect of CO_2 adsorption pressure and phase change

Two major studies are found in the literature, in which the coal strength reductions of two coal ranks, saturated under varying CO_2 sorption pressures were evaluated. Perera et al. (2013) conducted CO_2 adsorption experiments on bituminous coal with sorption pressure varying from 0 MPa to 16 MPa at 33 ºC, whereas Ranathunga et al. (2016) used Australian brown coal with a 0 MPa to 10 MPa CO_2 sorption pressure range at 35 ºC. The studies have selected temperatures and pressure ranges covering both subcritical and supercritical CO_2 phases to distinguish the effect of CO_2 phase change on coal strength. Both studies found a similar trend, where supercritical CO_2 adsorption causes a significant strength reduction compared to subcritical CO_2.

As reported by Bae and Bhatia (2006), the adsorbed amount of CO_2 on to coal matrix increases substantially with the CO_2 phase change from subcritical to supercritical. Perera et al. (2011) observed a greater coal matrix swelling of up to a factor of two, under supercritical CO_2 adsorption, compared to subcritical CO_2 adsorption. Hence, the significant strength reduction was related to the increased CO_2 adsorption under supercritical state and the consequent swelling of the coal matrix. Moreover, Kendall et al. (1999) observed a greater capacity of supercritical CO_2 for polymerization of organic compounds, which could lead to plasticization of coal structure in the presence of supercritical CO_2, contributing to further strength reduction.

2.3.1.3 Effect of CO_2 saturation time

Experimental procedures adopted by researchers used different CO_2 saturation times to treat the coal mass before mechanical loading. For instance, Ettinger and Lamba (1957) treated the samples for 13 h, Ates and Barron (1988) saturated for 24 h, Czapliński and Hołda (1982) treated for 48 h, Viete and Ranjith (2006) used 72 h, Vinokurova et al. (1988) treated for 3.5 days, Perera et al. (2013) treated for 7 days, Ranjith et al. (2010) treated for 14 days, Vishal et al. (2015) treated for 21 days, Bagga et al. (2015) treated for 25 and 45 days, etc. An attempt was made by Masoudian et al. (2014) to determine the optimum gas injection time and associated mechanical alterations, in which the samples were treated with CO_2 at 1 MPa confining pressure and CO_2 injection pressure for 24, 72 and 168 h, and subjected to tri-axial loading. Results suggested that 72 h is a reasonable period to allow for the CO_2-induced effects to develop, beyond which no significant strength alteration was observed *(see Figure 2-4 (a))*. Bagga et al. (2015) conducted a mechanical test on Indian coal, treated with CO_2 at 5 MPa pressure for 25 and 45 days. They found 41% and 65% of strength reductions, and 23.1% and 29.7% of Young's modulus reductions, after 25 days and 45 days of CO_2 saturation, respectively *(see Figure 2-4 (b)).*

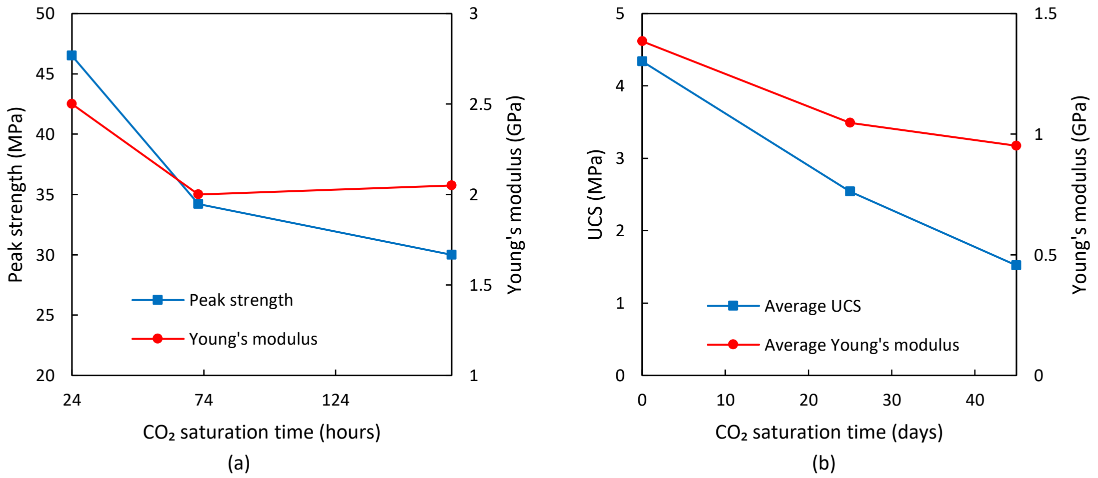

Figure 2-4 – Variation of strength and Young's modulus of a) Australian black coal and, b) Indian coal with CO_2 saturation time (modified after a) Masoudian et al. (2014), b) Bagga et al. (2015))

It is apparent that there is no standard or fixed CO_2 saturation period; thus, careful attention should be paid when comparing and interpreting literature. Since CO_2-ECBM projects are designed to sequester CO_2 for a significant geological period, the experimental results with low saturation periods may not particularly represent the actual conditions. Therefore, it is vital to further investigate how the coal strength alters with CO_2 saturation time.

2.3.1.4 Effect of coal seam characteristics

Even for similar CO_2 saturation conditions, the magnitude of the strength alteration can be varied, depending on the coal seam properties, such as coal rank, type, grade, bedding planes, cleat characteristics like cleat density and orientation, and *in-situ* stress field and orientation. A study was initiated by Ranjith and Perera (2012) to compare the effect of coal rank on CO_2 interaction-induced strength alteration. They used bituminous coal and Lignite, saturated with CO_2 at 1 MPa – 3 MPa pressures for 7 days. Results revealed that although there is a strength reduction in Lignite, the reduction is not as high as that of bituminous coal. In fact, the strength reduction in bituminous coal at 3 MPa saturation pressure was around 43%, which is about 4.5 times higher than the strength reduction in Lignite (9.6%) *(see Figure 2-5)*. Similarly, Jasinge (2010) found a 6.8% strength reduction of low-rank coal saturated with CO_2 under 5 MPa confining pressure and 3 MPa saturation pressure, which is significantly lower than the strength reduction found by Masoudian et al. (2014) on bituminous coal, saturated with CO_2.

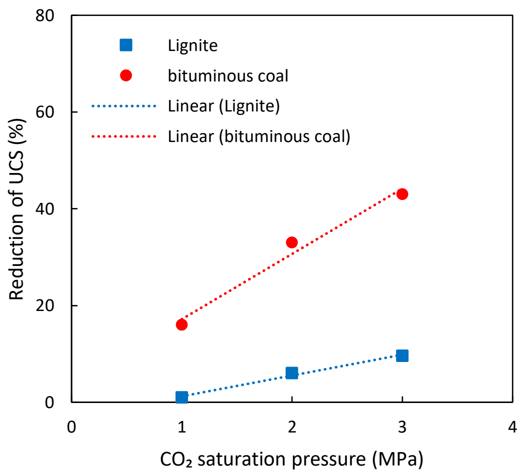

Figure 2-5 – Comparison of UCS reduction in bituminous coal and Lignite (modified after Ranjith and Perera (2012))

The observed difference may be partly due to the diverse chemical properties of coal ranks and the influence of it on the surface energy. Higher rank coals have more adsorption sites for CO_2 than lower rank coals, and consequently, they have more swelling potential upon CO_2

adsorption. Besides, the coal cleat system may also be a reason for the observed difference. According to Botnen et al. (2009) and Laubach et al. (1998), the coal cleat system develops with increasing maturity, where bituminous coal that has experienced a higher degree of coalification exhibits a well-developed cleat system, compared to low-rank Lignite. It is possible that the well-developed fracture network in high-rank coal provides easier CO_2 invasion, contributing to a larger strength reduction.

2.3.2 Causative factors for the CO_2 interaction-induced strength alterations

Above discussed studies confirm that CO_2 interaction causes mechanical strength alteration in coal, depending on CO_2 interaction conditions, its geo-environment and coal seam characteristics. However, the experimental results should be backed up and justified with proper theoretical explanations, as explained below.

2.3.2.1 Change in surface energy

One of the prominent theories established in explaining the CO_2 interaction-induced coal strength reduction is the adsorptive surface energy reduction, which is known as the 'Rehbinder effect' (da C Andrade et al., 1950). The effect postulates the strength reduction of material, due to change in the concentration of a surface-active adsorbate and consequently the surface energy, by combining two fundamental theories: 1) Gibbs adsorption equation (Gibbs, 1879) and 2) Griffith's failure criterion (Griffith, 1921). As apparent from Gibbs (1879)'s equation, surface energy of a material can be diminished due to: 1) an uncompensated increment of the concentration of an existing adsorbate, 2) any modification in the adsorption environment that enhances the chemical potential of an existing adsorbate, or 3) replacement of an adsorbate with another potential and highly-reactive adsorbate. Concurrently, Griffith (1921)'s failure criterion provides an expression for the material failure, based on the required tensile stress to create a new fracture surface. The reduction in surface energy would decrease the tensile stress at the fracture-tip, which is needed to create a new fracture surface. Consequently, any modification to the adsorbate-adsorbent system that causes surface energy reduction would result in a weakening of the material. By combining two theories, the strength reduction caused by the adsorption-induced surface energy reduction can be expressed as,

$$d\sigma = \sqrt{\frac{2E\sum_i(\Gamma_i d\mu_i)}{\pi a}} \qquad \text{............... [2-2]}$$

where, $d\sigma$ is stress change, E is Young's modulus, Γ_i is surface concentration of i^{th} adsorbate, $d\mu_i$ is chemical potential change of the i^{th} adsorbate and a is half-length of the fracture.

It is well-established that CO_2 is a highly-reactive adsorbate with a surface-active nature and a higher adsorption capacity. Thus, the adsorption of CO_2 on to the coal matrix can significantly affect the strength of the coal mass, due to associated surface energy reduction.

2.3.2.2 Plasticization and swelling effects

Another well-established explanation on the CO_2-induced strength reduction of coal is the plasticization effect, in which the coal is considered as a polymer-structure and CO_2 as a plasticizer. In fact, coal mass is typically considered as a glassy-structure at ambient temperature, where the energy required for the inter-molecular interactions are higher than the thermal-energy available. Therefore, the coal molecular structure is considered to be 'frozen' in place, which restricts the freedom of movement of coal-molecules, and the structure retains its shape and acts as a highly-brittle material, due to cross-linked macro-molecules (Green et al., 1991; Lucht et al., 1987). When CO_2 is in contact with coal mass, it re-arranges the coal structure into a newer form that has a higher entropy or a lower energy state, resulting in a reduction of the glass-transition temperature (Larsen, 2004). This transition from the glassy-state to the rubbery-state is usually considered as a possible reason for the CO_2 adsorption-induced swelling effect and consequent strength alteration. An attempt was made by Gathitu et al. (2009) and Masoudian et al. (2014) to visualize the change in coal surface before and after CO_2 saturation, through SEM imaging. Their images distinguish the features of natural and CO_2-saturated bituminous coal micro-structure. It is noticeable that CO_2-saturated coal exhibits a smoother surface and the structural features are generally smaller than those from the natural sample. The surface seems amorphous at some spots, which are possibly the plasticised parts of coal. Thus, the plasticization effect is considered as one of the governing phenomena that causes mechanical degradation in CO_2-interacted coal.

2.3.2.3 Swelling- and shrinkage-induced micro-cracking

The injection of CO_2 molecules into a water-saturated coal mass may cause a two-phase flow interaction process (Sun et al., 2016) that promotes the desorption of water molecules from the micro- and meso-pore structure of coal, upon the CO_2 invasion. This may result in a drying effect and possibly induce shrinkage cracks in the coal mass (Brenner, 1984), contributing to the strength reduction to some extent. For example, Wen et al. (2017), analysed the SEM images of two locations of a coal specimen, before and after CO_2 saturation. A direct comparison between images confirms that CO_2 interaction causes new micro-cracks, which are propagated from the existing fractures of the coal mass. Moreover, most of the previous CO_2 interaction and strength tests were conducted under unconfined condition, where the samples were allowed to simply react with CO_2 in a reaction chamber and tested under uni-axial condition, without applying any confinement on the samples. The absence of a confining pressure on the coal mass can cause a free and outward swelling, inducing more micro-cracks in coal internal structure. Overall, CO_2 adsorption causes micro-cracks due to shrinkage, differential- and free- swelling, and may be due to chemical interactions, contributing to the mechanical degradation in the coal mass.

2.3.2.4 Dissolution of minerals due to chemical interactions

Although coal is predominantly composed of macerals, the influence of the presence of minerals on CO_2 interaction cannot be omitted, especially in high-rank coal. Along with the coalification, minerals are formed in coal structure, which is often found as a filling material in natural cleats and pores. Even though most studies were focused on pure CO_2 interaction-induced alterations of dry coal, geo-environments with water+CO_2 systems may trigger numerous additional chemical reactions, conceivably contributing to the mechanical degradation in coal mass. As stated in Eq. 2-1, depending on the CO_2 solubility, formation of carbonic acid with CO_2 dissolution in formation water may decrease the pore fluid's pH value, which causes dissolution of minerals and release of ion from mineral surfaces (Apps et al., 2010). For instance, an analysis of SEM images extracted from a coal specimen before and after treatment with a CO_2+water system, clearly shows the dissolution of pore and cleat filling minerals after CO_2+water treatment (Guo et al., 2018). Such dissolution of pore and cleat filling minerals contributes to the strength reduction in coal mass by: 1) significantly reducing the bond-energy of the pore structure, 2) affecting the grain-to-grain contact in the coal mass (Feucht and Logan, 1990), and 3) creating secondary porosity systems, within primary pores (Marbler et al., 2013).

The facts discussed in section 2.3 confirm that CO_2 interaction causes severe mechanical property alterations in coal mass. However, since coal is an anisotropic and heterogeneous material, the mechanical alteration may be varied; thus, should be assessed properly by aiming at the specific reservoir characteristics, prior to the implementation of CO_2 sequestration projects.

2.4 Chapter summary

This chapter provides a comprehensive review of the effect of CO_2 interaction on coal flow and mechanical property alternations. The chapter covers two primary sections that are the CO_2 flow–adsorption–deformation process during CO_2 sequestration and the CO_2 interaction-induced mechanical alterations occur in complex coal structure. Major parts of the two sections are covered with parts extracted from journal review publications (Sampath et al., 2019; Sampath et al., 2017), produced during the candidature. The literature review was conducted to identify the current research gaps in the study area and to define the research objectives. Then, a comprehensive review on each aspect was carried out to gain the specific and in-depth knowledge on the corresponding areas before commencing the experimental, numerical and statistical analyses.

In summary, the literature review concludes that CO_2 flow–adsorption–coal deformation process is a complicated process that needs to be addressed effectively through experimental and numerical investigations. The numerical models should adopt DFM modelling approaches that explicitly represent the fracture network in geometry because the effect of the fracture network is quite dominant in coal, and the hydro-mechanical alterations can be highly-heterogeneous and localized. Further, the coal-CO_2 interaction causes severe modifications in mechanical properties and more studies are required to evaluate the temporal alterations, and the localized damages occur in anisotropic and heterogeneous coal masses. They should be evaluated experimentally in the sense of static and dynamic strength parameters, and the experimental results should be used to develop numerical and statistical models and to forecast the strength modifications under given *in-situ* conditions. The current research work was carried out based on this literature review and is presented in the subsequent chapters.

CHAPTER 3

Experimental procedures

3 Experimental procedures

3.1 Chapter overview and structure

This chapter outlines the materials, instruments and the analysing methods adopted in the study to complete the experimental analyses – that were conducted to obtain the required experimental data to understand the concepts and to validate the developed models. Although each method is discussed comprehensively in the respective chapter, a general overview is provided here to give a better approach to the thesis. Figure 3-1 illustrates the overview of the chapter, in which the sample acquisition and preparation, sample characterisation and analysing methods are categorized and listed, by referring to each chapter. Following sections explain each method in detail, including the testing procedures, testing parameters, corresponding instruments and the research facilities/platforms.

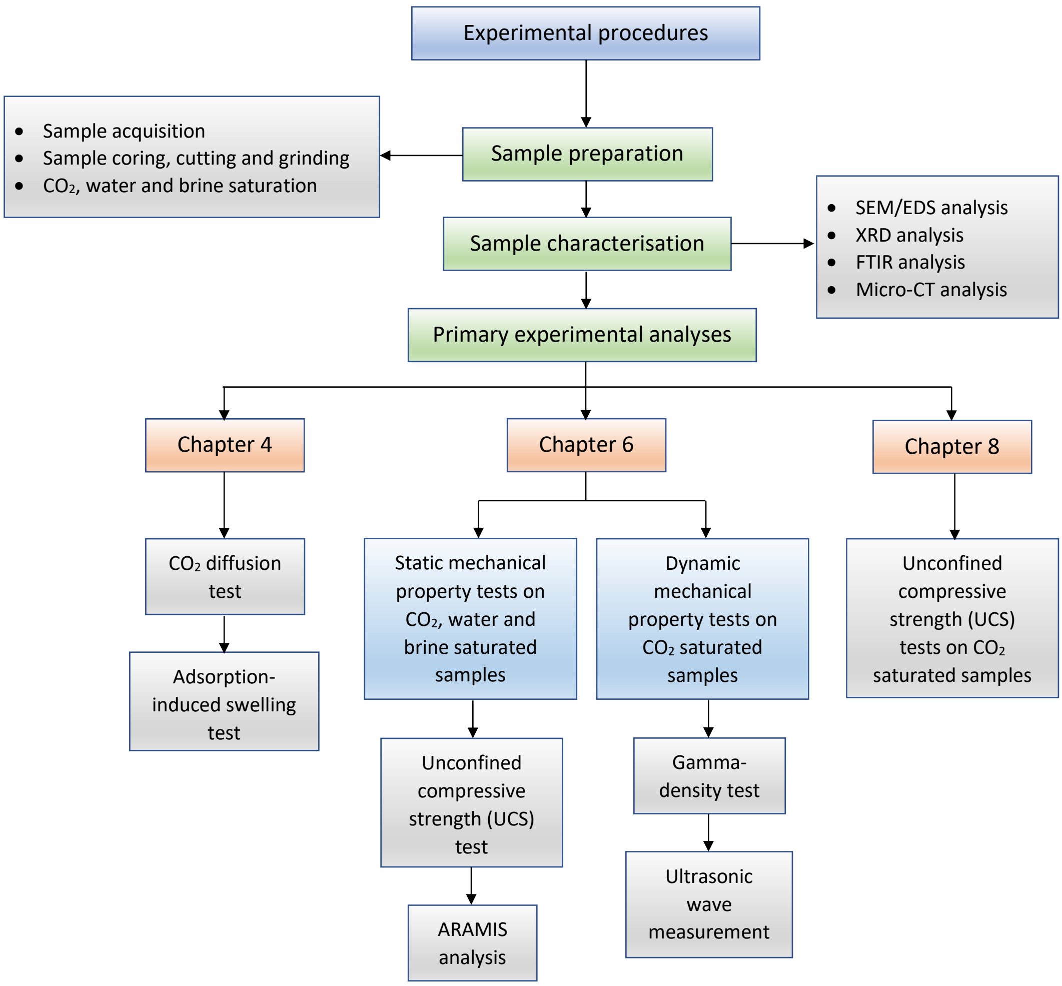

Figure 3-1 – Schematic diagram of the utilization of sample preparation, characterization and experimental analyses in each chapter.

3.2 Sample preparation

3.2.1 Sample acquisition

The analyses of the experiments were conducted with primarily two main coal ranks: 1) Lignite – acquired from Loy Yang mine, Latrobe Valley, Gippsland basin of Australia and, 2) High-volatile bituminous coal – obtained from Tashan mine, Shanxi province of China. The Loy Yang Lignite are formed later in the stratigraphic sequence and are low-rank Tertiary (Miocene) coal (Grigore and Sakurovs, 2016; Holdgate, 2005). However, the formation of Gippsland basin is related to the breakup of Gondwana that caused the separation of Australia from Antarctica (Bishop, 2000). The Tashan coal mine that belongs to Datong coal field in Shanxi province is formed in early Permian stage (Yu and Zhao, 2011; Zhu and Lin, 2015), hence is more matured and higher in rank.

The geo-graphical locations of Loy Yang mine, Australia and Tashan mine, China are given in Holda (1986) and Wu et al. (2017), whereas the stratigraphic sequences of Lignite and bituminous coal are given in Holdgate et al. (1995) and Zhu and Lin (2015), respectively. The coal samples were retrieved as blocks with approximate dimensions of 300 × 300 × 300 mm^3 from the mines and were double-sealed using polyethylene-films, immediately after retrieved from their respective mines. This was done carefully but immediately to prevent the moisture loss from the samples as much as possible. The sealed samples were then transported and kept in the fog room in deep earth engineering research laboratory (DEERL), Monash University until tested, in order to prevent any sample damage and moisture loss *(see Figure 3-2)*.

Typical characteristics of the two coal types are given in Table 3-1. Since both coal types are predominantly composed of maceral phase, it is important to quantify the maceral content of each coal type. According to Durie (1991) the maceral component alone in Loy Yang coal consists of 89.6% of Huminite (Vitrinite), 9.6% of Liptinite and 0.9% of Inertinite. Further, both maceral and mineral components of Bituminous coal from Tashan mine consist of 30% of Huminite (Vitrinite), 53.67% of Inertinite, 2.67% of Exinite and 13.67% of total mineral matter content (Wang et al., 2018).

Figure 3-2 – Acquisition of coal samples as blocks and double sealed with polyethylene-films until the sample preparation to prevent the moisture loss during transportation and storage.

Table 3-1 – Typical characteristics of coal types used in the study (Li et al., 2012; Sampath et al., 2018; Zhang et al., 2014)

Coal seam characteristics		**Values**	
		Lignite - Loy Yang mine	High-volatile bituminous coal – Tashan mine
Average bulk density		1130 kgm^{-3}	1460 kgm^{-3}
Average porosity		0.37	0.0423
Average unconfined compressive strength		1.45 MPa	9.95 MPa
Average Young's modulus		98.5 MPa	3.1 GPa
Proximate analysis	Fixed carbon[1]	48 %	62.4 %
	Ash[1]	1.5 %	8.2 %
	Volatile matter[1]	52.3 %	27.8 %
	Moisture[2]	59.4 %	1.6 %
Ultimate analysis	Carbon[1]	68.4 %	76.9 %
	Oxygen[1]	24.9%	7.2 %
	Nitrogen[1]	0.56 %	0.83 %
	Hydrogen[1]	4.9 %	4.3 %

[1] wt. % dry basis, [2] wt. % as received.

3.2.2 Sample coring, cutting and grinding

Since the static and dynamic mechanical testings were conducted on coal core samples, a systematic sample preparation procedure was adopted prior to testing. The complete preparation process involves sample coring, cutting and grinding to obtain coal core specimens with 76 mm in length and 38 mm in diameter, which was carried out in DEERL. Initially, the coal blocks were cored to a 38 mm diameter using the coring machine, that consists of adjustable core barrels with end-diamond cutters and has the capability of performing both wet and dry coring. The wet coring method was used to obtain smooth core walls and to prevent sample damage due to heat and friction *(see Figure 3-3 (a))*. Then the cored samples were cut to a length of about 80 – 82 mm with the diamond cutter, in which the wet cutting with a low cutting rate was adopted to prevent the sample damage *(see Figure 3-3 (b))*. Both ends of the cores were then ground with a rock grinder to get parallel, flat and smooth surfaces to make sure an even load distribution and to secure an exact length of 76 mm in the final core sample *(see Figure 3-3 (c))*. The prepared samples were wrapped in polyethylene films and preserved in the fog room in DEERL until the testing.

In preparation for the sorption-induced swelling experiment, another sample was cut into a 10 × 10 × 10 mm^3 matrix block, with the diamond cutting machine *(see Figure 3-3 (b))*. The sample was ground and polished to obtain even surfaces to affix strain gauges in order to measure the swelling strains. Further, a 10 mm in height and 20 mm in diameter cylindrical coal sample was prepared for the CO_2 diffusion test. Then the specimens were vacuum-dried for 48 h, in order to eliminate moisture, impurities or air entangled in the pores.

(a) (b) (c)

Figure 3-3 – Machines used for the sample preparation process: a) coring machine, b) cutting machine and, c) grinding machine.

3.2.3 CO_2 + water/brine saturation of coal

The core samples, prepared according to the description given in section 3.2.2 were vacuum dried for 24 h to eliminate any impurities in coal pores and to remove entrapped air. The water saturation was done using vacuum chambers, in which the samples were inserted in the chambers, filled with de-ionized water, sealed the chamber and connected to a vacuum pump to create a vacuum condition inside the chamber for a rapid and effective saturation *(see Figure 3-4 (a))*. The samples were allowed to saturate until the desired saturation level is reached, and then the saturated samples were retrieved and preserved until the mechanical testing.

Since most potential coal seams are saturated with brine with various NaCl concentrations, the saturations of coal specimens were done with brine to simulate accurate *in-situ* conditions, in which the effect of brine+CO_2 on the mechanical properties of coal is specifically analysed. The pure CO_2, water+CO_2 and brine+CO_2 saturations were conducted in high-pressure/temperature reaction chambers available in DEERL. The chambers are stainless steel cells having an internal diameter of 60 mm and a depth of 100 mm, which are connected to a temperature controller and a syringe pump to control the temperature and pressure, respectively. The cells have the capacities of 100 °C temperature and 50 MPa of cell pressure, that is ideal for CO_2 saturation experiments at supercritical-phase *(see Figure 3-4 (b))*. The experimental procedure includes: 1) inserting the samples into the cells, 2) filling with the relevant saturation solution, 3) sealing the cells and connecting to temperature and pressure regulators and, 4) increasing the pressure/temperature values up to the required level. Once, the desired levels were reached, the samples were allowed to interact up to a pre-defined period, during which the temperature and pressure values were monitored continuously and regulated at constant values. The saturated samples were retrieved from the cells after the desired saturation period by slowly releasing the cell pressure to secure the structural integrity of the samples during the pressure release. The retrieved samples were preserved until the mechanical testing.

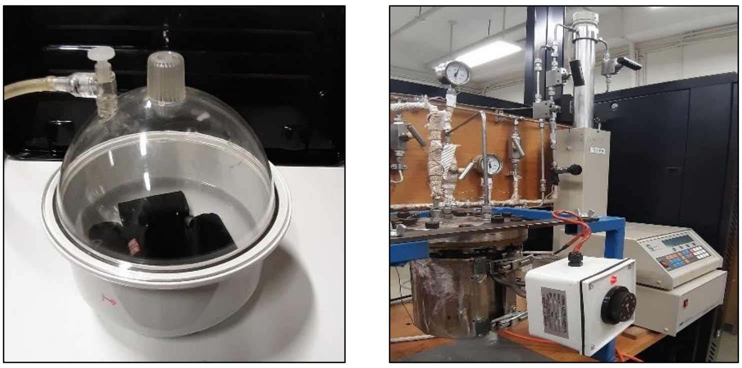

(a) (b)

Figure 3-4 – a) Vacuum chamber used to conduct water saturation and, b) reaction chamber used to conduct pure CO_2, water+CO_2 and brine+CO_2 saturations.

3.3 Sample characterisation

The detailed characterisation of the acquired coal samples has been done prior to testing, in order to identify the physical properties, chemical elemental composition, mineral/maceral composition and the micro-structural details. The characterisation results were used to discuss and interpret the primary test results.

3.3.1 Scanning electron microscope - energy dispersive spectrometry (SEM-EDS) analysis

SEM-EDS analyses were carried out before each experiment to determine the chemical components available in the specimens. This was done with an instrument accessible at TrACEES platform, geology node of the University of Melbourne *(see Figure 3-5 (a))*. The system is an OXFORD INCA that includes a liquid N_2 cooled Si-Li detector and an ATW2 thin detector window that allow the collection of x-rays between B and U. The analysis can identify the weight %, atomic %, etc. of a number of elements contained in coal including C, O, Al, Si, S, K, Cu, etc. *(see Figure 3-5 (b))*.

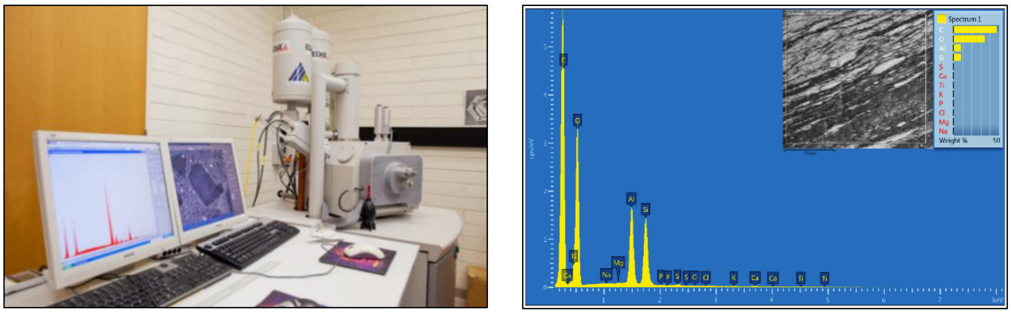

(a) (b)

Figure 3-5 – a) OXFORD INCA instrument used for SEM-EDS analysis and, b) typical SEM-EDS results indicating the elemental composition of a representative sample.

3.3.2 X-ray diffraction (XRD) analysis

Coal seams consist of a mineral phase, in which the quantity, quality and the spatial distribution vary with the coal rank and the formation process. The spatial disposition of the high-dense mineral phase introduces a considerable heterogeneity and anisotropy into coal, causing severe localized alterations during CO_2 interaction. Hence, detailed identification of the available mineral types in a particular coal sample is essential prior to the primary experiments. In order to detect the mineral types of coal specimens, XRD analyses were conducted at materials characterisation and fabrication platform (MCFP) of the University of Melbourne. Diffraction data were obtained with a Bruker-D8 X-ray diffractometer that includes Ni-filtered, Cu-kα radiation (1.54 Å) *(see Figure 3-6 (a))*. Data were collected with a step size of 0.02° between 5 – 85° 2θ, and a scan rate of 1.0 s/step. The diffracted background intensities at lower angles were minimized by an anti-scatter blade, in which an incident beam divergence of 1° was used with 2.5° Soller-slit in the diffracted beam. The sample was spun at 15 rpm. Phase recognition was done with *Diffrac.EVA V4.1* software with *ICDD PDF4+ 2018* database and quantitative Rietveld analysis was carried out using *Bruker Diffrac^{plus} Topas* software to quantify the identified crystalline phases. The analysis is able to identify several mineral types, including Kaolinite, Calcite, Siderite, Ankerite, etc., and their respective weight % in various coal ranks *(see Figure 3-6 (b))*.

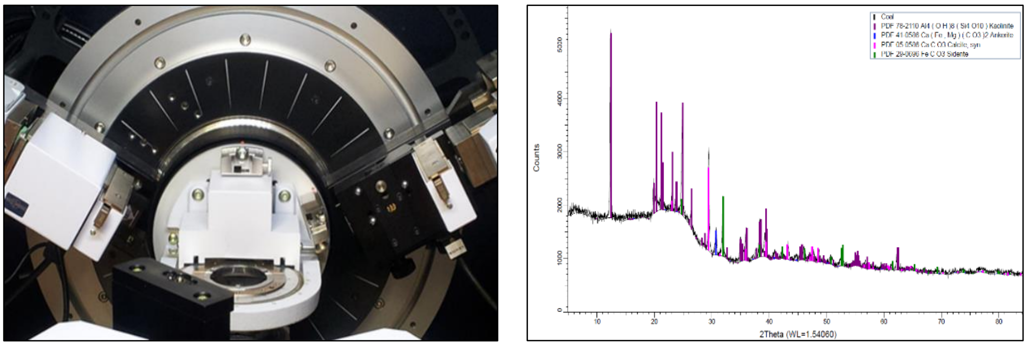

(a) (b)

Figure 3-6 – a) D8 advance diffractometer used for X-ray diffraction (XRD) analysis and, b) typical XRD results showing the mineral composition of a representative specimen.

3.3.3 Fourier-transform infrared spectroscopy (FT-IR)

Coal consists of a significant maceral phase that can be altered during CO_2 interaction, causing hydrocarbon mobilization and change in functional groups. Hence, detailed analyses on the coal macro-molecular structure before and after CO_2 interaction were carried out to distinguish such alterations, using FT-IR. The specimen preparation procedure includes mixing coal with finely ground Potassium bromide (KBr) in an agate mortar with coal: KBr weight ratio of 1:100 and forming pellets by pressing for 120 s at a pressure of 10 MPa. The KBr was kept at a temperature of 40 ºC to prevent moisture absorption. The FT-IR analysis was carried out with a Tensor 27 FT-IR spectrometer (Bruker Corporation of Germany) using the subsequent analysing parameters: 1) number of scans: 100/sample, 2) spectral region: 4000 cm^{-1} to 400 cm^{-1} and, 3) resolution: 4 cm^{-1}. The analysis was carried out 4 times for each condition (i.e. before and after CO_2 interaction), and the averaged resultant spectrums were considered for the interpretation, in order to get accurate and reliable results. The detailed procedure of sample preparation is shown in Figure 3-7. The resultant spectrums were used to detect the modifications in the coal macro-molecular structure that includes aromatic structures, aliphatic structures, oxygen-containing groups and hydroxyl groups.

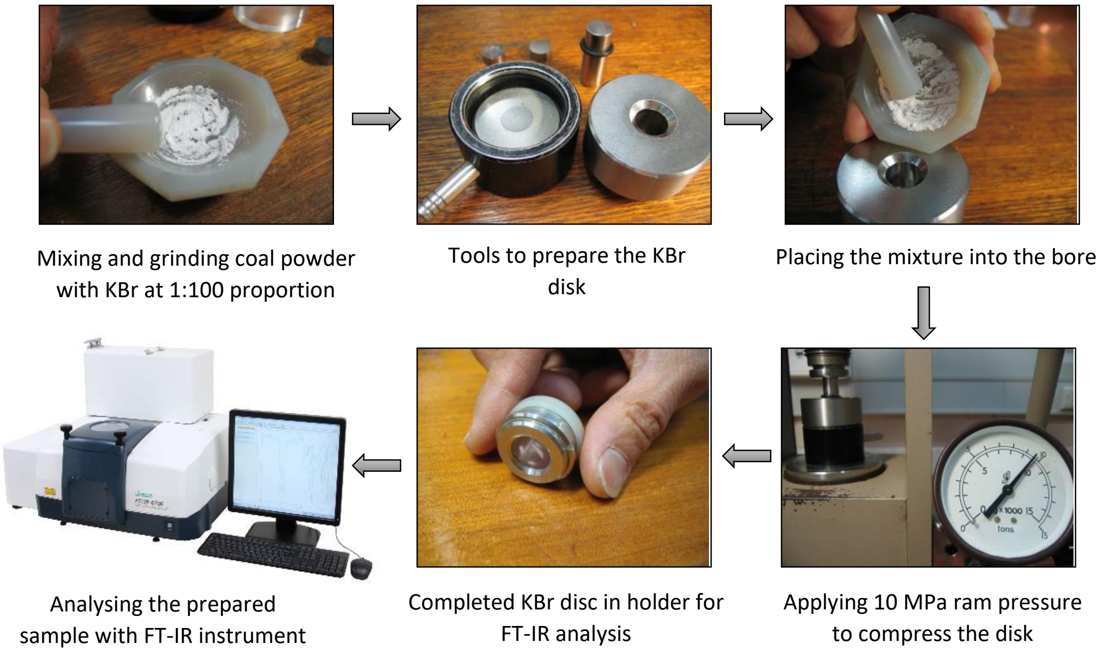

Figure 3-7 – Experimental procedure for FT-IR analysis.

3.3.4 Micro-computed tomography (Micro-CT)

Micro-CT analyses were conducted on coal specimens to evaluate the spatial disposition of mineral/maceral phases and the variation of fracture distributions. The analyses were done on natural samples and the samples after CO_2 saturation, compressive strength tests and CO_2-based fracturing tests. Since the whole core samples of 76 mm in length and 38 mm in diameter were needed to be scanned in most cases, Australian Synchrotron imaging and medical beamline (IMBL) facility was used for the micro-CT scanning. The x-ray beam and the other parameters in the Synchrotron facility have the capability of scanning large-scale samples at a sufficiently higher resolution *(see Figure 3-8 (a))*. Unlike the polychromatic beam in laboratory micro-CT scanning instruments, the monochromatic synchrotron radiation avoids the beam hardening effect and improves the image quality, while increasing the scanning speed. The X-ray source with high intensity enables high spatial resolutions in images, that is ideal for analysing micro-structural details in coal. The schematic diagram of the monochromatic X-ray beam transmitting through a sample is illustrated in Figure 3-8 (b). The imaging parameters and specifications of the micro-CT scanning utilized in the experiments are given in Table 3-2. The tomographic data reconstruction, stitching and the pre-processing were done with *XLICT-workflow* and *IMBL pre-processing* software in Synchrotron ASCI. The post-data analysis was carried out in M3 *MASSIVE* super-computer cluster at Monash University, in which the image segmentation, quantification, and visualization were done with *AVIZO 9.0* image analysis software.

(a)

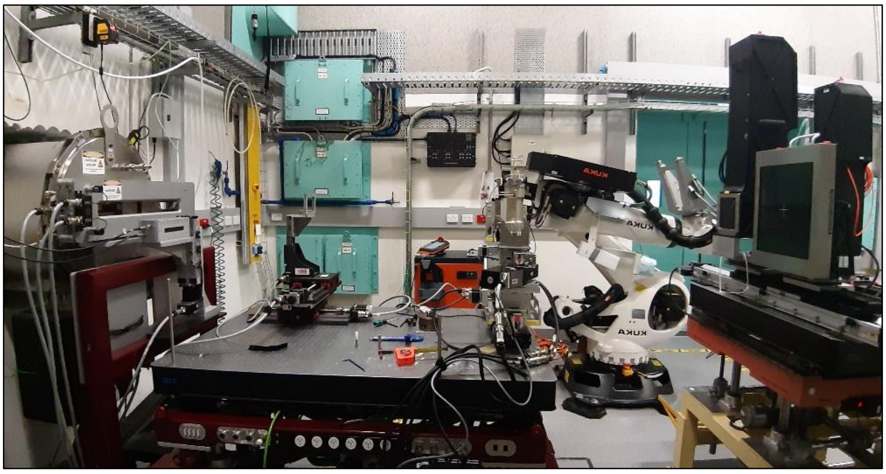

(b)

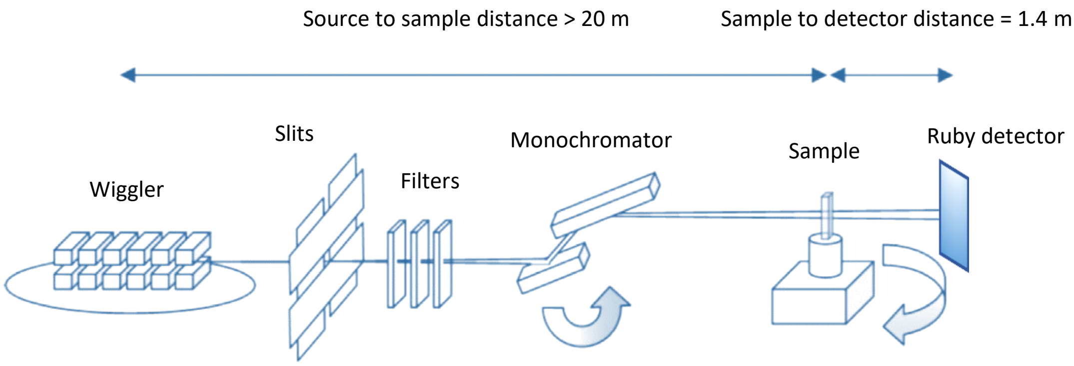

Figure 3-8 – a) Australian Synchrotron IMBL facility used for full-scale micro-CT analyses and, b) schematic diagram of monochromatic X-ray beam transmitting through a sample (modified after Stevenson et al. (2012)).

Table 3-2 – Specifications and imaging parameters of the micro-CT analyses.

Scanning parameters	**Specifications**
X-ray beam	Monochromatic
Scanning mode	Mode 3 – Hutch 3B
Detector type	Ruby detector with 20 μm screen and 150 mm lens
Energy of x-ray	40 keV (for Lignite) and 50 keV (for Bituminous coal)
Size of a voxel	16 μm
Distance from detector to sample	1.4 m
Filter	None
Total no. of projections	3 segments/sample, 1800 projections/segment

3.4 Primary experimental analyses

3.4.1 CO_2 diffusion experiment

The diffusion constant for modelling the CO_2 diffusion process in chapter 4 was found by conducting a laboratory diffusion test on a high-volatile bituminous coal specimen in DEERL. A coal matrix with 10 mm in height and 20 mm in diameter was allowed to interact with CO_2 in a reaction chamber at a constant temperature of 40 °C and a CO_2 pressure of 10 MPa for 72 h. The experimental setup is illustrated in Figure 3-9, which is a rock-tri-axial setup, specially modified for the purpose. Once, the system reached the full pressure equilibrium, the cell pressure was instantly brought to the atmospheric pressure by opening outlet valve and then it was immediately connected to a gas-flow meter, in order to record the temporal total gas count that diffused from the coal matrix. The recorded data were then fitted with a suitable analytical model to calculate the diffusion constant, as further explained in chapter 4.

3.4.2 CO_2 adsorption-induced coal swelling experiments

The numerical model validation explained in chapter 4 was done by conducting a CO_2 adsorption-induced swelling experiment, in which the volumetric swelling of a cubic coal matrix was measured with time and compared with the numerical results. The coal matrix block was prepared, as explained in section 3.2.2, and strain gauges were attached in the orthogonal directions on the sample to determine the volumetric swelling. The strain gauges are FLA-2 type, 2 mm strain gauges with high repeatability and reliability and operating temperature ranging from -20°C to +80°C. The test procedure is similar to that in section 3.4.1, where the cell was heated up to 40 °C of temperature and the cell pressure was increased up to 10 MPa by inserting CO_2 into the cell at an injection rate of 90 ml/min *(see Figure 3-9)*. The cell pressure was maintained constant, and the volumetric strain was measured with time until the sample reached the swelling equilibrium.

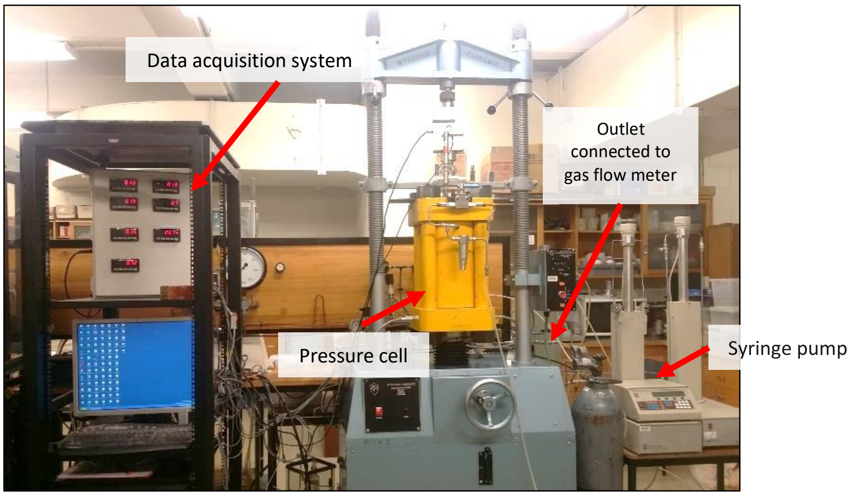

Figure 3-9 – Experimental setup adopted to conduct the CO_2 diffusion and swelling experiments.

3.4.3 Unconfined compressive strength (UCS) analysis

The mechanical strengths of natural and saturated core samples were measured with UCS tests using a Shimadzu AG9 uniaxial compression machine, a dual column electromechanical test frame – floor model, available in DEERL *(see Figure 3-10 (a))*. The machine has a loading capacity of 300 kN and a high-speed data sampling rate of 1 kHz that improves efficiency and ensures the capturing of minute strength alterations. The loading was applied with a displacement control method, where the loading rate was selected to achieve the failure of the sample within 2 – 15 min, according to ASTM guidelines (ASTM-D.2938). The load application and the axial displacement histories were recorded with a data acquisition system integrated with *DeFriend* software. Further, it is acknowledged that the *in-situ* confining pressure of potential coal seams can be increased up to 20 MPa, depending on their burial depths. Hence, tri-axial test results obtained from previous studies have also been used to validate models under confined conditions.

3.4.4 ARAMIS analysis

The axial strains and the lateral strains of the specimens during UCS tests were measured with ARAMIS photogrammetric equipment, which is an optical non-contact deformation measuring system *(see Figure 3-10 (a))*. A pair of highly-sensitive cameras were used to capture the speckle images in pixel format, and the sample deformations were recorded in the sub-micrometre range by following the discrete correlated areas of the captured images. In order to exclusively identify the correlated areas in the corresponding images, the test samples should have an adequate variation in tone and contrast. This was accomplished by painting the specimen core surfaces with matt-white colour, and then by spreading matt-black dots *(see Figure 3-10 (b))*. The stereo images were analysed with the *ARAMIS* software, and the axial and lateral strains during the loading were evaluated with an optical non-contact metrology system. The axial, lateral and volumetric strains were determined by averaging the strains at longitudinal- and cross-sections of the sample.

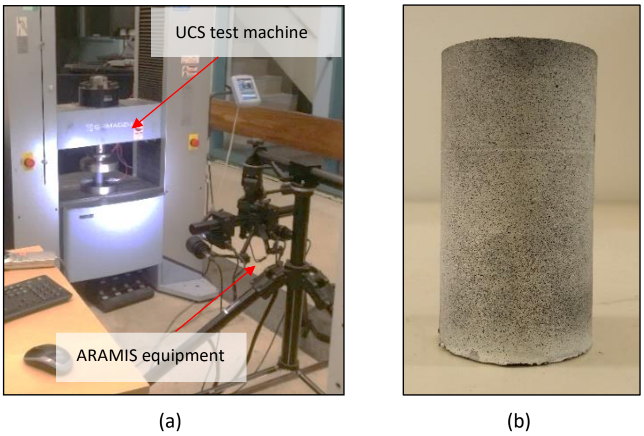

Figure 3-10 – a) UCS testing machine and the ARAMIS equipment and, b) prepared core sample for UCS and ARAMIS testing.

3.4.5 Gamma-density test

Experimental analysis done in Chapter 6 requires orientation-based densities of heterogeneous and anisotropic coal specimens, which was obtained using the gamma-ray attenuation method (GAM). The method is based on the gamma photon beam interaction with different components of the rock specimen, in which the probability of interaction process represents the linear attenuation coefficient (μ'). For heterogeneous rock specimens, μ' replicates the contributions from solid organic and mineral components, saturation fluid and air. Thus, bulk density is sensitive to the measured orientation and the wave path. A standard multi-sensor core logger (MSCL-S) from Geotek was utilized to measure the bulk densities of coal specimens at four radial directions, in order to distinguish the density variations (*see Figure 3-11)*. The gamma-ray source contains a radioactive 10 milli-curie Caesium-137 capsule, whereas the detector consists of an integral photomultiplier tube with a 3” thick NaI(TI) crystal. The core specimens were placed between the fixed source and detector, and were rotated around their longitudinal-axes to measure the densities at corresponding orientations. The obtained gamma attenuation values were used in a pre-calibrated model to determine the density values.

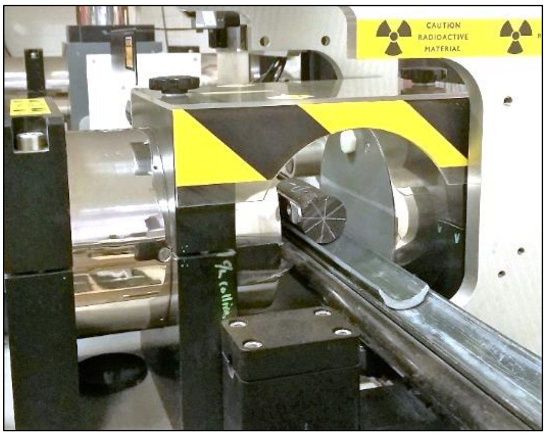

Figure 3-11 – Density measurement of the core sample using the multi-sensor core logger.

3.4.6 Ultrasonic wave measurement

Ultrasonic wave measurements were recorded by measuring the time taken by P and S waves to propagate through the considered core specimen. The delay times were used to compute the corresponding velocities and then to correlate to dynamic moduli through a developed set of pre-defined equations. The P and S wave velocities of heterogeneous coal samples were obtained with Pundit Lab+ device at pre-defined orientations that include one axial measurement and four radial measurements at 45^{o} intervals. The device consists of 250 Hz transducers, where the P and S wave ratio is less than -30 dB; thus, can generate both wave motions. The ultrasonic wave measurements were captured with a precision of 0.1 μs, at a time range of 0.1 - 9999 μs. The device was pre-calibrated using a standard rod prior to experiments, and the surfaces of the transducers were coated with a sonic-couplant for accurate wave measurements. Since the probe gains and the transmission amplitude should be adjusted to get legible waveforms according to the material being tested, following parameters were used during the measurements: 1) probe gain for P waves – 500×, 2) probe gain for S waves – 200× and, 3) pulse amplitude – 500 V. The transmitter to receiver distance through the sample, P and S wave delay times were incorporated to determine the corresponding velocities and subsequently the dynamic moduli at each measured orientation.

3.5 Chapter summary

This chapter summarises the sample preparation, characterisation and the experimental analysing methods used in this doctoral study to complete the defined objectives. The study content consists of a number of experimental analyses that were carried out to assess the flow and mechanical alterations, to validate the numerical models and to develop the statistical model. Since each analysing method is specific to the respective study and requires unique groundwork, systematic sample preparation processes were carried out prior to the main experiments – as explained in this chapter. Further, it is imperative to identify the features of the coal specimens used in the experiments, as the experimental results are largely dependent on the characteristics of the coal specimens. Therefore, detailed chemical and physical characterisations were also carried out on each sample to identify their intrinsic characteristics. The results were then used to interpret the main experimental results at the latter stages of the analyses.

Overall, the chapter discusses the sample acquisition from coal mines, sample preparation process including coring, cutting and grinding, sample saturation and sample characterising methods such as SEM-EDS analysis, XRD analysis and FT-IR analysis, and finally a sample imaging technique at micro-scale – i.e. micro-CT. Each description contains the procedure in detail, including the analysing parameters, instruments and the corresponding research facility or platform, where the analyses were carried out. Finally, the major experimental procedures relevant to the primary analyses – including diffusion tests, adsorption-induced swelling tests and strength tests were discussed with the details of their corresponding instrumentations. Moreover, schematic diagrams of the experimental setups and actual photographs of the samples and instruments are provided in each section for further clarification.

Part 2:

Evaluation of CO_2 flow behaviour and the subsequent alterations in coal structure

(Chapters 4 and 5)

CHAPTER 4

Evaluation of CO_2 flow behaviour, adsorption and the mechanical deformation of coal matrix

4 Evaluation of CO_2 flow behaviour, adsorption and the mechanical deformation of coal matrix

4.1 Chapter overview and structure

One of the unique features of coal seams compared to other geological reservoirs is its natural cleat system. Once CO_2 is injected to a coal reservoir during sequestration process, it first flows through the cleat system as a pressure-driven flow and then slowly adsorbs on to the cleats' surfaces and gradually diffuses into the coal matrix. The diffused CO_2 then adsorbs on to potential adsorption sites in the coal matrix, causing the matrix swelling. It is therefore clear that the CO_2 flow behaviour in coal involves several complex internal processes, coupled with each other. It is imperative to separately understand the flow behaviour in fractures/cleats and matrix, and the consequent mechanical deformation. Since a typical coal seam consists of countless coal matrices with different shapes and sizes, direct modelling of the fully-coupled process by taking all the underpinning physics into account is quite complicated. Hence, as the first step, this chapter is focused on understanding the CO_2 flow behaviour and mechanical deformation of the coal matrix by considering the underpinning coupled processes – i.e. diffusion, adsorption, and swelling.

A comprehensive experimentally-validated numerical model was developed to evaluate this process in a single coal matrix, in which the multiple diffusion mechanisms in nano-scale matrix pores under *in-situ* reservoir conditions were modelled using a theoretically-extended diffusion modelling approach. Moreover, the time- and pressure-dependent adsorption-induced matrix swelling was modelled, and the simulation was validated with experimental results for various coal types and matrix geometries. Finally, a sensitivity analysis was conducted to assess the effect of different parameters on the fully-coupled diffusion–adsorption–swelling process, including Langmuir constants, pore size, pore pressure, etc. The chapter comprehensively describes the entire study, which is presented as a peer-reviewed journal paper.

4.2 Journal paper: CO_2 diffusion and adsorption-induced swelling of coal matrix

This section is presented as the author-accepted manuscript of a peer-reviewed article published in "Fuel". The journal is a Q1 journal with impact factor of 5.13.

Citation:

- Sampath K. H. S. M., Perera M. S. A., Matthai S. K., Ranjith P. G., Li D. Y. (2020). *Modelling of fully-coupled CO_2 diffusion and adsorption-induced coal matrix swelling*. Fuel, 262, 116486.

Journal paper title: Modelling of fully-coupled CO_2 diffusion and adsorption-induced coal matrix swelling

Author's names: K.H.S.M. Sampath[1], *M.S.A. Perera[1], S.K. Matthai[1], P.G. Ranjith[2], Li Dong-yin[3]

[1]Department of Infrastructure Engineering, Engineering Block B, Grattan Street, Parkville, The University of Melbourne, Victoria 3010, Australia.

[2]Department of Civil Engineering, Monash University, Clayton Campus, Victoria 3800, Australia.

[3]School of Energy Science and Engineering, Henan Polytechnic University, Jiaozuo 454000, China.

Abstract

Multiple CO_2 diffusion mechanisms coexist in the coal matrix in certain pore pressure ranges, and the subsequent CO_2 adsorption-induced matrix swelling alters the hydro-mechanical properties of the seam. We investigate the CO_2 diffusion/adsorption-induced swelling behaviour of the coal matrix, through a fully-coupled gas flow–adsorption–coal deformation model. Besides the constant diffusion coefficient-based approach, the multiple diffusion mechanisms, including slip flow and Knudsen diffusion are further modelled with a theoretically-extended diffusion approach. The two models are validated with the CO_2 adsorption and volumetric swelling data to confirm the models' reliability on simulating the CO_2 diffusion/adsorption-induced swelling behaviour and to guarantee their time-dependent solving performance. The spatial and temporal analysis demonstrates that a larger fraction of matrix swelling occurs well before the coal matrix reaches its pressure equilibrium, confirming the fact that adsorption-induced swelling starts immediately with the coal-CO_2 interaction. The sensitivity analysis concludes that although the maximum adsorbed amount of CO_2 at the pressure equilibrium increases with the increasing applied CO_2 boundary pressure, the increment is not particularly linear, but gradually reaching a plateau at higher applied boundary pressures. The CO_2 adsorption and the coal matrix swelling are highly-sensitive to the Langmuir sorption constant and the Langmuir volumetric strain constant, respectively; thus, should be precisely determined for a given coal type – to accurately model the adsorption-swelling process. The extended diffusion approach reveals that the total flow conductance through the matrix increases moderately with the increasing pore pressure but

changes substantially with the pore radius. The slip flow increases exponentially with the pore pressure at large pore sizes (i.e. $r_t \geq 50\ nm$), in which almost 100% of the contribution is provided by the slip flow mechanism at pore pressures greater than 1 MPa. In contrast, at very low pore pressures (i.e. $p < 0.5\ MPa$), the Knudsen diffusion contributes almost 100% to the total flow conductance, irrespective of the pore size. With decreasing pore size, the contribution from Knudsen diffusion starts to increase, confirming that the Knudsen diffusion mechanism becomes predominant at relatively smaller pore channels, even at larger pore pressure conditions.

Keywords: *coal matrix, CO_2 diffusion, CO_2 adsorption, matrix swelling*

4.2.1 Introduction

CO_2 geo-sequestration and CO_2-enhanced coalbed methane (ECBM) extraction techniques involve the injection of CO_2 into coal reservoirs to safely sequester anthropogenic CO_2 while promoting the desorption of CBM from the coal seam (Sampath et al., 2017). The process exploits the stronger affinity of CO_2 to adsorb on to the coal matrix, resulting in effectively displacing the in-built methane. However, coal-CO_2 interaction is a complex multi geophysical-chemical process that significantly affects the sequestration mechanism due to alterations in the hydro-mechanical properties of coal. The polymer-like coal macro-molecular structure is readily subjected to CO_2-induced plasticization, causing the coal matrix swelling (Goodman et al., 2006) and, mobilization of hydrocarbons (Kolak et al., 2015) and dissolution of pore-filling minerals (Gunter et al., 1997) may alter the coal physico-chemical properties. The consequent permeability reduction declines the CO_2 injectivity, and the damaged mechanical competency poses risks of premature CO_2 break-through to production wells, rendering storage efforts ineffective and risky (Sampath et al., 2019b). In general, coal seams consist of a dual-porosity system, in which the macroscopic pore structure contains face and butt cleats that govern the coal permeability, whereas the intact coal matrix blocks contain micro-pores that control the CO_2 diffusion and adsorption, and act as principal reservoirs for gas storage *(see Figure 4-1 (a))* (Shi and Durucan, 2005). The injected CO_2 flows through the cleat system, diffuses through the coal matrix and adsorbs on to potential adsorption sites, causing the coal matrix swelling. The swelling of individual coal matrix blocks plays a significant role in gas migration through coal, as it governs the fracture aperture and the overall permeability of the seam.

Several experimental investigations and numerical modelling have been conducted to provide an insight into the complex physics-based structural alterations in coal (Chen et al., 2017; Sampath et al., 2019a; Sampath et al., 2019c; Shi and Durucan, 2003; Zhang et al., 2013; Zhang et al., 2016). In theoretical and numerical modelling, the coal structure is approximated to a matchstick or a cubic coal model with separated-individual matrix blocks in a stacked structure *(see Figure 4-1 (b))*. The influence of CO_2 adsorption-induced coal matrix swelling on the evolution of permeability and porosity was widely modelled based on this approach. In fact, Chen et al. (2010) investigated the impact of deformation of coal matrix on the CO_2 injectivity under *in-situ* conditions and found that the net-change in coal permeability associated with gas diffusion is significantly controlled by the differential matrix swelling and effective stresses. By coupling the gas diffusion in matrix micro-pores and mechanical deformation, Wei et al. (2019) found that gas adsorption causes significant alterations in the micro-pore structure and the consequent reduction in gas diffusion coefficient replicates the adverse effects on the gas transport. Liu et al. (2010) modelled the interaction of adjacent coal matrix blocks by providing contact bridges and proposed a new permeability model that couples the multi-physics of coal-gas interaction.

It is evident that although the macroscopic coal cleat system controls the major flow paths and permeability, the micro-porous coal matrix plays an imperative role on gas diffusion, adsorption and the overall hydro-mechanical properties of coal, due to CO_2 adsorption-induced matrix swelling. The complete process is governed by multiple properties of the coal matrix, including 1) pore size distribution and pore connectivity – that govern the gas diffusion mechanism in the matrix, 2) available adsorption sites – that govern the adsorption capacity and 3) swelling potential – that governs the coal deformation and controls the cleat permeability. Hence, the complex physical processes occurring in the coal matrix should be deeply studied through accurate modelling to understand the overall modifications in coal reservoirs. This study investigates the CO_2 diffusion and adsorption-induced swelling of an individual coal matrix block, through cross-coupling of multiple extended-diffusion mechanisms, variable porosity and adsorption-induced mechanical deformation. Accurate matrix pore attributes including effective porosity and equivalent pore radii were determined from a FIB-SEM-based pore characterisation analysis to incorporate in the model, which was then validated with CO_2 diffusion and adsorption-induced swelling experiments – conducted under supercritical-phase condition. The time- and pressure-dependent nature of CO_2 diffusion, adsorption and swelling were then studied through a sensitivity analysis.

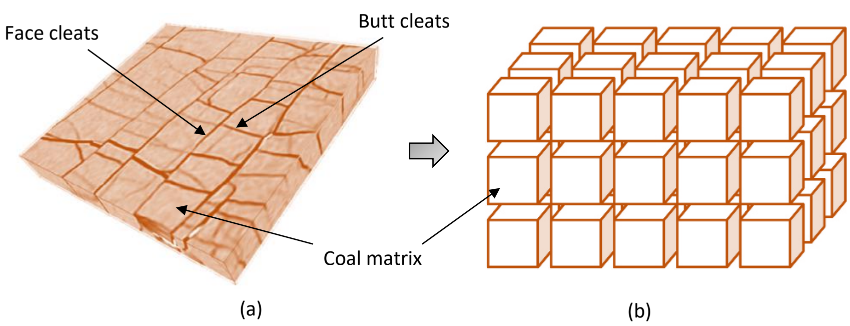

Figure 4-1 - a) Micro-CT image-based 3D-reconstruction of a coal section indicating face cleats, butt cleats and coal matrix blocks (Jing et al., 2016) and, b) representative approximation of coal structure.

4.2.2 The theoretical approach of CO_2 diffusion and adsorption-induced coal matrix swelling

This section explains the governing equations used for the fully-coupled diffusion, adsorption, porosity and deformation models. The derivations are based on the following assumptions: 1) the coal matrix is a homogeneous, elastic and isotopic continuum, 2) system is isothermal, and 3) gas contained within the pores is ideal.

4.2.2.1 Mechanical deformation model

The strain-displacement relationship for a homogeneous and isotropic medium is expressed as,

$$\varepsilon_{ij} = \frac{1}{2}(u_{i,j} + u_{j,i}) \quad \text{........... [4-1]}$$

where, ε_{ij} is the component of the total-strain tensor and u_i is the displacement component. The equilibrium equation is expressed as,

$$\sigma_{ij,j} + f_i = 0 \quad \text{........... [4-2]}$$

where, σ_{ij} is the component of the total-stress tensor and f_i denotes the body force component.

Gas transport causes significant modifications in effective stress, resulting in matrix deformation, in which the deformation is defined by a Navier-type equation for linear poro-elastic media, including pore pressure and adsorption-induced strain as additional body forces. The gas adsorption-induced strain (ε_s) is assumed to result in isotropic normal strains only, which can be treated analogously to thermal expansion in porous media (Palmer and Mansoori, 1996). Hence, the constitutive relation for the deformed coal matrix is expressed as,

$$\varepsilon_{ij} = \frac{1}{2G}\sigma_{ij} - \left(\frac{1}{6G} - \frac{1}{9K}\right)\sigma_{kk}\delta_{ij} + \frac{\alpha}{3K}p\delta_{ij} + \frac{\varepsilon_s}{3}\delta_{ij} \quad \text{........... [4-3]}$$

where, G is the shear modulus ($= E/2(1+\upsilon)$), K is the bulk modulus ($= E/3(1-2\upsilon)$), α is the Biot coefficient ($= 1 - K/K_s$), E is the Young's modulus, υ is the Poisson's ratio, K_s is the bulk modulus of the coal grains, $\sigma_{kk} = \sigma_{11} + \sigma_{22} + \sigma_{33}$, δ_{ij} is the Kronecker delta, and p is the gas pressure within the pores. Combination of Eqs. 4-1 – 4-3 yields the Navier-type equation, expressed as (Seidle et al., 1992),

$$Gu_{i,kk} + \frac{G}{1-2\upsilon}u_{k,ki} - \alpha p_{,i} - K\varepsilon_{s,i} + f_i = 0 \quad \text{........... [4-4]}$$

Eq. 4-4 is the governing equation for coal deformation, which accounts for the pore pressure and adsorption-induced deformation, in which the coupling term – the gas pressure (p) can be solved from the gas transport equation.

4.2.2.2 Porosity evolution model

In the numerical simulations, the variable porosity and the permeability are coupled with coal deformation. A number of porosity and permeability models such as Seidle-Huitt model (Seidle et al., 1992), Palmer-Mansoori model (Palmer and Mansoori, 1996), Shi-Durucan model (Shi and Durucan, 2004), Cui-Bustin model (Cui and Bustin, 2005) and Robertson-Christiansen model (Robertson and Christiansen, 2006) have been developed to account for the deformation-based alterations. Each model is developed under various assumptions; thus, is limited for specific stress/strain conditions. This study considers a more general porosity model, which accounts for the variable stress conditions (Zhang et al., 2008). The model assumes that the porosity is controlled by the effective volumetric strain (S), which is associated with the gas adsorption-induced volumetric strain, the grain volumetric strain and the matrix volumetric strain associated with the effective stress, that are inter-dependent on each other. Hence, the general porosity model can be expressed as,

$$\phi = \frac{1}{1+S}[(1+S_0)\phi_0 + \alpha(S - S_0)] \qquad \text{………… [4-5]}$$

where, ϕ is the porosity, $S = \varepsilon_V + p/K_s - \varepsilon_s$ and $S_0 = (P_0/K_s) - \varepsilon_{s_0}$. ϕ_0 and P_0 are the initial porosity and pore pressure, respectively. The initial volumetric strain $\left(\varepsilon_{V_0}\right)$ is assumed to be zero. The detailed derivation of the general porosity model is given elsewhere (Zhang et al., 2008).

The total matrix volumetric strain (ε_V) can be derived from Eq. 4-3 and is expressed as,

$$\varepsilon_V = -\frac{1}{K}(\bar{\sigma} - \alpha p) + \varepsilon_s \qquad \text{………… [4-6]}$$

where, $\varepsilon_V = \varepsilon_{11} + \varepsilon_{22} + \varepsilon_{33}$, $\bar{\sigma}$ is the mean compressive stress ($= -\sigma_{kk}/3$).

A Langmuir-type equation is used to model gas adsorption-induced volumetric strain (ε_s), as it has been identified as a reasonably accurate model through experimental verifications, to model the gas adsorption on coal (Harpalani and Schraufnagel, 1990).

$$\varepsilon_s = \varepsilon_L \frac{p}{P_L + p} \qquad \text{………… [4-7]}$$

where, ε_L and P_L are the Langmuir volumetric strain constant and the Langmuir pressure constant, respectively.

If the strains in the coal matrix are infinitesimal, i.e.,

$$S \ll 1 \; and \; S_0 \ll 1 \qquad \text{………… [4-8]}$$

Eq. 4-5 can be simplified as,

$$\phi = \phi_0 + \alpha(S - S_0) \qquad \text{………… [4-9]}$$

Moreover, in the present study, we assume that a single coal block matrix is deformed under unconstrained condition (i.e. free swelling). Hence, by combining Eq. 4-9, expressions for S and S_0 and the relationship between K and K_s, the general porosity model can be modified for unconstrained condition as (Chen et al., 2013),

$$\phi = \phi_0 + \alpha(\frac{\Delta p}{K}) \quad \text{……….. [4-10]}$$

The porosity model defines the interactions between the gas flow and the coal deformation. Ultimately, the porosity is a function of pore pressure (p), which acts as the cross-coupling term in the governing equations of coal deformation and gas transport.

4.2.2.3 Phase 01 - Gas transport model with simple diffusion analysis

The balance equation for gas transport is established based on the principle of mass conservation. The Fick's second law is applied to the coal matrix, assuming the spatial gradient of the mass flux is equal to the temporal derivative of the total gas content (Crank, 1979).

$$\frac{\partial m}{\partial t} + \nabla . J = 0 \quad \text{……….. [4-11]}$$

where, m is the total gas content, which includes free-phase gas (m_f) and adsorbed-phase gas (m_a) (Saghafi et al., 2007), and J is the total mass flux.

The free-phase gas content is expressed as,

$$m_f = \rho_g \phi \quad \text{……….. [4-12]}$$

where, ρ_g is the gas density. According to the equation of state, the gas density is proportional to the pore gas pressure (p) and is described as,

$$\rho_g = \frac{M_g}{ZRT} p \quad \text{……….. [4-13]}$$

where, M_g is the molar mass of gas, R is the universal gas constant, T is the temperature and Z is the correction-factor which accounts for the non-ideal behaviour of gas. From Eqs. 4-12 and 4-13, the free-phase gas can be written as,

$$m_f = \frac{M_g}{ZRT} \phi p \quad \text{……….. [4-14]}$$

Despite the heterogeneity of the adsorption sites in coal, the adsorbed-phase gas content can be expressed by the Langmuir-type model as,

$$m_a = (1 - \phi)\rho_{ga}\rho_c \frac{V_L p}{p + p_L} \quad \text{……….. [4-15]}$$

where, $\rho_{ga}(= M_g P_a/ZRT)$ is the gas density at standard conditions, P_a is the atmospheric pressure, ρ_c is the coal density, V_L and P_L represent the Langmuir sorption and pressure constants, respectively.

Hence, the total gas content is,

$$m = \frac{M_g}{ZRT}\phi p + (1-\phi)\frac{M_g P_a}{ZRT}\rho_c \frac{V_L p}{p+P_L} \qquad \text{........... [4-16]}$$

As the first phase of modelling, we assume a simple diffusion model with a constant diffusion coefficient, which is specific to the coal sample being considered. By combining Eq. 4-11 and the general form of Fick's law, the mass balance equation for this case can be written as,

$$\frac{\partial m}{\partial t} + \nabla.(-D_g M_g \nabla \mathrm{C}) = 0 \qquad \text{........... [4-17]}$$

where, D_g is the gas diffusion coefficient and C is the gas concentration that can be expressed by the real gas flow as,

$$C = \frac{n_f}{V_f} = \frac{p}{ZRT} \qquad \text{........... [4-18]}$$

where, n_f is free gas molar volume, V_f is free gas volume.

By adding Eqs. 4-16 and 4-18 into Eq. 4-17, the governing equation for gas diffusion in coal matrix with a constant diffusion coefficient can be derived and simplified as,

$$\left[\phi + (1-\phi)P_a\rho_c\frac{V_L P_L}{(p+P_L)^2}\right]\frac{\partial p}{\partial t} + \left(p - P_a\rho_c\frac{V_L p}{p+P_L}\right)\frac{\partial \emptyset}{\partial t} - \nabla(D_g \nabla p) = 0 \qquad \text{........... [4-19]}$$

The diffusion coefficient under a particular experimental condition can be obtained by plotting and fitting the diffusion data with a suitable analytical diffusivity model. In Eq. 4-19, the ϕ is a function of CO_2 adsorption-induced strain, which is dependent on the pore-pressure. Hence, Eqs. 4-4 and 4-19 are coupled through the porosity relation and the pore pressure evolution.

4.2.2.4 Phase 02 - Gas transport model with theoretically-extended diffusion analysis

CO_2 diffusion in the coal matrix is a complicated process that differs from other conventional reservoirs due to the intricate nano-scale pore network and the gas storage process. Since modelling the diffusion with a simple diffusion coefficient may be conservative for such a complex process, we extend the CO_2 diffusion modelling by considering multiple diffusion mechanisms. In general, the diffusion mechanisms are classified according to the Knudsen number (Kn), which is defined as the ratio of the molecular mean free path to the pore diameter that represents the degree of the collision of gas molecules with each other and pore walls. The molecular mean free path (λ) and the Knudsen number (Kn) are expressed as in Eqs. 4-20 and 4-21, respectively (Civan, 2010).

$$\lambda = \frac{\mu}{p}\sqrt{\frac{\pi ZRT}{2M_g}} \quad \text{........... [4-20]}$$

$$Kn = \frac{\lambda}{2r_t} \quad \text{........... [4-21]}$$

where, μ is the viscosity of gas and r_t is the pore radius.

As illustrated in Figure 4-2, the transport mechanism when $Kn < 0.001$ is known as no-slip flow or continuum flow, where the velocity of gas molecules of pore wall is zero and Darcy's law is valid. When $0.001 < Kn < 10$, the transport mechanism is considered as rarefied gas transport, in which the velocity of gas molecules of pore wall is no longer zero and Darcy's law is not valid. The rarefied transport mechanism can be subdivided to slip flow ($0.001 < Kn < 0.1$) and transition flow ($0.1 < Kn < 10$), which consists of Knudsen diffusion (Fathi and Akkutlu, 2012; Hadjiconstantinou, 2006). Free-molecular flow exists at $Kn > 10$ (Wu et al., 2016).

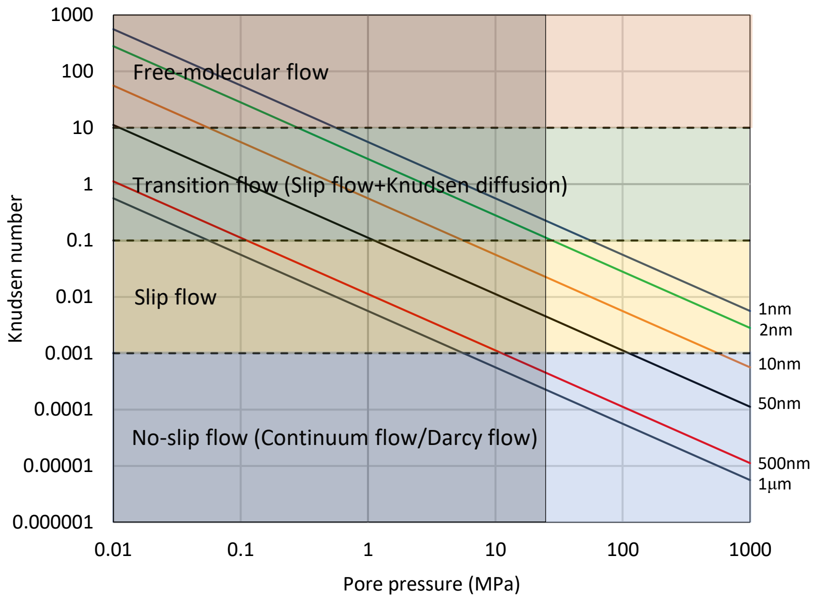

Figure 4-2 – Variation of Knudsen number with pore pressure for different pore sizes, highlighting the dominant flow mechanism ranges.

In a typical coal reservoir, the pore pressure varies approximately up to 20 MPa, which implies that multiple gas transport mechanisms coexist in the coal matrix in certain pressure ranges, depending on the pore size distribution. Furthermore, as highlighted in Figure 4-2, no-slip flow is not significant in matrix nano-pores (varying from 1 nm to 1 µm), under typical pore pressure conditions. Hence, it is apparent that the bulk gas transport in nano-pores is generally governed by slip flow, Knudsen diffusion and free-molecular flow. To replicate the complex gas diffusion, it is essential to derive a constitutive equation that describes the multiple diffusion mechanisms. Since the contribution from each mechanism is pressure- and pore size-dependent, linear-sum of each flux often results in errors. Wu et al. (2016) recently proposed a weight-based summation model to overcome this issue, which accounts for the Knudsen number and thus the pressure- and pore size-dependent contribution of each flux. In the current study, we assume that the total mass flux of bulk gas transport (J_b) through nano-pores is the result of a combination of slip flow and Knudsen diffusion with appropriate weights,

$$J_b = \omega_v J_v + \omega_k J_k \qquad \text{........... [4-22]}$$

where, J_b is the total mass flux for bulk gas transport, J_v is the slip mass flux, J_k is the Knudsen diffusion mass flux and ω_v, ω_k are the weighting factors for slip flow and Knudsen diffusion, as given in Eqs. 4-23 and 4-24, respectively. The weighting factors were derived by considering the ratios of nano-pore wall-molecule frequency and the ratio of the molecules' collision frequency to the total collision frequency (Wu et al., 2016).

$$\omega_v = \frac{1}{1+Kn} \qquad \text{........... [4-23]}$$

$$\omega_k = \frac{1}{1+\frac{1}{Kn}} \qquad \text{........... [4-24]}$$

The expression for slip mass flux is derived by making necessary modifications in the conventional no-slip flow equation. Gas transport in macro-pores when the inter-molecular collision is prominent is governed by the viscous flow in the bulk gas phase and is driven by the pressure gradient. Hence, the no-slip mass flux in a porous media with ϕ porosity can be described by the Hagen-Poiseuille equation as (Bird et al., 2007),

$$J_v = -\zeta_b \frac{{r_t}^2 p M_g}{8\mu ZRT} \nabla p \qquad \text{........... [4-25]}$$

where, ζ_b $(= \phi/\tau)$ is the correction factor for bulk gas transport in coal pores, τ is the tortuosity factor of porous media. The derivation of the ζ_b correction factor is given in Appendix 4A.

With the decreasing pore-size and consequently the increasing Knudsen number, the gas viscosity deviates from the definition of conventional gas viscosity due to rarefication effect. Hence, for the gas diffusion in nano-pores with large Knudsen numbers, no-slip flow is not applicable, but slip flow becomes dominant. By considering the rarefied and slip effects, the modified equation for the slip flow of gas can be expressed as (Karniadakis et al., 2006),

$$J_v = -(1 + \alpha' Kn)\left(1 + \frac{4Kn}{1-bKn}\right) \zeta_b \frac{{r_t}^2 p M_g}{8\mu ZRT} \nabla p \qquad \text{........... [4-26]}$$

where, $\alpha' \left(= \alpha_0 \frac{2}{\pi} \tan^{-1}\left(\alpha_1 Kn^{\beta}\right)\right)$ is rarefied effect coefficient, b is gas slip constant, α_1 and β are fitting parameters, and α_0 is rarefied effect constant when $Kn \to \infty$.

When $1 < Kn < 10$, the collisions between pore walls and gas molecules become prominent, and the gas transport mechanism is called the Knudsen diffusion, which can be written in the form of the pressure gradient. The Knudsen diffusion flux with negligible surface roughness and viscous effects in nano-pores is described as (Darabi et al., 2012),

$$J_k = -\frac{M_g D_K}{ZRT} \nabla p \qquad \text{………… [4-27]}$$

$$D_K = \zeta_b \frac{2r_t}{3} \sqrt{\frac{8RT}{\pi M_g}} \qquad \text{………… [4-28]}$$

where, D_K is the Knudsen diffusion coefficient for coal (Javadpour et al., 2007).

Combination of Eqs. 4-27 and 4-28, yields the Knudsen diffusion flux as,

$$J_k = -\frac{2}{3} \zeta_b \frac{r_t}{Z} \sqrt{\frac{8M_g}{\pi RT}} \nabla p \qquad \text{………… [4-29]}$$

By adding Eqs. 4-26 and 4-29 in Eq. 4-22, the total mass flux for bulk gas transport in nano-porous coal matrix with weighted slip flow and Knudsen diffusion can be expressed as,

$$\mathrm{J}_b = -\omega_v (1 + \alpha' Kn) \left(1 + \frac{4Kn}{1 - bKn}\right) \zeta_b \frac{{r_t}^2 p M_g}{8\mu ZRT} \nabla p - \omega_k \frac{2}{3} \zeta_b \frac{r_t}{Z} \sqrt{\frac{8M_g}{\pi RT}} \nabla p \qquad \text{………… [4-30]}$$

Hence, the equation for gas transport in the coal matrix with extended diffusion mechanisms can be expressed by adding Eqs. 4-16 and 4-30 in Eq. 4-11.

$$\left[\phi + (1 - \phi) P_a \rho_c \frac{V_L P_L}{(p + P_L)^2}\right] \frac{\partial p}{\partial t} + \left(p - P_a \rho_c \frac{V_L p}{p + P_L}\right) \frac{\partial \emptyset}{\partial t} - \nabla . \left(\left(\omega_v (1 + \alpha' Kn) \left(1 + \frac{4Kn}{1 - bKn}\right) \zeta_b \frac{{r_t}^2 p}{8\mu} + \omega_k \frac{2}{3} \zeta_b r_t \sqrt{\frac{8RT}{\pi M_g}}\right) \nabla p\right) = 0$$

………… [4-31]

The mass flux in Eq. 4-31 is derived by approximating the nano-pore network of the coal matrix to a bundle of nano-channels model, where the pore radius r_t is defined as the average radius of a single nano-channel. Since the total mass flux is significantly dependent on the pore size, defining a suitable pore radius is imperative for accurate modelling of a particular coal matrix. In the present study, we used pore network data obtained from a FIB-SEM analysis (Zhou et al., 2017) on a similar rank coal matrix block to determine the pore size distribution and subsequently the equivalent pore radius for modelling. The equivalent pore radius was derived by equating the total mass flow through the porous media to that of the bundle of nano-channels model – that consists of nano-channels with exact pore sizes and frequencies *(see Eq. 4-32)*, as in the original coal matrix. See Appendix 4A for the detailed derivation.

$$r_t = \sqrt{\frac{\sum_{i=1}^{m} n_i {r_i}^4}{\sum_{i=1}^{m} n_i {r_i}^2}} \qquad \text{………… [4-32]}$$

where, r_i is the radius of the i^{th} pore size and n_i is the frequency of the pores with r_i radius.

4.2.3 Experimental analysis

The experimental analysis was designed 1) to determine the CO_2 diffusion coefficient of coal – to use in the first phase of modelling and 2) to measure the CO_2 adsorption-induced volumetric strain with time – to use for the model validation. The maximum pressure and temperature values were selected to simulate the *in-situ* conditions and the supercritical-phase of CO_2, by considering the geothermal gradient and the overburden pressure of potential coal seams.

4.2.3.1 Sample acquisition, characterization and preparation

The coal samples were acquired from Tashan coal mine in Shanxi province, China. Table 4-1 illustrates the results of the proximate analysis, according to which the coal rank was classified as high-volatile bituminous coal. The samples were selected from cleats-free areas to represent the pure coal matrix. One sample was prepared for adsorption-induced swelling experiment by cutting into a cubical block with 10 × 10 × 10 mm^3, using diamond cutting machine in deep earth engineering research laboratory (DEERL), Monash University, Australia. The sample was then ground to achieve smooth surfaces to attach the strain gauges and to measure the swelling-induced strains. Moreover, a cylindrical coal disk with 20 mm diameter and 10 mm height was prepared for the CO_2 diffusion experiment. Prepared samples were vacuum dried for 48 h, prior to experiments to remove air, moisture or impurities entrapped in coal pores.

Table 4-1 – Proximate analysis results.

Composition	% by weight on dry basis
Moisture	1.20
Ash	13.35
Volatile matter	25.40
Fixed carbon	60.05

4.2.3.2 CO_2 diffusion experiment

CO_2 diffusion experiment was conducted in a high-pressure reaction chamber in DEERL, as illustrated in Figure 4-3. The prepared coal disk was placed in the pressure cell, and the cell was degassed for 24 h by a vacuum pump to remove the air inside the cell. Then, the cell was heated and maintained at a constant temperature of 40 ^{o}C, using the heating element. The heated cell was injected with CO_2 at 90 ml/min flow rate using a syringe pump, and the cell pressure was maintained at 10 MPa for 72 h to achieve the CO_2 adsorption equilibrium in the sample. After the equilibrium, the outlet valve was opened suddenly, bringing the cell pressure rapidly back to the atmospheric pressure. Once the atmospheric pressure was reached, the outlet was connected immediately to a gas flow meter, and the total gas count that desorbed and diffused through the sample was measured with time. The experimental data were fitted with an appropriate analytical diffusivity model to determine the CO_2 diffusion coefficient.

4.2.3.3 CO_2 adsorption-induced coal matrix swelling

Three strain gauges were affixed on orthogonal surfaces of the prepared cubical coal sample to monitor the strains in the three orthogonal directions and to calculate the volumetric strain. The experimental procedure is similar as in section 4.2.3.2, in which the sample was placed in the cell, degassed and heated up to the temperature of 40 ^{o}C. Then, the CO_2 was injected at a constant flow rate, and the cell pressure was allowed to reach up to 10 MPa, within 60 mins and maintained constantly throughout the experiment, while the strain gauge measurements were recorded continuously with time.

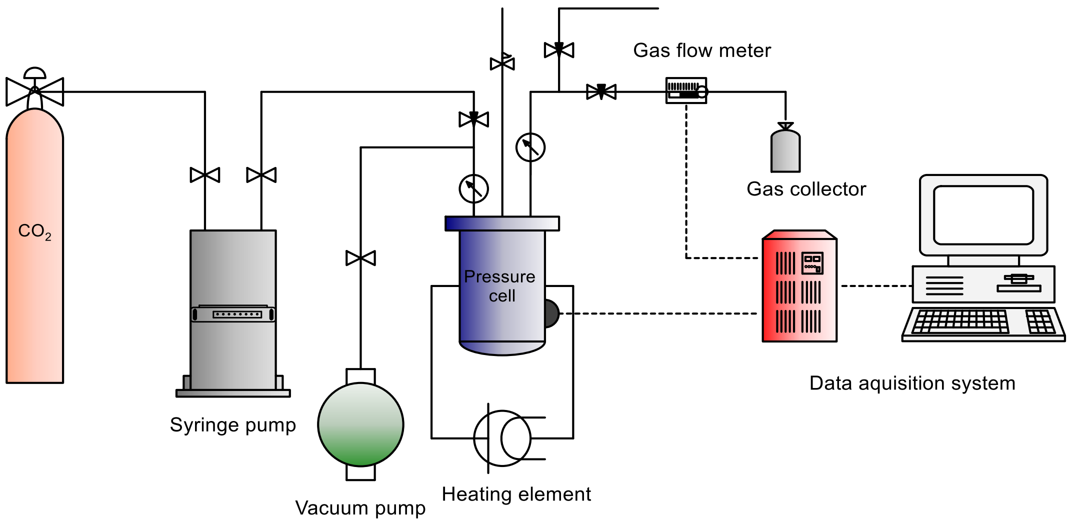

Figure 4-3 – Schematic diagram of the experimental setup used for the CO_2 diffusion and adsorption-induced swelling experiments.

4.2.4 Boundary/initial conditions and model parameters

As in the CO_2 adsorption-induced swelling experiment, a 10 × 10 × 10 mm^3 cubical block was modelled *(see Figure 4-4)* using COMSOL Multiphysics software, by coupling the governing equations for coal deformation (Eq. 4-4) and gas diffusion (Eq. 4-19 and 4-31) combined with porosity model (Eq. 4-10). For the Navier-type Eq. 4-4, the displacement and stress conditions on the boundary are defined as,

$$u_i = \tilde{u}_i(t) \qquad \text{on } \partial\Omega \qquad \text{………… [4-33]}$$

$$\sigma_{ij} n_j = \tilde{F}_i(t) \qquad \text{on } \partial\Omega \qquad \text{………… [4-34]}$$

where, $\tilde{u}_i$ and $\tilde{F}_i$ are the component of known displacement and stress on the boundary $\partial\Omega$ and n_j is the unit vector normal to the boundary. As shown in Figure 4-4, the prescribed displacement of the bottom boundary was fixed in all directions, and all the other boundaries were allowed to deform freely to simulate the unconstrained condition. The CO_2 pressure is applied as boundary stress at all boundaries. The initial displacement and stress conditions in the domain are defined as,

$$u_i(0) = u_0 \qquad \text{in } \Omega \qquad \text{………… [4-35]}$$

$$\sigma_{ij}(0) = \sigma_0 \qquad \text{in } \Omega \qquad \text{………… [4-36]}$$

where, u_0 and σ_0 are initial displacement and stress in the domain Ω, respectively, which were set to be zero initially. Dirichlet boundary condition for the gas diffusion in Eq. 4-19 and Eq. 4-31 is defined as,

$$p = \tilde{p}_i(t) \qquad \text{on } \partial\Omega \qquad \text{………… [4-37]}$$

where, $\tilde{p}_i(t)$ is the specified gas pressure on the boundary. In order to simulate the experimental settings, a piecewise function was adopted to apply a linearly increasing gas pressure on all boundaries (P_{CO_2}), that is increasing from atmospheric pressure to 10 MPa within 60 min and remains constant throughout the simulation *(see Figure 4-5)*. In addition, a ramped pressure application helps the model to converge rapidly during the simulations. The initial condition for the gas flow is defined as,

$$p(0) = P_0 \qquad \text{in } \Omega \qquad \text{………… [4-38]}$$

where, the initial pore pressure (P_0) in the domain was set to atmospheric pressure (P_a).

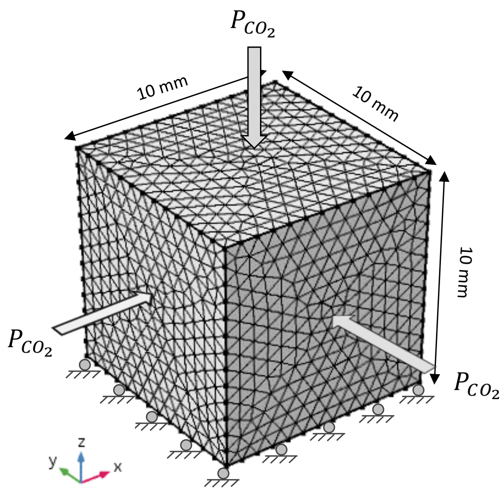

Figure 4-4 – Geometry and boundary conditions of the modelled cubical block.

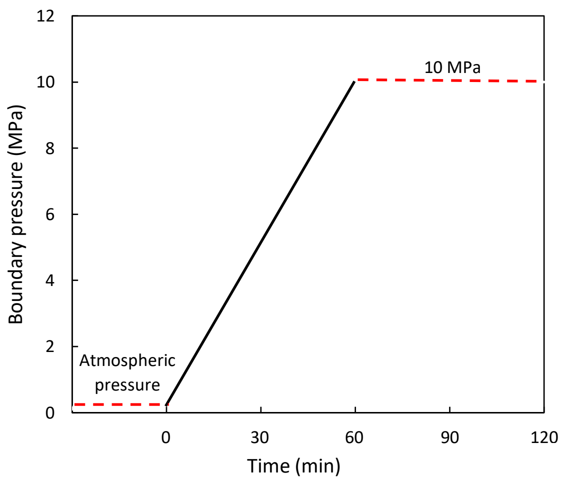

Figure 4-5 – The piecewise function adopted to specify the boundary gas pressure on the model.

The coal properties and modelling parameters obtained from experimental data (Mazumder et al., 2008; Robertson and Christiansen, 2005) and supplementary sources (Shi and Durucan, 2004; Wu et al., 2016) are listed in Table 4-2. The mechanical parameters including density, Poisson's ratio, Young's modulus, etc. were selected to represent typical coal types that are potential for CO_2 sequestration and CBM production. The extended diffusion fitting parameters were selected by considering nano-scale pore attributes of coal. Two of the significant influential parameters – i.e. equivalent pore radius and CO_2 diffusion coefficient were determined from literature and current experimental results. In fact, the equivalent pore radius and the effective porosity were determined from the pore size distribution data obtained from a FIB-SEM analysis conducted by Zhou et al. (2017) *(see Figure 4-6 (a))* on a similar coal type, in which the pore size and corresponding frequencies are substituted in Eq. 4-32 to determine the equivalent pore radius. Moreover, the CO_2 diffusion coefficient of the particular coal type was determined by a diffusion experiment conducted as described in section 4.2.3.2 and by fitting the data with an appropriate diffusivity model. Although uni-pore and bi-disperse models well-describe the gas diffusion in coal matrix, both models assume that the coal particles are spherical with uniform radius; thus, the fitting experiments are often conducted on pulverized coal samples. In the present study, we conducted the diffusion experiment on a 20 mm diameter coal disk to represent the gas diffusion in the bulk coal matrix and subsequently, the diffusion coefficient was determined by fitting the data with an analytical model – defined for the diffusion in a cylindrical domain (Crank, 1979) *(see Figure 4-6 (b))*. The diffusivity model is expressed as,

$$\frac{V_t}{V_\infty} = 1 - \sum_{n=1}^{\infty} \frac{4}{a^2 \alpha_n^2} exp\left(-D_g \alpha_n^2 t\right) \qquad \text{[4-39]}$$

where, V_t is the quantity of diffused gas in time t, V_∞ is the corresponding quantity after infinite time, D_g is the diffusion coefficient, a is the radius of the cylinder, α_n s are roots of $J_0(a\alpha_n) = 0$, in which $J_0(x)$ is the Bessel function of first kind of order zero.

Table 4-2 - The coal properties and modelling parameters used for the numerical simulation.

Parameter	Value
Coal density ($\boldsymbol{\rho_c}$) ($\boldsymbol{kg/m^3}$)	1440
Initial porosity ($\boldsymbol{\phi_0}$)	0.02377
Young's modulus ($\boldsymbol{E}$) ($\boldsymbol{MPa}$)	2713
Poisson's ratio ($\boldsymbol{\upsilon}$)	0.339
Biot's coefficient ($\boldsymbol{\alpha}$)	0.8
Langmuir sorption constant ($\boldsymbol{V_L}$) ($\boldsymbol{m^3/kg}$)	0.0477
Langmuir pressure ($\boldsymbol{P_L}$) ($\boldsymbol{MPa}$)	8.44
Langmuir volumetric strain constant ($\boldsymbol{\varepsilon_L}$)	0.02095
CO_2 diffusion coefficient ($\boldsymbol{D_g}$) ($\boldsymbol{m^2/s}$)	3.76×10^{-11}
Atmospheric pressure ($\boldsymbol{P_a}$) ($\boldsymbol{kPa}$)	101.325
Temperature ($\boldsymbol{T}$) ($^o\boldsymbol{C}$)	40
Molar mass of CO_2 ($\boldsymbol{M_g}$) ($\boldsymbol{g/mol}$)	44.01
Universal gas constant ($\boldsymbol{R}$) ($\boldsymbol{J/mol.K}$)	8.314
Dynamic gas viscosity ($\boldsymbol{\mu}$) ($\boldsymbol{Pa.s}$)	1.84×10^{-5}
Pore radius ($\boldsymbol{r_t}$) ($\boldsymbol{nm}$)	182
Tortuosity factor ($\boldsymbol{\tau}$)	10
Fitting parameter ($\boldsymbol{\alpha_1}$)	4
Rarefaction coefficient at $\boldsymbol{Kn} \rightarrow \infty$ ($\boldsymbol{\alpha_0}$)	1.19
Fitting parameter ($\boldsymbol{\beta}$)	0.4
Gas slip constant ($\boldsymbol{b}$)	-1

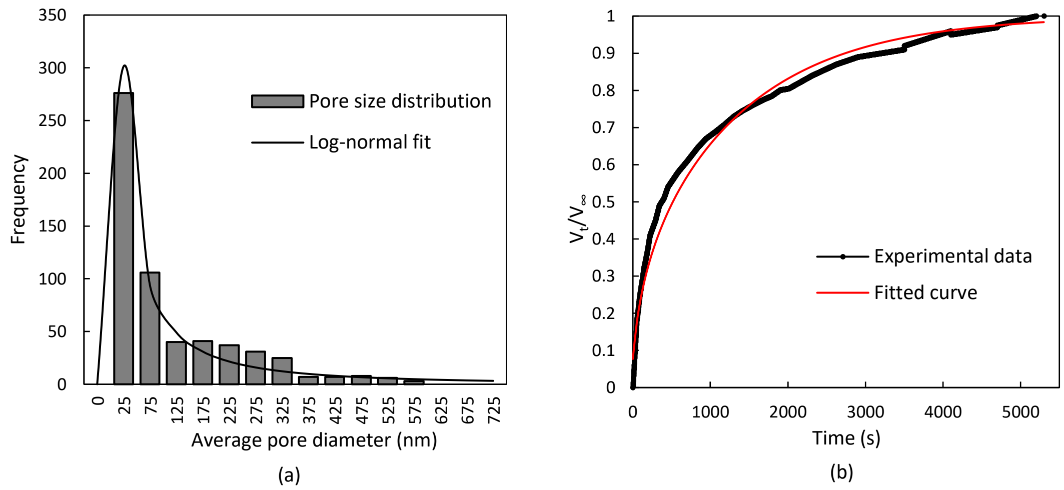

Figure 4-6 – a) Pore size distribution data used to determine the connected porosity and equivalent pore radius *(refer Eq. 4-32)* (Zhou et al., 2017) and, b) current experimental diffusion data fitted with the analytical model to obtain the CO_2 diffusion coefficient of the particular coal type.

4.2.5 Results and discussion

4.2.5.1 Validation of model performance

The numerical models were validated with the current experimental results and two other sets of experimental data obtained from the literature (Day et al., 2008; Pini et al., 2009). According to the experimental descriptions given in the corresponding literature, two different 3D-geometric models were used for numerical simulations, in which the CO_2 adsorption-induced volumetric swelling vs. CO_2 pore pressure variation was fitted with the two numerical models: 1) model with constant diffusion coefficient and 2) model with theoretically-extended diffusion. Furthermore, as explained in section 4.2.3.3, another experiment was designed to evaluate the temporal swelling effect in CO_2-interacted coal, and the data were fitted with the two models to validate the time-dependent solving performance of the models. The geometric and modelling details of each validation-model are given in Table 4-3.

Figure 4-7 illustrates the results of the three validation-models. The CO_2 adsorption-induced volumetric swelling significantly depends on the coal rank (Durucan et al., 2009). Accordingly, the modelled volumetric strain values are primarily dependent on the Langmuir volumetric strain constant (ε_L); thus, were adjusted in each model to best fit the modelling curves with the experimental data *(see Table 4-3)*. Figure 4-7 (a) and (b) depict that both models with constant diffusion coefficient and extended diffusion are capable of successfully simulating the CO_2 adsorption-induced volumetric strain variation with CO_2 pore pressure for different coal ranks and for different matrix geometries, omitting the initial slight shrinkage caused by the boundary pressure. Figure 4-7 (c) illustrates the model validation results with the current experimental data. The temporal volumetric swelling of coal depends on the CO_2 diffusivity in the coal matrix, which is simulated in the numerical model by 1) the CO_2 diffusion coefficient – in the constant diffusion coefficient model and, 2) the equivalent pore radius – in the extended diffusion model. We used the CO_2 diffusion coefficient of 3.76×10^{-11} m^2/s and the equivalent pore radius of 182 nm, as obtained from the diffusion experiment and FIB-SEM analysis results, respectively. As illustrated in Figure 4-7 (c), both models successfully fit the experimental data, which confirms the models' reliability on simulating the time-dependent nature of CO_2 diffusion/adsorption-induced coal matrix swelling. It is apparent that initially, the sample volumetric strain started to decrease due to shrinkage caused by the applied CO_2 boundary pressure and again increased with the CO_2 diffusion and adsorption-induced swelling. This is accurately simulated in the models by applying the CO_2 pressure as boundary stress, as explained in section 4.2.4. Both experimental and modelling results infer that a significant fraction of CO_2 adsorption-induced coal matrix swelling occurs in the initial phase of coal-CO_2 interaction. This is in line with Karacan (2003), who explains that CO_2 adsorbs relatively rapidly on to the matrix and the adsorption-induced swelling occurs as soon as the adsorption takes place. The overall model validation results conclude that both models can effectively predict the CO_2 diffusion/adsorption in the coal matrix and the consequent coal matrix swelling. However, unlike the constant diffusion coefficient model, the theoretically extended diffusion model gives provision for evaluating the effect of different flow mechanisms on the CO_2 diffusion/adsorption-induced coal matrix swelling that can be analysed through a sensitivity analysis.

Table 4-3 – Geometric and modelling parameters used for the validation-models.

Parameters	**Values**		
	Day et al. (2008)	Pini et al. (2009)	Current experiment
Model geometry	$30 \times 10 \times 10$ mm^3 block	20 mm diameter cylindrical disk	$10 \times 10 \times 10$ mm^3 block
CO_2 boundary pressure	15 MPa	13 MPa	10 MPa
Temperature	40 ºC	45 ºC	40 ºC
Langmuir volumetric strain constant ($\boldsymbol{\varepsilon_L}$)	0.0150	0.0201	0.02095

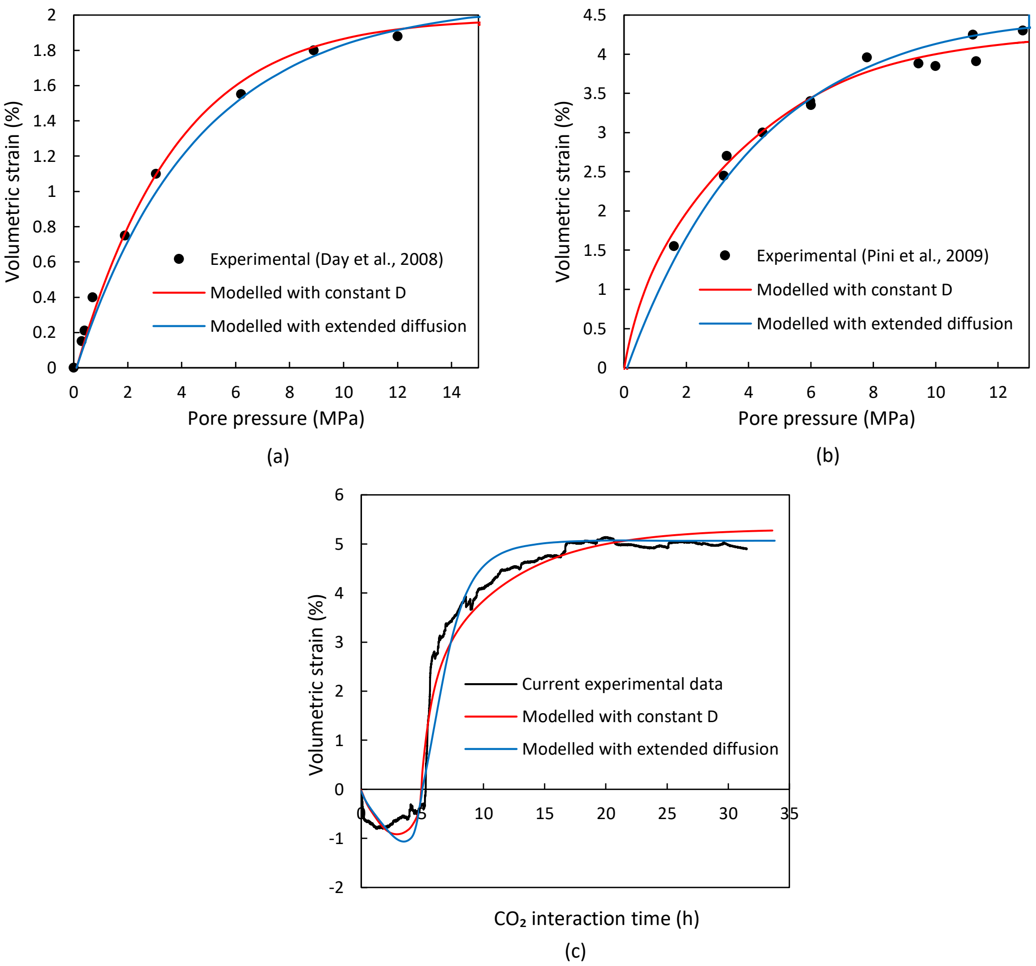

Figure 4-7 – Model validation with experimental data: Fitting the volumetric strain vs. CO_2 pore pressure with a) Day et al. (2008)'s data and, b) Pini et al. (2009)'s data, and c) fitting the volumetric strain vs. CO_2 interaction time with current experimental data.

4.2.5.2 Model performance-based sensitivity analysis

In this section, we conduct a sensitivity analysis with the verified models to evaluate the effects of various parameters on the coupled gas flow–adsorption–deformation process. Figure 4-8 illustrates the spatial and temporal distribution of pore pressure, which depicts the CO_2 diffusion process in the coal matrix. The corresponding model parameters are listed in Table 4-2. Since the coal matrix is initially exposed to equal pressure in all boundaries, CO_2 diffuses symmetrically from the external surfaces to the middle of the coal matrix block, depending on the pressure gradient, diffusion coefficient and the pore network attributes of the corresponding models. It is apparent that pore pressure in the centre of the matrix has not reached the boundary pressure (i.e. the pressure equilibrium) even after 17 h of CO_2 interaction. However, a larger fraction of swelling (about 96% from the final swelling equilibrium) has already been completed by that time *(see Figure 4-7 (c))*, confirming the fact that adsorption-induced coal matrix swelling starts to occur as soon as the coal-CO_2 interaction takes place.

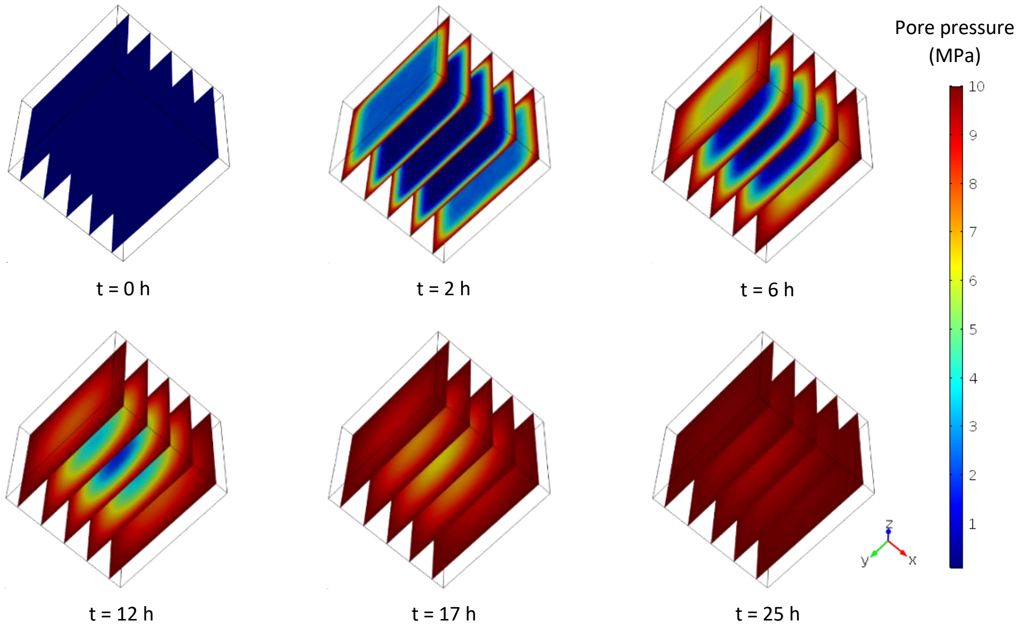

Figure 4-8 – Simulation results showing the spatial and temporal distribution of CO_2 diffusion-induced pore pressure in the coal matrix.

4.2.5.2.1 Effect of applied CO_2 pressure on the adsorbed amount of CO_2

The adsorbed amount of CO_2 is an important measurement in the domain of CO_2-sequestration, as it controls the quantity of CO_2 that can be stored in a particular coal seam and therefore the feasibility of the process. Hence, the variation of the adsorbed amount of CO_2 with applied CO_2 boundary pressure is first analysed using the constant diffusion coefficient model, due to easy interpretation. We quantify the adsorbed amount of CO_2 in the coal matrix block at time t ($m_{a(t)}$) by considering the volume integration of the geometric model, as given in Eq. 4-40 (Wang et al., 2017).

$$m_{a(t)} = \iiint \left|(1-\phi)\frac{M_g P_a}{ZRT}\rho_c \frac{V_L p}{p+P_L}\right|_t \qquad \text{............ [4-40]}$$

Figure 4-9 shows the variation of the adsorbed amount of CO_2 for different applied CO_2 boundary pressures. Each boundary pressure is applied with a piecewise function, as shown in Figure 4-5. In the numerical simulation, the average pore pressure in the coal matrix block is calculated by considering the spatial distribution of pressure in the whole 3D geometric volume, which yields misinterpretations, if the results are directly compared with each other. This is because, although a higher boundary pressure results in a higher average pore pressure for a given time t, CO_2 has not actually diffused into the coal matrix properly and therefore the adsorbed amount of CO_2 is less. In contrast, in the case of low boundary pressure, more pressure distribution and therefore more CO_2 diffusion into the coal matrix is required to generate the same average pore pressure, resulting in a higher adsorbed amount of CO_2. Hence, the average pore pressure-based comparison would be numerically controversial. Therefore, we use the normalized average pore pressure (p_N) *(see Eq. 4-41)* to directly compare the variation of the adsorbed amount of CO_2 with different applied boundary pressures *(see Figure 4-9)*. The normalized average pore pressure of 1 indicates the pressure equilibrium condition at a particular applied boundary pressure.

$$Normalized\ average\ pore\ pressure\ (p_N) = \frac{average\ pore\ pressure\ in\ the\ matrix}{applied\ boundary\ pressure} \quad \ldots\ldots \quad [4\text{-}41]$$

As shown in Figure 4-9 (a), the slopes of the CO_2 adsorption curves increase with the increasing applied boundary pressure. This is because the higher the applied boundary pressure, the larger the exerted pressure gradient on the coal matrix, causing rapid CO_2 diffusion and adsorption on to the coal matrix. Moreover, the maximum adsorbed amount of CO_2 at the pressure equilibrium (i.e. $p_N = 1$) also increases with the increasing applied CO_2 pressure. For instance, the maximum adsorbed amount has been increased by 17.12%, 30.47% and 41.18% at 8 MPa, 10 MPa and 12 MPa applied boundary pressures respectively, compared to the 6 MPa applied boundary pressure. Figure 4-9 (b), which is produced by extracting the maximum adsorbed amount of CO_2 at each equilibrium pressure, clearly shows the increasing trend between the maximum adsorbed amount and the applied boundary pressure. Since the adsorbed amount of CO_2 is dependent on the pore pressure *(see Eq. 4-40)*, a higher equilibrium pore pressure (i.e. applied boundary pressure) obviously results in a higher maximum adsorbed amount of CO_2. However, it is noticeable that the increment is not particularly linear, but gradually reaching a plateau at higher applied boundary pressures.

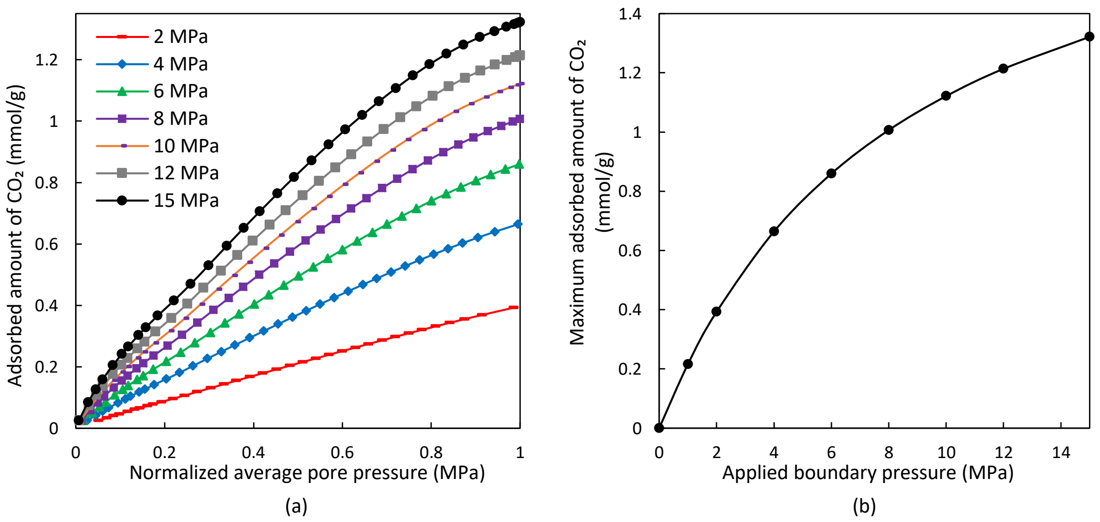

Figure 4-9 – a) Variation of the adsorbed amount of CO_2 in the coal matrix with the normalized average pore pressure for different CO_2 boundary pressures and, b) variation of the maximum adsorbed amount of CO_2 with the applied boundary pressure (i.e. equilibrium pressure).

4.2.5.2.2 Effect of the Langmuir sorption and volumetric strain constants on the CO_2 adsorption-induced coal matrix swelling

In a CO_2 sequestration process, the CO_2 adsorption capacity and the consequent coal matrix swelling play significant roles, as they govern the efficiency and the long-term feasibility of the project. In the modelling of CO_2 diffusion/adsorption-induced coal swelling, the two important processes – i.e. CO_2 adsorption and coal matrix swelling are predominantly dependent on the Langmuir sorption constant and the Langmuir volumetric strain constant, respectively. The two parameters vary with the intrinsic properties of the coal type and are often determined by fitting the experimental data with a Langmuir-type equation. In this section, we conduct a sensitivity analysis to evaluate the effect of two parameters on the CO_2 adsorption capacity and the volumetric swelling of the matrix, using the constant diffusion coefficient model. Simulation strategy of varying the two Langmuir constants is given in Table 4-4.

Table 4-4 – Simulation strategy of varying the Langmuir sorption constant (V_L) and the Langmuir volumetric strain constant (ε_L), and the simulation results.

Case	Original V_L	Original ε_L	V_L/ε_L ratio	Multiplier (m)	Adjusted V_L	Adjusted ε_L	Simulation results			
							Maximum adsorbed amount of CO_2 (mmol/g)	Δ% in Maximum adsorbed amount of CO_2	Maximum volumetric strain (%)	Δ% in maximum volumetric strain
Case 01	0.0477	0.02095	2.28	0.5	0.0239	0.0105	0.561	-49.8	3.419	-31.7
Case 02				1	0.0477	0.0209	1.117	0	5.009	0
Case 03				1.5	0.0716	0.0314	1.644	47.2	6.548	30.7
Case 04				2	0.0954	0.0419	2.118	89.5	8.032	60.3

We analyse four cases, in which both parameters are multiplied by a multiplier (m) while keeping the V_L/ε_L ratio constant in all cases. For instance, $m = 1$ (i.e. case 02) depicts the original modelling results, whereas $m = 2$ case outcomes the results when both constants are multiplied by a factor of 2. Figure 4-10 (a) and (b) illustrate the variation of the adsorbed amount of CO_2 and the volumetric strain with simulation time, respectively, in all four cases. It should be noted that here we omit the initial matrix shrinkage caused by the CO_2 boundary pressure and only consider the swelling part, due to easy interpretation. It is apparent from the figure that the adsorption-swelling process is highly-sensitive to the Langmuir constants. In fact, as given in Table 4-4, the maximum adsorption capacity in the coal matrix has been increased by 47.1% and 89.5%, when the Langmuir constants are multiplied by 1.5 and 2, respectively. In contrast, it has been reduced almost by 50%, when the Langmuir constants are half of their original values. Similarly, the maximum volumetric strain has been changed by -31.7%, 30.7% and 60.3%, when the Langmuir constants are multiplied by 0.5, 1.5 and 2, respectively. Figure 4-10 (c) directly shows the variation of the volumetric strain with the adsorbed amount of CO_2 in all four cases. It is noticeable that with the increasing Langmuir constants, gradients of the curves gradually become identical, forming a single curve but both maximum adsorbed amount of CO_2 and volumetric strain keep increasing with the increasing Langmuir constants. Hence, the sensitivity analysis concludes that the Langmuir sorption constant and the Langmuir volumetric strain constant have a significant impact on the CO_2 adsorption-induced coal swelling process; thus, should be accurately determined for a given coal type, before setting the model parameters.

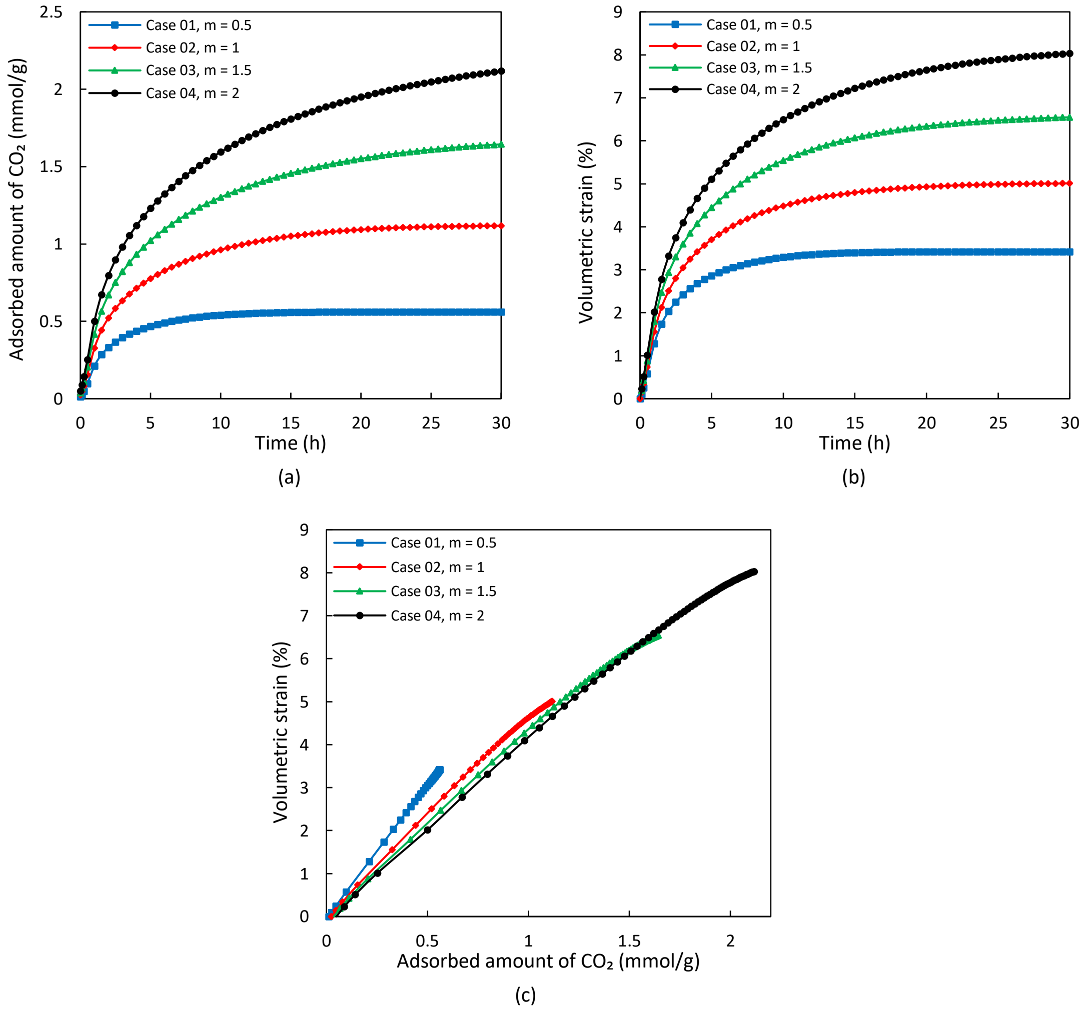

Figure 4-10 – Simulation results showing the sensitivity of the model to the Langmuir sorption constant (V_L) and the Langmuir volumetric strain constant (ε_L).

4.2.5.2.3 Effect of pore attributes on the nano-scale CO_2 diffusion mechanisms

The CO_2 adsorption and swelling behaviour and its temporal and spatial variations partially depend on the CO_2 diffusion mechanisms, especially due to the nano-scale pore size distribution in the coal matrix. With the theoretically-extended diffusion modelling approach, we further analyse the significance of individual diffusion mechanisms in the coal matrix with respect to pore attributes and pore pressure variation. As discussed in section 4.2.2.4, multiple diffusion mechanisms coexist in the coal matrix in certain pore pressure ranges, and their contributions to the bulk gas transport vary with the pore pressure and the characteristics of the available migration channels (Wu et al., 2016). In this section, we conduct a sensitivity analysis to evaluate how the overall CO_2 diffusion varies with the pore radius and how each diffusion mechanism (i.e. slip flow and Knudsen diffusion) contributes to the total gas transport under typical reservoir pore pressure conditions. The slip flow conductance (C_v) and the Knudsen diffusion conductance (C_k) with their corresponding weighting factors are determined by Eqs. 4-42 and 4-43, respectively.

$$C_v = \frac{1}{(1+kn)}(1+\alpha' Kn)\left(1+\frac{4Kn}{1-bKn}\right)\zeta_b \frac{{r_t}^2 p M_g}{8\mu Z R T} \qquad \text{……….. [4-42]}$$

$$C_k = \frac{1}{\left(1+\frac{1}{Kn}\right)}\frac{2}{3}\zeta_b \frac{r_t}{Z}\sqrt{\frac{8M_g}{\pi R T}} \qquad \text{……….. [4-43]}$$

Contribution of each flow mechanisms to the total flow conductance ($C_t = C_v + C_k$) are calculated by Eqs. 4-44 and 4-45, as follows.

$$Slip\ flow\ contribution = \frac{C_v}{C_v + C_k} \times 100\% \qquad \text{……….. [4-44]}$$

$$Knudsen\ diffusion\ contribution = \frac{C_k}{C_v + C_k} \times 100\% \qquad \text{……….. [4-45]}$$

An analysis point at A≡ (4 mm, 4 mm, 4 mm) in the geometric model is selected for the conductance analysis. Figure 4-11 (a) illustrates the variation of the total flow conductance with pore pressure for different pore sizes, where it depicts that the total flow conductance increases moderately with the increasing pore pressure but changes significantly with the pore radius. For instance, as shown in Figure 4-11 (b), compared to the flow conductance at 182 nm pore-scale – that is the original modelling parameter, the flow conductance significantly reduces with the decreasing pore size. In fact, the conductance has been reduced by 50-70% at all pore pressures, when the pore size reduces from 182 to 100 nm. Also, the reduction is as high as 99% at 1 nm and 10 nm pore sizes, compared to 182 nm. In contrast, a significant increment in the conductance can be observed at larger pore sizes (i.e. 300 nm). The increment is 119.3% higher, even at a lower pore pressure of 0.1 MPa. This continues to increase with the increasing pore pressure, reaching up to 171.1% of increment at 10 MPa pore pressure. This observation is well-expected in practical scenarios, as a coal matrix with large pore sizes provides better migration channels and easy-flow paths for the gas molecules to diffuse through the matrix, increasing the total flow conductance. If the effect of pore pressure is considered, both 1 MPa and 10 MPa isobars are identical for all pore sizes *(see Figure 4-11 (b))*, which suggests that no significant conductance change occurs at greater pore pressures (i.e. $p \geq 1\ MPa$). However, the overall change in the conductance suggests that a large fraction of the change occurs at lower pore pressures. This is clearly exemplified in the internal graph in Figure 4-11 (b), which shows that the change in the flow conductance compared to 182 nm pore-scale significantly varies at lower pore pressures (i.e. $p < 1\ MPa$) and remains approximately constant at larger pore pressure conditions.

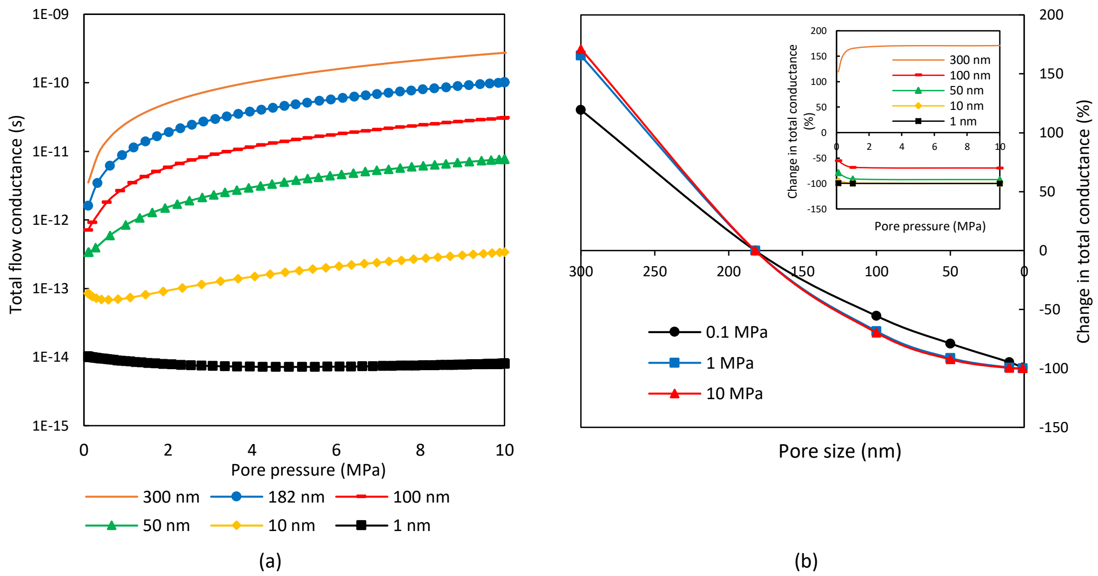

Figure 4-11 – a) Variation of the total flow conductance with pore pressure for different pore sizes and, b) change in the total flow conductance (compared to 182 nm pore size) with pore size for different pore pressures. Note: internal graph in figure b further illustrates the change in the total flow conductance (compared to 182 nm pore size) with pore pressure for different pore sizes.

Figure 4-12 shows the contributions of slip flow and Knudsen diffusion to the total flow conductance, as determined from Eqs. 4-44 and 4-45. The slip flow increases exponentially with the pore pressure at large pore sizes (i.e. $r_t \geq 50\ nm$), in which almost 100% of the contribution is provided by the slip flow mechanism at pore pressures greater than 1 MPa. However, at very low pore pressures (i.e. $p < 0.5\ MPa$), the situation is reversed, where the Knudsen diffusion contributes almost 100% to the total flow conductance, irrespective of the pore size. With the decreasing pore size, the contribution from the Knudsen diffusion starts to increase, confirming the fact that the Knudsen diffusion mechanism becomes predominant at relatively smaller pore channels, even at larger pore pressure conditions. Moreover, at very small pore sizes (i.e. $r_t \approx 1\ nm$), both slip flow and Knudsen diffusion contributions show a more linear variation with the increasing pore pressure, in contrast to the exponential variation at large pore sizes. The results are in line with the analytical results of Wu et al. (2016), who analysed the multiple transport mechanisms through nano-pores of shale gas reservoirs.

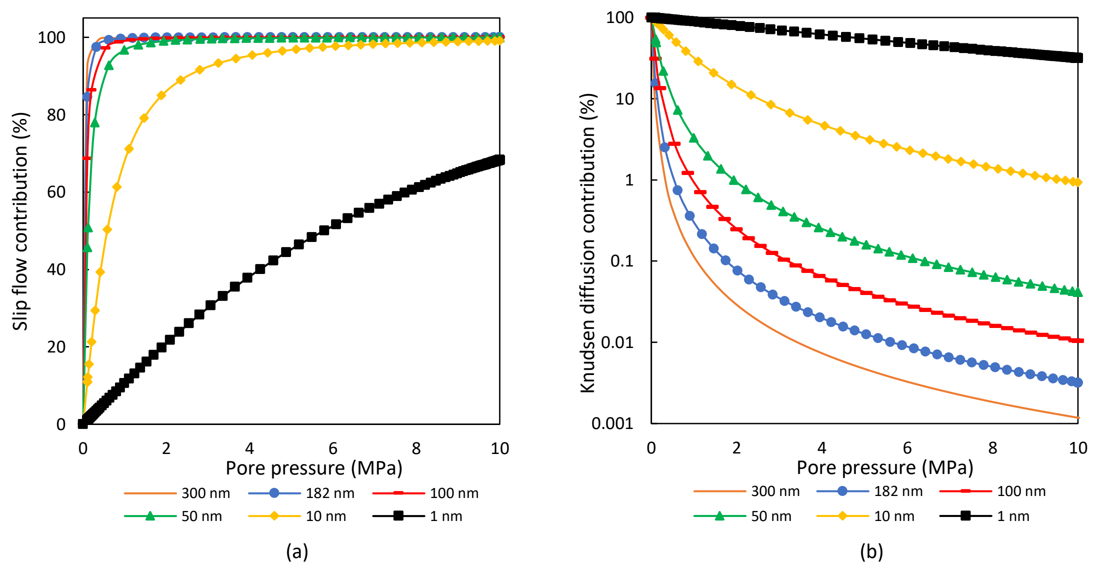

Figure 4-12 – Contribution share of each transport mechanism with pore pressure: a) Slip flow contribution and, b) Knudsen diffusion contribution to the total flow conductance.

4.2.6 Summary and recommendations

Overall, the modelling results provide conclusive evidence that the CO_2 diffusion/adsorption-induced coal matrix swelling depends on multiple factors including the gas pressure gradient, pore attributes, sorption and swelling characteristics of the coal type – modelled with Langmuir constants. Furthermore, the simulation results elucidate that the diffusion mechanisms at nano-scale pore networks are primarily dependent on the pore pressure and pore attributes, and their contribution to the overall gas flow varies continuously with the stress environment and the complexity of the pore network. In general, the results infer that the CO_2 adsorption causes a significant matrix swelling that reduces the fracture aperture in a dual-porosity system and consequently affects the permeability of the seam. This can substantially reduce the CO_2 injectivity into the seam and the CBM production, resulting in a hindered project efficiency in the long-run.

Although we assume that the coal matrix is homogeneous and calculate a single pore radius that theoretically provides the same total mass flow through the porous media *(see section 4.2.2.4)*, the heterogeneous coal matrix consists of complex pore networks with spatially varying pore attributes such as multiple pore sizes. Hence, the gas flow mechanisms through the coal matrix are highly-localized, where different diffusion mechanisms can be predominant at different locations at a certain time, which makes the analysis highly-complex. Therefore, more focused analyses on the localized flow regimes are recommended on this domain to accurately model the gas flow through nano-scale porous media. There exist many other gas flow mechanisms including free-molecular flow and surface diffusion, which may become dominant under certain reservoir conditions, and therefore should be further analysed in detail. Moreover, there exist many other influential parameters, such as Young's modulus, tortuosity of the pore network, connected porosity, etc. – that are not investigated in the current study but may have a significant impact on the coupled gas flow-deformation process. Also, since the current study only considers a single matrix block to analyse the diffusion/swelling mechanisms comprehensively, extended modelling of multiple-block interaction and the consequent fracture aperture variation and the permeability reduction is recommended for further analysis.

4.2.7 Conclusions

A fully-coupled gas flow-adsorption-deformation model was developed to simulate the CO_2 diffusion/adsorption-induced coal matrix swelling with considering the multiple diffusion mechanisms at nano-scale. Following conclusions are made, based on the simulation results.

- The spatial and temporal distribution of pore pressure in the coal matrix concludes that the coal matrix starts to swell immediately with the exposure to the CO_2 environment and a larger fraction of volumetric swelling occurs long before the coal matrix reaches its final pressure equilibrium.
- Since the adsorbed amount of CO_2 in the coal matrix is pore pressure-dependent, it increases with the increasing CO_2 boundary pressure, but gradually starts to level-off at higher equilibrium pressures.
- The sensitivity analysis concludes that the CO_2 adsorption and the consequent swelling are highly-dependent on the Langmuir constants; thus, should be precisely determined for the accurate modelling of the coupled process in a given coal type.
- The total flow conductance (i.e. slip flow + Knudsen diffusion) is moderately and highly-sensitive to the pore pressure and pore size, respectively. At large pore sizes, the contribution of slip flow to the total flow increases substantially with the increasing pore pressure. In contrast, the Knudsen diffusion contributes almost 100% to the total flow at lower pore pressures, regardless of the pore size. However, the Knudsen diffusion gradually becomes predominant with the reducing pore size, even at larger pore pressure conditions.

Appendix 4A – Derivation of the correction factor and the equivalent pore radius for bulk gas transport in the coal matrix

Hagen-Poiseuille's equation for mass transport through a single straight nano-channel with radius r can be expressed as (Bird et al., 2007),

$$J_v = -\frac{r^2 p}{8\mu}\frac{M_g}{ZRT}\nabla p \quad \text{........... [4A-1]}$$

To extend this into the mass transport through porous media, consider that a coal reservoir consisting of n nano-pores is represented by a cube with the permeability of k_a, the porosity of ϕ, the length of l_b and the sectional area of A_b. This can be approximated to a bundle of nano-channels model, assuming that there exist a n number of capillaries with the following single-channel average properties: radius of r_t, permeability of k_t, length of l_t, and sectional area of A_t.

Assuming a similar mass flow through the porous media and the nano-channels model, the total mass flow (q_t) in both cases can be expressed as,

$$q_t = -\frac{k_a}{\mu}\rho A_b \frac{dp}{l_b} = -n\frac{k_t}{\mu}\rho A_t \frac{dp}{l_t} \quad \text{........... [4A-2]}$$

Hence from Eq. 4A-2, we get,

$$\frac{k_a A_b}{l_b} = \frac{n k_t A_t}{l_t} \quad \text{........... [4A-3]}$$

The relationship between the capillary number and the capillary size, and the tortuosity of the nano-pores can be expressed as in Eqs. 4A-4 and 4A-5, respectively

$$\phi A_b = n A_t \quad \text{........... [4A-4]}$$

$$\tau = \frac{l_t}{l_b} \quad \text{........... [4A-5]}$$

Adding Eqs. 4A-4 and 4A-5 into Eq. 4A-3 yields,

$$k_a = \frac{\phi}{\tau}k_t = \zeta_b k_t \quad \text{........... [4A-6]}$$

Hence, the total mass flow through the porous media, in terms of the permeability of a single nano-pore channel becomes,

$$q_t = -\zeta_b k_t \frac{\rho A_b}{\mu}\frac{dp}{l_b} \quad \text{........... [4A-7]}$$

Moreover, the mass flux through the porous media is expressed as,

$$J_v = -\zeta_b k_t \frac{\rho}{\mu}\nabla p \quad \text{........... [4A-8]}$$

For a capillary pore channel, the permeability $k_t = \frac{{r_t}^2}{8}$ and from the equation of state, $\rho = \frac{M_g}{ZRT} p$. Hence, Eq. 4A-8 can be written as,

$$J_v = -\zeta_b \frac{{r_t}^2 p}{8\mu} \frac{M_g}{ZRT} \nabla p \quad \text{………… [4A-9]}$$

This is the mass flux for a porous media assuming a single channel radius and accounting for the porosity and the tortuosity of coal matrix. However, the pore network of coal matrix consists of different size pore channels, depending on the pore size distribution. Hence, rather than using an arbitrary value, the average pore size (r_t) in Eq. 4A-9 should be determined to incorporate the actual pore size distribution while preserving a similar mass flow.

In order to determine this equivalent r, we introduce a third porous system that has a m number of pore sizes, in which the i^{th} pore size has a frequency of n_i, an average pore radius of r_i, a cross-sectional area of A_i, a permeability of k_i and an equal channel length of l_t. Hence, the total mass flow in the third system can be expressed as,

$$q_t = -\frac{\sum_{i=1}^{m} n_i k_i A_i}{\mu} \rho \frac{dp}{l_t} \quad \text{………… [4A-10]}$$

Equating, Eq. 4A-2 to 4A-10 yields,

$$n k_t A_t = \sum_{i=1}^{m} n_i k_i A_i \quad \text{………… [4A-11]}$$

Moreover, the total areas contribute to mass transport in the two cases are,

$$n A_t = \sum_{i=1}^{m} n_i A_i \quad \text{………… [4A-12]}$$

Combining Eq. 4A-12, $A_i = \pi {r_i}^2$ and $k_i = \frac{{r_i}^2}{8}$, Eq. 4A-11 can be expressed as,

$$\frac{{r_t}^2}{8} \sum_{i=1}^{m} n_i \pi {r_i}^2 = \sum_{i=1}^{m} n_i \frac{{r_i}^2}{8} \pi {r_i}^2 \quad \text{………… [4A-13]}$$

By simplifying Eq. 4A-13, the equivalent pore radius that accounts for the pore size distribution of the porous medium and has the same mass transport as in the first system becomes,

$$r_t = \sqrt{\frac{\sum_{i=1}^{m} n_i {r_i}^4}{\sum_{i=1}^{m} n_i {r_i}^2}} \quad \text{………… [4A-14]}$$

Reference

Bird, R. B., Stewart, W. E., & Lightfoot, E. N. (2007). *Transport phenomena*: John Wiley & Sons.

Chen, R., Qin, Y., Wei, C., Wang, L., Wang, Y., & Zhang, P. (2017). Changes in pore structure of coal associated with Sc-CO2 extraction during CO2-ECBM. *Applied Sciences, 7*(9), 931.

Chen, Z., Liu, J., Elsworth, D., Connell, L. D., & Pan, Z. (2010). Impact of CO2 injection and differential deformation on CO2 injectivity under in-situ stress conditions. *International Journal of Coal Geology, 81*(2), 97-108.

Chen, Z., Liu, J., Elsworth, D., Pan, Z., & Wang, S. (2013). Roles of coal heterogeneity on evolution of coal permeability under unconstrained boundary conditions. *Journal of Natural Gas Science and Engineering, 15*, 38-52.

Civan, F. (2010). Effective correlation of apparent gas permeability in tight porous media. *Transport in Porous Media, 82*(2), 375-384.

Crank, J. (1979). *The mathematics of diffusion*: Oxford university press.

Cui, X., & Bustin, R. M. (2005). Volumetric strain associated with methane desorption and its impact on coalbed gas production from deep coal seams. *Aapg Bulletin, 89*(9), 1181-1202.

Darabi, H., Ettehad, A., Javadpour, F., & Sepehrnoori, K. (2012). Gas flow in ultra-tight shale strata. *Journal of Fluid Mechanics, 710*, 641-658.

Day, S., Fry, R., & Sakurovs, R. (2008). Swelling of Australian coals in supercritical CO2. *International Journal of Coal Geology, 74*(1), 41-52.

Durucan, S., Ahsanb, M., & Shia, J.-Q. (2009). Matrix shrinkage and swelling characteristics of European coals. *Energy Procedia, 1*(1), 3055-3062.

Fathi, E., & Akkutlu, I. Y. (2012). Mass transport of adsorbed-phase in stochastic porous medium with fluctuating porosity field and nonlinear gas adsorption kinetics. *Transport in Porous Media, 91*(1), 5-33.

Goodman, A. L., Favors, R. N., & Larsen, J. (2006). Argonne Coal Structure Rearrangement Caused by Sorption of CO2. *Energy & Fuels, 20*(6), 2537-2543.

Gunter, W. D., Gentzis, T., Rottenfusser, B. A., & Richardson, R. J. H. (1997). Deep coalbed methane in Alberta, Canada: a fuel resource with the potential of zero greenhouse gas emissions. *Energy Conversion and Management, 38*, S217-S222.

Hadjiconstantinou, N. G. (2006). The limits of Navier-Stokes theory and kinetic extensions for describing small-scale gaseous hydrodynamics. *Physics of Fluids, 18*(11), 111301.

Harpalani, S., & Schraufnagel, R. A. (1990). Shrinkage of coal matrix with release of gas and its impact on permeability of coal. *Fuel, 69*(5), 551-556.

Javadpour, F., Fisher, D., & Unsworth, M. (2007). Nanoscale gas flow in shale gas sediments. *Journal of Canadian Petroleum Technology, 46*(10).

Jing, Y., Armstrong, R. T., Ramandi, H. L., & Mostaghimi, P. (2016). Coal cleat reconstruction using micro-computed tomography imaging. *Fuel, 181*, 286-299.

Karacan, C. Ö. (2003). Heterogeneous Sorption and Swelling in a Confined and Stressed Coal during CO_2 Injection. *Energy & Fuels, 17*(6), 1595-1608.

Karniadakis, G., Beskok, A., & Aluru, N. (2006). *Microflows and nanoflows: fundamentals and simulation* (Vol. 29): Springer Science & Business Media.

Kolak, J. J., Hackley, P. C., Ruppert, L. F., Warwick, P. D., & Burruss, R. C. (2015). Using ground and intact coal samples to evaluate hydrocarbon fate during supercritical CO2 injection into coal beds: effects of particle size and coal moisture. *Energy & Fuels, 29*(8), 5187-5203.

Liu, J., Chen, Z., Elsworth, D., Miao, X., & Mao, X. (2010). Evaluation of stress-controlled coal swelling processes. *International Journal of Coal Geology, 83*(4), 446-455.

Mazumder, S., Wolf, K., Van Hemert, P., & Busch, A. (2008). Laboratory experiments on environmental friendly means to improve coalbed methane production by carbon dioxide/flue gas injection. *Transport in Porous Media, 75*(1), 63-92.

Palmer, I., & Mansoori, J. (1996). *How permeability depends on stress and pore pressure in coalbeds: a new model.* Paper presented at the SPE annual technical conference and exhibition.

Pini, R., Ottiger, S., Burlini, L., Storti, G., & Mazzotti, M. (2009). CO_2 storage through ECBM recovery: An experimental and modeling study. *Energy Procedia, 1*(1), 1711-1717.

Robertson, E. P., & Christiansen, R. L. (2005). *Modeling permeability in coal using sorption-induced strain data*. Retrieved from

Robertson, E. P., & Christiansen, R. L. (2006). *A permeability model for coal and other fractured, sorptive-elastic media*. Retrieved from

Saghafi, A., Faiz, M., & Roberts, D. (2007). CO_2 storage and gas diffusivity properties of coals from Sydney Basin, Australia. *International Journal of Coal Geology, 70*(1-3), 240-254.

Sampath, K. H. S. M., Perera, M., Li, D. Y., Ranjith, P., & Matthai, S. (2019a). Characterization of dynamic mechanical alterations of supercritical CO_2-interacted coal through gamma-ray attenuation, ultrasonic and X-ray computed tomography techniques. *Journal of Petroleum Science and Engineering, 174*, 268-280.

Sampath, K. H. S. M., Perera, M. S. A., Ranjith, P. G., & Matthai, S. K. (2019b). CO_2 interaction induced mechanical characteristics alterations in coal: A review. *International Journal of Coal Geology, 204*, 113-129.

Sampath, K. H. S. M., Perera, M. S. A., Ranjith, P. G., Matthai, S. K., & Dong yin, L. (2019c). Qualitative and quantitative evaluation of the alteration of micro-fracture characteristics of supercritical CO_2-interacted coal. *The Journal of supercritical fluids, 147*, 90-101.

Sampath, K. H. S. M., Perera, M. S. A., Ranjith, P. G., Matthai, S. K., Rathnaweera, T., Zhang, G., & Tao, X. (2017). CH_4-CO_2 gas exchange and supercritical CO_2 based hydraulic fracturing as CBM production-accelerating techniques: A review. *Journal of CO2 Utilization, 22*, 212-230.

Seidle, J., Jeansonne, M., & Erickson, D. (1992). *Application of matchstick geometry to stress dependent permeability in coals.* Paper presented at the SPE rocky mountain regional meeting.

Shi, J., & Durucan, S. (2004). Drawdown induced changes in permeability of coalbeds: a new interpretation of the reservoir response to primary recovery. *Transport in Porous Media, 56*(1), 1-16.

Shi, J., & Durucan, S. (2005). CO_2 storage in deep unminable coal seams. *Oil & Gas Science and Technology, 60*(3), 547-558.

Shi, J. Q., & Durucan, S. (2003). A bidisperse pore diffusion model for methane displacement desorption in coal by CO_2 injection. *Fuel, 82*(10), 1219-1229.

Wang, G., Ren, T., Qi, Q., Lin, J., Liu, Q., & Zhang, J. (2017). Determining the diffusion coefficient of gas diffusion in coal: development of numerical solution. *Fuel, 196*, 47-58.

Wei, M., Liu, Y., Liu, J., Elsworth, D., & Zhou, F. (2019). Micro-scale investigation on coupling of gas diffusion and mechanical deformation of shale. *Journal of Petroleum Science and Engineering, 175*, 961-970.

Wu, K., Chen, Z., Li, X., Guo, C., & Wei, M. (2016). A model for multiple transport mechanisms through nanopores of shale gas reservoirs with real gas effect–adsorption-mechanic coupling. *International Journal of Heat and Mass Transfer, 93*, 408-426.

Zhang, D., Gu, L., Li, S., Lian, P., & Tao, J. (2013). Interactions of supercritical CO2 with coal. *Energy & Fuels, 27*(1), 387-393.

Zhang, H., Liu, J., & Elsworth, D. (2008). How sorption-induced matrix deformation affects gas flow in coal seams: a new FE model. *International Journal of Rock Mechanics and Mining Sciences, 45*(8), 1226-1236.

Zhang, Y., Lebedev, M., Sarmadivaleh, M., Barifcani, A., & Iglauer, S. (2016). Swelling-induced changes in coal microstructure due to supercritical CO_2 injection. *Geophysical Research Letters, 43*(17), 9077-9083.

Zhou, S., Liu, D., Cai, Y., Yao, Y., & Li, Z. (2017). 3D characterization and quantitative evaluation of pore-fracture networks of two Chinese coals using FIB-SEM tomography. *International Journal of Coal Geology, 174*, 41-54.

4.3 Chapter summary

The matrix system of a coal seam plays a vital role in the context of CO_2 sequestration because it controls the process productivity and the ultimate CO_2 storage capacity of a given coal reservoir. CO_2 flow behaviour and mechanical deformation of coal matrix depend on various coupled processes such as CO_2 diffusion, adsorption and matrix swelling. This was studied in detail by developing a comprehensive modelling platform with taking all the underpinning processes and their coupled behaviours into account. A set of laboratory experiments were also carried out to discover the underlying science and to obtain the required data for the model validation. Since the fully-coupled process in an actual coal seam is quite complicated due to the associated multi-physics and the complex geometry, the CO_2 flow behaviour in a single matrix was considered in this study by accurately incorporating the underpinning coupling mechanisms.

In fact, a typical coal matrix consists of a complicated nano-scale pore network, in which the CO_2 flow is governed by multiple diffusion mechanisms, based on the pore characteristics and the pore pressure. The diffusion process in coal matrix was modelled in this study using two methods: 1) constant diffusion coefficient method and, 2) theoretically-extended diffusion approach that includes the combined effect of slip flow and Knudsen diffusion. Moreover, the CO_2 adsorption and the swelling effects were incorporated in the model with Langmuir-type models. The two models developed with the aforementioned diffusion approaches were validated with experimental studies by considering various coal types and different matrix geometries. Finally, a sensitivity analysis was carried out with the validated models to analyse the diffusion-adsorption-swelling process further. Overall, the results conclude that both diffusion approaches can be successfully utilized in modelling the CO_2 diffusion process in the coal matrices and the extended diffusion approach can be further used to analyse the pore size and pore pressure dependency of each diffusion mechanism at *in-situ* reservoir conditions. The results reveal that the total flow conductance rises moderately and substantially with the pore pressure and pore size, respectively. The contribution from each diffusion mechanism is dependent on both pore size and pore pressure, in which the flow is dominated by Knudsen diffusion at smaller pores, and the slip flow dominates the CO_2 flow in large pores. Moreover, the adsorption and swelling processes are found to be highly-sensitive to the Langmuir parameters; thus, should be estimated correctly for a given coal rank, to precisely model the fully-coupled process of a targeted coal reservoir.

Overall, the study confirms that the hydro-mechanical alterations in a CO_2-interacted coal matrix can be successfully modelled by taking the fully-coupled CO_2 flow-adsorption-swelling process into account. Hence, as the next step, the developed matrix-scale model is extended to simulate the CO_2 flow behaviour and mechanical deformation in an entire coal mass by incorporating the coal cleats/fractures. This is explained in Chapter 5.

CHAPTER 5

Evaluation of fully-coupled CO_2 flow behaviour, adsorption and the mechanical deformation of fractured coal seams

5 Evaluation of fully-coupled CO_2 flow behaviour, adsorption and the mechanical deformation of fractured coal seams

5.1 Chapter overview and structure

Natural cleat system is one of the most vital properties of typical coal seams that control the CO_2 flow behaviour through the seam. It governs the major flow paths in the seam that carry the injected CO_2 from the wellbores to the adsorption sites. The fracture properties such as fracture aperture, density, orientation, interconnectivity are the crucial factors that control the fracture permeability, and thus the overall flow behaviour. However, many experimental studies show that the coal permeability reduces upon CO_2 interaction, due to the CO_2 interaction-induced matrix swelling. This is one of the major drawbacks identified in CO_2 sequestration in coal, because this matrix swelling-induced permeability reduction can significantly decline the CO_2 injectivity into the seam, hampering the productivity of the process.

Therefore, it is imperative to comprehensively evaluate the possible changes that occur in the fractured coal structure due to CO_2 interaction and how it affects the CO_2 sequestration process in coal. By taking this into account, this chapter provides an extension to chapter 4, in which the CO_2 flow–coal deformation process is further modelled in a fractured coal geometry, by considering multiple matrix block interactions. The effect of explicit fracture network is incorporated in the model with a discrete fracture matrix (DFM) modelling approach. The chapter consists of two sections for modelling the single-phase and two-phase flow behaviours – that represent realistic fluid flow behaviours in coal seams.

In the first section of the chapter, the pure CO_2 interaction (i.e. single-phase flow) was modelled, and the model was initially validated with an experimental study conducted on a single-fractured core sample to confirm the reliability of the DFM approach in modelling the fully-coupled process. The study was then extended on a complex fracture geometry – that represents a natural coal cleat system. The fracture geometry was built from a stochastically simplified 3D-DFM geometry, which was developed based on an actual micro-CT image. The results were discussed in terms of the variations of pore pressure, matrix swelling, fracture aperture, permeability, contact pressure, etc. A manuscript was produced from the model results and submitted to the International Journal of Rock Mechanics and Mining Sciences (Q1 journal with impact factor of 3.77), which is currently under review. Hence, the first section is presented in the exact form of the submitted manuscript.

- Sampath K. H. S. M., Perera M. S. A., Matthai S. K., Ranjith P. G. *Discrete fracture matrix modelling of fully-coupled CO_2 flow–deformation process in fractured coal*. International Journal of Rock Mechanics and Mining Sciences (under review).

The second section of the chapter presents a similar DFM modelling approach, but with the two-phase flow behaviour of CO_2. Since most coal seams – potential for CO_2 sequestration are saturated with pore fluids with different chemistries, it is important to assess the effect of pore fluid condition and the saturation degree of coal seams, and how they affect the ultimate CO_2 flow behaviour and the deformation of coal. Based on that, the drainage process or the CO_2 injection process combined with the mechanical deformation of coal seam with a water-wet fracture network was modelled considering a number of multi-physics such as effect of water, free and dissolved gas in the water-wet fractures, free and adsorbed gas in coal matrix, matrix swelling, variation in local fracture aperture and permeability, contact modelling, frictional interfaces, etc. Due to the vast complexity of the fully-coupled process, a 2D-DFM geometry with 6 matrix blocks and uniform fracture apertures was adopted in the model to minimize the computational cost. The section is presented as a regular thesis section.

5.2 Discrete fracture matrix (DFM) modelling of CO_2 flow – deformation process in fractured coal: Single-phase flow

Journal paper title: Discrete fracture matrix modelling of fully-coupled CO_2 flow – deformation processes in fractured coal

Author's names: K.H.S.M. Sampath[1], *M.S.A. Perera[1], D. Elsworth[2], S.K.M. Matthai[1], P.G. Ranjith[3], Li Dong-yin[4]

[1]Department of Infrastructure Engineering, Engineering Block B, Grattan Street, Parkville, The University of Melbourne, Victoria 3010, Australia.

[2]Energy and Mineral Engineering, G3 Centre and EMS Energy Institute, Pennsylvania State University, University Park, PA 16802, USA

[3]Department of Civil Engineering, Monash University, Clayton Campus, Victoria 3800, Australia.

[4]School of Energy Science and Engineering, Henan Polytechnic University, Jiaozuo 454000, 12 China.

Abstract

CO_2 interaction causes complex mechanical deformations and flow modifications in coal, depending on the spatial disposition of the fracture-matrix system. Sorption-induced matrix swelling reduces the local fracture aperture and correspondingly the fracture permeability, consequently influencing gas flow throughout the seam. Since these modifications are highly -heterogeneous and -localized, an explicitly-represented geometric model is essential for the accurate modelling of the fully-coupled process. In this study, the CO_2 flow – coal deformation process is implemented in a numerical model at the scale of coal constituents (i.e. matrix blocks and cleats), through the inclusion of a spatially distributed 3D – discrete fracture matrix (DFM) network. Fracture geometry is generated from a stochastically simplified 2D fracture network obtained from micro-CT imaging. The approach is initially validated against experimental results from a single-fractured coal specimen and the analysis extended to the complex fracture geometry. The spatial and temporal evolutions of fracture/matrix pressure, adsorbed mass of CO_2, adsorption-induced swelling, alterations in local fracture aperture and permeability, and contact modelling at fully fracture closure are specifically analysed with comparison against no-swelling behaviour. Results indicate that the high-permeability fracture pathways provide initial easy access for the CO_2 to diffuse into the coal matrix, causing sorption-induced matrix swelling. Although the individual matrix blocks exhibit a slight shrinkage immediately upon injection of high fluid pressures within the fractures, sorption-induced swelling rapidly overcomes this, resulting in an overall volume expansion at full pressure equilibration. This is turn causes a significant reduction in fracture aperture and permeability. The magnitude of the local fracture

aperture reduction depends on the swelling behaviour of the bounding matrix, that leads to essentially full-closure of small fractures, causing significant localized flow modifications to further CO_2 injection in the vicinity of the particular fractures. The contact modelling approach identifies the timing and locations of fully-closing fractures in the complex geometry, where butt cleats exhibiting initial small apertures are prone to fully-close, compared to larger aperture face cleats that retain flow.

Keywords: *coal, CO_2 interaction, hydro-mechanical coupling, sorption-swelling, DFM modelling*

5.2.1 Introduction

High growth in population coupled with rapid industrialization have increased annual rate of global primary energy consumption by 2.9%, comprising the fastest growth rate since 2010. Consequently, global CO_2 emissions from fossil fuel combustion was elevated by 1–1.5% in 2019, with concomitant impacts on environment and health (BP, 2019; Enerdata, 2019). Numerous measures address this issue, specifically focusing on minimising levels of atmospheric CO_2 and impacts on global temperatures. Among a number of viable options, CO_2 geo-sequestration in deep coal seams has been identified as a promising solution - coal serves as a sorptive reservoir for the CO_2 with significant worldwide capacity, longevity and security. Besides, the greater adsorption potential of CO_2 to coal, relative to methane, allows CO_2 flooding to concomitantly boost the sweep efficiency of native methane, enhancing coalbed methane (CBM) production and further offsetting the cost of CO_2 storage. This, in turn increases the contribution of natural gas to total energy consumption, with a significant increment of 4.7% apparent in 2019, representing one of the strongest growth-rates in utilization in over 30 years (BP, 2019; Enerdata, 2019).

Coal is an extremely complex and heterogeneous material. This is due to its unique process of formation – coalification, and in particular due to the complex geometry of the resulting natural cleat system (Sampath et al., 2017). Injection of large quantities of CO_2 into coal reservoirs triggers complex coal-CO_2 interactions, triggering a complex hydro-mechanical response, in particular, that due to adsorption-induced swelling. The combined roles of the fracture network, ambient stress and gas pressure contribute to the fully-coupled response to gas transport, adsorption and the consequent swelling, that make the analysis rather complex (Durucan and Shi, 2009; Pan and Connell, 2007). For instance, the permeability, that generally governs gas transport within the coal reservoir is mediated by cleat aperture (Harpalani and Chen, 1997). Thus, any change in cleat aperture, driven either by effective stresses or sorption-induced swelling, will modify the coal permeability and ultimately impact gas transport throughout the seam (Gray, 1987).

Changes in the gas flow behaviour and the subsequent reduction in CO_2 injectivity due to swelling-induced permeability alteration are investigated by previous studies – by conducting experiments at both laboratory- and field-scales and by developing numerical and analytical models representing specific reservoir conditions (Oudinot et al., 2011; Pekot and Reeves, 2002; Perera et al., 2011; Ranathunga et al., 2015; Wu et al., 2011). For instance, a substantial drop in CO_2 injectivity into the seam was observed in the Fruitland Coal Fairway CO_2 sequestration project, with a reported drop from an initial 7.08×10^4 m^3/day to 1.42×10^4 m^3/day after about one year (Oudinot et al., 2011). This observed reduction in CO_2 injectivity substantially hinders the efficiency of sequestration projects. Laboratory-scale tri-axial experiments replicating *in-situ* stress conditions also reveal large permeability reductions with increasing injection pressures, especially beyond the critical point of CO_2 (i.e. 31.1 ºC and 7.38 MPa) (Perera et al., 2011; Ranathunga et al., 2015). Based on theoretical and empirical approaches, several permeability evolution models (e.g. Robertson-Christiansen (Robertson and Christiansen, 2006), Palmer-Mansoori (Palmer and Mansoori, 1996), Seidle-Huitt (Seidle et al., 1992), Cui-Bustin (Cui and Bustin, 2005) and Shi-Durucan (Shi and Durucan, 2004)) have been developed to account for the dynamic evolution of coal permeability. However, these models are either single- or multi-continuum models or analytical formulations, which are derived from a scalar porosity variable. Thus, these often fail to address the spatial and temporal variation of fracture permeability in a typical coal reservoir with a complex fracture network. Recognizing the dominant impact of the fracture network on CO_2 flow in fractured coals has prompted the development of discrete fracture matrix (DFM) models, in which fractures are explicitly and discretely represented in the geometric model. Initial approaches assumed the matrix to be impermeable and that fluid flow was restricted to the fracture network (Hyman et al., 2015). Later DFM models accommodated flow in the matrix to investigate the effect of free and adsorbed gas on gas production in fractured reservoirs including cleat-scale models (Wang, 2018). For instance, Bertrand et al. (2019) recently developed a cleat-scale DFM model to simulate the evolution of coal permeability due to adsorption-induced strain.

In this study, the fully-coupled process of CO_2 flow – coal deformation is implemented in a numerical model at the scale of coal constituents (i.e. matrix blocks and cleats). The spatial and temporal variation of fracture permeability is specifically analysed by including a spatially distributed 3D – discrete fracture matrix (DFM) network, stochastically generated from a reference micro-CT image. Since the fracture network is explicitly represented in the geometric model, the fracture permeability is directly determined as a function of local fracture aperture – defining the local evolution of permeability. A model containing a single fracture is initially developed and validated against experimental observations of permeability evolution to confirm the reliability of the model. The simulation is then extended to DFMs of realistic complexity and large spatial extent. Finally, a comparison between the effect of swelling and no-swelling behaviour on CO_2 flow is presented to highlight the significance of CO_2 adsorption-induced swelling on the modification of flow in coal.

5.2.2 The Discrete fracture matrix (DFM) modelling approach

Since single- or multi-continuum models provide no geometric distinction between fracture and matrix domains, they fail to evaluate spatial or localized alterations of influential parameters in a complex fracture geometry. In contrast, the DFM modelling approach treats fractures, matrix and interfaces as separate geometric objects. This is essential in modelling complex coal reservoirs, since each feature should be explicitly represented due to their dominating impact on the fully-coupled process (Berre et al., 2019). Although DFM modelling is conceptually simpler than continuum modelling, as it avoids the application of transfer functions by explicitly meshing each domain, special care should be taken when defining the geometry to reduce the excessive computational cost. In the context of DFM modelling, unlike mixed-dimensional or hybrid approaches, equi-dimensional representation of fractures necessitates a very fine mesh to avoid large aspect ratios of the individual cells. Since the current study incorporates the interaction of multiple physical fields, including stress- and time-dependent aperture variation, hydro-mechanical coupling and contact modelling, that interact through both contact interfaces of the fracture surface, an equi-dimensional DFM modelling approach is appropriate, irrespective of the significant computational burden. Hence, in the current study, we adopt an equi-dimensional DFM modelling approach, in which the complete problem is decomposed into a set of three problems – one for each sub-domain, linked through a transmission conditions (Tunc et al., 2012). Further, the local fracture aperture is calculated directly from the deformed geometry, as the distance between the two bounding surfaces of the fracture, and combined with the hydro-mechanical model to simulate the fully-coupled process.

5.2.3 Theoretical approach for the hydro-mechanical model

A typical coal structure consists of an orthogonal cleat system, including face cleats and butt cleats, with the coal matrix resident-between. The cleat network governs the coal permeability, while the intact coal matrix blocks control the diffusion and adsorption of CO_2, and act as the potential reservoir for gas storage (Sampath et al., 2020; Shi and Durucan, 2005). In our theoretical approach, the coal structure is conceptualized as a bundle of matchsticks representing individual coal matrix blocks, in which the void spaces between adjacent matrix boundaries form the fracture network (Ma et al., 2011). The fully-coupled process includes CO_2 flow through the fractures, diffusion through the coal matrix, adsorption to potential adsorption sites and the accommodation of adsorption-induced matrix swelling that alters fracture aperture and effective stress and subsequently changes fracture permeability *(see Figure 5-1)*. Implementing this process in a complex DFM model requires a number of theoretical considerations together with defined –stress and –displacement conditions for fracture and matrix domains at relevant boundaries.

In summary, the fully-coupled process adopted in the current study can be segregated as follows: 1) CO_2 flow through the fractures conforms to Darcy's law and CO_2 diffusion through the coal matrix is represented by Fick's second law with stress-invariant diffusion coefficient, 2) CO_2 adsorption and matrix swelling are defined by a Langmuir-type model, 3) coal deformation is coupled to the flow equations through effective stresses and adsorption-induced swelling, 4) fracture permeability is defined as a function of fracture aperture and is calculated locally from the deformed geometry in each solution step, 5) effects of fracture fluid pressure and fracture stiffness are included at fracture-matrix interface boundaries, 6) contact models and frictional interfaces are defined, where the two fracture surfaces contact and 7) stress and displacement boundary conditions are applied to represent *in-situ* reservoir conditions. The following sub-sections describe the complete hydro-mechanical approach in detail, in which the derivations are based on the assumptions that: 1) the coal matrix is an elastic, homogeneous and isotopic continuum, 2) the gas contained within the fractures and pores is ideal, and 3) the system is isothermal.

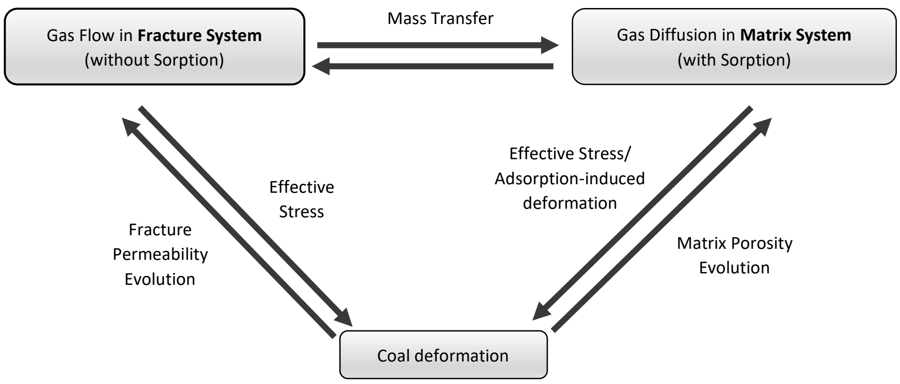

Figure 5-1 – Schematic of cross-coupling relationships among gas flow in fractures, diffusion in matrix and coal deformation.

5.2.3.1 Gas-transport system

Gas transport in coal consists of: 1) longitudinal free gas flow in the fracture domain (Ω_f) – that occurs along the fractures, 2) diffusion through the matrix domain (Ω_m) – that accounts for the free and adsorbed gas and 3) transverse flow across the domain interfaces (Γ_{m,f_1} and Γ_{m,f_2}) – that represents gas transfer between fracture and the matrix at fracture-matrix interface boundaries *(see Figure 5-2 (a))*.

5.2.3.1.1 Gas flow in fractures

The governing equation for gas transport in the fractures is expressed as;

$$\frac{\partial(\phi_f \rho_{g,f})}{\partial t} + \nabla(\rho_{g,f} q_L) = Q_s \qquad \text{………… [5-1]}$$

where, ϕ_f is the fracture porosity, $\rho_{g,f}$ is the density of gas in fractures, q_L is the longitudinal flow along the fracture and Q_s is the source/sink term.

As specified by the equation of state (EOS), the density of gas in the fractures is proportional to the gas pressure and is defined as,

$$\rho_{g,f} = \frac{M_g}{RT} p_f \qquad \text{………… [5-2]}$$

where, M_g is the molar mass of gas, R is the universal gas constant, T is the temperature and p_f is the gas pressure in the fracture domain.

The longitudinal gas flow along the fractures is defined by Darcy’s law as (Darcy, 1856),

$$q_L = -\frac{k_f}{\mu} \nabla p_f \qquad \text{………… [5-3]}$$

where, k_f is the fracture permeability and μ is the dynamic viscosity of the gas.

Under the assumption that a particular fracture can be defined as conducting flow between two closely-spaced parallel plates formed by adjacent matrix walls and neglecting the fracture roughness, the fracture permeability can be defined as a function of fracture aperture as (Witherspoon et al., 1980);

$$k_f = \frac{b}{12}^2 \qquad \text{…………….. [5-4]}$$

where, b is the fracture aperture.

In the governing equation for gas transport within fractures, the permeability is a function of the local fracture aperture that varies with the effective stress and the adsorption-induced swelling deformation of the bounding coal matrix. Hence, the fracture flow is coupled to the mechanical deformation.

5.2.3.1.2 Gas flow in the matrix

Gas flow within the matrix is established from mass conservation with Fick's second law defining the rate of transport. Assuming that the temporal derivative of the gas content is equal to the spatial gradient of the mass flux (Crank, 1979), then,

$$\frac{\partial m}{\partial t} + \nabla . J = 0 \qquad \text{[5-5]}$$

where, m is the total gas content and J is the total mass flux.

The total gas content consists of a free-phase gas and an adsorbed-phase gas – that can be expressed in terms of a Langmuir-type model, regardless of the heterogeneity of the adsorption sites in the coal (Saghafi et al., 2007). Thus, the total gas content is expressed as,

$$m = \frac{M_g}{RT}\phi_m p_m + (1-\phi_m)\frac{M_g P_a}{RT}\rho_c \frac{V_L p_m}{p_m + P_L} \qquad \text{[5-6]}$$

where, ϕ_m is the matrix porosity, p_m is the matrix pore pressure, P_a is the atmospheric pressure, ρ_c is the density of coal, and V_L and P_L are the Langmuir sorption constant and Langmuir pressure constant, respectively.

Since the combination of coupled processes and the equi-dimensional modelling approach are both highly complex, we adopt a stress-invariant constant diffusion coefficient to represent gas diffusion in the coal matrix. This has proven reasonably accurate for coal (Sampath et al., 2020). Hence, the governing equation for gas flow, that accounts for both free- and adsorbed-gas phases can be defined as,

$$\left[\phi_m + (1-\phi_m)P_a\rho_c \frac{V_L P_L}{(p_m+P_L)^2}\right]\frac{\partial p_m}{\partial t} + \left(p_m - P_a\rho_c\frac{V_L p}{p+P_L}\right)\frac{\partial \phi_m}{\partial t} - \nabla(D_g \nabla p_m) = 0 \qquad \text{[5-7]}$$

where, D_g is the gas diffusion coefficient.

The diffusion coefficient may be obtained by fitting observations of pressure or gas mass with an appropriate analytical diffusivity model (Sampath et al., 2020). Moreover, the porosity, ϕ_m, is dependent on the adsorption-induced strain; thus, the gas flow in the matrix is also coupled with the mechanical deformation.

5.2.3.1.3 Gas transfer between fracture and matrix

In the equi-dimensional DFM modelling, gas transmission between the sub-domains (i.e. Ω_f and Ω_m) accommodating transverse flow between fracture and the matrix are resolved as flux and pressure continuity across the fracture-matrix interface boundaries (i.e. Γ_{m,f_1} and Γ_{m,f_2}) *(see Figure 5-2 (a))* (Tunc et al., 2012);

$$q_{T,f}.\boldsymbol{n} = q_{T,m}.\boldsymbol{n} \quad \text{on} \quad \Gamma_{m,f_1} \text{ and } \Gamma_{m,f_2} \qquad \text{[5-8]}$$

$$p_f = p_m \quad \text{on} \quad \Gamma_{m,f_1} \text{ and } \Gamma_{m,f_2} \qquad \text{[5-9]}$$

where, $\boldsymbol{n}$ is the unit normal vector and $q_{T,i}$ is the transverse flow ($i = f, m$).

5.2.3.2 Mechanical system

5.2.3.2.1 Coal matrix deformation

The relationship linking infinitesimal strains to displacements for the elastic, homogeneous and isotopic coal matrix is defined as,

$$\varepsilon_{ij} = \frac{1}{2}(u_{i,j} + u_{j,i}) \qquad \text{[5-10]}$$

where, ε_{ij} and u_i are the component of the total-strain tensor and the component of displacement, respectively.

Mechanical equilibrium is expressed as,

$$\sigma_{ij,j} + f_i = 0 \qquad \text{[5-11]}$$

where, σ_{ij} and f_i are the component of the total-stress tensor and the component of body force, respectively.

The CO_2 interaction-induced mechanical deformation in the coal matrix is defined by a Navier-type equation for linear poro-elastic media, in which the adsorption-induced strain (ε_s) and the matrix pore pressure (p_m) are included as additional body forces. Since, ε_s is assumed to produce isotropic normal strains only, it is treated analogously to thermal expansion (Palmer and Mansoori, 1996). For a system that contains a single gas phase, the swelling strain, ε_s, can be expressed by a Langmuir-type model (Cui and Bustin, 2005; Harpalani and Schraufnagel, 1990; Robertson and Christiansen, 2006), and is defined as;

$$\varepsilon_s = \varepsilon_L \frac{p_m}{p_m + P_L} \qquad \text{[5-12]}$$

where, ε_L is the Langmuir volumetric strain constant.

Hence, the extended constitutive relation for the coal matrix deformation is given as,

$$\varepsilon_{ij} = \frac{1}{2G}\sigma_{ij} - \left(\frac{1}{6G} - \frac{1}{9K}\right)\sigma_{kk}\delta_{ij} + \frac{\alpha}{3K}p_m\delta_{ij} + \frac{\varepsilon_s}{3}\delta_{ij} \qquad \text{[5-13]}$$

where α is the Biot's coefficient, $\sigma_{kk} = \sigma_{11} + \sigma_{22} + \sigma_{33}$ and δ_{ij} is the Kronecker delta, and G and K are the shear and bulk moduli of coal, defined as,

$$G = \frac{E}{2(1+\upsilon)} \qquad \text{................ [5-14]}$$

$$K = \frac{E}{3(1-2\upsilon))} \qquad \text{................ [5-15]}$$

where, E and υ are the Young's modulus and the Poisson's ratio of the coal matrix, respectively.

Combining Eqs. 5-10, 5-11 and 5-13 yields the Navier-type governing equation for coal matrix deformation,

$$Gu_{i,kk} + \frac{G}{1-2\upsilon}u_{k,ki} - \alpha p_{m,i} - K\varepsilon_{s,i} + f_i = 0 \qquad \text{................ [5-16]}$$

that is coupled with the gas-transport system through matrix pore pressure.

5.2.3.2.2 Stresses on fracture-matrix interfaces and contact modelling with friction

The deforming smooth fracture closes as a linear function of applied normal stress (Lepillier et al., 2019). The fracture fluid pressure acts as a surface pressure on the fracture-matrix interface, modulating the fracture aperture through effective stress *(see Figure 5-2 (b))*. Hence, both effects from fracture stiffness and fracture fluid pressure are applied as surface normal pressures on the fracture-matrix interfaces. It should be noted that the fracture stiffness can be best represented as a hyperbolic function with respect to fracture aperture. However, due to the large complexity of the geometric model and the fully-coupled process, a constant normal fracture stiffness is assumed in the current study. The relationship between the normal stress and the fracture closure can be expressed as (Bertrand et al., 2019),

$$\sigma_n = \sigma_0 + \Delta p_f + K_n \Delta b \qquad \text{................ [5-17]}$$

where, σ_n is the normal total stress, σ_0 is the initial total stress, $\Delta p_f (= p_f - P_0)$ is the change in gas pressure within the fracture, K_n is the normal fracture stiffness and $\Delta b (= b_0 - b)$ is the fracture closure. P_0 and b_0 are the initial pore pressure and the initial fracture aperture, respectively.

Contact pairs with frictional interfaces are defined at fracture-matrix interfaces, where the fracture surfaces are likely to contact due to full closure. The interface behaviour, where normal contact forces develop with fracture closure, is modelled with a no penetration rule using a penalty algorithm (Agheshlui et al., 2018), in order to avoid fracture inter-penetration. This method is more convenient, as the results are directly computed from the penalty stiffness and displacements, thus, no extra degrees of freedom are required to separately determine the contact pressure and the friction traction vector. The frictional interface is defined by a Coulomb friction model, in which the tangential stress required for sliding is expressed as (Coulomb, 1773),

$$\tau = F\,\sigma'_n \qquad \text{[5-18]}$$

where, τ is the tangential stress, F is the coefficient of friction and σ'_n is the effective stress normal to the fracture surface.

The fully-coupled hydro-mechanical system described in this section is implemented in COMSOL Multiphysics software, validated and interpreted as a DFM geometric model, as explained in the following sections.

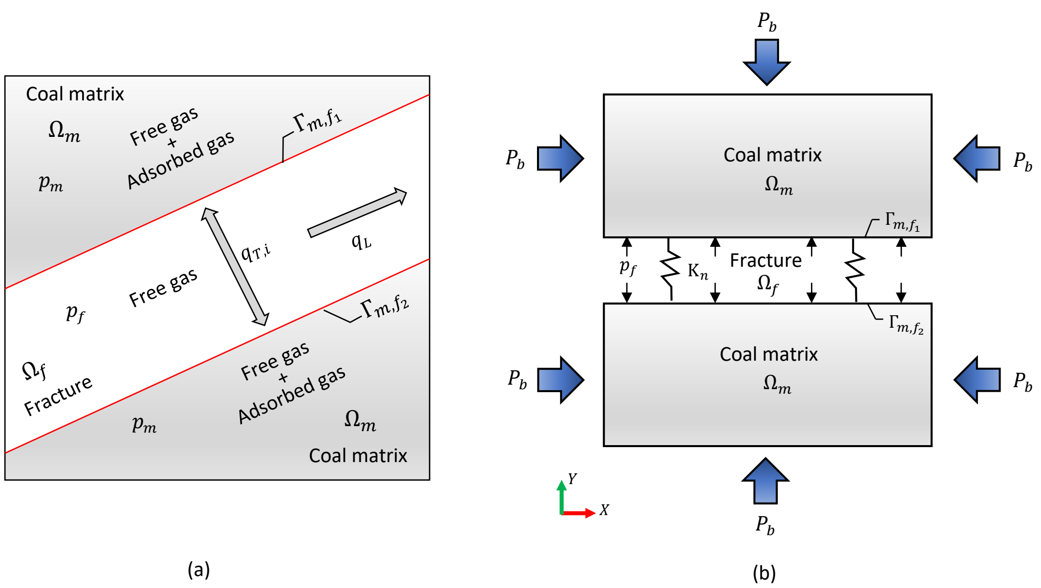

Figure 5-2 – a) The flow model within the fracture and matrix domains, indicating both longitudinal and transverse flows and the corresponding pressure terms and, b) definition of the mechanical system of the fractured medium as analogous to a linear spring-closure system.

5.2.4 Model validation

The model is first validated against permeability results obtained from a lab-scale experimental study, conducted under *in-situ* stress conditions, on a single-fracture within coal, before extending the solution to a realistic fractured geometry.

5.2.4.1 Model geometry and simulation procedure

The geometry for validation follows experimental details for flow along a longitudinally fractured core (Siriwardane et al., 2009). The CO_2 permeability experiment was conducted on a 38 mm in diameter × 76 mm in length cylindrical coal sample with an artificially induced-single fracture along its longitudinal axis. Accordingly, the DFM geometric model was defined with a single, longitudinal fracture with a constant fracture aperture of 1 mm, as shown in Figure 5-3. The required coal properties and the model parameters are obtained from the experimental study (Siriwardane et al., 2009) and supplementary sources (Kang et al., 2019; Masoudian et al., 2014; Mazumder et al., 2008; Robertson and Christiansen, 2005) as listed in Table 5-1. The fracture permeability was measured directly from the geometry and the fracture representing open pore space assumes a porosity of unity. In the experiment: 1) a confining pressure of 20 MPa was first applied to the sample to simulate *in-situ* tri-axial stress conditions with, 2) a CO_2 injection pressure of 10 MPa then applied as a piecewise function to the base of the sample to simulate the gradual injection of CO_2 (from atmospheric pressure to 10 MPa, within 1 hour). The model simulation was run until full pressure equilibration with the temporal evolution of average permeability calculated according to Eq. 5-4 and compared with the experimental results.

Table 5-1 – Parameters used for validation.

Parameter	Value
Coal density ($\boldsymbol{\rho_c}$) ($\boldsymbol{kg/m^3}$)	1440
Matrix porosity ($\boldsymbol{\phi_m}$)	0.0075
Fracture porosity ($\boldsymbol{\phi_f}$)	1
Poisson's ratio ($\boldsymbol{\upsilon}$)	0.339
Young’s modulus ($\boldsymbol{E}$) ($\boldsymbol{MPa}$)	3713
Normal fracture stiffness ($\boldsymbol{K_n}$) ($\boldsymbol{GPa/m}$)	60
Coefficient of friction ($\boldsymbol{F}$)	0.6
Langmuir sorption constant ($\boldsymbol{V_L}$) ($\boldsymbol{m^3/kg}$)	0.0477
Langmuir pressure constant ($\boldsymbol{P_L}$) ($\boldsymbol{MPa}$)	8.44
Langmuir volumetric strain constant ($\boldsymbol{\varepsilon_L}$)	0.029
Gas diffusion coefficient ($\boldsymbol{D_g}$) ($\boldsymbol{m^2/s}$)	3.76×10^{-10}
Biot's coefficient ($\boldsymbol{\alpha}$)	0.6
Temperature ($\boldsymbol{T}$) ($^o\boldsymbol{C}$)	25
Molar mass of CO_2 ($\boldsymbol{M_g}$) ($\boldsymbol{g/mol}$)	44.01
Density of CO_2 at STP ($\boldsymbol{\rho_{CO_2}}$) ($\boldsymbol{g/ml}$)	0.00196
Dynamic viscosity ($\boldsymbol{\mu}$) ($\boldsymbol{Pa.s}$)	1.84×10^{-5}
Initial pore pressure ($\boldsymbol{P_0}$) ($\boldsymbol{MPa}$)	0.101325
Universal gas constant ($\boldsymbol{R}$) ($\boldsymbol{J/mol.K}$)	8.314

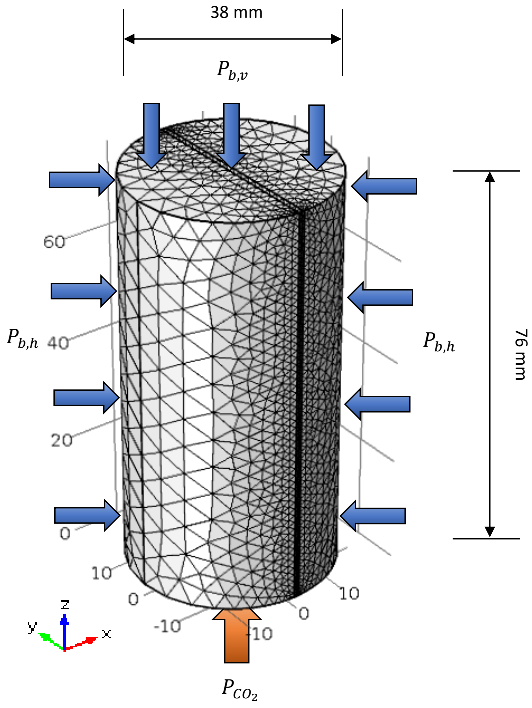

Figure 5-3 – The single-fractured DFM geometric model utilized for the validation; developed after Siriwardane et al. (2009).

5.2.4.2 Modelling results

We compare experimental observations against calculations of the permeability ratio to validate the model. Figure 5-4 illustrates the variation of permeability ratio with CO_2 interaction time. The direct comparison between simulation and experimental results indicate that the model is capable of successfully capturing the sense and magnitude of the permeability reduction and the variation of permeability ratio with CO_2 interaction time. It is apparent that a large permeability reduction occurs at the beginning of the injection and gradually reduces in rate of permeability reduction with increasing time. A 97.1% modelled reduction is observed after only ~27.5% of the total duration of the simulation, similar to the experimental observations. This is due to the immediate inception of matrix swelling with CO_2 injection (Karacan, 2003), rapidly closing fractures and consequently reducing the fracture permeability. Hence, the validation confirms the reliability of implementing the fully-coupled hydro-mechanical process in an equi-dimensional DFM model. We then extend this analysis to a complex fracture geometry.

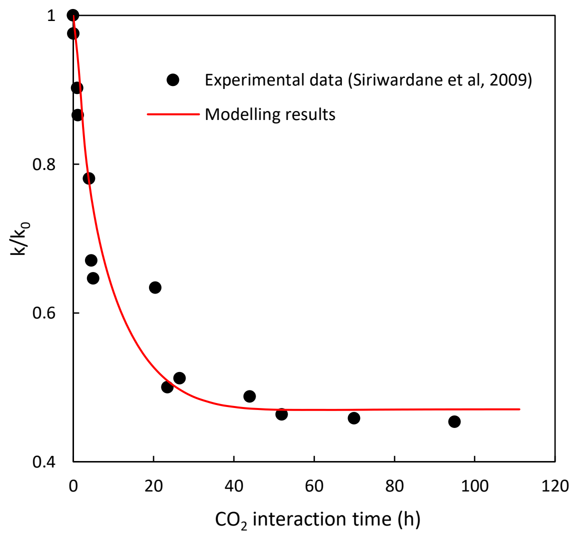

Figure 5-4 – Variation of permeability ratio with CO_2 interaction time: Modelling results fitted to experimental data from Siriwardane et al. (2009).

5.2.5 Simulation of a complex DFM model

The validated simulation procedure is then applied to a complex DFM model, that represents a typical coal cleat network. Although the validation was completed on a model containing a single large fracture, the same modelling approach and the theoretical background are adopted in representing the complex DFM model - in order to confirm the reliability and the accuracy of the modelling results.

5.2.5.1 Model geometry and simulation procedure

A typical coal structure consists of an intricate orthogonal network of face and butt cleats. Face cleats are the most prominent cleat type that are persistent, widely-spread and laterally extensive. Conversely, butt cleats are formed after the extensive face cleats and terminate where they abut face cleats (McCulloch et al., 1974; Sampath et al., 2017). The complex spatial disposition of the cleat network induces a large heterogeneity within the coal seam, that requires the application of complex DFM modelling. The cleat system itself is highly-disordered and complex, and thus difficult to represent in a 3D-DFM geometric model that incorporates the fully-coupled physical interactions, due to the excessive required computational burden. One possible way of circumventing this issue is to stochastically generate a simplified DFM model, while preserving the key attributes of the cleat structure, connectivity and aperture distribution (Cacas et al., 1990; Elmo et al., 2014; Gao et al., 2014). Since many studies simply generate DFM models stochastically, only by considering statistical descriptions of the fracture network, they often disregard the original connectivity of face cleats and butt cleats. Such models are rendered incapable of accurately representing the actual coal cleat system. A novel method that overcomes this issue is by integrating fracture mechanics into a probabilistic framework (Jing et al., 2016). This procedure mimics the natural cleat formation process to reproduce cleat network patterns (i.e. generating the face cleats first, followed by the butt cleats); thus, is able to preserve the main structural and topological attributes of the cleat network. Hence, a stochastically reconstructed DFM model extracted from Jing et al. (2016) was used in the current study to develop the 3D-DFM geometric model.

The simplified fracture network was used to generate an equi-dimensional DFM model by separating the fracture and matrix domains and defining the fracture-matrix interfaces while still preserving the local fracture aperture distribution and fracture connectivity. To define more realistic boundary conditions, the coal mass was modelled in three-dimensions by extruding the 2D geometry. The fractures were generated as smooth and straight fractures and the sharp edges at interconnections were minimized to the fullest extent to reduce the geometric and meshing complexity, and subsequently the computational intricacy and burden. The generated 3D-geometry was then re-scaled to represent a lab-scale coal specimen with the final dimensions of 76 mm × 82 mm × 5 mm and with fracture aperture ranging from 0.2 mm to 1 mm *(see Figure 5-5)*. The meshed geometry is the next important step that controls the fidelity of the model in representing the fracture geometry, solution accuracy and computational burden. Figure 5-6 (a) shows the meshed-model, in which a finer mesh is adopted toward matrix-fracture interfaces (i.e. fractures) to improve the accuracy and a combination of element types were used to generate the complete mesh. The mesh comprises 20717 tetrahedral elements, 11897 triangular elements, 2610 edge elements and 406 vertex elements, with the maximum element size limited to 7.2 mm.

A gas diffusion coefficient (D_g) of 6.58 $\times 10^{-11}$ m^2/s, temperature (T) of 40 ºC, matrix porosity (ϕ_m) of 0.0237, Langmuir volumetric strain constant (ε_L) of 0.0256 and normal fracture stiffness (K_n) of 5 GPa/m were used in the simulation with other mechanical and hydraulic properties similar to those given in Table 5-1. Boundary displacement conditions were applied to the model including constrained displacements in all directions at the base and constrained displacements in the x- and y- directions at the side walls to mimic *in-situ* reservoir conditions (Agheshlui et al., 2018; Bertrand et al., 2019). For the boundary stress conditions, an overburden stress ($P_{b,v}$) of 15 MPa was applied at the top surface and a horizontal stress ($P_{b,h}$) of 12 MPa was assigned to the side walls to replicate an extensional tectonic regime (Agheshlui et al., 2018) *(see Figure 5-6 (a))*. A CO_2 injection pressure was applied to one side of the model as a piecewise incremented function. The simulation was run until full pressure equilibrium with temporal and spatial analyses completed by considering five points of interest, distributed throughout the geometry as shown in Figure 5-6 (b).

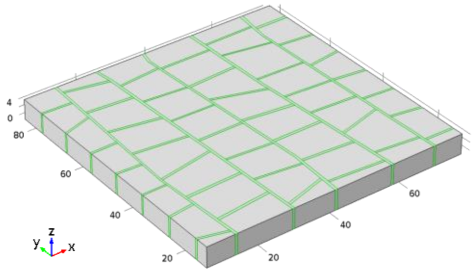

Figure 5-5 – Extruded and re-scaled 3D-geometric model developed based on the stochastically simplified and reconstructed DFM model from Jing et al. (2016).

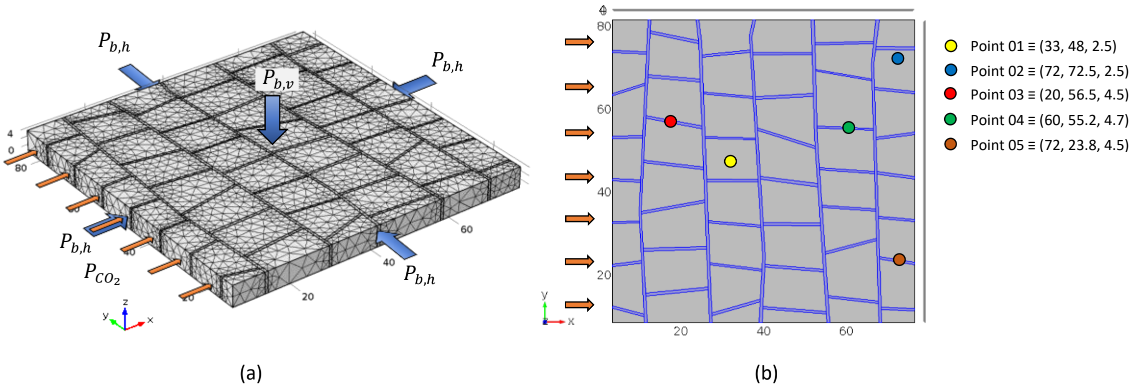

Figure 5-6 – a) Geometric model, indicating the meshing, boundary pressures and the location of CO_2 injection and, b) plan view of the geometry, indicating the points of interest used to analyse spatial variations in simulation variables.

5.2.5.2 Modelling results

The temporal and spatial analyses are conducted in terms of the evolution of fracture and matrix pressures, adsorbed mass of CO_2, matrix volumetric swelling, fracture aperture and permeability, and contact pressures within the model. Moreover, the results are compared with the case of absent swelling (no-swelling behaviour), in order to emphasize the significance of CO_2-induced coal matrix swelling on the overall flow behaviour.

5.2.5.2.1 Analysis of pore pressure development

Figure 5-7 shows the evolution of the pressure distribution throughout the coal mass at different times. This clearly exhibits the rapid flow of CO_2 through the fracture network, due to its high permeability, compared to the slow diffusion into the coal matrix. The injected CO_2 first flows through the high-permeability fractures then diffuses into the coal matrix from the fracture-matrix interfaces. The colour bar displays the CO_2 pore pressure values, ranging from atmospheric pressure at the beginning of the simulation to 10 MPa at full pressure equilibrium. Since the geometry represents a lab-scale sample, it takes only a minute time to fully penetrate the major interconnected fractures in the network to equilibrium pressure. This is clearly shown in Figure 5-8 (a), illustrating the evolution of fracture pressure with time at three points of interest in the fracture domain. It is notable that all three points follow a similar trend in pressure development without exhibiting any difference over this specific time scale, irrespective of their spatial disposition in the fracture domain. This is because the fractures are open (porosity of unity) and the fracture permeability is calculated from the parallel-plate law *(see Eq. 5-4)*, which in turn yields a high fracture permeability. This would be different if the initial fracture permeability is low, possibly due to the presence of granular infill. In that case, the fracture permeability would be better defined in terms of an effective diameter of the filling grains representing the pore throat diameter (Zhang et al., 2018), which may then defined as a function of the initial fracture permeability and change in the local fracture aperture (Chilingar, 1964; Liu et al., 1999).

In contrast, since the matrix domain exhibits a delayed-pore pressure development due to its low diffusivity, it is possible to clearly differentiate the spatial signatures of pressure evolution in the matrix domain, within the defined time frame. For instance, as shown in Figure 5-8 (b), the pressure development at point 02 is more rapid at the beginning than point 01. This is because, although point 02 is further away from the CO_2 injection point, it is closer to an interface with a high-permeability fracture – that provides a rapid pathway for the CO_2 to reach that point. Conversely, point 01 is located in the centre of a coal matrix block, that hinders rapid access for the CO_2, delaying pressure development *(see Figure 5-6 (b))*. However, this temporal variation also depends on the diffusive properties (i.e. gas diffusion coefficient (D_g)) of the coal matrix – thus should be precisely determined through an experimental analysis. Overall, this spatial analysis emphasizes the importance of the existing fracture network on the complex pore pressure development within the coal mass, that can only be resolved through a DFM modelling approach.

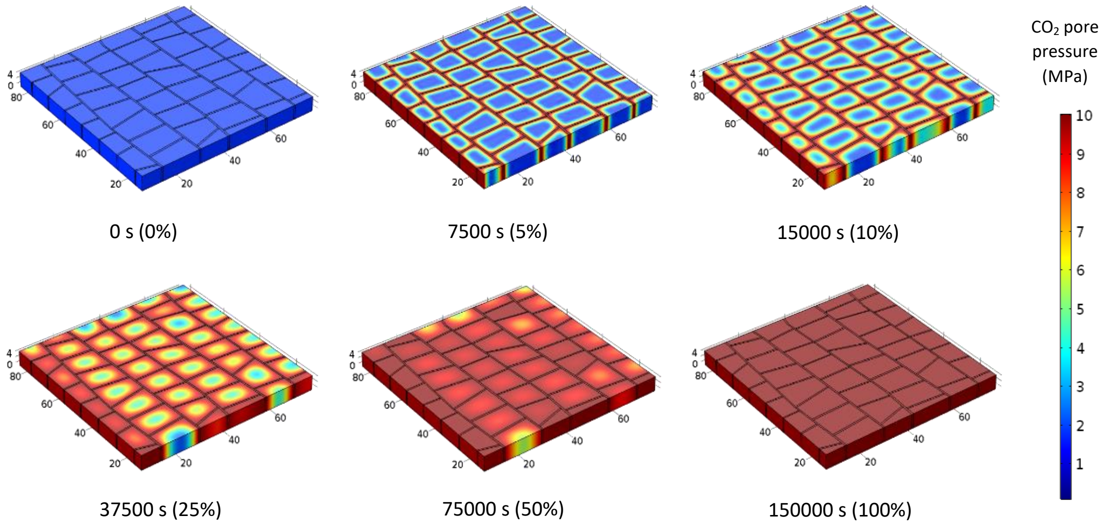

Figure 5-7 – Temporal and spatial variation of CO_2 pore pressure development in the coal mass.

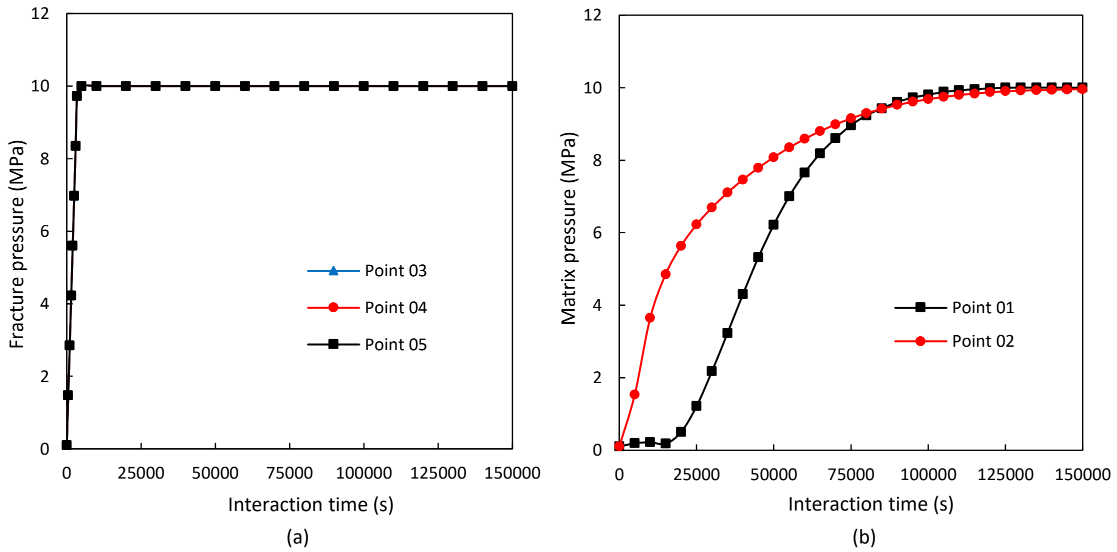

Figure 5-8 – Variation of a) fracture pressure and, b) matrix pressure with CO_2 interaction time.

5.2.5.2.2 Adsorbed mass of CO_2 and evolution of matrix swelling

Measurements defining the adsorbed mass of CO_2 and matrix swelling are vital in the context of CO_2 geo-sequestration, as they control the amount of CO_2 that can be effectively stored in a certain coal reservoir – this then governs the efficiency and the long-term feasibility of the project. The total adsorbed mass depends on the adsorption potential and the available adsorption sites within the coal matrix blocks. The adsorptive mass is controlled by the sorption response with rates controlled by diffusion coefficient and block size – larger diffusion coefficients and smaller block sizes/fracture spacing promote more rapid sorption. Since the complex DFM model consists of several coal matrix blocks with different shapes and sizes, we selected single matrix blocks to comprehensively analyse the adsorbed amount and the volumetric swelling *(highlighted in Figure 5-9)*. The adsorbed amount of CO_2 in a particular coal matrix block at time t ($m_{a(t)}$) is quantified through the volume integration of the selected matrix block, as (Sampath et al., 2020; Wang et al., 2017).

$$m_{a(t)} = \iiint \left| (1-\phi_m) \frac{M_g P_a}{RT} \rho_c \frac{V_L p_m}{p_m + P_L} \right|_t \quad \text{................ [5-19]}$$

Figure 5-9 (a) illustrates the variation of the adsorbed amount of CO_2 in the selected matrix block with CO_2 interaction time and with the average pore pressure. It is apparent that the adsorbed mass initially increases rapidly but gradually asymptotes to a constant with increasing interaction time, as the matrix block reaches pressure equilibrium. Moreover, the adsorbed mass shows a near-linear increment with the average pore pressure. This is since sorption is linearly related to pressure in the early stages of Langmuir sorption. This deviates from the linear trend near pressure equilibrium at higher relative pressures as all the available adsorption sites are occupied.

Figure 5-9 (b) shows the variation in volumetric strain of the selected coal matrix block with CO_2 interaction time and for an average pore pressure, in which the results are compared with the no-swelling behaviour – that represents the response to a non-sorbing gas (e.g. He or N_2). The initial volumetric strain of the matrix block is slightly negative, implying shrinkage, due to the compression driven by the applied fracture fluid pressure on the fracture-matrix interfaces. The rapid fluid pressure permeation through the high-permeability fracture domain creates an additional surface pressure on all matrix boundaries, causing universal shrinkage at the beginning of injection. However, this is gradually overcome by the diffusion and adsorption-induced swelling of the coal matrix, resulting in an overall volume expansion at the full pressure equilibrium. The final sorption-induced swelling is significantly larger than the initial surface pressure-induced shrinkage *(see Figure 5-9 (b))*. In the absence of swelling behaviour, the volumetric strain begins negative with the initial injection then rebounds to near null as the pressure equilibrates. This is a consequence of initial compaction of the block as the fracture pressure applies a large effective stress on the block, that ultimately dissipates as fluid permeates the block and the effective stresses between block and fracture equilibrate. The differences in strains for sorbing and non-sorbing gases clearly distinguishes the impacts of a highly-reactive gas (i.e. CO_2) with that of a relatively non-reactive gas like N_2. Further, it is apparent that the volumetric strain caused by the adsorption is significantly faster than the accumulation of matrix pressure shown in Figure 5-8 (b). This may be related to the rapid adsorption of CO_2 and the consequent swelling that occurs during coal-CO_2 interaction. In fact, CO_2 adsorbs rapidly on to the coal matrix during CO_2 injection (Karacan, 2003), causing immediate coal matrix swelling, as soon as the interaction takes place. This in turn may possibly induce large swelling strains in coal even at relatively low pore pressures.

The sorption-induced volumetric swelling or the volume expansion of individual matrix blocks can significantly affect the local fracture aperture and subsequently the flow behaviour, which is further discussed in the following section. In our theoretical approach, the adsorbed mass of CO_2 and the matrix swelling are modulated by Langmuir-type equations, where the two phenomena are dependent on the Langmuir sorption constant (V_L) and the Langmuir volumetric strain constant (ε_L), respectively. Hence, the values of the two parameters should be precisely determined experimentally for any given coal rank, before incorporating them in the fully-coupled hydro-mechanical model, as the coupled process is controlled by the two parameters.

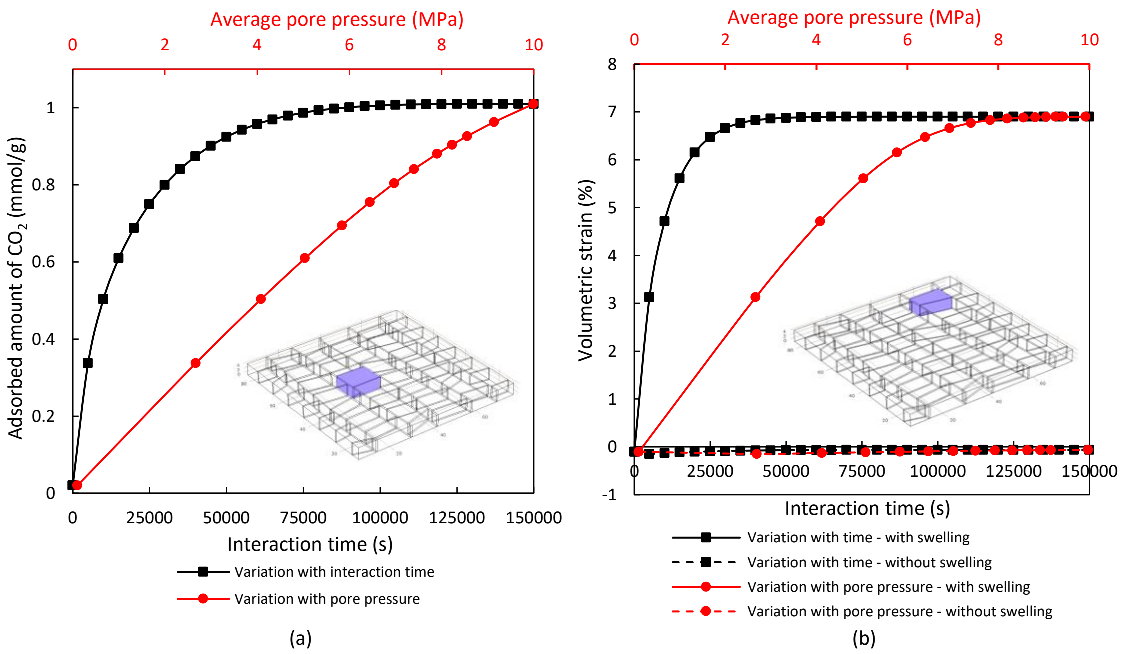

Figure 5-9 – a) Variation of the adsorbed mass of CO_2 in a selected coal matrix block with CO_2 interaction time and with average CO_2 pore pressure and, b) variation of the volumetric strain of a selected coal matrix block with CO_2 interaction time and with average CO_2 pore pressure. Note that the strain results are plotted together for cases both with- and without-swelling, for direct comparison.

5.2.5.2.3 Evolution of fracture aperture and fracture permeability variation

Fracture permeability, defined as a function of fracture aperture is an important parameter that governs gas flow behaviour in fractured reservoirs. The fracture aperture in the coal reservoir is stress-dependent and varies with a change in both the effective stress and the magnitude of sorption-induced swelling. A major advantage of DFM modelling is that the spatial and localized changes in fracture aperture can be efficiently evaluated, as the fracture network is defined explicitly in the geometric model.

Figure 5-10 shows the fracture network comprising both face and butt cleats, representative of the cleat system of a typical coal reservoir. The local fracture aperture is measured directly from the geometry, as the distance between the bounding matrix walls. The fracture network consists of fractures with the apertures ranging from 0.2 mm to 1 mm, whereas the apertures of the face cleats are greater than 0.5 mm in the original geometry *(see Figure 5-10 (a))*. A direct comparison between the original and the fully-CO_2-interacted fracture network implies that apertures of both face and butt cleats have been reduced significantly following CO_2 exposure, due to the adsorption-induced swelling of the adjacent matrix blocks. In fact, some fractures are near-completely closed due to their initial very low fracture aperture and the swelling behaviour of the bounding matrix *(see Figure 5-10 (b))*. It should be noted that, since the displacements of the basal boundaries are constrained at all directions, fracture apertures at this basal plane remain constant throughout the injection. Figure 5-11 shows the temporal variation of local fracture aperture at three points of interest in the fracture domain *(see Figure 5-6 (b))*, including one near fully-closed fracture (i.e. point 04). Again, the fractures dilate slightly as the injection pressure is applied and immediately/rapidly permeates the fracture network. This is congruent with the volumetric swelling results, in which the matrix blocks show a slight shrinkage at the beginning, causing this slight increase in aperture *(see Figure 5-9 (b))*. Importantly, since we adopt a no-penetration rule for the contact modelling, the separation between fracture walls remains zero at full-closure, without being negative, since no inter-penetration between the two bounding matrix walls is allowed during the swelling deformation. This is an accurate representation of real response. Furthermore, the dotted-lines of Figure 5-11 indicate the fracture aperture variation in absent-swelling, where the final deformations are small, by comparison with the case for swelling.

In single- or multi-continuum modelling and analytical approaches, the variations of fracture aperture or permeability with the pore pressure increment are often analysed without accommodating details of the spatial geometry and heterogeneity. However, in a fractured reservoir, the local fracture aperture and permeability are critically dependent on the deformation of the coal matrix in the vicinity of the fracture, rather than on the overall reservoir behaviour. This factor is explicitly accommodated in DFM approaches where variation in the aperture of three fractures of interest are plotted against the average pore pressure developed in the bounding coal matrix *(see Figure 5-12)*. It is apparent that the fracture aperture reduces significantly with increasing average pore pressure in the bounding coal matrix, due to matrix swelling. Crucially, the magnitude of local aperture reduction depends on the shape, size and the swelling potential of bounding matrix block; thus, they vary from fracture to fracture. For instance, the fracture apertures are reduced by 66%, 99% and 75% at points 3, 4 and 5, respectively. This clearly demonstrates that the hydro-mechanical behaviour of fractured reservoirs is highly-localized, and that accurate representation of this behaviour relies upon explicit descriptions of fracture geometry.

Figure 5-13 shows the temporal variation of fracture permeability ratio at three points of interest in the fracture domain, both with- and without-swelling behaviour. Since fracture permeability is defined as a function of local fracture aperture, the evolution of permeability follows a similar trend to that for aperture variation. Permeability reduces significantly with CO_2 interaction, due to adsorption-induced swelling. This is consistent with prior results obtained by Bertrand et al. (2019), in which they have used the multi-dimensional DFM modelling approach to analyse the permeability variation of CO_2-interacted fractured coal. In fact, they have observed a similar trend in permeability reduction with CO_2 interaction time, which is caused by the change in effective stress and the adsorption-induced swelling. The early-time permeability change is detailed in the zoomed-in inset of Figure 5-13, which highlights the slight permeability increase due to the initial injection – caused by the fluid pressure applied on the bounding walls of the fracture and compression of the matrix. The permeability of some fractures (i.e. at point 04) reduces to almost zero, due to near full-closure of the respective fracture. Such changes in permeability of the fracture network will result in large changes in both permeability and especially in permeability anisotropy. These changes will significantly impact flow behaviour in the coal seam to further CO_2 injection phases, ultimately hindering CO_2 injectivity and therefore the feasibility of the sequestration projects.

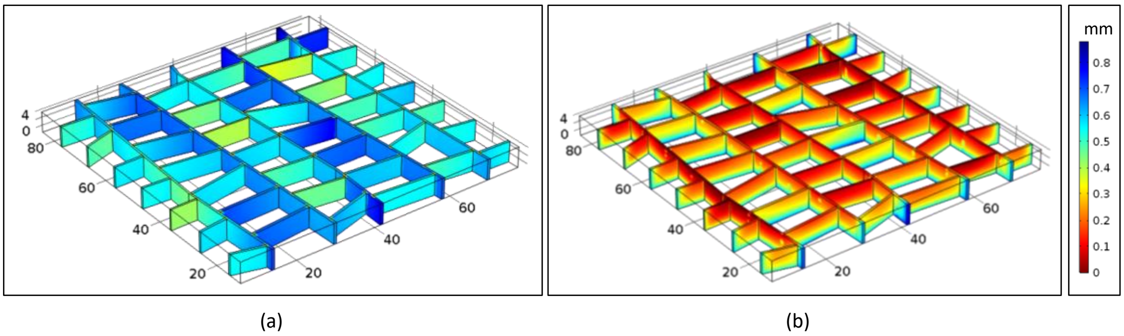

Figure 5-10 – Spatial variation of fracture aperture: a) before CO_2 injection (at 0 s) and, b) after full pressure equilibration (at 150000 s).

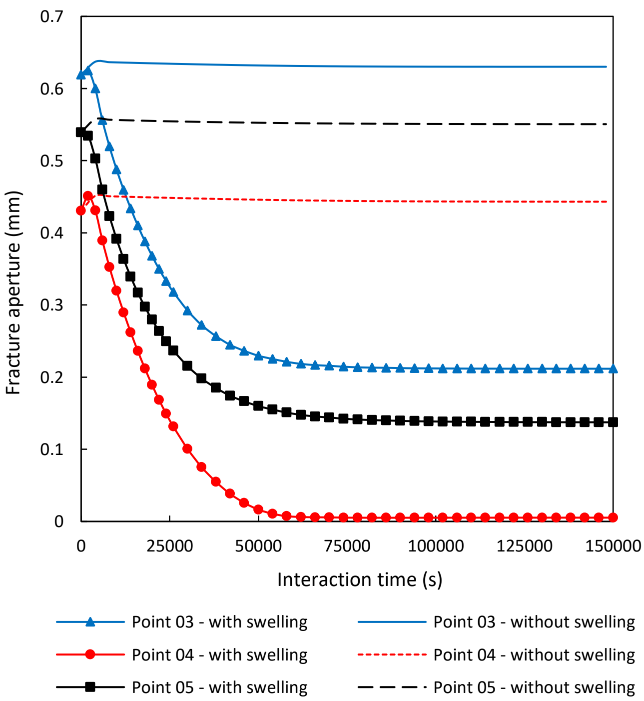

Figure 5-11 – Temporal variation of fracture aperture both with- and without-swelling.

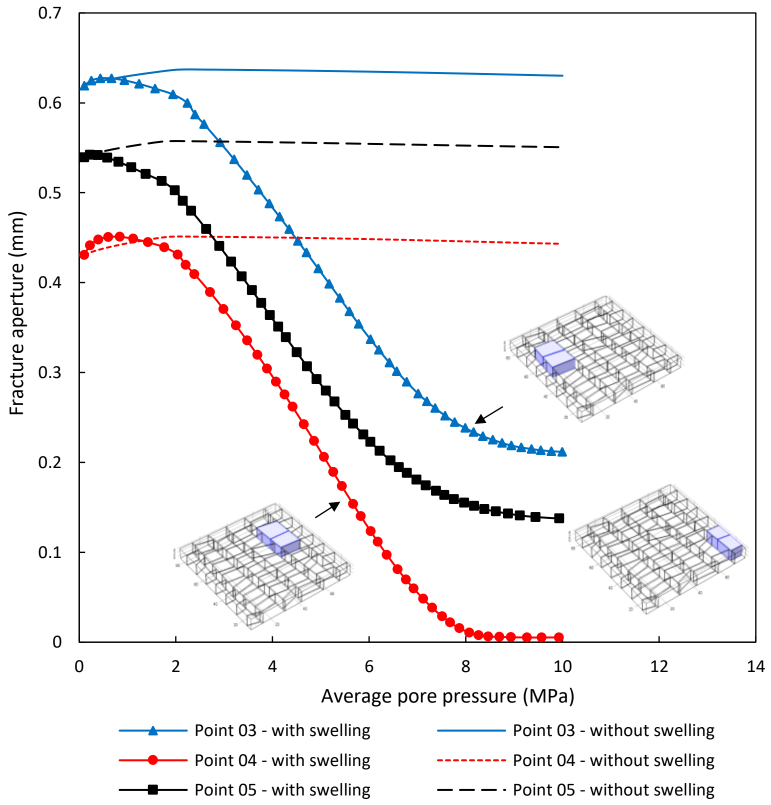

Figure 5-12 – Variation of fracture aperture with average pore pressure in the bounding coal matrix.

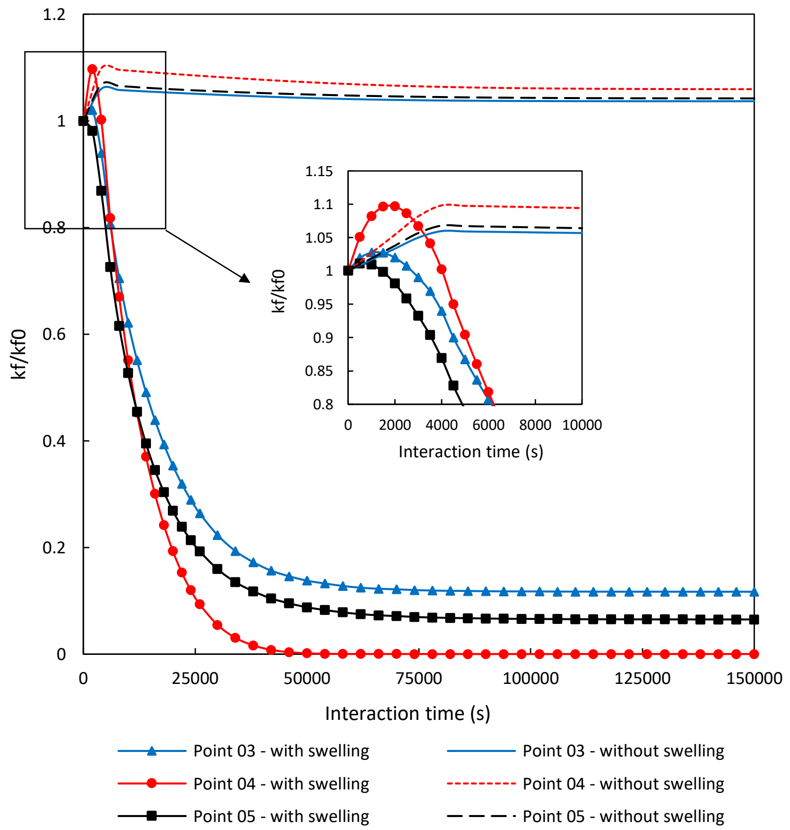

Figure 5-13 – Temporal variation of fracture permeability ratio with- and without-swelling conditions.

5.2.5.2.4 Evolution of fracture contact pressure

Depending on the initial fracture aperture and the swelling deformation of the bounding matrix, some fractures may fully close at maximum pressures – resulting in significant contact pressures. The fracture walls are defined as frictional interfaces and the contact pairs retained separated by a no-penetration *(see Sections 5.2.3.2.2 and 5.2.5.2.3)*. The magnitude of the contact pressure depends competitively on the boundary pressure, fracture fluid pressure and swelling-induced stress. Figure 5-14 illustrates the locations and the magnitudes of the resulting contact pressures, that directly indicates the locations of the near fully-closed fractures in the complex geometry. Noticeably, the butt cleats preferentially close to zero apertures over the face cleats. The lack of closure of fractures at the base of the model domain is merely an artefact of the full displacement restraint boundary condition applied on that boundary. Figure 5-15 shows the temporal variation of the maximum normal contact pressure on a selected fracture. Initially, the contact pressure remains small (zero) until the two surfaces contact, and then increases continuously with further swelling of the bounding matrix, until the system reaches pressure and swelling equilibria within the matrix. The point of initiation and the magnitude of the evolving contact pressures varies spatially, depending on the local hydro-mechanical properties of the fractures and matrix. Further, one should pay special attention when selecting the boundary conditions, including displacement and stress conditions, as they can largely affect the overall mechanical deformation of the model and therefore the entire CO_2 flow behaviour. The most appropriate and realistic boundary conditions should be defined to accurately model the entire process.

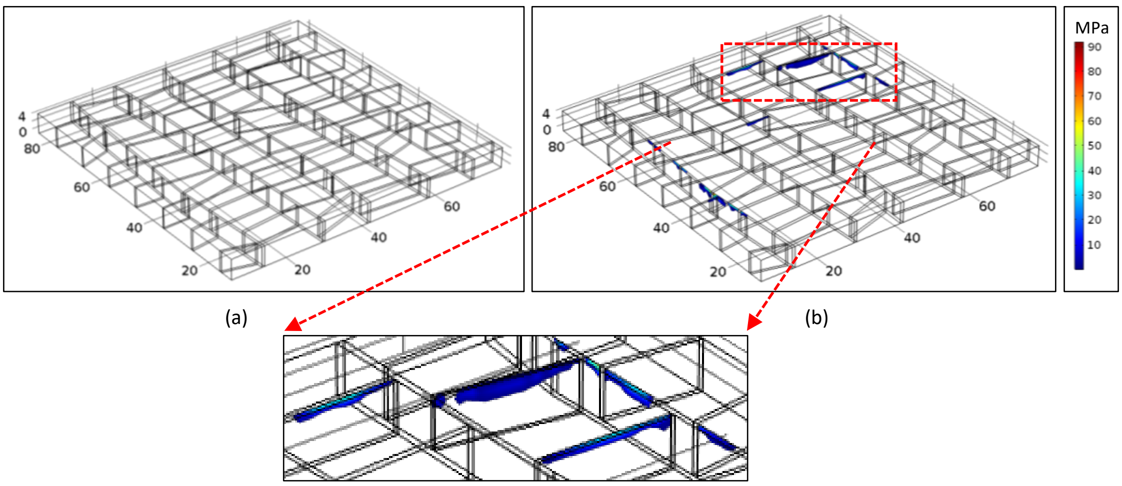

Figure 5-14 – Spatial variation of normal contact pressure: a) before CO_2 injection (at 0 s) and, b) after full pressure equilibration (at 150000 s), indicating the locations of fully-closed fractures.

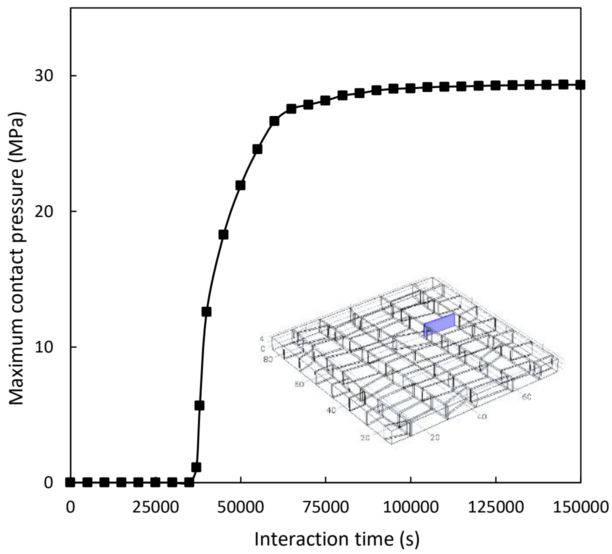

Figure 5-15 – Variation of maximum contact pressure with CO_2 interaction time, within a fully-closed fracture.

Overall, the current DFM model of a representative coal mass with a complex fracture network suggests that CO_2 interaction-induced hydro-mechanical response is highly sensitive to fracture geometry and connectivity – in addition to the manifestation of complex physical-couplings and feedbacks. The use of an equi-dimensional DFM modelling approach accommodates realistic fully-coupled processes by further including the development of contact forces and frictional forces on the fracture walls as the fractures fully close. Furthermore, since fracture permeability is defined as a function of local fracture aperture, where the aperture is measured from the deformed geometry at each solution step, it provides an accurate path to the time-dependent solution. The use of micro-CT images to constrain the key attributes of real fracture networks in coal, including fracture apertures, interconnectivity, and the structure of face and butt cleats provides a more accurate approach to model the realistic flow behaviour in fractured coal. Note that the computational burden for direct equi-dimensional DFM modelling of the micro-structure at reservoir scale would be prohibitive. However, the stochastically-developed lab-scale geometric model presented in the current study is useful in understanding key characteristics and controls of a representative elementary volume and presents a strong foundation for explicit DFM modelling of the hydro-mechanical behaviour of CO_2-interactions in coal.

5.2.6 Conclusions

An equi-dimensional DFM modelling approach is adopted to model the fully-coupled CO_2 flow – deformation process in a representative elementary volume of a fractured coal mass. The evolution of fracture/matrix pressures, adsorbed mass of CO_2, adsorption-induced volumetric swelling, change in local fracture aperture and permeability and development of contact stresses are specifically analysed through an explicit geometric model. The following conclusions are made, based on the simulation results:

- The geometry and connectivity of the natural cleat system exerts a first-order control on CO_2 flow behaviour in coal, in which CO_2 flow through a connected fracture network provides rapid pathways for CO_2 migration through the reservoir and thereby to coal matrix blocks. The distribution of fracture network affects the temporal and spatial rates of saturation of the corresponding coal matrix blocks. The highly-permeable fracture network percolates near immediately, compared to the low rate of diffusive transport into the matrix blocks. Hence, pressure development in the near-fracture regions of the matrix material is relatively rapid, compared to their interior.

- Individual matrix blocks exhibit a slight shrinkage in early-time due to the fracture fluid pressure applied to the matrix boundaries. This initial shrinkage is countered as adsorption-induced volumetric swelling dominates in later-time, resulting in a net volume expansion at full pressure equilibration.

- The fully-coupled simulation affirms that CO_2 adsorption-induced swelling of the coal matrix dominates the response and reduced rates of CO_2 injection into the interior of the reservoir. This results as the volume expansion of the matrix blocks reduces the local fracture aperture and therefore the fracture permeability. As introduced in this study, the real-time evaluation of fracture aperture and consequent fracture permeability is important when simulating the fully-coupled time-dependent process.

- Furthermore, depending on the initial fracture aperture and the swelling behaviour of the bounding matrix, some fractures may near-fully close, drastically reducing local permeability and significantly increasing permeability anisotropy. These factors will significantly impact CO_2 injectivity.

- Specifically, this equi-dimensional DFM modelling approach, incorporating robust accommodation of fracture contact mechanics identifies the locations of full fracture closure during CO_2 injection – these closing fractures are preferentially butt cleats - due to their originally smaller fracture apertures.

Overall, the results suggest that the CO_2 interaction-induced flow modifications in a fractured coal reservoir is a highly-complex and localized process and is thus best resolved through fully-coupled DFM modelling.

Reference

Agheshlui, H., Sedaghat, M. H., & Matthai, S. (2018). Stress influence on fracture aperture and permeability of fragmented rocks. *Journal of Geophysical Research: Solid Earth, 123*(5), 3578-3592.

Berre, I., Doster, F., & Keilegavlen, E. (2019). Flow in fractured porous media: A review of conceptual models and discretization approaches. *Transport in Porous Media, 130*(1), 215-236.

Bertrand, F., Buzzi, O., & Collin, F. (2019). Cleat-scale modelling of the coal permeability evolution due to sorption-induced strain. *International Journal of Coal Geology, 216*, 103320.

BP. (2019). Statistical Review of World Energy, 68th edition.

Cacas, M.-C., Ledoux, E., de Marsily, G., Tillie, B., Barbreau, A., Durand, E., Feuga, B., & Peaudecerf, P. (1990). Modeling fracture flow with a stochastic discrete fracture network: calibration and validation: 1. The flow model. *Water Resources Research, 26*(3), 479-489.

Chilingar, G. V. (1964). Relationship between porosity, permeability, and grain-size distribution of sands and sandstones *Developments in Sedimentology* (Vol. 1, pp. 71-75): Elsevier.

Coulomb, C. A. (1773). Sur une application des regles de maximums et minimums a quelques problemes de statistique relatifs a larchitesture. *Académie Royale de Science Memorie Mechanics and Mining Sciences, 7*, 343–382.

Crank, J. (1979). *The mathematics of diffusion*: Oxford university press.

Cui, X., & Bustin, R. M. (2005). Volumetric strain associated with methane desorption and its impact on coalbed gas production from deep coal seams. *Aapg Bulletin, 89*(9), 1181-1202.

Darcy, H. P. G. (1856). *Les Fontaines publiques de la ville de Dijon. Exposition et application des principes à suivre et des formules à employer dans les questions de distribution d'eau, etc*: V. Dalamont.

Durucan, S., & Shi, J. Q. (2009). Improving the CO_2 well injectivity and enhanced coalbed methane production performance in coal seams. *International Journal of Coal Geology, 77*(1), 214-221.

Elmo, D., Rogers, S., Stead, D., & Eberhardt, E. (2014). Discrete Fracture Network approach to characterise rock mass fragmentation and implications for geomechanical upscaling. *Mining Technology, 123*(3), 149-161.

Enerdata. (2019). Energy-related CO_2 emissions 2019 estimates - Analyst Brief. *Enerdata Executive Brief*.

Gao, F., Stead, D., & Kang, H. (2014). Numerical investigation of the scale effect and anisotropy in the strength and deformability of coal. *International Journal of Coal Geology, 136*, 25-37.

Gray, I. (1987). Reservoir engineering in coal seams: Part 1-The physical process of gas storage and movement in coal seams. *SPE Reservoir Engineering, 2*(1), 28-34.

Harpalani, S., & Chen, G. (1997). Influence of gas production induced volumetric strain on permeability of coal. *Geotechnical & Geological Engineering, 15*(4), 303-325.

Harpalani, S., & Schraufnagel, R. A. (1990). Shrinkage of coal matrix with release of gas and its impact on permeability of coal. *Fuel, 69*(5), 551-556.

Hyman, J. D., Karra, S., Makedonska, N., Gable, C. W., Painter, S. L., & Viswanathan, H. S. (2015). dfnWorks: A discrete fracture network framework for modeling subsurface flow and transport. *Computers & Geosciences, 84*, 10-19.

Jing, Y., Armstrong, R. T., Ramandi, H. L., & Mostaghimi, P. (2016). Coal cleat reconstruction using micro-computed tomography imaging. *Fuel, 181*, 286-299.

Kang, J., Zhang, B., Wang, J., Wu, J., Wang, L., Yin, B., & Kang, T. (2019). Mechanical testing of anthracite to assess its surface energy and temperature dependence. *Fuel, 239*, 76-86.

Karacan, C. Ö. (2003). Heterogeneous Sorption and Swelling in a Confined and Stressed Coal during CO_2 Injection. *Energy & Fuels, 17*(6), 1595-1608.

Lepillier, B., Daniilidis, A., Gholizadeh, N. D., Bruna, P.-O., Kummerow, J., & Bruhn, D. (2019). A fracture flow permeability and stress dependency simulation applied to multi-reservoirs, multi-production scenarios analysis. *Geothermal Energy, 7*(1), 24.

Liu, J., Elsworth, D., & Brady, B. (1999). Linking stress-dependent effective porosity and hydraulic conductivity fields to RMR. *International Journal of Rock Mechanics and Mining Sciences, 36*(5), 581-596.

Ma, Q., Harpalani, S., & Liu, S. (2011). A simplified permeability model for coalbed methane reservoirs based on matchstick strain and constant volume theory. *International Journal of Coal Geology, 85*(1), 43-48.

Masoudian, M. S., Airey, D. W., & El-Zein, A. (2014). Experimental investigations on the effect of CO_2 on mechanics of coal. *International Journal of Coal Geology, 128*, 12-23.

Mazumder, S., Wolf, K., Van Hemert, P., & Busch, A. (2008). Laboratory experiments on environmental friendly means to improve coalbed methane production by carbon dioxide/flue gas injection. *Transport in Porous Media, 75*(1), 63-92.

McCulloch, C. M., Deul, M., & Jeran, P. W. (1974). *Cleats in Bituminous Coalbeds*. Retrieved from U.S. Bureau of Mines:

Oudinot, A. Y., Koperna, G. J., Philip, Z. G., Liu, N., Heath, J. E., Wells, A., Young, G. B., & Wilson, T. (2011). CO_2 injection performance in the Fruitland coal fairway, San Juan Basin: results of a field pilot. *Spe Journal, 16*(04), 864-879.

Palmer, I., & Mansoori, J. (1996). *How permeability depends on stress and pore pressure in coalbeds: a new model.* Paper presented at the SPE annual technical conference and exhibition.

Pan, Z., & Connell, L. D. (2007). A theoretical model for gas adsorption-induced coal swelling. *International Journal of Coal Geology, 69*(4), 243-252.

Pekot, L. J., & Reeves, S. R. (2002). *Modeling coal matrix shrinkage and differential swelling with CO_2 injection for enhanced coalbed methane recovery and carbon sequestration applications*. Retrieved from

Perera, M., Ranjith, P., Airey, D., & Choi, S.-K. (2011). Sub-and super-critical carbon dioxide flow behavior in naturally fractured black coal: An experimental study. *Fuel, 90*(11), 3390-3397.

Ranathunga, A. S., Perera, M. S. A., Ranjith, P. G., Jub, Y., Vishal, V., & Silva, P. N. K. D. (2015). A macro-scale experimental study of sub- and super-critical CO_2 flow behaviour in Victorian brown coal. *Fuel, 158*, 864–873.

Robertson, E. P., & Christiansen, R. L. (2005). *Modeling permeability in coal using sorption-induced strain data*. Retrieved from

Robertson, E. P., & Christiansen, R. L. (2006). *A permeability model for coal and other fractured, sorptive-elastic media*. Retrieved from

Saghafi, A., Faiz, M., & Roberts, D. (2007). CO_2 storage and gas diffusivity properties of coals from Sydney Basin, Australia. *International Journal of Coal Geology, 70*(1-3), 240-254.

Sampath, K. H. S. M., Perera, M., Matthai, S., Ranjith, P., & Dong-yin, L. (2020). Modelling of fully-coupled CO_2 diffusion and adsorption-induced coal matrix swelling. *Fuel, 262*, 116486.

Sampath, K. H. S. M., Perera, M. S. A., Ranjith, P. G., Matthai, S. K., Rathnaweera, T., Zhang, G., & Tao, X. (2017). CH_4-CO_2 gas exchange and supercritical CO_2 based hydraulic fracturing as CBM production-accelerating techniques: A review. *Journal of CO2 Utilization, 22*, 212-230.

Seidle, J., Jeansonne, M., & Erickson, D. (1992). *Application of matchstick geometry to stress dependent permeability in coals.* Paper presented at the SPE rocky mountain regional meeting.

Shi, J., & Durucan, S. (2004). Drawdown induced changes in permeability of coalbeds: a new interpretation of the reservoir response to primary recovery. *Transport in Porous Media, 56*(1), 1-16.

Shi, J., & Durucan, S. (2005). CO_2 storage in deep unminable coal seams. *Oil & Gas Science and Technology, 60*(3), 547-558.

Siriwardane, H., Haljasmaa, I., McLendon, R., Irdi, G., Soong, Y., & Bromhal, G. (2009). Influence of carbon dioxide on coal permeability determined by pressure transient methods. *International Journal of Coal Geology, 77*(1-2), 109-118.

Tunc, X., Faille, I., Gallouët, T., Cacas, M. C., & Havé, P. (2012). A model for conductive faults with non-matching grids. *Computational Geosciences, 16*(2), 277-296.

Wang, G., Ren, T., Qi, Q., Lin, J., Liu, Q., & Zhang, J. (2017). Determining the diffusion coefficient of gas diffusion in coal: development of numerical solution. *Fuel, 196*, 47-58.

Wang, H. (2018). Discrete fracture networks modeling of shale gas production and revisit rate transient analysis in heterogeneous fractured reservoirs. *Journal of Petroleum Science and Engineering, 169*, 796-812.

Witherspoon, P. A., Wang, J. S., Iwai, K., & Gale, J. E. (1980). Validity of cubic law for fluid flow in a deformable rock fracture. *Water Resources Research, 16*(6), 1016-1024.

Wu, Y., Liu, J., Elsworth, D., Siriwardane, H., & Miao, X. (2011). Evolution of coal permeability: Contribution of heterogeneous swelling processes. *International Journal of Coal Geology, 88*(2-3), 152-162.

Zhang, S., Liu, J., Wei, M., & Elsworth, D. (2018). Coal permeability maps under the influence of multiple coupled processes. *International Journal of Coal Geology, 187*, 71-82.

5.3 Discrete fracture matrix (DFM) modelling of CO_2 flow – deformation process in fractured coal: Two-phase flow

5.3.1 Introduction

Section 5.2 presents a DFM modelling approach to simulate the fully-coupled CO_2 flow-coal deformation process in a fractured coal mass, by considering the pure CO_2 gas flow – i.e. single-phase flow behaviour. However, under *in-situ* reservoir conditions, typical coal seams are saturated with pore fluids with different chemistries (Van Voast, 2003) and therefore the combined effect of both pore fluid and injected CO_2 has to be considered (i.e. two-phase flow behaviour), when modelling the fully-coupled process. Although previous studies have comprehensively investigated the two-phase flow behaviour in coal during CO_2 sequestration and CBM extraction (Fan et al., 2019; Liu and Smirnov, 2008; Yang et al., 2019), most of the numerical models were developed using single- or multi-continuum models, neglecting the explicit fracture networks in model geometries. This is a major research gap in this context because the explicit representation of the fracture network is quite imperative due to its dominant impact on the entire process. This section provides an extension to the single-phase flow model presented in section 5.2, in which a DFM model was developed, considering the combined effect of both water and CO_2 interaction, coupled with the mechanical deformation. The subsequent sections explain the theoretical approach, modelling results, discussion and conclusions.

5.3.2 Theoretical approach for the hydro-mechanical model

The DFM modelling approach and the theoretical approach for the fully-coupled hydro-mechanical model are somewhat similar to the single-phase flow model, as described in sections 5.2.2 and 5.2.3, respectively. However, since the theoretical approach for the two-phase flow is complicated than that for the single-phase flow model – that requires a set of supplementary equations to solve the complete problem, the extended theoretical approach is re-explained in this section. In fact, the simulation was done considering the drainage process, where the injection of non-wetting phase (i.e. CO_2) replaces the wetting phase (i.e. water) in coal, and therefore the saturation of wetting phase reduces with CO_2 pressure development. The entire approach consists of modelling the concurrent CO_2 and water flows in the fractures, CO_2 diffusion and adsorption in matrices, adsorption-induced swelling deformation, fracture aperture and fracture permeability variations, effect of fracture fluid pressure and fracture stiffness on deformation, contact modelling with frictional interfaces, and defined stress and displacement conditions at boundaries to mimic the *in-situ* reservoir conditions. The complete process can be disintegrated into hydraulic and mechanical problems, with cross-coupling terms, as described in the following sub-sections.

5.3.2.1 Hydraulic-transport system

The hydraulic problem is solved by considering the: 1) longitudinal water flow, free and dissolved gas flow in fracture domain (Ω_f) – that occurs along the fractures, 2) gas diffusion through the matrix domain (Ω_m) – that accounts for the free and adsorbed gas and 3) transverse gas flow across the domain interfaces (Γ_{m,f_1} and Γ_{m,f_2}) – that represents gas transfer between fracture and the matrix at fracture-matrix interface boundaries. The transverse flow for water is disregarded since water is not considered in the matrix domain (Bertrand et al., 2019; Fan et al., 2019; Yang et al., 2019).

The two-phase flow in fractured geological reservoirs is complicated because water and CO_2 are interrelated and interact with each other in the fracture domain. The mass conservation for the water and gas phases in the fracture system can be formulated as in Eq. 5-20 and 5-21, respectively. Note that the mass conversation equation for gas-phase includes both free gas and the dissolved gas in water.

$$\frac{\partial(m_w)}{\partial t} + \nabla.(\rho_w u_w) = Q_w \qquad \text{[5-20]}$$

$$\left[\frac{\partial(m_{f,g})}{\partial t} + \nabla.\left(\rho_{f,g} u_{f,g}\right)\right]_{free\ gas} + \left[\frac{\partial(m_{f,w,g})}{\partial t} + \nabla.\left(\rho_{f,w,g} u_w\right)\right]_{dissolved\ gas} = Q_g \qquad \text{[5-21]}$$

where, m_w, $m_{f,g}$ and $m_{f,w,g}$ are the mass of water, mass of free gas in fractures and the mass of dissolved gas in fractures, respectively. Similarly, ρ_w, $\rho_{f,g}$ and $\rho_{f,w,g}$ are the density of water, density of free gas in fractures and density of dissolved gas in fractures, respectively. u_w and $u_{f,g}$ respectively represent the velocities of water and gas in fractures, and Q_w and Q_g are the water and gas sources/sinks, respectively.

The masses of each phase can be defined in terms of saturation as in Eq. 5-22.

$$\begin{cases} m_w = S_w \phi_f \rho_w \\ m_{f,g} = S_g \phi_f \rho_{f,g} \\ m_{f,w,g} = S_w \phi_f \rho_{f,w,g} \end{cases} \qquad \text{[5-22]}$$

where, ϕ_f is the fracture porosity and S_w and S_g are the water and gas saturations, respectively.

The relationship between S_w and S_g is defined in Eq. 5-23.

$$S_w + S_g = 1 \qquad \text{[5-23]}$$

The densities of each phase are defined as functions of the pressure of the corresponding phase and can be expressed as in Eq. 5-24.

$$\begin{cases} \rho_w = \rho_{w0}[1 + C_w(p_w - p_{w0})] \\ \rho_{f,g} = \frac{M_g}{RT} p_{f,g} \\ \rho_{f,w,g} = H_g \rho_{f,g} \end{cases} \qquad \text{[5-24]}$$

where, ρ_{w0} is the liquid density at the pressure p_{w0}, p_w is the water pressure in fractures, C_w is the liquid compressibility, $p_{f,g}$ is gas pressure in the fractures and H_g is Henry's coefficient.

Velocities of the water and gas can be expressed with Darcy's law (Darcy, 1856), including the Klingenberg effect as follows.

$$\begin{cases} u_w = -\frac{k_f k_{rw}}{\mu_w} \nabla p_w \\ u_{f,g} = -\frac{k_f k_{rg}}{\mu_g} \left(1 + \frac{b_K}{p_{f,g}}\right) \nabla p_{f,g} \end{cases} \qquad \text{[5-25]}$$

where, $k_f (= \frac{b}{12}^2)$ is the absolute fracture permeability, that is defined as a function of local fracture aperture (b), μ_w and μ_g are the dynamic viscosity of water and gas, b_K is the Klingenberg factor, and k_{rw} and k_{rg} are the relative permeabilities of water and gas, respectively.

By combining Eq. 5-20 to 5-25, and considering the variable porosity and density terms in each phase, the governing equations for water flow and gas flow in fractures can be derived as given in Eq. 5-26 and 5-27, respectively.

$$S_w \phi_f \frac{\partial(\rho_w)}{\partial t} + \phi_f \rho_w \frac{\partial(S_w)}{\partial t} + S_w \rho_w \frac{\partial(\phi_f)}{\partial t} + \nabla.\left(-\rho_w \frac{k_f k_{rw}}{\mu_w} \nabla p_w\right) = Q_w \qquad \text{[5-26]}$$

$$\left[S_g \phi_f \frac{\partial(\rho_{f,g})}{\partial t} + \phi_f \rho_{f,g} \frac{\partial(S_g)}{\partial t} + S_g \rho_{f,g} \frac{\partial(\phi_f)}{\partial t} + \nabla.\left(-\rho_{f,g} \frac{k_f k_{rg}}{\mu_g}\left(1 + \frac{b_K}{p_{f,g}}\right) \nabla p_{f,g}\right)\right]_{free} + \left[H_g S_w \phi_f \frac{\partial(\rho_{f,g})}{\partial t} + H_g \phi_f \rho_{f,g} \frac{\partial(S_w)}{\partial t} + H_g S_w \rho_{f,g} \frac{\partial(\phi_f)}{\partial t} + \nabla.\left(-H_g \rho_{f,g} \frac{k_f k_{rw}}{\mu_w} \nabla p_w\right)\right]_{dissolved} = Q_g \qquad \text{[5-27]}$$

In Eq. 5-26 and 5-27, S_w, S_g and ρ_w, $\rho_{f,g}$ are defined in Eq. 5-23 and 5-24, respectively, k_f varies with local fracture aperture; thus, depends on the mechanical deformation. Since there is no water flow across the fracture matrix interface, the source/sink term for water (Q_w) becomes zero. The total fracture pressure (p_f) in fracture network is the combination of pressure from water and gas with their corresponding saturations, and can be defined as,

$$p_f = S_w p_w + S_g p_{f,g} \qquad \text{[5-28]}$$

The concept of the saturation-dependent relative permeability is introduced to incorporate the simultaneous water and gas flow in fracture domain under un-saturated condition. The relative permeability accounts for the reduction in permeability of a particular phase (i.e. gas or water) in the range of partially- to fully-saturation. In the initial development of the theory of relative permeability, the simplest form of relative permeability model was developed by Romm (1966), known as ‘X-model, which assumes that the space used by one phase is unavailable for the other phase. It outcomes a linear relationship between relative permeability and saturation with end-points at 0 and 1 *(see Figure 5-16)*. The respective relative permeabilities are defined in Eq. 5-29.

$$\begin{cases} k_{rw} = S_w \\ k_{rg} = S_g = 1 - S_w \end{cases} \qquad \text{…………} \ [5\text{-}29]$$

As apparent in Eq. 5-29, the summation of the relative permeabilities of water and gas equals 1, implying that the phase-interference is disregarded and thus each phase follows its own path without impeding the other. However, the X-model may no longer valid for a flow through a real fracture, if the phase-interference is noteworthy under given conditions. Hence, an advanced model was introduced by Fourar and Lenormand (1998), by taking the interference between the two phases into account, through viscous consideration. This model, known as viscous coupling model or the pipe flow model *(see Figure 5-16)* can be used to the simultaneous two-phase flow between planar interfaces, by considering the water as the wetting phase that is in contact with fracture surfaces and CO_2 as the non-wetting phase.

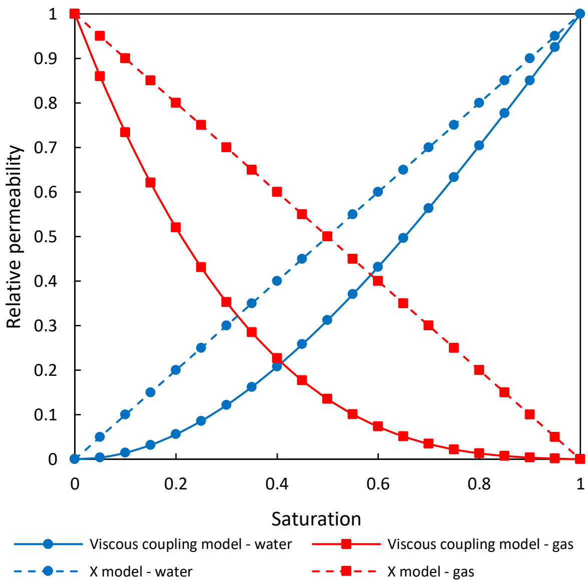

Figure 5-16 – The relative permeability curves of water and gas, considering X model and viscous coupling model.

The current study adopts the viscous coupling model for defining the saturation-dependent relative permeabilities, that is derived by assimilating the Stokes' equation and can be defined as in Eq. 5-30. The complete derivation is given elsewhere (Bertrand et al., 2019).

$$\begin{cases} k_{rw} = \frac{{S_w}^2}{2}(3 - S_w) \\ \\ k_{rg} = (1 - S_w)^3 + \frac{3}{2}\mu_{g/w} S_w (1 - S_w)(2 - S_w) \end{cases} \quad \text{………..} [5\text{-}30]$$

where, $\mu_{g/w}$ $(= \frac{\mu_g}{\mu_w})$ is the viscosity ratio between gas and water. Note that, for the two-phase flow with water and gas, the viscosity ratio $(\mu_{g/w})$ is less than 1 and therefore, the latter term of k_{rg} equation becomes negligible.

Since the relative permeability generally depends on saturation but is not directly equivalent, a retention-curve is needed to define the degree of saturation from primary unknowns, i.e. gas and water pressures. The definition of the retention curve infers the distribution of the apertures of the fractures in a fractured porous media. At macro-scale, the fractures are either filled with water or gas in certain fractures depending on the capillary pressure, whereas at micro-scale, the capillary pressure model should take the two-phase flow effect in a single fracture into account. The capillary pressure for the flow between two parallel plates (i.e. a single planar fracture) can be expressed in terms of fracture aperture, as in Eq. 5-31 (Hadi, 2016).

$$p_c = \frac{2\sigma \cos\theta}{b} \quad \text{………..} [5\text{-}31]$$

where, p_c is the capillary pressure, θ is the contact angle, σ is the surface tension, and b is the local fracture aperture.

The Eq. 5-31 signifies the dependency of capillary pressure on the local fracture aperture and is used by researchers to model the two-phase flow in partially saturated porous media (Wang and Narasimhan, 1985). This equation implies that the capillary pressures are weaker and stronger in broader and narrower fractures, respectively. Further, by considering the irregular shape of the fracture wall, and the respective wall as a fractal-object, the fracture is replaced with a fractal distribution of capillary-tubes with varying sizes, and the relationship defined in Eq. 5-31 can be further utilized to derive the capillary pressure of an irregular fracture at micro-scale. This derivation outcomes a retention curve in the form of Brooks-Corey equation, as given in Eq. 5-32, and is utilized in the current study to define the capillary pressure. The complete derivation is given elsewhere (Bertrand et al., 2019).

$$p_c = p_e(Se)^{-1/\beta} \quad \text{………..} [5\text{-}32]$$

where, p_e is the capillary entry pressure, β is the pore size factor, and Se is the effective saturation, defined as,

$$Se = \frac{S_w - S_{wr}}{1 - S_{wr} - S_{gr}} \qquad \text{………… [5-33]}$$

where, S_{wr} is the irreducible water saturation, S_{gr} is the residual gas saturation.

Relationship between fracture gas pressure and water pressure may be defined as,

$$p_{f,g} - p_w = p_c \qquad \text{………… [5-34]}$$

Since it is assumed that only the gas phase enters the matrix from the fracture-matrix interfaces, the gas flow in the matrix is modelled similar to the single-phase modelling, as defined in section 5.2.3.1.2. In fact, the governing equation is defined in the form of Fick's second law, by considering free and adsorbed gas phases in coal matrix – defined with Langmuir-type model and the constant diffusion coefficient approach. Hence, the equation of gas flow in matrix is defined as in Eq. 5-35.

$$\left[\phi_m + (1-\phi_m)P_a\rho_c \frac{V_L P_L}{(p_{m,g}+P_L)^2}\right]\frac{\partial p_{m,g}}{\partial t} + \left(p_{m,g} - P_a\rho_c \frac{V_L p_{m,g}}{p_{m,g}+P_L}\right)\frac{\partial \phi_m}{\partial t} - \nabla(D_g \nabla p_{m,g}) = Q_s \qquad \text{……. [5-35]}$$

where, $p_{m,g}$ is the matrix gas pressure.

In the equi-dimensional DFM modelling approach, the transverse gas flow between fracture and the matrix domains are resolved as flux and pressure continuities across the fracture-matrix interface boundaries (i.e. Γ_{m,f_1} and Γ_{m,f_2}), as defined in Eq. 5-36 and 5-37. (Tunc et al., 2012);

$$q_{T,f,g}.\boldsymbol{n} = q_{T,m,g}.\boldsymbol{n} \qquad \text{on} \qquad \Gamma_{m,f_1} \text{ and } \Gamma_{m,f_2} \qquad \text{……………. [5-36]}$$

$$p_{f,g} = p_{m,g} \qquad \text{on} \qquad \Gamma_{m,f_1} \text{ and } \Gamma_{m,f_2} \qquad \text{……………. [5-37]}$$

where, $\boldsymbol{n}$ is the unit normal vector and $q_{T,i,g}$ is the transverse gas flow ($i = f, m$).

5.3.2.2 Mechanical system

The mechanical problem is resolved similar to the approach explained in section 5.2.3.2, in which the coal deformation is coupled with the flow problem, by considering gas pore pressure and gas adsorption-induced swelling, fracture fluid pressure and fracture stiffness. Hence, the Navier-type governing equation for coal matrix deformation given in Eq. 5-16 is re-written in terms of matrix gas pressure ($p_{m,g}$), and is expressed as,

$$Gu_{i,kk} + \frac{G}{1-2v}u_{k,ki} - \alpha p_{m,g,i} - K\varepsilon_{s,i} + f_i = 0 \qquad \text{…………….. [5-38]}$$

where, $\varepsilon_s \left(= \varepsilon_L \frac{p_{m,g}}{p_{m,g}+P_L}\right)$ is the adsorption-induced strain due to gas pressure in matrix, and all the other terms are similar to that defined in Eq. 5-16.

Further, the effect of fracture stiffness is included assuming a constant normal fracture stiffness, and the fracture fluid pressure is applied on the fracture walls as a surface pressure *(see Figure 5-2 (b))*. Hence, the relationship between normal stress and fracture closure is defined as in Eq. 5-17, in which the fracture fluid pressure is defined as in Eq. 5-28. Further, the contact pairs and frictional interfaces are defined at the fracture-matrix interfaces – that are likely to contact during deformation, with no-penetration rule and the Coulomb frictional method, respectively *(see Eq. 5-18)*. The stress and displacement conditions are defined in model boundaries, mimicking the *in-situ* conditions, as explained in the following section.

5.3.3 Model geometry and simulation procedure

Because of the intricacy of fully-coupled, hydro-mechanical process and the adopted DFM modelling approach, the model geometry was defined in 2D with 6 matrix blocks and fracture aperture varying in a range of 0.4 – 0.6 mm *(see Figure 5-17)*. In the DFM model, the fractures were modelled as the spaces between matrices, in which the fracture aperture varies with the deformation of bounding matrices – due to fracture flow pressure, confining pressure, adsorption-induced swelling stress and boundary pressures. Since the fracture network was defined explicitly in the geometry, the model – integrated with a time-dependent solver, is capable of simulating the temporal and spatial variations of each parameter in both fracture and matrix domains. The local fracture aperture was determined in each solving step using the deformed model geometry and was used to calculate the corresponding absolute fracture permeability at a certain point, which then was used as a coupling term in the hydraulic problem – thus the continuous variation of water and CO_2 flows with the mechanical deformation was captured accurately. The simulation was run in COMSOL multi-physics software, where the saturation and pressure variation in fracture and matrix domains were modelled with different modules because the governing equations were substantially modified from the conventional ones to account for the two-phase flow, variable permeability, diffusion and adsorption *(see Eq. 5-26, 5-27 and 5-35)*. In the simulating procedure, a confining pressure of 10 MPa was applied on the outer boundary of each matrix block to mimic the *in-situ* reservoir conditions *(see Figure 5-17)*. The fracture domain was considered as water-wet with an initial water saturation of 0.8. To simulate the drainage process or the CO_2 injection procedure, and to ensure rapid convergence, the CO_2 pressure was applied into one fracture from the left side at 8 MPa injection pressure. A finer mesh was adopted near the narrow regions (i.e. fracture boundaries and interconnections) to improve the simulation accuracy. The required properties and model parameters related to two-phase flow and coal deformation were obtained from experimental studies and supplementary sources (Fan et al., 2019; Masoudian et al., 2014; Robertson and Christiansen, 2005; Yang et al., 2019) and are given in Table 5-2.

Table 5-2 – Parameters used in the model.

Parameter	Value
Coal density ($\boldsymbol{\rho_c}$) ($\boldsymbol{kg/m^3}$)	1440
Biot's coefficient ($\boldsymbol{\alpha}$)	0.8
Normal fracture stiffness ($\boldsymbol{K_n}$) ($\boldsymbol{GPa/m}$)	60
Poisson's ratio ($\boldsymbol{\upsilon}$)	0.339
Young’s modulus ($\boldsymbol{E}$) ($\boldsymbol{MPa}$)	3713
Coefficient of friction ($\boldsymbol{F}$)	0.6
Matrix porosity ($\boldsymbol{\phi_m}$)	0.02377
Fracture porosity ($\boldsymbol{\phi_f}$)	1
Langmuir sorption constant ($\boldsymbol{V_L}$) ($\boldsymbol{m^3/kg}$)	0.0477
Langmuir pressure constant ($\boldsymbol{P_L}$) ($\boldsymbol{MPa}$)	4.64
Langmuir volumetric strain constant ($\boldsymbol{\varepsilon_L}$)	0.0297
Gas diffusion coefficient ($\boldsymbol{D_g}$) ($\boldsymbol{m^2/s}$)	9.48×10^{-11}
Initial gas pressure in fractures ($\boldsymbol{P_{f,g0}}$) ($\boldsymbol{MPa}$)	0.101325
Initial gas pressure in matrix ($\boldsymbol{P_{m,g0}}$) ($\boldsymbol{MPa}$)	0.101325
Initial water saturation ($\boldsymbol{S_{w0}}$)	0.8
Temperature ($\boldsymbol{T}$) ($^o\boldsymbol{C}$)	40
Henry’s coefficient ($\boldsymbol{H_g}$)	0.0347
Dynamic viscosity of gas ($\boldsymbol{\mu_g}$) ($\boldsymbol{Pa.s}$)	1.84×10^{-5}
Dynamic viscosity of water ($\boldsymbol{\mu_w}$) ($\boldsymbol{Pa.s}$)	1.01×10^{-3}
Klingenberg factor ($\boldsymbol{b_K}$)	0.76
Density of CO_2 at STP ($\boldsymbol{\rho_{CO_2}}$) ($\boldsymbol{g/ml}$)	0.00196
Density of water at $\boldsymbol{p_{w0}}$ ($\boldsymbol{\rho_{w0}}$) ($\boldsymbol{kg/m^3}$)	1000
Compressibility of water ($\boldsymbol{C_w}$) ($\boldsymbol{1/Pa}$)	5×10^{-5}
Molar mass of CO_2 ($\boldsymbol{M_g}$) ($\boldsymbol{g/mol}$)	44.01
Universal gas constant ($\boldsymbol{R}$) ($\boldsymbol{J/mol.K}$)	8.314
Entry capillary pressure ($\boldsymbol{P_e}$) ($\boldsymbol{Pa}$)	2×10^4
Pore size factor ($\boldsymbol{\beta}$)	2
Irreducible water saturation ($\boldsymbol{S_{wr}}$)	0.2
Residual gas saturation ($\boldsymbol{S_{gr}}$)	0.05

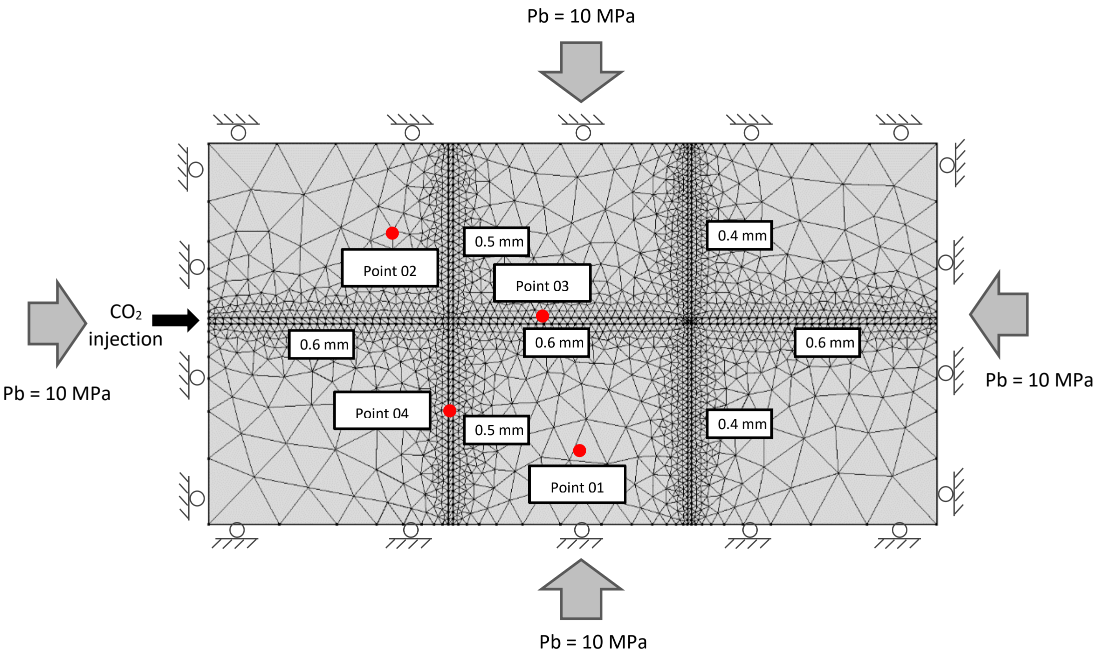

Figure 5-17 - Geometric model, indicating the meshing, boundary pressures and displacement, the CO_2 injection and, the points of interest used to analyse the spatial variations.

5.3.4 Modelling results

The model results are discussed in terms of water and gas saturation variation, temporal and spatial variations of pressure distribution, adsorption-induced matrix swelling, fracture aperture and permeability reductions, by considering four points of interest distributed throughout the geometry – i.e. two points are in the fracture domain, and other two are in the matrix domain *(see Figure 5-17)*.

The accurate definition of the relative permeability curves and the retention curve is imperative in modelling the simultaneous water and gas flow in the fracture domain, within the defined saturation range. Figure 5-18 (a) and (b) illustrate the variations of the water and gas relative permeabilities, and the capillary pressure with water saturation, respectively. In fact, the figure compares the analytical models defined in Eq. 5-30 and 5-32 with the direct outcome of the simulation results, which shows a good fit within the defined saturation range – i.e. between initial water saturation and the irreducible water saturation, confirming model's solution accuracy of the two-phase flow behaviour in the fracture domain. As apparent in Figure 5-19 (a), with the drainage process or the CO_2 injection takes place, the wetting phase (water) is displaced by the non-wetting phase (CO_2), reducing the water saturation in water-wet fractures from initial saturation to irreducible saturation. It should be noted that the axis of gas pressure is in log-scale, and a majority of phase change occurs in relatively low gas pressure, during the drainage process. This is in line with the experimental and numerical results presented by Liu and Smirnov (2008), who analysed the CO_2 sequestration process in coal seams with a variably saturated simulation. The reduction of water saturation concurrently causes the relative permeability and the capillary pressure changes *(see Figure 5-18)*, affecting the two-phase flow behaviour in fractures.

Converse to the water saturation decrement, Figure 5-19 (a) further illustrates that the CO_2 saturation rises with the increment of CO_2 partial pressure in the fractures. With this increment of CO_2 pressure, CO_2 starts to diffuse into the matrices through the fracture-matrix interfaces due to the induced pressure difference between the two domains, causing the CO_2 adsorption-induced swelling. Figure 5-19 (b) illustrates the temporal variation of matrix pore pressure at two points of interest that signifies the increasing trend of CO_2 pressure with the CO_2 interaction time. The deviation between the two curves highlights the difference in the spatial disposition of two points, in which point 02 shows a rapid pressure development, as the particular point is located closer to the high-permeable fracture boundary, compared to point 01 – that provides easy access for the CO_2 to reach the location during the CO_2 injection process. Both points show a rapid pressure development at the beginning due to the large initial pressure gradient, and gradually level off by reaching the pressure equilibrium at 8 MPa. However, the time frame for the pressure equilibrium is dependent on the coal type, that is defined by the diffusion coefficient in the model, and should be determined accurately.

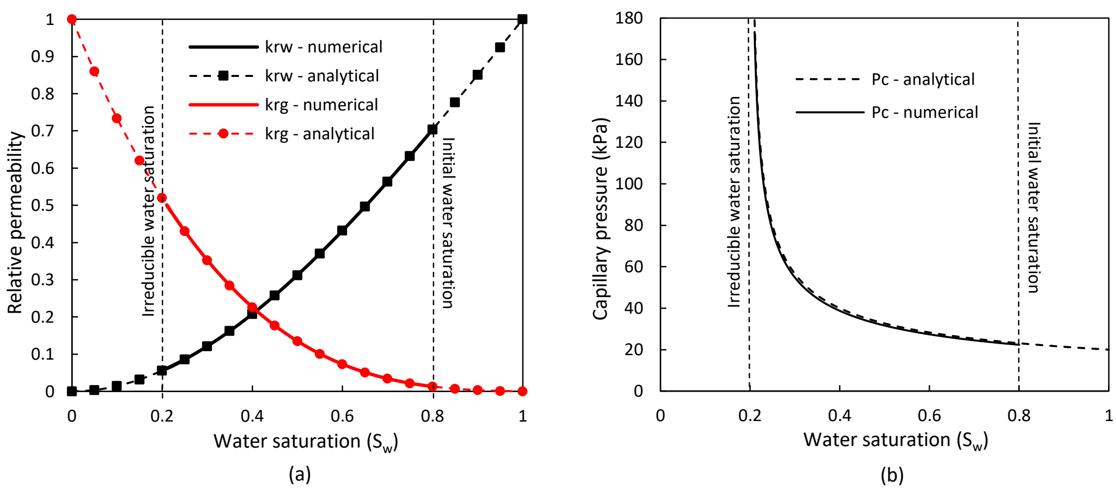

Figure 5-18– Comparison of analytical and numerical results between the range of initial and irreducible water saturation: a) relative permeabilities and, b) capillary pressure curve.

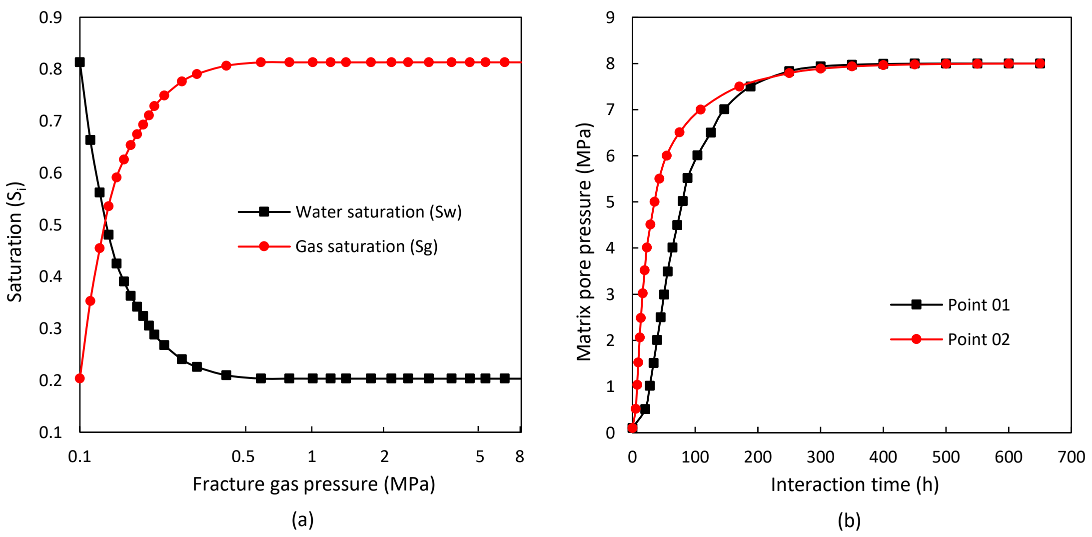

Figure 5-19 – a) Variation of water and gas saturations with the fracture gas pressure and, b) variation of matrix pore pressure at two points of interest with CO_2 interaction time.

The adsorbed amount of CO_2 is calculated with the volume integral of the matrix domain of the geometry, as defined in Eq. 5-19. Figure 5-20 shows the variations of the adsorbed amount of CO_2 with the CO_2 interaction time and with the average matrix pore pressure, in which the temporal adsorbed CO_2 variation follows a similar trend as the temporal pressure variation *(see Figure 5-19 (b))* because the adsorbed amount is simply a function of the matrix pore pressure. This is confirmed by the adsorbed amount vs matrix pore pressure variation, as the respective curve exemplifies more or less a linear trend in the given pressure range. However, it should be expected for the process to reach a maximum adsorption capacity and levels off at a particular elevated CO_2 pore pressure, due to the invasion of all the possible/potential adsorption sites by the CO_2 molecules with the increment of CO_2 pressure. This, in fact, depends on the coal type of the targeted reservoir and should be evaluated accurately prior to the implementation of the project. Further, the CO_2 adsorption causes volumetric swelling of the coal matrix, which has been identified as a significant drawback of the sequestration process. Figure 5-21 illustrates the variation of the volumetric strain of two points of interest in the matrix domain with the CO_2 interaction time. Similar to single-phase flow model explained in section 5.2, the volumetric strain outcomes a negative value at the beginning, due to the shrinkage effect induced by the confining pressure and fracture fluid pressure (includes both water and gas phases), applied as a surface pressure on the matrix walls. With the increment of CO_2 pore pressure in the matrix, the CO_2 adsorption-induced swelling takes place and therefore the volumetric strain increases, resulting in an overall volume expansion of the coal matrix at the equilibrium. This can consequently close down the coal fracture network, hindering the fracture conductivity and ultimately further CO_2 injectivity into the reservoir.

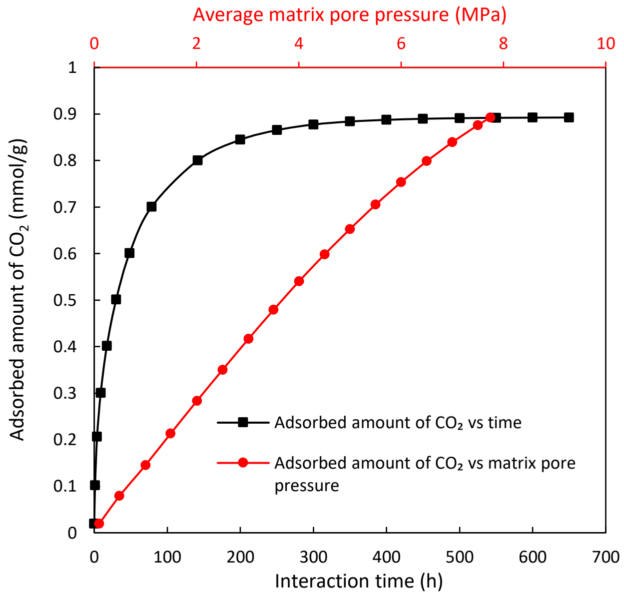

Figure 5-20 – Variation of adsorbed amount of CO_2 with CO_2 interaction time and matrix pore pressure.

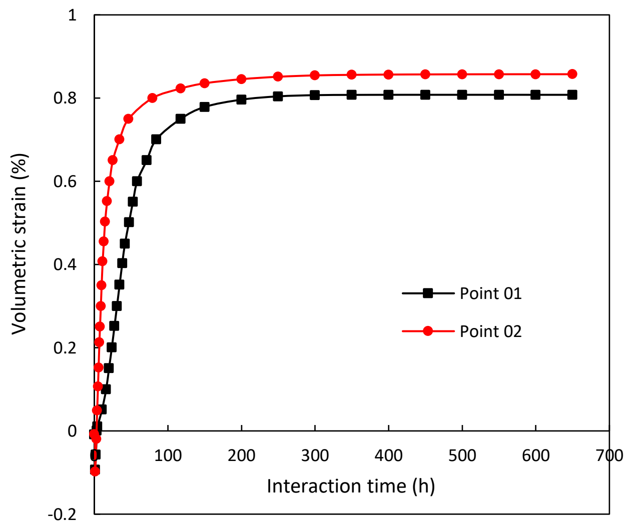

Figure 5-21 – Variation of volumetric swelling at two points of interest with CO_2 interaction time.

The natural fracture network plays an imperative role in the CO_2 flow behaviour of fractured coal reservoirs by controlling the major flow paths and the ultimate reservoir permeability. The fracture network in coal is highly-stress-dependent; thus, varies temporally and spatially during the CO_2 injection process, due to the variation of pore pressure, fracture fluid pressure, boundary pressures and adsorption-induced swelling. DFM modelling of the fully-coupled process with the inclusion of an explicit fracture network provides the provision to analyse the variations of local fracture apertures with given variables of interest. Figure 5-22 (a) illustrates the temporal variation of fracture aperture at two points of interest – that represents two fractures with initial apertures of 0.6 mm and 0.5 mm. The variation depicts a decreasing trend with the increasing CO_2 interaction time, due to sorption-induced swelling of bounding matrices.

As magnified in the internal graph in Figure 5-22 (a), a slight increment in fracture aperture occurs at the beginning, because of the matrix shrinkage induced by the confining pressure and fracture fluid pressure. Nevertheless, this increment is rather insignificant when compared with the overall aperture reduction at the swelling equilibrium. Further, as explained in section 5.2, the local aperture variation is highly-dependent on the deformation of the bounding matrices, which is basically governed by the pore pressure development of the respective matrices. Hence, Figure 5-22 (b) shows the variation of fracture aperture with the average pore pressure development of their corresponding bounding matrices, which implies that the aperture variation is in fact controlled by the bounding matrix deformation.

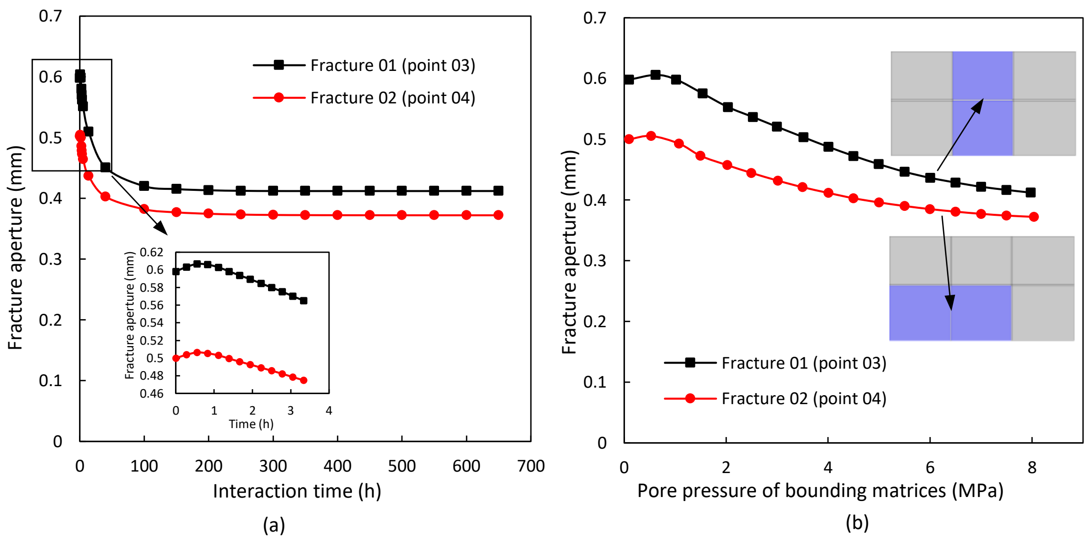

Figure 5-22 – Variation of fracture aperture at two points of interest with a) CO_2 interaction time and, b) average pore pressure of bounding matrices of the corresponding fracture.

Figure 5-23 illustrates the variation of fracture permeability ratio at the same two points of interest, in which the variation depicts a trend similar to the fracture aperture variation because the fracture permeability is defined directly as a function of the local fracture aperture (i.e. with the parallel plate law). The overall reduction in the fracture permeability at the pressure equilibrium infers that the CO_2 adsorption-induced matrix swelling has a noteworthy impact on the CO_2 flow behaviour. Even though fracture flow is quite rapid during the primary CO_2 injection phase due to the relatively large fracture permeabilities caused by fully-opened natural fractures, the latter CO_2 injection phases (secondary/tertiary) or further increment in CO_2 pore pressure may be largely affected by the hydro-mechanical modifications, that are already occurred during the first phase. In fact, this may result in a significant hindrance of further CO_2 injection into coal, due to obstructed fracture flow through the seam, resulting in an inefficient CO_2 sequestration process.

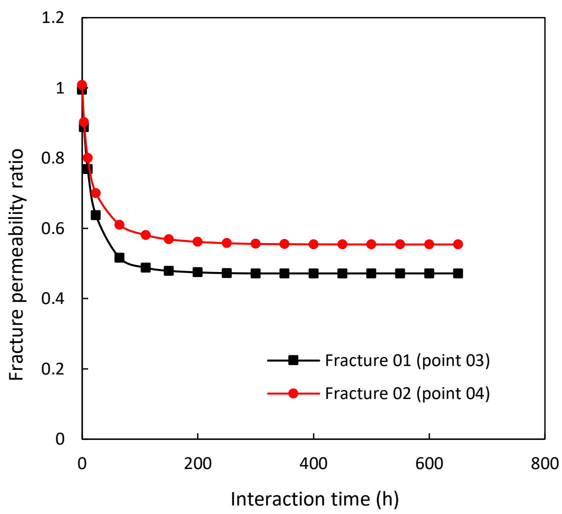

Figure 5-23 – Variation of fracture permeability ratio at two points of interest with CO_2 interaction time.

5.3.5 Conclusions

This study presents a DFM modelling study of the fully-coupled CO_2 flow-adsorption-deformation process in fractured coal, with the inclusion of the two-phase flow behaviour in a water-wet fracture network. The study specifically investigates the gas and water flow behaviour in fractures, in terms of their saturation and partial pressure variations, CO_2 diffusion and adsorption in coal matrices, adsorption-induced matrix swelling and the subsequent variations in local fracture aperture and fracture permeability. The following conclusions were made based on the simulation results:

- With the drainage process or the CO_2 injection process takes place, the water saturation decreases rapidly in the water-wet fracture network at a relatively low gas pressure and concurrently, the gas saturation increases. This simultaneously alters the relative permeabilities and the capillary pressure, affecting the two-phase flow behaviour.
- The increment in partial gas pressure in the fracture network triggers CO_2 diffusion process in the matrices, due to the induced pressure gradient, and the CO_2 diffusion causes CO_2 pore pressure development in matrix pores, resulting in swelling.
- The multifaceted coal deformation process, mainly contributed by the adsorption-induced swelling, leads to the alterations in the stress-dependent local fracture aperture and consequently the fracture permeability, resulting in substantial hydro-mechanical modifications in the coal structure.
- The structural modifications occur during the primary CO_2 injection process may adversely affect the secondary/tertiary injection phases of the process, due to the fracture closure-induced flow modifications in coal, resulting in an inefficient CO_2 sequestration process in the long-run.

5.4 Chapter summary

The productivity of a CO_2 sequestration process in a coal seam greatly depends on the CO_2 injectivity and the flow behaviour, which is basically controlled by the natural fracture network of the coal seam. Comprehensive understanding of the CO_2 interaction-induced alterations occur in the fracture-matrix system, and the consequent alterations in flow behaviour are crucial for a successful sequestration process. This study evaluates the CO_2 flow behaviour-adsorption-deformation process of a fractured coal reservoir by developing a numerical model – validated with experimental data. In fact, this chapter introduces a DFM modelling approach to investigate the fully-coupled process in a coal mass with a discrete fracture network and multiple matrix blocks. Since the effect of the fracture network of coal is dominant, it is essential to explicitly represent the fracture network in the model geometry to evaluate the localized and heterogeneous alterations. Therefore, adopting a DFM modelling approach is crucial in this aspect, rather than using single- or multi-continuum models with scalar porosity/permeability variables.

Overall, the results suggest that the current DFM approach is capable of modelling the fully-coupled hydro-mechanical modifications in coal, by considering the CO_2 flow in coal fractures, diffusion and adsorption in coal matrices and the subsequent matrix swelling that alters the local fracture aperture and the fracture permeability. Further, the models are able to simulate the contact pressures and frictional forces developed in the fracture interfaces due to the fully-closure of the respective fracture. This signifies the permeability reductions and the subsequent localized-flow alterations in the vicinity of the fractures that may occur during further CO_2 injection into the modified coal seam. The comparison of model results between swelling and no-swelling behaviour highlights that the sorption-induced matrix swelling caused by reactive gases like CO_2 has a substantial impact on the pore pressure development in the seam. Thus, it is crucial to accurately incorporate this swelling behaviour in models in order to predict the flow alterations and mechanical deformations during the CO_2 sequestration in coal. The two-phase flow model further highlights that the effect of pore fluid in terms of the saturation degree has a noteworthy influence on the overall CO_2 flow behaviour in fractured coal during the drainage process. The complicated flow regimes arise due to the saturation-dependent relative permeabilities, and the fracture aperture-dependent capillary effect should be accurately incorporated when modelling the concurrent water and CO_2 flows in water-wet fractures.

In general, the current modelling study concludes that the CO_2 interaction causes adverse modifications in the fractured coal structure, which in turn causes alterations in fracture permeability and the CO_2 flow behaviour in the seam, which can hinder the productivity of the sequestration process. Hence, it is important to precisely predict such alterations of targeted coal reservoirs through numerical simulations – prior to the implementation of sequestration projects.

Part 3:

Evaluation of CO_2 interaction-induced mechanical property alterations in coal

(Chapters 6, 7 and 8)

CHAPTER 6

Experimental analysis of static and dynamic mechanical property alterations in CO_2-interacted coal

6 Experimental analysis of static and dynamic mechanical property alterations in CO_2-interacted coal

6.1 Chapter overview and structure

CO_2 interaction results in large mechanical property alterations in coal due to several physical and chemical reactions. Consequently, this may pose great threats to the reservoir integrity and may cause CO_2 outbursts and back migration to the atmosphere or adjacent aquifers. This can be catastrophic in some cases, putting the environment and the local habitats at great risk. A deep understanding of the level of mechanical degradation and the causative factors is thus essential for a safer CO_2 sequestration process. Systematic experimental analyses focused on evaluating different influential parameters are essential to bring science into the field and to understand the underpinning physics. This chapter contains two sections that provide lab-scale experimental studies conducted on CO_2-interacted coal at the supercritical-phase, in which the two sections are dedicated to evaluating the static and dynamic mechanical property alterations.

In the first section, the alterations in static mechanical properties including unconfined/uni-axial compressive strength (UCS), Young's modulus and brittleness index are evaluated, by considering CO_2+various pore fluid conditions and different CO_2 interaction times. The study used Lignite from Loy Yang mine, Latrobe valley, Victoria, because: 1) most of the Victorian coal are Latrobe valley brown coal, hence results can be specifically related to Victoria, 2) there are plenty of studies conducted using Victorian brown coal, hence the current results can be directly compared and interpreted with the literature, and 3) the current study specifically evaluates the effect of CO_2 interaction with coal, in which the presence of methane is disregarded due to the large complexity of the combined interactions and the consequent alterations.

In fact, previous studies reveal that the mechanical alterations depend on multiple factors such as coal rank, characteristics of the cleat system, pore fluid condition, CO_2 pore pressure, temperature, CO_2 interaction time, etc. However, only a minor attention has been paid towards the effects of pore fluid condition and the CO_2 interaction time on the mechanical property alterations. Hence, this study was targeted to study how the pore fluid characteristics: i.e. brine concentration, combined with $CO_{2,}$ affect the level of mechanical degradation in coal. Moreover, the temporal alterations in mechanical properties were investigated by interacting coal specimens with CO_2 under similar saturation conditions for various periods and, then conducting the mechanical testings on the CO_2-interacted specimens. The section further provides 1) a deformation evaluation, based on the ARAMIS analysis, 2) a qualitative/quantitative evaluation of the fracture characteristics of the failed samples, using micro-CT imaging technique and, 3) an evaluation of the macro-molecular structural alterations, using FT-IR analysis. All the results were mutually used to interpret the primarily observed mechanical alterations.

The second section discusses the alterations in gamma densities and ultrasonic wave measurement-based dynamic mechanical properties of a particular CO_2-interacted coal specimen, repeatedly tested at different CO_2 interaction times, under unconfined condition. The static laboratory mechanical testings are more likely to provide information on the bulk sample failure and are unable to evaluate the localized damages of a heterogeneous coal specimen precisely. Coal is a vastly complex material to deal with, because of its unique formation process called coalification. The spatial dispositions of the minerals, macerals, natural cleat system and the nano-scale matrix pore network induce a large heterogeneity and anisotropy into coal, rendering localized damages upon CO_2 interaction. Hence, a sensitive mechanical testing method is essential to analyse such localized alterations, rather than utilizing traditional testing methods. This setback is overcome in this experimental study by conducting sensitive dynamic mechanical tests on a CO_2-interacted coal core specimen by using ultrasonic wave measurement technique. Further, instead of directly measuring bulk density of the specimens using conventional weight-based methods, the gamma-attenuation method was used in the present study to measure densities at specified orientations, and the results were combined with the ultrasonic wave data to precisely determine the anisotropic dynamic mechanical property alterations. A micro-CT study was conducted to visualize and quantify the spatial disposition of macerals/minerals and fractures in the coal specimen and combined with the mechanical testing data to interpret the observed mechanical localizations and anisotropies. Importantly, measurements were taken on the same coal specimen at various CO_2 interaction periods at the supercritical-phase of CO_2, and the temporal alterations in coal mechanical properties were accurately determined based on the experimental results.

Following two sections provide the detailed experimental procedure, results, discussion and the conclusions of the two experimental studies, which are presented in the form of published articles.

6.2 Journal paper: Static mechanical property alterations in CO_2-interacted coal

This section is presented as the author-accepted manuscript of a peer-reviewed article published in "Engineering Geology". The journal is a Q1 journal with impact factor of 3.91.

Citation:

- Sampath K. H. S. M., Perera M. S. A., Li D. Y., Ranjith P.G., Matthai, S. K. (2019). *Evaluation of the mechanical behaviour of brine+ CO_2 saturated brown coal under mono-cyclic uni-axial compression*. Engineering Geology, 263, 105312.

Journal paper title: Evaluation of the mechanical behaviour of brine+ CO_2 saturated brown coal under mono-cyclic uni-axial compression

Authors' names: K.H.S.M. Sampath[1], M.S.A. Perera[1,2], * Dong-yin Li[3], P.G. Ranjith[2], S.K. Matthai[1]

[1]Department of Infrastructure Engineering, Engineering Block B, Grattan Street, Parkville, The University of Melbourne, Victoria 3010, Australia.

[2]Department of Civil Engineering, Monash University, Clayton Campus, Victoria 3800, Australia.

[3]School of Energy Science and Engineering, Henan Polytechnic University, Jiaozuo 454000, China.

Abstract

CO_2 sequestration necessitates CO_2 injection into coal seams that are saturated under various pore fluid conditions, resulting in alterations in mechanical properties. In this study, we evaluate the effect of pore fluid chemistry and the interaction time on the coal mechanical degradation. Uni-axial compressive strength (UCS) tests, ARAMIS photogrammetric analysis, micro-CT imaging, and Fourier transform infrared spectroscopy (FT-IR) are combinedly used to evaluate such alterations and to interpret the causative factors in water, water+CO_2, 10% brine+CO_2 and 20% brine+CO_2 saturated coal. The results indicate that irrespective of the pore fluid chemistry, mechanical parameters including UCS, Young's modulus and brittleness index reduce significantly in saturated coal, due to moisture adsorption-induced softening effect. The presence of CO_2 in pore fluids causes additional alterations in each mechanical property, due to the corrosive chemical interactions occur in acidic environments, CO_2 adsorption-induced energy reduction and plasticization-induced alterations in coal macro-molecular structure. The direct comparison of FT-IR spectrums of natural and CO_2-interacted coal concludes that CO_2 interaction causes alterations in the coal macro-molecular structure possibly causing the mechanical degradation of coal mass due to plasticization effect and the extraction of pore-constricting hydrocarbons. The volumetric strain analysis and micro-CT image-based 3D-reconstruction infer that water, water+CO_2 and 10% brine+CO_2 saturation increase the ductile properties of coal, resulting in a dilatancy deformation and extensive fracturing, upon mechanical loading. In contrast, the higher order of NaCl concentrations (i.e. 20% brine) in pore fluid causes NaCl

crystallization in coal, resulting in an elevated brittleness and consequently altering the sample deformation, failure pattern and fracturing mechanism. Although, softening effect and chemical interactions cause continues mechanical degradation with increasing saturation time in all saturation conditions, a significant strength reduction occurs at a short-term saturation period, and the latter longer saturations have caused only gradual strength reductions, probably due to the rapid CO_2 adsorption process on to coal matrix.

Keywords: *coal seam, mechanical behaviour, brine saturation, supercritical* CO_2

6.2.1 Introduction

Growth of anthropogenic CO_2 level has become one of the foremost drivers of global warming, inferring the necessity of exploring viable ways to mitigate the atmospheric CO_2 content. Geo-sequestration of CO_2 in the subsurface of oil and gas reservoirs, deep saline aquifers and deep un-mineable coal beds is identified as one of the most effective and realistic disposal methods. Of these methods, the geo-sequestration of CO_2 in coal reservoirs has gained an increasing attention, as it adsorbs large quantities of CO_2 due to its relatively larger surface area and is associated with enhanced coal bed methane (ECBM) recovery.

However, unlike other rock formations, coal seams are composed of partially decomposed vegetation and are subjected to the coalification process over a significant geological period; thus, possess complex macro-molecular structures (Teichmüller and Teichmüller, 1966). Moreover, the presence of minerals and their spatial disposition introduce heterogeneity and anisotropy into coal. The injected CO_2 interacts with coal, causing significant alterations in its physical and chemical structures and consequently affects the hydro-mechanical properties of the seam, such as reductions of permeability and strength (Perera et al., 2011; Stevens et al., 2001; Vishal et al., 2013). Permeability reduction may decline the CO_2 injectivity into the seam in the long-run, and the degradation of mechanical properties may damage the host-rock and pose threats of CO_2 back-migration into the atmosphere (Busch and Gensterblum, 2011). Consequently, the CO_2 sequestration encounters multiple drawbacks, which hinders the process effectivity, while triggering social and environmental hazards.

Most potential coal seams exist at deep underground locations, in which they are fully or partially saturated with coal seam gas (CSG) water, with varying ionic concentrations. As revealed by Van Voast (2003) and Taulis and Milke (2013), the CSG water contains a substantial amount of Cl^- and Na^+ ions that act as brine, with varying ionic concentrations. Presence of moisture or brine itself in CSG water may adversely affect the mechanical characteristics of the seam (Li and Wang, 2019; Sampath et al., 2018). For instance, Sampath et al. (2018) conducted UCS tests on brown coal samples, saturated with varying brine concentrations and showed that the softening effect caused by moisture adsorption and chemical interactions between the coal mass and the ions in the brine solution can significantly reduce the coal strength. The tested samples exhibited higher plastic deformations and a dilatancy behaviour due to the softer nature induced by brine saturation. Despite this fact, many CO_2-related studies often ignore the influence of the presence of brine in CSG water and the combined effect of brine+CO_2 on the mechanical behaviour of coal. In fact, a part of the injected CO_2 dissolves in the CSG water and forms carbonic acid, resulting in an acidic environment *(see Eq. 6-1)*. Consequently, a number of corrosive chemical interactions occur, which cause the dissolution of minerals and lead to irreversible changes in coal structure. As revealed by Marbler et al. (2013), the dissolution of pore filling calcite creates a secondary pores within the primary porosity system, weakening the rock mass pore structure.

$$CO_2 + H_20 \leftrightarrow H_2CO_3 \leftrightarrow H^+ + HC0_3{}^- \qquad \text{………… [6-1]}$$

Although numerous studies have been conducted to evaluate the brine+CO_2 interaction-induced strength alterations in various rock types (Lyu et al., 2018; Perera et al., 2018; Rathnaweera et al., 2014; Shukla et al., 2013), its effect on coal mechanical parameters is still not clearly understood. Importantly, the effect of brine concentration in the pore fluid and the effect of saturation time on the coal mechanical properties are not deeply investigated. One of the most common and efficacious techniques of characterizing mechanical parameters of bulk rock specimens is UCS experiments. The technique is well-established and widely used for mechanical characterization, as it is easy to conduct, inexpensive, rapid and importantly, meaningful strength parameters such as Young's modulus, brittleness index are derived from stress-strain curves to interpret the mechanical competency of the rock (Hawkes and Mellor, 1970; Li et al., 1998).

This paper investigates the alterations of coal mechanical properties under different brine+CO_2 saturation conditions. The study is specifically focused on evaluating the effect of different brine concentrations, the effect of saturation time and the combined effect of brine+CO_2 on the coal mechanical properties, while CO_2 is under supercritical condition. The primary mechanical test series is combined with 1) SEM-EDS analysis – to analyse the coal composition, interior coal structure and to identify the chemical elemental composition, 2) ARAMIS photogrammetric analysis – to analyse the strain variation and sample deformation, 3) micro-CT analysis - to qualitatively and quantitatively evaluate the coal micro-structure at failure and, 4) FT-IR – to evaluate the CO_2-induced alterations in coal macro-molecular structure. These multiple analyses are collectively utilized to evaluate the brine+CO_2-induced mechanical alterations in coal and to highlight the possible causative factors.

6.2.2 Experimental procedure

6.2.2.1 Sample acquisition and characterization

The samples were obtained from Loy-Yang open cut mine, Latrobe Valley, Victoria, Australia. The geo-graphical location of the coal basin is illustrated in Figure 6-1 (Holdgate et al., 2014). Coal seams typically exist 10 to 20 m below the ground surface, and the layer thickness varies from 100 m to 230 m where the multiple seams coalesce. The samples are low-rank brown coal samples, and the typical properties are given in Table 6-1. All the samples were acquired as blocks of about 300 ×300 ×300 mm^3 from the mine and were double-sealed with polyethylene films, as soon as retrieved from the coal mine. Then, the sealed samples were preserved in a fog room in deep earth engineering laboratory (DEERL), Monash University until the sample preparation, to avoid any moisture loss from the samples.

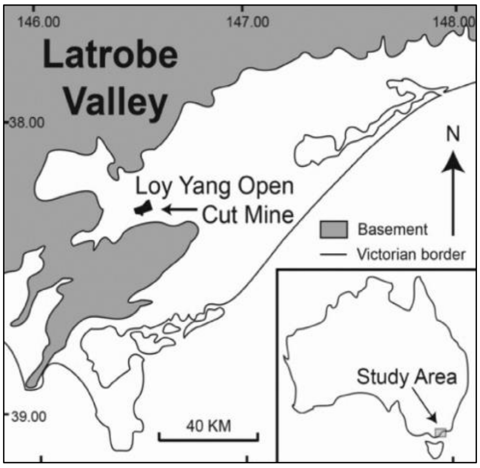

Figure 6-1 – Geo-graphical location of the Loy-Yang mine, Victoria, Australia (Holdgate et al., 2014).

Table 6-1 - Typical characteristics of the Latrobe Valley brown coal (Sakaguchi et al., 2008).

Coal seam characteristics			**Values**
Average bulk density			1130 kgm^{-3}
Average dry density			700 kgm^{-3}
Proximate analysis results	Fixed carbon	Wt. % (dry ash-free basis)	48%
	Ash		1.5%
	Volatile matter		52.3%
	Moisture	Wt. % (as received)	59.4%
Ultimate analysis results	Carbon	Wt. % (dry ash free basis)	68.4%
	Oxygen (by difference)		24.9%
	Nitrogen		0.56%
	Hydrogen		4.9%

6.2.2.2 Sample preparation and experimental conditions

Congruent with ASTM specifications (ASTM-D.4543), coal blocks were cored and cut using diamond coring and cutting machines, respectively to obtain core samples of 38 mm in diameter and 76 mm in length at DEERL. In total, 11 conditions were tested, in which 3 samples were used under each saturation condition, and the results were averaged to have an accurate and reliable interpretation. The testing conditions are given in Table 6-2.

Table 6-2 - Sample testing conditions and saturation time.

Testing condition	Brine concentration (by weight %)	Saturation time
As received	-	-
De-ionized water saturated	0%	45 days
De-ionized water+CO_2 saturated	0%	1 day
		14 days
		45 days
Brine+CO_2 saturated	10%	1 day
		14 days
		45 days
Brine+CO_2 saturated	20%	1 day
		14 days
		45 days

6.2.2.3 De-ionized water saturation and brine+CO_2 saturation

The prepared core samples were initially fully vacuum dried for 24 h to remove entrapped air and impurities from the coal pores. The de-ionized water saturation experiment was carried out in a vacuum chamber, and the brine+CO_2 saturation experiments were carried out in high-pressure reaction chambers at DEERL. The brine concentrations were selected to simulate natural brine concentration levels in typical coal reservoirs. Three reaction chambers were used to carry out the experiments simultaneously under different saturation conditions (i.e. de-ionized water and brine with 10% and 20% concentrations). Each reaction chamber consists of a stainless-steel cell with a diameter of 60 mm and a depth of 100 mm. The CO_2 was injected and regulated by a syringe pump with a capacity of 50 MPa injection pressure, and the temperature was maintained by a heating belt attached to the cell *(see Figure 6-2)*. Initially, the samples were inserted into the cells and filled with corresponding saturation solution. Then the cells were attached to the syringe pump, and CO_2 was injected at 90 ml/min injection rate. Considering the overburden pressure and the geothermal gradient of the coal seam, the CO_2 saturation pressure of 10 MPa and the temperature of 40 ºC were used to simulate *in-situ* reservoir conditions and the supercritical-phase of CO_2. Once the desired pressure and temperature conditions were reached, the cells were sealed and allowed to saturate for the pre-defined saturation periods as given in Table 6-2 (i.e. 1 day, 14 days and 45 days). During the saturation period, the pressure and temperature inside the cells were continuously monitored and kept at constant levels. Once the desired saturation was achieved, the samples were retrieved from the cell after gradually depressurizing the chambers, to avoid any damage to the structural integrity of samples, due to the rapid gas release. The retrieved samples were preserved by double-sealing with polyethylene films, until the mechanical testing.

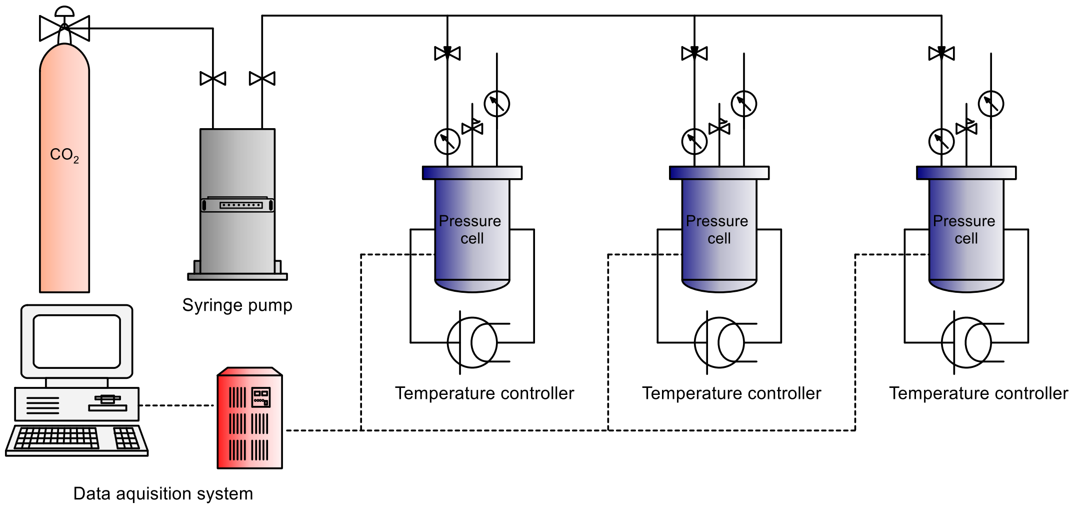

Figure 6-2 - Schematic diagram of the high pressure/temperature reaction chamber system used for the simultaneous brine+CO_2 saturation.

6.2.2.4 ARAMIS photogrammetric analysis and uni-axial compressive strength (UCS) test

The ARAMIS photogrammetric instrument, equipped with two extremely sensitive cameras, captures the strain variations and sample deformations by tracing the corelated areas in the stereo-images. Hence, samples need variations in tone and contrast to unequivocally match the corelated areas. This was achieved by painting the sample surface with flat white colour and subsequently spraying mat-black dots on the surface, prior to UCS experiments. The compression tests were carried out on a Shimadzu AG9 Uni-axial compression machine, at a loading rate of 0.2 mm/min, in which the loading rate was fixed to ensure a sample failure within 2–15 min, congruent with ASTM standards (ASTM-D.2938). The loading and the vertical displacement histories were recorded using a data acquisition system attached to the UCS machine *(see Figure 6-3 (a))*. The lateral strains and the sample deformations were captured with the ARAMIS photogrammetric equipment, in which the lateral and axial strains were calculated by averaging the strains at different cross-sections and longitudinal sections of the samples, respectively *(see Figure 6-3 (b))*.

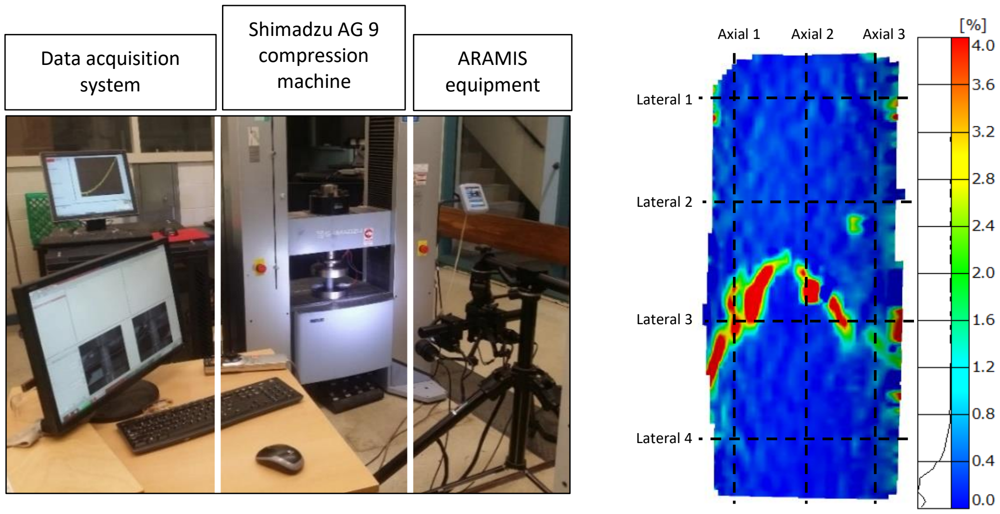

(a) (b)

Figure 6-3 – a) Complete experimental setup used for coal UCS testing and, b) a typical ARAMIS strain colour map that shows the four cross-sections and three longitudinal-sections used to compute average lateral and axial strains of samples.

6.2.2.5 Micro-computed tomography (micro-CT)

Micro-CT analysis has been widely used by researchers to characterize main features in coal, including macerals, minerals, and micro-fractures (Sampath et al., 2019a; Sampath et al., 2019c; Yao et al., 2009). In the present study, we qualitatively and quantitatively analyse the fracture characteristics of coal specimens to evaluate the induced fracture geometry and failure patterns. One representative sample from each saturation condition was selected at failure and scanned in Australian synchrotron imaging and medical beamline (IMBL) facility. Table 6-3 gives the scanning parameters. For the direct comparison purpose, all the samples were scanned with the same scanning parameters and followed the same procedure for the 3D-segmentation and quantification. The image analysis was done with *AVIZO* image analysis software, in *MASSIVE* supercomputer cluster, Monash University.

Table 6-3 - Imaging parameters and specification of the micro-CT analysis.

Scanning parameters	Specifications
X-ray beam type	Monochromatic
Mode	Mode 3-Hutch 3b
Detector	Ruby with a 150 mm lens and a 20 μm screen
X-ray energy	40 keV
Voxel size	16 μm
Distance from sample to detector	1.4 m

6.2.2.6 Fourier transform infrared spectroscopy (FT-IR)

An FT-IR analysis was carried out on a natural coal sample and a CO_2-interacted sample to differentiate the alterations in coal macro-molecular structure and to relate it to the observed mechanical alterations. Two identical samples with particle size no larger than 74 µm (200 mesh) were initially fully vacuum dried for 48 h. The latter sample was allowed to interact with supercritical CO_2 (S-CO_2) under 10 MPa pressure and 40 ºC of temperature for 45 days in a reaction chamber. Both samples were then subjected to the same preparation procedure, followed by the FT-IR analysis with the same analysis parameters. In fact, samples were prepared in Potassium bromide (KBr) pellets at a 1:100 (coal: KBr) weight ratio, in which the samples were mixed with ground KBr in an agate mortar, then pressed for 2 min under 10 MPa pressure to form pellets (Iglesias et al., 1995). The analysis was performed using a Tensor 27 FT-IR spectrometer (Bruker Corporation, Germany) with following settings: spectral region – 4000 cm^{-1} to 400 cm^{-1}, resolution – 4 cm^{-1}, number of scans per sample – 100. A pure ground KBr pellet was used to obtain the background spectrum, and all the spectrums were subjected to baseline correction. 4 samples under each condition (i.e. natural and S-CO_2-interacted coal) were tested, and the resultant averaged spectrums were used for the interpretation.

6.2.3 Results and discussion

6.2.3.1 Chemical characterization

SEM-EDS analysis was conducted on several regions of a selected brown coal sample to confirm the chemical constituents contained in coal. Figure 6-4 illustrates the results of a representative location. As apparent from the results, no other chemical elements were found in the sample, except carbon (C) and oxygen (O). The analysis confirmed that the coal sample does not contain any significant inorganic constituents; accordingly, no significant mineral composition. This is in line with previous studies, which revealed that the mineral composition of low-rank coal is typically below 2% and the concentration of discrete minerals is less than 1% (Grigore and Sakurovs, 2016; Ruan and Ward, 2002). Hence, it can be assumed that any mechanical characteristic variation observed during the experiment should not be due to the alterations in mineral phase, but solely due to the interaction of brine and CO_2 with coal macerals. The maceral component contains numerous organic compounds, including hydrocarbons and functional groups in coal macro-molecular structure. Hence, the saturation-induced alterations in coal macro-molecular structure are quite significant in low-rank brown coal and may have a significant contribution to the coal strength alterations in the absence of the mineral component.

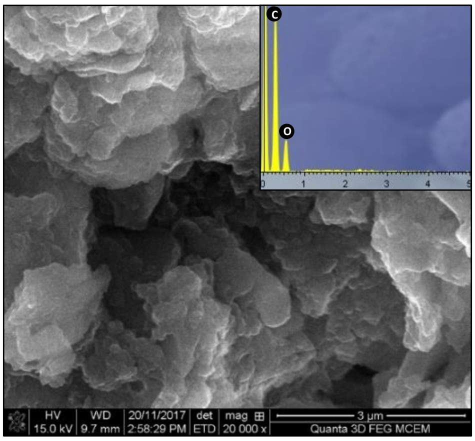

Figure 6-4 - SEM-EDS graph, showing the chemical elemental composition of the coal sample.

6.2.3.2 Alterations of mechanical properties with saturation condition

The variation of mechanical properties with saturation condition is discussed under this section, in which the results of the samples saturated for a similar time period (i.e. 45 days) were selected for the comparison, and the as-received condition was considered as the reference. Since all the samples were vacuum dried before saturation, the as-received samples were basically at the dry state during the mechanical testing. The argument behind the selection is that, since the saturation time is similar for all samples, the observed differences should be due to the differed properties of the saturation fluid. Overall, three mechanical properties are discussed: 1) UCS, 2) Young's modulus (E) and, 3) brittleness index (BI). The three parameters have distinct physical significances and are often used to interpret rock mechanical behaviour in different ways. In fact, UCS and Young's modulus are used in analytical and numerical models to simulate the strength properties and to develop constitutive models with empirical relationships. The experimental techniques are well established with approved specifications, and numerous data are readily available in the literature for easy comparison purpose. In the current study, all the parameters were determined from the stress-strain curves, in which the UCS was determined by dividing the peak load from the sample loading area. E and BI were calculated from Eq. 6-2 and 6-3, respectively, with referring Figure 6-5.

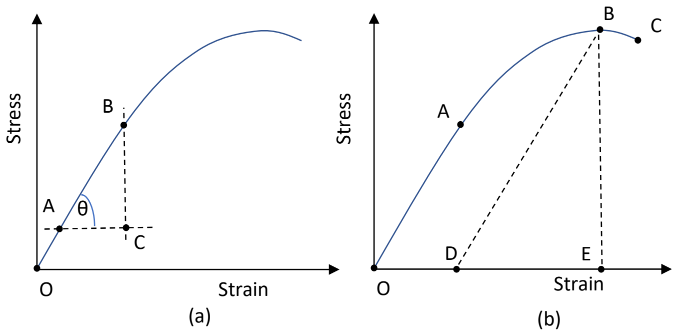

Figure 6-5 - Determination of a) Young's modulus *(refer Eq. 6-2)* and, b) brittleness index *(refer Eq. 6-3)*.

$$Young's\ modulus\ (E) = \frac{stress}{strain} = \frac{BC}{AC} \qquad \text{........... [6-2]}$$

$$Brittleness\ index\ (BI) = \frac{reversible\ strain}{total\ strain} = \frac{DE}{OE} \qquad \text{........... [6-3]}$$

Figure 6-6 exemplifies the variation of UCS with different saturation conditions. UCS of water, water+CO_2, and brine+CO_2 saturated samples have been reduced significantly after 45 days of saturation, compared to natural (as-received) sample. In fact, the reductions of UCS in all cases are about 40% to 50%, where the highest strength reduction is observed in water+CO_2 saturation condition – i.e. 53.1%. The reduction may be attributed to the absorbance of moisture and the consequent softening effect in the coal mass, irrespective of the pore fluid type (Vásárhelyi, 2003; Vásárhelyi and Ván, 2006). As explained by Van Eeckhout (1976), the moisture can reduce the strength of rock mass due to the reduction in fracture energy, increment of pore pressure, reduction of capillary tension, frictional reduction and corrosive deterioration. Moreover, the moisture and CO_2 adsorption-induced coal matrix swelling, and the consequent volume enlargement may also contribute to the coal strength reduction due to the decreased capillary pressure and the volume relaxation.

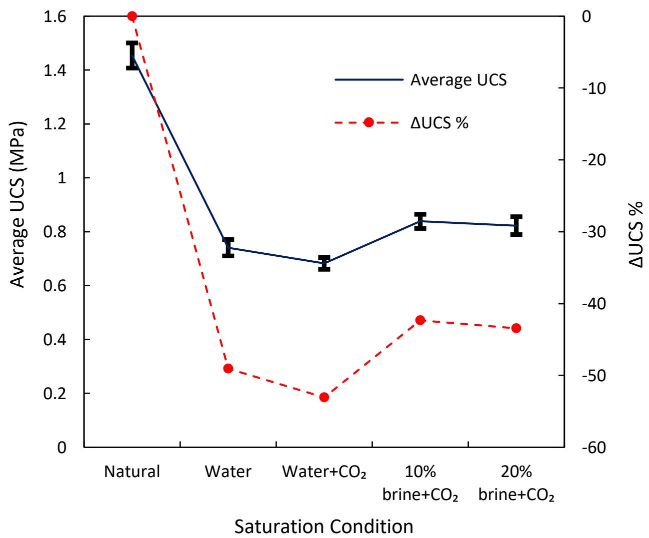

Figure 6-6 - Variation of average UCS and the reduction of UCS (compared to natural condition) with different saturation conditions. Note: Equal saturation time of 45 days was used at each condition.

Furthermore, there is a slight strength reduction of 7.8% in water+CO_2 saturation condition compared to water saturation, which depicts the influence of the presence of CO_2 on strength alterations in brown coal. The formation of carbonic acid due to CO_2 dissolution in pore fluid may trigger the corrosive chemical interactions and accelerate the deterioration process. Interestingly, the brine+CO_2 saturation conditions show a slightly elevated strength, compared to water+CO_2 condition. The slight strength regain may be due to the NaCl crystallization within the coal structure. This observation is in line with many previous studies, in which researchers observed slight strength increments in different rock types with increasing NaCl concentration in the pore fluid (Rathnaweera et al., 2014; Sampath et al., 2018; Shukla et al., 2013). Although a strength regain in brine saturation condition is observed in the current study, the change in the NaCl concentration in brine has not significantly influenced the mechanical strength of the coal mass, as both 10% and 20% brine concentrations show approximately similar strength increments of 22.8% and 20.5%, respectively, compared to water+CO_2 saturation condition.

Figure 6-7 shows the variation of Young's modulus with different saturation conditions, but with the same saturation time of 45 days. Young's modulus is a mechanical parameter that measures the stiffness of a material. It represents how much a material can be deformed under a certain loading, and the reduction of Young's modulus of a material basically represents the increased ductile behaviour. As apparent from Figure 6-7, similar to UCS, Young's modulus has been reduced significantly at all the saturation conditions, compared to the natural sample. In fact, the reduction percentages are 45.9%, 63.8%, 63.3% and 63.3% in water, water+CO_2, 10% brine+CO_2 and 20% brine+CO_2 saturated samples, respectively, which exemplifies the significance of the moisture interaction on the coal stiffness reduction and on the increment of ductility. Moreover, Kuvaev and Panchenko (1975) related the reduction of Young's modulus of coal to the increment of its toughness. Hence, the results conclude that presence of pore fluid significantly modifies the stiffness and toughness of brown coal. It is apparent from the figure that the presence of CO_2 in the pore fluid causes a large reduction in Young's modulus, compared to water saturation condition alone. This may be due to the weakening of the rock grain structure by the chemical interactions occur in a CO_2-rich environment that possibly reduces the elastic properties of the rock (Marbler et al., 2013). Perera et al. (2013) related the CO_2-induced Young's modulus reduction to the coal structural modifications occur due to CO_2 interaction. Coal structure contains a glassy, high-energy, cross-linked and strained macro-molecular structure that hinders the coal molecules' freedom to move, resulting in a brittle nature (Larsen, 2004; Sampath et al., 2019b). The CO_2 dissolution in coal changes the coal polymer structure by expanding the free volume of coal, consequently reducing Young's modulus. However, the results depict that NaCl concentration of the pore fluid does not have a considerable influence on the reduction of Young's modulus in brown coal, as the reductions in all the brine saturation conditions (i.e. 0% (water), 10% and 20% of NaCl concentrations) are approximately similar.

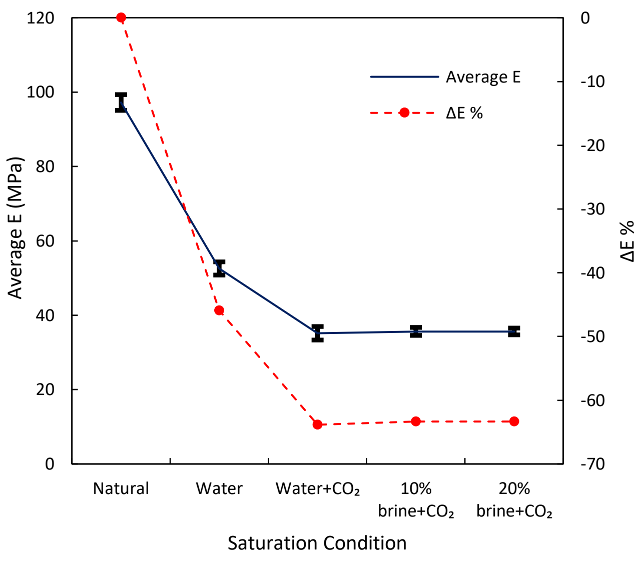

Figure 6-7 - Variation of average Young's modulus (E) and reduction of Young's modulus (compared to natural condition) with different saturation conditions. Note: Equal saturation time of 45 days was used at each condition.

The term 'brittleness' is generally used in the rock-engineering field to interpret the failure characteristics of rocks and is often quantified by a parameter called 'brittleness index'. Since 'brittleness' has no apparent uniform definition, researchers defined it based on various approaches, such as stress-strain, Mohr's envelop, tensile or compressive strength, reversible energy, micro- and macro-hardness approaches. In this study, we use the stress-strain approach *(see Eq. 6-3 and Figure 6-5)*, as it is suitable for friable materials like coal (Hucka and Das, 1974).

Figure 6-8 indicates that the variation of BI with saturation condition follows a 'U-shape' trend, where the water saturation and water+CO_2 saturation have moderately reduced the BI of coal, compared to the natural condition. In fact, they have been reduced by 13.2% and 16.8%, respectively. This is quite possible because moisture absorbance can reduce the brittle properties of coal mass due to the softening effect, as discussed under UCS and E variation sections. The presence of CO_2 and the consequent alternations in pore fluid chemistry has induced a further reduction in brittleness (i.e. 4.1% reduction, compared to water saturation), highlighting the influence of CO_2 on coal BI. Furthermore, unlike UCS and Young's modulus results, the minimum BI value is given in 10% brine+CO_2 saturation condition, which indicates that the presence of brine in pore fluid influence the brittleness significantly, over other mechanical parameters. In fact, the BI value of 10% brine+CO_2 saturation has been reduced by 18.2%, compared to the natural condition. Interestingly, the BI has been increased again at 20% brine+CO_2 saturation condition, reversing the reducing trend, where the increment is about 44.8%, compared to the 10% brine+CO_2 saturation condition. This can be happened possibly due to NaCl crystallization effect in coal pores at a higher order of NaCl concentration. Accordingly, the accumulation of brittle NaCl crystals in coal pores have imparted a brittleness in the bulk sample. However, still, the BI is less than that of the natural condition, which depicts the domination of moisture- and CO_2-induced softening effect. It should be noted that the maximum NaCl concentration used in the current study (i.e. 20% by weight) is less than the solubility limit of NaCl in water (~ 36.5% of NaCl by weight at 40 ºC). Therefore, the crystallization process may not occur during the saturation period due to the lower concentration of NaCl in the saturation solution. These crystals may be formed during the preparation of saturated samples for UCS and ARAMIS testing, in which the samples had to be subjected to a short-term drying, in order to paint the sample surfaces for ARAMIS-based strain capturing. This may evaporate some water from near-surface pores and cause the precipitation of some NaCl crystals at higher order of NaCl concentrations (i.e. 20%), resulting in a slightly higher brittleness in the bulk sample (Fryer and Szladow, 1973; Sampath et al., 2018). Hence, we recommend adopting more controlled experimental procedures to evaluate the NaCl crystallization process in brine-saturated coal.

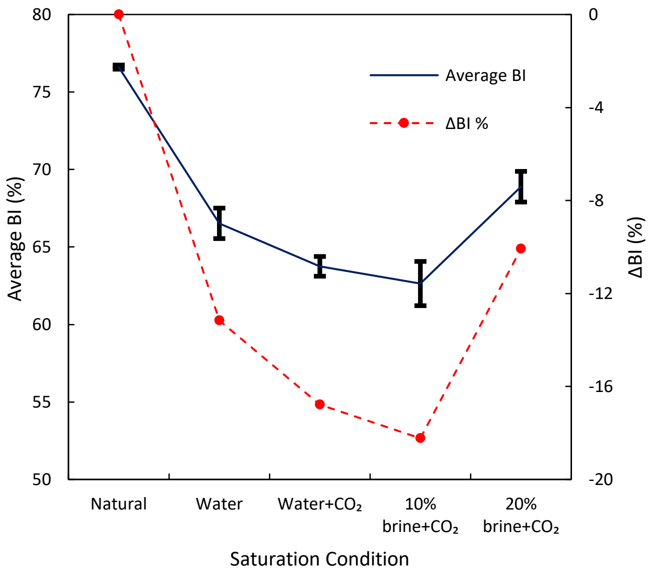

Figure 6-8 - Variation of average brittleness index (BI) and the reduction of BI (compared to natural condition) with different saturation conditions. Note: Equal saturation time of 45 days was used at each condition.

6.2.3.3 Alterations in mechanical properties with saturation time

The alterations of mechanical properties with varying saturation time is comprehensively discussed in this section. Three saturation conditions: i.e. 1) water+CO_2, 2) 10% brine+CO_2 and, 3) 20% brine+CO_2 are selected for the comparison, and the natural condition is used as the reference. As shown in Table 6-2, the samples were saturated for 0 days (natural or as-received sample), 1 day, 14 days and 45 days under three aforementioned saturation conditions and the resultant temporal alterations in the averaged mechanical properties are illustrated in Figure 6-9.

As apparent from Figure 6-9, both UCS and Young's modulus reduce with the increasing saturation time, irrespective of the saturation condition. This is understandable, as the higher the saturation time, the higher the effect of softening and chemical interactions, resulting in continuously weakening coal structures with increasing saturation time. Interestingly, in all the saturation conditions, significant strength reductions occurred at a short-term saturation period (i.e. after 1 day of saturation), and the latter longer saturations have caused only gradual strength reductions. In fact, the short-term UCS reduction rates of water+CO_2, 10% brine+CO_2 and 20% brine+CO_2 saturation conditions are 36.3%, 16.5% and 23.9%, whereas that in long-term saturation condition (i.e. up to 45 days) are only 1.2%, 0.94% and 0.96%, respectively. This observation is similar in the case of Young's moduli variations as well, confirming the adverse influence of the CO_2 saturation on overall mechanical properties of coal. The results are in line with Ranathunga et al. (2016), in which they have observed large strength reductions in S-CO_2-interacted brown coal within a very short time period and only minute strength reductions afterwards. The observed complex strength alterations can be related to the CO_2 adsorption process in the coal matrix. As explained by Karacan (2003), CO_2 starts to adsorb on to coal matrix as soon as the interaction took place, altering the coal macro-molecular structure. Consequently, it may lead to rapid mechanical degradation in the CO_2-interacted coal mass, resulting in large UCS and Young's modulus reductions in short-term.

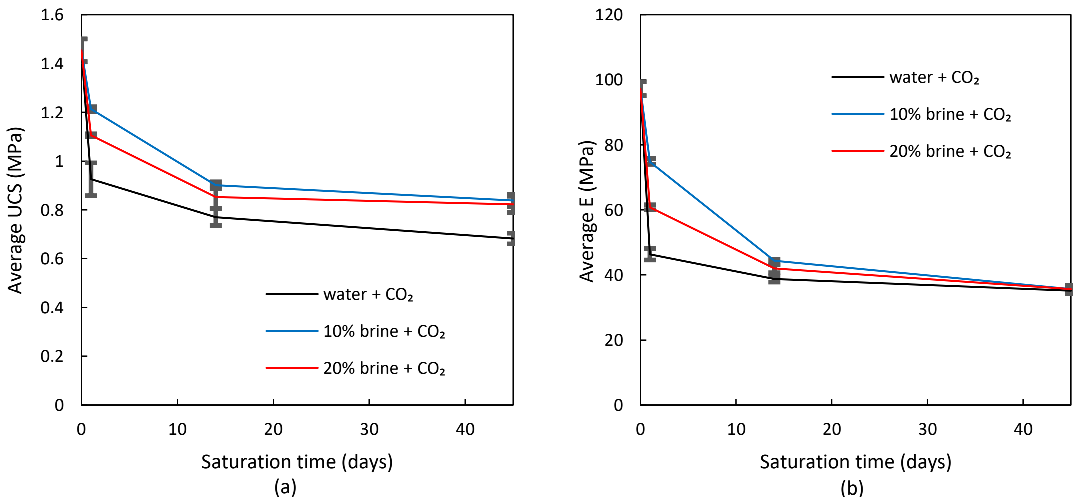

Figure 6-9 – Variation of a) average UCS and, b) average Young's modulus with saturation time for different saturation conditions.

6.2.3.4 Analysis of sample deformation based on ARAMIS results

ARAMIS is a non-destructive, non-contact and material independent measuring system. It is utilized to continuously capture the variation of strains in bulk rock specimens, subjected to continuous loading (Lyu et al., 2016; Pickerd, 2013; Rathnaweera et al., 2014). Both horizontal and vertical strains captured at pre-defined time steps provide information on the sample deformation during load application. In this study, the sample deformation behaviour upon loading is visualized with strain colour maps and analysed with the volumetric strain data collected from the ARAMIS photogrammetric technique *(see Figure 6-3 (b))*, in which the volumetric strains are calculated with averaged lateral and axial strains by referring to Eq. 6-4.

$$\varepsilon_v = \varepsilon_a + 2 \times \varepsilon_l \qquad \text{……….. [6-4]}$$

where, ε_v is the volumetric strain, ε_a is the average axial strain, ε_l is the average lateral strain. Note that the axial and lateral strains are defined as positive for compression and negative for expansion.

Figure 6-10 illustrates the strain colour maps of each saturation condition which visualizes the sample deformation and strain distribution at mechanical failure. The colour distribution range was set to a common scale for the direct comparison purpose.

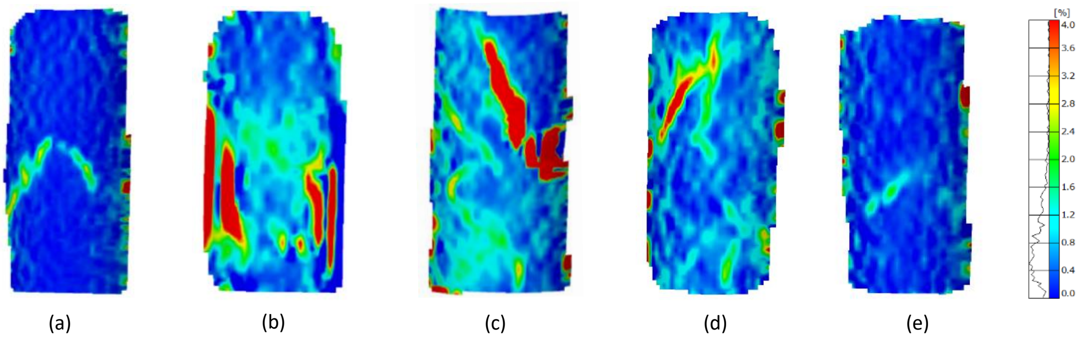

Figure 6-10 - Strain distribution colour maps of representative specimens from each saturation condition: a) natural (as-received) sample, b) water saturated sample, c) water+CO_2 interacted sample, d) 10% brine+CO_2 interacted sample and, e) 20% brine+CO_2 interacted sample.

Moreover, Figure 6-11 depicts volumetric strain variation with the axial stress of representative samples in each saturation condition. Similar to section 6.2.3.2, the saturation time is the same for each condition – 45 days. As can be seen from the figures, the natural sample shows a compaction behaviour until the sample failure, which confirms the brittle nature of the sample at the natural condition. In contrast, the water, water+CO_2 and 10% brine+CO_2 samples show compaction followed by dilatancy behaviour, indicating the volume expansion and the ductile nature of the bulk samples after their respective saturation periods, which is caused by the softening effect and the corrosive chemical interactions. In contrast, the 20% brine+CO_2 saturated sample again shows only a compaction behaviour during the complete loading period. The absence of dilatancy behaviour confirms the brittle nature of the samples, caused by the NaCl crystallization effect at a higher order of NaCl concentrations, as discussed previously. All the volumetric strain analysis results are in line with the BI results, which illustrate that natural and 20% brine+CO_2 saturated samples are more brittle than the samples saturated under other saturation conditions. However, it should be noted that the brittleness in the natural sample is due to the dry and intrinsic brittle nature of the coal macro-molecular structure, but that in the 20% brine+CO_2 saturated sample should be due to the NaCl crystal precipitation during the short-term drying process because it is confirmed that the original macro-molecular structure of the CO_2+brine saturated samples are already altered due to the softening effect and chemical interactions.

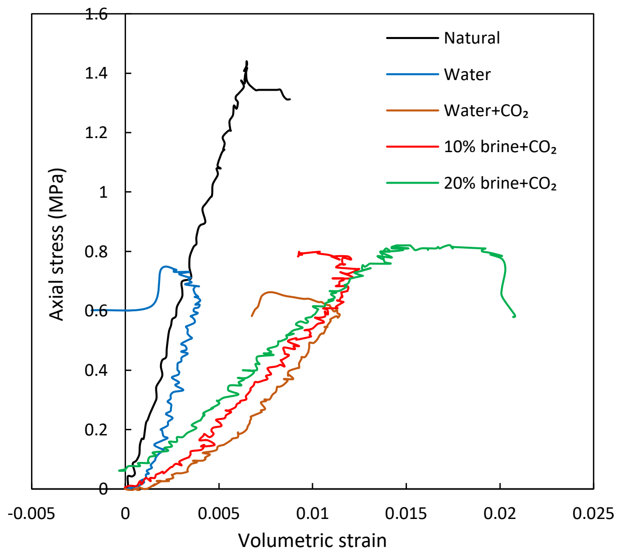

Figure 6-11 - Variation of volumetric strain vs axial stress of representative samples at each saturation condition.

6.2.3.5 Fracture quantification based on micro-CT 3D-reconstructed data

Evaluation of the fracture propagation within the sample upon mechanical loading is important because the effectivity and safety of the rock stimulation processes are greatly dependent on the fracture attributes, including fracture density and geometry. One of the commonly used techniques to visualize and quantify the fracture properties is micro-CT image-based analysis (Hirono et al., 2003; Karpyn et al., 2009). The method was often used by a number of researchers to evaluate various fracture attributes of coal, including fracture density, orientation, length, aperture, etc. In this section, we quantify the induced fracture fraction of representative samples from each saturation condition, after the mechanical failure. The micro-CT data of selected samples were 3D-reconstructed, and the fracture networks were segmented with a number of image-analysing tools. The workflow for the post-analysis and segmentation process is illustrated in Figure 6-12 (Sampath et al., 2019c). The fracture fraction was determined as per Eq. 6-5.

$$Fracture\ fraction = \frac{segmented\ fracture\ volume}{total\ sample\ volume} \quad \text{........... [6-5]}$$

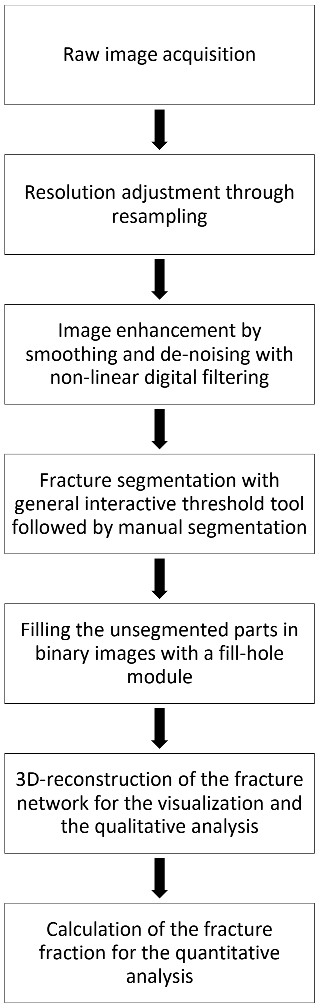

Figure 6-12 – The workflow adopted for the qualitative and quantitative analysis of micro-CT data.

Figure 6-13 illustrates the 3D-reconstructed images of the failed samples, in which the segmented fracture networks are shown in red colour. The reconstructed image of each sample indicates the failure patterns and induced fracture networks upon loading. Moreover, Figure 6-14 exemplifies the variation of calculated fracture fraction in each sample saturated with different pore fluid conditions. The visualization in Figure 6-13 confirms that natural sample has been failed under a general material failure through axial splitting and the corresponding induced fracture fraction is about 1.16%. The samples saturated with water+CO_2 and 10% brine+CO_2 show a less-distributed fracture network, compared to natural condition *(see Figure 6-13)*. Conversely, Figure 6-14 depicts that fracture fractions in these two cases are higher than that of the natural condition. In fact, increments in fracture fractions compared to natural sample are

17.2% and 20.2% in the two cases, respectively. The possible reason for this contradiction is - although two samples consist of less-distributed fracture networks confirmed by the visualization, the induced few fractures are highly-extensive and have large fracture apertures, resulting in a higher fracture fraction. The volumetric strain analysis also supports this fact, because samples saturated with these two conditions show a large dilatancy behaviour upon loading, which can possibly widen the induced fractures due to volume expansion and the large non-elastic deformations undergone by the samples before failure. Furthermore, the 20% brine+CO_2 saturated sample exhibits the highest fracture fraction among all the conditions, where the increment of fracture fraction is about 88.1%, compared to natural condition *(see Figure 6-14)*. This is probably due to the brittle nature of the sample that causes the formation of a large number of tiny, brittle fractures, resulting in a high-dense but thinner fracture network. As apparent from Figure 6-13, the induced fracture network in this particular sample is thinner and well-distributed, which supports the explanation. This fact is confirmed by the BI results, in which the sample shows an increment in BI, due to NaCl crystallization at a higher order of NaCl concentrations *(see Figure 6-8)*. The elevated brittleness and the absence of dilatancy behaviour have prevented the large deformations and extensive fracturing before the bulk failure of the sample. Hence, it can be concluded that brittle nature induced by NaCl precipitation in samples alters the sample deformation, failure pattern and fracturing mechanism in samples. However, it should be noted that the quantification results are dependent on micro-CT image voxel-size and subsequently, the segmentation process. Since the scanning of large coal specimens at full-scale limits the image voxel-size, it often fails to detect tiny fracture characteristics, slightly altering the quantification results.

The overall results of the mechanical parameter analysis suggest that a significant mechanical degradation occurs in water, brine and CO_2 interacted coal mass and the extent of the degradation and the failure mechanism greatly depend on the pore fluid condition and the saturation time. It should be highlighted that the influence of moisture itself has a noteworthy adverse effect on coal mechanical properties, irrespective of the pore fluid type, as it is noticeable that the variation of pore fluid chemistry has caused only minute alterations in coal mechanical properties, compared to the overall effect of moisture. Moreover, the presence of CO_2 in pore fluid can cause further mechanical degradations due to CO_2 interaction-induced corrosive chemical interactions, adsorption-induced energy reduction and alterations in coal macro-molecular structure due to plasticization effect. It is worthwhile to highlight that the selected brown coal specimens do not have a significant mineral matter content. The mineral component increases with the increasing coal rank, and the effect of mineral dissolution can adversely affect the overall mechanical properties as well as the induced fracture properties at failure; thus, can cause localized and spatially heterogeneous damages in the bulk coal specimens.

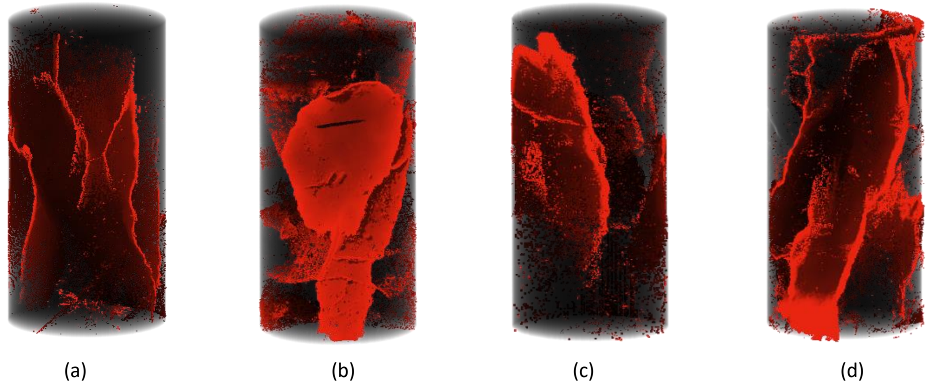

Figure 6-13 - Micro-CT image-based 3D-reconstruction of the failed samples, indicating the failure patterns and induced fracture networks of; a) natural (as-received) sample, b) water+CO_2 interacted sample, c) 10% brine+CO_2 interacted sample and, d) 20% brine+CO_2 interacted sample.

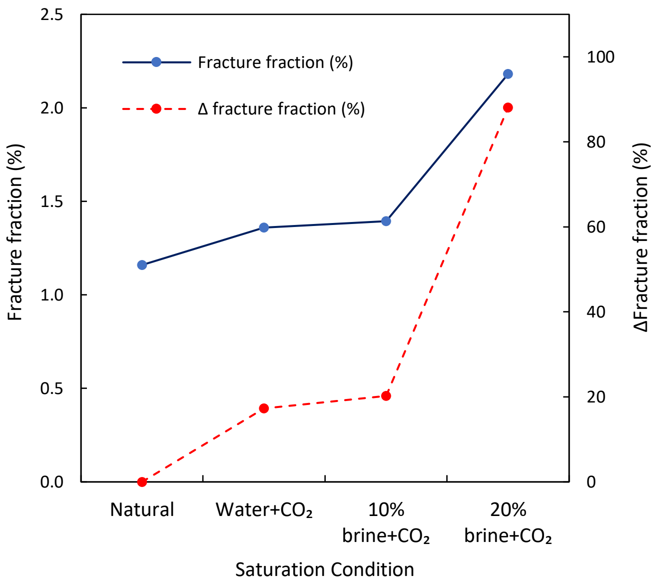

Figure 6-14 - Variation of fracture fraction with different saturation conditions. Note: The fracture fractions were calculated based on micro-CT 3D-reconstructed data of representative samples at failure *(refer Figure 6-13)*.

6.2.3.6 S-CO_2-induced alterations in coal macro-molecular structure

FT-IR is often used for identifying the alterations in coal macro-molecular structure, including hydrocarbons and functional groups, because each bond structure produces a distinctive molecular-vibration spectrum, upon the absorption of infrared radiation. The technique is widely used to determine coal chemical functional groups and to accurately display the semiquantitative ratios and types of functional groups (Liu et al., 2018; Mastalerz et al., 2010; Zhang et al., 2018). Since the absorption peaks and their positions in the infrared spectrum provides the information on the different functional groups of the overall molecular structure, the direct comparison of absorption peaks before and after S-CO_2 saturation can be used to interpret the S-CO_2-induced alterations in the coal macro-molecular structure. The coal structure is typically formed of a number of aromatic rings, heterocyclic or alicyclic rings, alkyl side chains and several functional groups including oxygen-, nitrogen- and sulphur-containing groups (Lucht et al., 1987). As explained by Larsen (2004), when CO_2 is in contact with coal mass, it diffuses through the coal matrix and acts as a plasticizer, resulting in a partial-break-down of the polymerized molecules and shortening the lengths of polymer chains. Since the polymer chain length is a function of the polymer strength, the reduction in the polymer chains' entanglement may possibly lead to a strength reduction in the coal mass. Moreover, the alterations in the macro-molecular structure of low-rank coal should have a significant impact on the observed mechanical degradation, as the low-rank coal are not matured enough to contain a considerable mineral composition – thus unable to trigger mineral dissolution-induced mechanical degradations.

Figure 6-15 illustrates the infrared spectrums of coal samples before and after 45 days of S-CO_2 interaction. To determine the alterations in the characteristic absorption peaks, the spectrograms are split into two regions: 1) 4000 cm^{-1} to 1500 cm^{-1} – functional group region and, 2) 1500 cm^{-1} to 400 cm^{-1} – fingerprint region, and the identifiable peaks in each region are highlighted and numbered. Functional group region contains few peaks that are typically associated with stretching vibration of functional groups, whereas fingerprint region contains complex peaks that are mainly due to the bending vibrations within the molecule. The fingerprint region of a given compound is unique and is generally used to distinguish between compounds. As apparent from Figure 6-15, there are several deviations in the peak intensities, which confirm the S-CO_2-induced alterations in coal macro-molecular structure. As identified from the analysis, the differences in the characteristic peaks between two spectrums confirm the alterations in several functional groups of the coal structure. In fact, each highlighted and numbered peak corresponds to a specific bonding type and a vibration: 1) intramolecular bonding of O – H due to moisture in the samples (3700 cm^{-1} – 3100 cm^{-1}), 2) and 3) symmetrical or anti-symmetrical stretching vibration in naphthenic and aliphatic bonds (–CH_3 and –CH_2) (2935 cm^{-1} – 2918 cm^{-1}, 2858 cm^{-1} – 2847 cm^{-1}), 4) vibrations in the carbonyl region, including aldehydes, ketones, and esters (1750 cm^{-1} – 1700 cm^{-1}), 5) stretching vibrations of aromatic or fused rings (C = C) (1635 cm^{-1} – 1595 cm^{-1}), 6) and 7) anti-symmetric, bending or out-of-plane vibration in –CH_3 and –CH_2 bonds (1400 cm^{-1} – 1375 cm^{-1}), 8) vibration of C – O bonds (or carbon hetero-atom single bonds, such as C – N, C – O, C – C, etc.) in epoxy compounds or ethers (1330 cm^{-1} –1060 cm^{-1}) and, 9) vibration of organic halides or minerals (850 cm^{-1} – 515 cm^{-1}). The direct comparison of two spectrums infers that S-CO_2 interaction has clearly weakened the absorption intensities of all the identifiable peaks in both regions, confirming the S-CO_2's ability to re-arrange the coal macro-molecular structure. Furthermore, as explained by Zhang et al. (2018), S-CO_2 can extract hydrocarbons and other containing-functional groups in fracture and coal pores, causing alterations in body structure and surface sites of coal. The extraction of hydrocarbons that constrict the pore throats may increase the pore connectivity and open up new adsorption sites, enhancing the CO_2 adsorption process in coal mass and consequently further contributing to the CO_2-induced mechanical degradation.

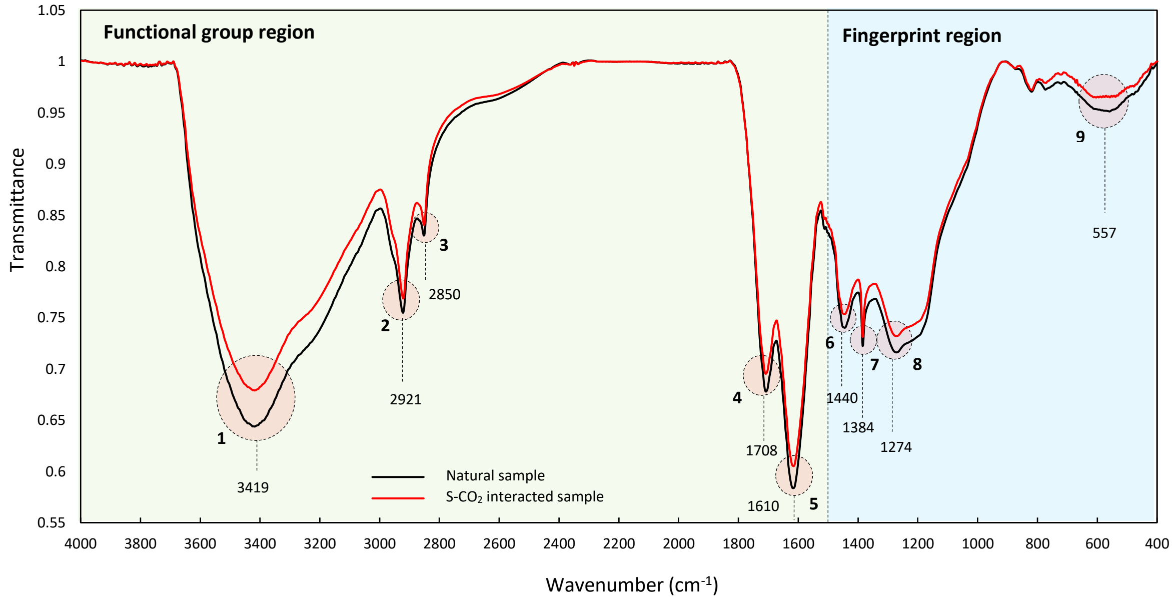

Figure 6-15 - FT-IR spectrums of the brown coal samples before and after S-CO_2 interaction for 45 days, highlighting the alterations in peak intensities of different functional groups.

Overall, the study concludes that the coal mechanical properties vary with both saturation condition and the saturation time. CO_2 sequestration and ECBM extraction in industry are incorporated with CO_2–CH_4 gas exchange process and several reservoir stimulation methods such as hydraulic fracturing technique. Use of S-CO_2 as an alternative propellent has become popular in the hydraulic fracturing industry due to excess usage of water in the conventional methods. All these techniques involve injection of large quantities of CO_2 into coal reservoirs, altering their hydro-mechanical properties. The strength degradation of the coal seam cause by coal + moisture + CO_2 interaction can severely damage the mechanical competency, causing numerous environmental and social hazards. Hence, the knowledge given by the study is imperative, as it comprehensively discusses the mechanical behaviour and alterations in fracture characteristics, both of which are salient for implementing safer and effective industrial projects.

6.2.4 Conclusions

CO_2 sequestration and ECBM techniques necessitate CO_2 injection into coal seams, triggering numerous alterations in their physical properties. Among various factors, the pore fluid chemistry and the saturation time play critical roles in governing coal mechanical properties. In this paper, we experimentally evaluate the alterations in mechanical properties of coal, saturated with water, water+CO_2, and brine+CO_2 for different saturation periods.

- UCS, Young's modulus and brittleness index reduce significantly after each saturation condition, compared to natural (as-received) condition, due to moisture adsorption-induced softening effect, irrespective of the pore fluid chemistry.
- The presence of CO_2 in pore fluids causes further degradation in each mechanical property, probably due to the corrosive chemical interactions occur in acidic environments, adsorption-induced energy reduction and alterations in coal macro-molecular structure due to the plasticization effect.
- The volumetric strain analysis and micro-CT analysis conclude that water, water+CO_2 and 10% brine+CO_2 saturation increase the ductile properties of coal, resulting in a dilatancy deformation and extensive fracturing, upon mechanical loading. In contrast, the higher order of NaCl concentrations in pore fluid causes NaCl crystallization in coal, resulting in an elevated brittleness. This NaCl precipitation alters the sample deformation, failure pattern and fracturing mechanism– eliminating the dilatancy behaviour.
- Both UCS and Young's modulus reduce with increasing saturation time, irrespective of the saturation condition, due to continuous softening effect and chemical interactions. Significant strength reductions occurred at a short-term saturation period, and the latter longer saturations have caused only gradual strength reductions, probably due to rapid CO_2 adsorption process on to coal matrix.
- The FT-IR analysis concludes that CO_2 interaction causes several alterations in the coal macro-molecular structure that leads to mechanical degradation of coal mass due to plasticization effect and the extraction of pore-constricting hydrocarbons.

References

ASTM-D.2938. Standard Test Method for Unconfined Compressive Strength of Intact Rock Core Specimens. ASTM International, West Conshohocken, PA.

ASTM-D.4543. Standard Practices for Preparing Rock Core Specimens and Determining Dimensional and Shape Tolerances. ASTM International, West Conshohocken, PA.

Busch, A., & Gensterblum, Y. (2011). CBM and CO_2-ECBM related sorption processes in coal: a review. *International Journal of Coal Geology, 87*(2), 49-71.

Fryer, J. F., & Szladow, A. J. (1973). Storage of coal samples. *Information series, 66*(Alberta Research).

Grigore, M., & Sakurovs, R. (2016). Inorganic matter in Victorian brown coals. *International Journal of Coal Geology, 154*(257-264).

Hawkes, I., & Mellor, M. (1970). Uniaxial testing in rock mechanics laboratories. *Engineering Geology, 4*(3), 179-285.

Hirono, T., Takahashi, M., & Nakashima, S. (2003). In situ visualization of fluid flow image within deformed rock by X-ray CT. *Engineering Geology, 70*(1-2), 37-46.

Holdgate, G. R., Wallace, M. W., Sluiter, I. R., Marcuccio, D., Fromhold, T. A., & Wagstaff, B. E. (2014). Was the Oligocene–Miocene a time of fire and rain? Insights from brown coals of the southeastern Australia Gippsland Basin. *Palaeogeography, Palaeoclimatology, Palaeoecology, 411*, 65-78.

Hucka, V., & Das, B. (1974). Brittleness determination of rocks by different methods. *International Journal of Rock Mechanics and Mining Sciences & Geomechanics Abstracts, 11*(10), 389-392.

Iglesias, M. J., Jimenez, A., Laggoun-Défarge, F., & Suarez-Ruiz, I. (1995). FTIR study of pure vitrains and associated coals. *Energy & Fuels, 9*(3), 458-466.

Karacan, C. Ö. (2003). Heterogeneous Sorption and Swelling in a Confined and Stressed Coal during CO_2 Injection. *Energy & Fuels, 17*(6), 1595-1608.

Karpyn, Z., Alajmi, A., Radaelli, F., Halleck, P., & Grader, A. (2009). X-ray CT and hydraulic evidence for a relationship between fracture conductivity and adjacent matrix porosity. *Engineering Geology, 103*(3-4), 139-145.

Kuvaev, N., & Panchenko, D. (1975). Effect of moisture on the dynamic strength of brown coals. *Journal of Mining Science, 11*(3), 220-222.

Larsen, J. W. (2004). The effects of dissolved CO_2 on coal structure and properties. *International Journal of Coal Geology, 57*(1), 63– 70.

Li, C., Prikryl, R., & Nordlund, E. (1998). The stress-strain behaviour of rock material related to fracture under compression. *Engineering Geology, 49*(3-4), 293-302.

Li, D., & Wang, W. (2019). Quantitative analysis of the influence of saturation on rock strength reduction considering the distribution of water. *Geomechanics and Geophysics for Geo-Energy and Geo-Resources*, 1-11.

Liu, S., Sang, S., Wang, T., Du, Y., Jia, J., & Fang, H. (2018). The effects of CO2 on organic groups in bituminous coal and high-rank coal via Fourier transform infrared spectroscopy. *Energy Exploration & Exploitation, 36*(6), 1566-1592.

Lucht, L. M., Larson, J. M., & Peppas, N. A. (1987). Macromolecular structure of coals. 9. Molecular structure and glass transition temperature. *Energy & Fuels, 1*(1), 56-58.

Lyu, Q., Long, X., Ranjith, P., Tan, J., Zhou, J., Wang, Z., & Luo, W. (2018). A laboratory study of geomechanical characteristics of black shales after sub-critical/super-critical CO 2+ brine saturation. *Geomechanics and Geophysics for Geo-Energy and Geo-Resources*, 1-16.

Lyu, Q., Long, X., Ranjith, P. G., & Kang, Y. (2016). Unconventional gas: Experimental study of the influence of subcritical carbon dioxide on the mechanical properties of black shale. *Energies, 9*(7), 516-530.

Marbler, H., Erickson, K. P., Schmidt, M., Lempp, C., & Pöllmann., H. (2013). Geomechanical and geochemical effects on sandstones caused by the reaction with supercritical CO_2: an experimental approach to in situ conditions in deep geological reservoirs. *Environmental Earth Sciences, 69*(6), 1981-1998.

Mastalerz, M., Drobniak, A., Walker, R., & Morse, D. (2010). Coal lithotypes before and after saturation with CO2; insights from micro-and mesoporosity, fluidity, and functional group distribution. *International Journal of Coal Geology, 83*(4), 467-474.

Perera, M., Sampath, K., Ranjith, P., & Rathnaweera, T. (2018). Effects of Pore Fluid Chemistry and Saturation Degree on the Fracability of Australian Warwick Siltstone. *Energies, 11*(10), 2795.

Perera, M. S. A., Ranjith, P. G., Choi, S. K., & Airey, D. (2011). The effects of sub-critical and super-critical carbon dioxide adsorption-induced coal matrix swelling on the permeability of naturally fractured black coal. *Energy, 36*(11), 6442-6450.

Perera, M. S. A., Ranjith, P. G., & Viete, D. R. (2013). Effects of gaseous and super-critical carbon dioxide saturation on the mechanical properties of bituminous coal from the Southern Sydney Basin. *Applied Energy, 110*, 73-81.

Pickerd, V. (2013). Optimisation and Validation of the ARAMIS Digital Image Correlation System for use in Large-scale High-strain-rate Events. *No. DSTO-TN-1203. Defense science and technology organization Victoria (Australia) Maritime division*.

Ranathunga, A. S., Perera, M. S. A., & Ranjith, P. G. (2016). Influence of CO_2 adsorption on the strength and elastic modulus of low rank Australian coal under confining pressure. *International Journal of Coal Geology, 167*, 148-156.

Rathnaweera, T. D., Ranjith, P. G., & Perera, M. S. A. (2014). Salinity-dependent strength and stress–strain characteristics of reservoir rocks in deep saline aquifers: An experimental study. *Fuel, 122*, 1-11.

Ruan, C.-D., & Ward, C. R. (2002). Quantitative X-ray powder diffraction analysis of clay minerals in Australian coals using Rietveld methods. *Applied Clay Science, 21*(5), 227-240.

Sakaguchi, M., Laursen, K., Nakagawa, H., & Miura, K. (2008). Hydrothermal upgrading of Loy Yang Brown coal—Effect of upgrading conditions on the characteristics of the products. *Fuel Processing Technology, 89*(4), 391-396.

Sampath, K. H. S. M., Perera, M., Li, D. Y., Ranjith, P., & Matthai, S. (2019a). Characterization of dynamic mechanical alterations of supercritical CO_2-interacted coal through gamma-ray attenuation, ultrasonic and X-ray computed tomography techniques. *Journal of Petroleum Science and Engineering, 174*, 268-280.

Sampath, K. H. S. M., Perera, M. S. A., Elsworth, D., Ranjith, P. G., Matthai, S. K., & Rathnaweera, T. (2018). Experimental Investigation on the Mechanical Behavior of Victorian Brown Coal under Brine Saturation. *Energy & Fuels, 32*(5), 5799-5811.

Sampath, K. H. S. M., Perera, M. S. A., Ranjith, P. G., & Matthai, S. K. (2019b). CO_2 interaction induced mechanical characteristics alterations in coal: A review. *International Journal of Coal Geology, 204*, 113-129.

Sampath, K. H. S. M., Perera, M. S. A., Ranjith, P. G., Matthai, S. K., & Dong yin, L. (2019c). Qualitative and quantitative evaluation of the alteration of micro-fracture characteristics of supercritical CO_2-interacted coal. *The Journal of supercritical fluids, 147*, 90-101.

Shukla, R., Ranjith, P. G., Choi, S. K., Haque, A., Yellishetty, M., & Hong, L. (2013). Mechanical behaviour of reservoir rock under brine saturation. *Rock Mechanics and Rock Engineering, 46*(1), 83-93.

Stevens, S., Kuuskraa, V., Gale, J., & Beecy, D. (2001). CO_2 Injection and Sequestration in Depleted Oil and Gas Fields and Deep Coal Seams: Worldwide Potential and Costs. *Environmental Geosciences, 8*(1), 200-209.

Taulis, M., & Milke, M. (2013). Chemical variability of groundwater samples collected from a coal seam gas exploration well, Maramarua, New Zealand. *Water Research, 47*(3), 1021-1034.

Teichmüller, M., & Teichmüller, R. (1966). Geological causes of coalification. *In Coal science, American Chemical Society, 55*, 133-155.

Van Eeckhout, E. M. (1976). The mechanisms of strength reduction due to moisture in coal mine shales. *International Journal of Rock Mechanics and Mining Sciences & Geomechanics Abstracts, 13*(2), 61-67.

Van Voast, W. A. (2003). Geochemical signature of formation waters associated with coalbed methane. *Aapg Bulletin, 87*(4), 667–676.

Vásárhelyi, B. (2003). Some observations regarding the strength and deformability of sandstones in dry and saturated conditions. *Bulletin of Engineering Geology and the Environment, 62*(3), 245-249.

Vásárhelyi, B., & Ván, P. (2006). Influence of water content on the strength of rock. *Engineering Geology, 84*(1-2), 70-74.

Vishal, V., Ranjith, P., Pradhan, S., & Singh, T. (2013). Permeability of sub-critical carbon dioxide in naturally fractured Indian bituminous coal at a range of down-hole stress conditions. *Engineering Geology, 167*, 148-156.

Yao, Y., Liu, D., Che, Y., Tang, D., Tang, S., & Huang, W. (2009). Non-destructive characterization of coal samples from China using microfocus X-ray computed tomography. *International Journal of Coal Geology, 80*(2), 113-123.

Zhang, K., Li, W., Cheng, Y., Dong, J., Tu, Q., & Zhang, R. (2018). Microscale Research on Effective Geosequestration of CO2 in Coal Reservoir: A Natural Analogue Study in Haishiwan Coalfield, China. *Geofluids, 2018*.

6.3 Journal paper: Dynamic mechanical property alterations in CO_2-interacted coal

This section is presented as the author-accepted manuscript of a peer-reviewed article published in "Journal of Petroleum Science and Engineering". The journal is a Q1 journal with impact factor of 2.89.

Citation:

- Sampath K. H. S. M., Perera M. S. A., Li D. Y., Ranjith P. G, Matthai S. K. (2019). *Characterization of dynamic mechanical alterations of supercritical CO_2-interacted coal through gamma-ray attenuation, ultrasonic and X-ray computed tomography techniques*. Journal of Petroleum Science and Engineering, 174, 268-280.

Journal paper title: Characterization of dynamic mechanical alterations of supercritical CO_2-interacted coal through gamma-ray attenuation, ultrasonic and X-ray computed tomography techniques

Authors' names: K.H.S.M. Sampath[1], *M.S.A. Perera[1], Dong-yin Li[3], P.G. Ranjith[2], S.K. Matthai[1]

[1]Department of Infrastructure Engineering, Engineering Block B, Grattan Street, Parkville, The University of Melbourne, Victoria 3010, Australia.

[2]Department of Civil Engineering, Monash University, Clayton Campus, Victoria 3800, Australia.

[3]School of Energy Science and Engineering, Henan Polytechnic University, Jiaozuo 454000, China.

Abstract

Coal-Supercritical CO_2 (S-CO_2) interaction causes severe mechanical alterations in coal that can possibly affect the mechanical competency and the coal seam integrity. Conventional static mechanical testings often fail to conduct repetitive and temporal measurements on coal specimens in the process of coal-S-CO_2 interaction; thus, unable to attain at decisive and reliable conclusions. Moreover, the said techniques fail to capture the mechanical anisotropies of heterogeneous coal mass that arise due to the complex spatial distribution of mineral/maceral phases and fracture network. We combine three non-destructive techniques, *viz.* gamma-ray attenuation, ultrasonic technique and micro-computed tomography to evaluate the S-CO_2 interaction-induced localized and anisotropic micro-structural alterations and the consequent mechanical response of a heterogeneous coal core specimen. Dynamic moduli were computed at radial and axial directions at natural condition, after 14 days and 45 days of S-CO_2 interaction, and the resultant mechanical alterations were elucidated with the 3D-reconstructed micro-CT data collected at the same stages. Visualization and quantification of coal micro-structure emphasize that S-CO_2-interacted coal mass is subjected to severe micro-cracking due to differential and free swelling, drying induced shrinkage and surface energy reduction, which can possibly lead to mechanical degradation.

Spatial distribution of minerals and fractures at specific orientations significantly affects the gamma and ultrasonic wave propagation; thus, can be successfully utilized to reflect the mechanical anisotropies. For the same CO_2 interaction condition and period, coal mass exhibits mechanical anisotropies and strength alterations at different levels, in which more heterogeneous mineral/maceral distribution causes significant localized mechanical alterations in mineral-rich areas, compared to that of comparatively homogeneous maceral-rich regions. Temporal evaluation of strength parameters suggests that regardless of the considered orientations, significant strength alterations occur at the initial stage of the coal-S-CO_2 interaction process and the longer interaction causes only a slight strength reduction. Overall results conclude that S-CO_2-induced mechanical property alterations in heterogeneous coal are highly-localized and anisotropic; thus, should be carefully evaluated in CO_2 sequestration and ECBM extraction processes.

Keywords: *coal seam, supercritical CO_2, dynamic moduli, heterogeneity, anisotropy*

6.3.1 Introduction

Enhanced coal bed methane extraction and CO_2 sequestration techniques are incorporated with the injection of anthropogenic CO_2 into coal reservoirs, causing coal-CO_2 interactions, which readily alter the coal seam micro-structural properties. In fact, due to CO_2 phase change under favourable pressure/temperature conditions and the unique formation process of coal reservoirs, coal-CO_2 interaction exhibits complex alterations. A thorough understanding of micro-structural alterations is essential, as the interaction can preferably affect the mechanical properties and the coal seam integrity. The heterogeneity and the anisotropy induced by cleat orientation and spatial mineral/maceral distribution make the analysis rather complex; thus, a deep understanding at micro-scale is essential for the precise evaluation of such alterations (Pal et al., 2015).

A number of studies conclude that coal seam mechanical properties significantly alter due to interactions with supercritical CO_2 (S-CO_2), in which the S-CO_2 adsorption on to coal matrix causes mineral dissolution, hydrocarbon mobilization, swelling/shrinkage and polymer structure rearrangements, resulting in the coal mass weakening (Perera et al., 2011; Ranathunga et al., 2016b; Viete and Ranjith, 2006). There exists a number of theoretical studies that explain the S-CO_2 interaction-induced mechanical alteration of coal. For instance, injected S-CO_2 molecules may adsorb on to coal matrix by desorbing water molecules during the two-phase flow interaction process (Sun et al., 2016; Sun et al., 2018), resulting in a drying effect that can cause shrinkage cracks (Brenner, 1984). Moreover, Griffith's fracture initiation criteria (Griffith, 1921) and Gibb's adsorption theory (Gibbs, 1879) can be combined to postulate the adsorption-induced fracture initiation in coal specimen. Distinct swelling rates of different components in coal structure may cause differential swelling (Karacan, 2003) and localized stress concentrations, resulting in phase boundary cracks. Overall mechanical alteration is a combination of these factors, which makes the evaluation more difficult.

Most of the laboratory testings utilized to evaluate the S-CO_2-induced coal mechanical response are associated with destructive techniques, such as uni-axial/tri-axial compression, tensile and shear testings on coal specimens. The aforementioned techniques often fail to provide precise information on localized or anisotropic damage on rock specimens, as the techniques are more likely to give information on the bulk specimen failure. The localized damage evaluation is important, as the coal mass responds at different levels for CO_2 adsorption, depending on its material distribution. For instance, Zhang et al. (2016a) showed that S-CO_2 adsorption causes cleat closure in the coal matrix, whereas new fracture formation in mineral phase due to internal swelling stress. Therefore, the localized alterations and the resultant mechanical response should be investigated to precisely understand the complex behaviour of S-CO_2-interacted coal. Moreover, the destructive tests often fail to obtain repetitive measurements on a selected coal specimen; thus, unable to provide reliable information on the coal mass damage as a function of S-CO_2 interaction time. The two setbacks of common mechanical evaluations can be eliminated by adopting a micro-structure visualization technique – to identify localized and anisotropic damage, and a non-destructive mechanical testing technique – to evaluate the temporal alterations of the S-CO_2-interacted coal mass strength.

Micro-computed tomography (micro-CT) and the seismic wave exploration are two non-destructive techniques, widely used for coal characterization. Micro-CT image analysis allows closer observations of coal micro-structure (Ramandi et al., 2017). Grey-scale images, obtained from CT scanning visualize the spatial distribution of components with varying threshold densities, and the 3D reconstruction through image segmentation permits the quantification of various parameters. Coal characteristics, including fracture network such as fracture density, aperture, orientation, and the pore volume, mineral distribution are key parameters of interest that can be visualized and quantified through micro-CT image analysis. High-resolution scanning of a selected coal specimen at different S-CO_2 interaction periods enables the precise evaluation of localized alterations in each component of the heterogeneous coal mass.

Ultrasonic testing is a non-destructive, non-intrusive technique, which is used to determine the P and S wave velocities, and consequently to compute the dynamic moduli. The technique is highly-sensitive and allows the elastic anisotropy measurements of rock specimens; thus, provides a good basis for evaluating the localized and anisotropic mechanical property alterations in heterogeneous coal specimens. The ultrasonic measurements were used by many researchers to examine the effect of different parameters on coal mass mechanical properties. For instance, the effect of stress orientation, the effect degree of water saturation (Liu et al., 2017), the effect of confining pressure (Wang et al., 2014), the effect of coal rank (Morcote et al., 2010) and the effect of fracture orientation (Cai et al., 2014) have been deeply investigated and proved that coal mechanical properties can be severely affected by the coal seam heterogeneity and anisotropy.

In this paper, we combine three non-destructive techniques: gamma-attenuation method, ultrasonic wave analysis and micro-CT image analysis to evaluate the localized and anisotropic micro-structural alterations and the consequent mechanical response, induced by S-CO_2 interaction of a heterogeneous coal core specimen. The analyses were conducted at three stages (i.e. 0 days (natural sample), 14 days and 45 days of S-CO_2 interaction), and the radial and axial ultrasonic wave measurements were obtained to evaluate the anisotropic mechanical alterations in the coal mass. Gamma-ray attenuation technique was used to determine the density anisotropies at the same orientations and to accurately compute the corresponding strength parameters. The resultant mechanical alterations were elucidated with 3D-reconstructed micro-CT image data collected at the same stages, in which the heterogeneous mineral distribution, micro-crack formation and their orientations were related to the observed anisotropic mechanical alterations.

6.3.2 Experimental procedure

6.3.2.1 Sample description

The sample, which is a high volatile bituminous coal was acquired from Tashan coal mine, Shanxi province of China, and a proximate analysis was carried out on a collected sample to determine the coal composition *(see Table 6-4)*. The sample was cored and cut to a 38 mm diameter and 76 mm length at deep earth engineering research laboratory (DEERL), to perform axial and radial wave measurements. An XRD analysis conducted on a mineral-rich area of a sample confirms that the sample predominantly comprises a Kaolinite mineral phase *(see Figure 6-16)*. The mineral phase is spatially dispositioned in a planar arrangement, resulting in clearly visible mineral layers in the core sample. The 3D-reconstructed data exhibits the spatial mineral and fracture distribution and the unique fabric formation, causing heterogeneity and anisotropy in the sample *(see Figure 6-17)*. Gamma density and ultrasonic measurements were taken at three points along the axial direction and at four radial directions, where the radial angles were defined with respect to the mineral layering plane *(see Figure 6-18)*.

Table 6-4 - Proximate analysis results of the used coal type

Composition	Moisture	Ash	Volatile matter	Fixed carbon
% by weight on dry basis	1.6	8.2	27.8	62.4

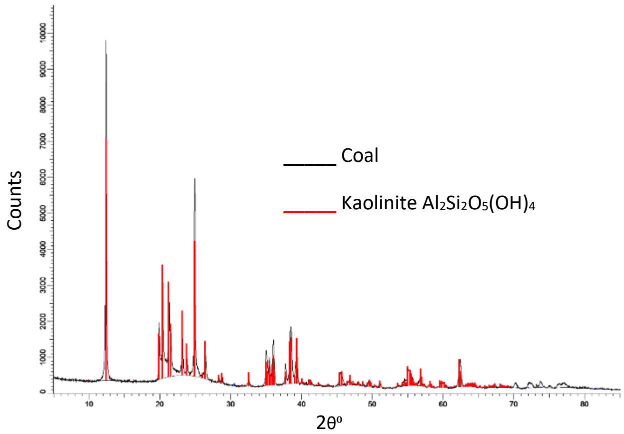

Figure 6-16 - XRD results, indicating the mineral composition of the coal type used for the analyses. Note that the predominant mineral type detected is Kaolinite.

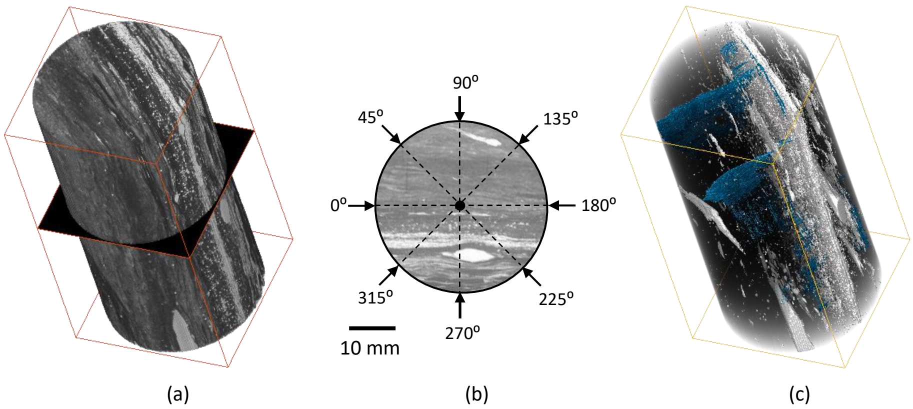

Figure 6-17 – a) Natural coal sample, indicating the mineral layering at a preferential orientation, b) a representative ortho-slice and the measured radial orientations with respect to the mineral layering and, c) 3D-reconstructed image of natural coal sample, indicating the coal mass (black), spatial distribution of mineral phase (white) and natural fractures (blue).

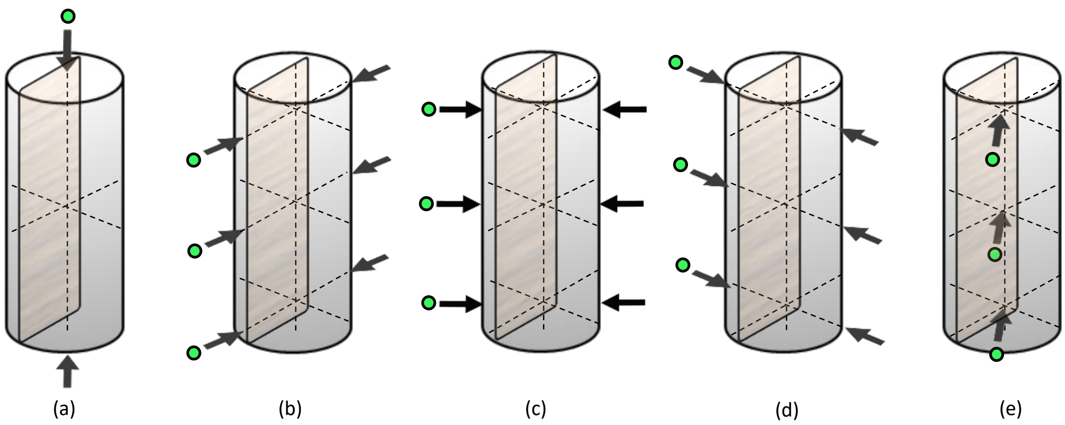

Figure 6-18 - Data measured orientations and points in core sample: a) axial, b) parallel to mineral layering plane ($0^o - 180^o$), c) on angle to mineral layering plane ($45^o - 225^o$), d) perpendicular to mineral layering plane ($90^o - 270^o$) and, e) on angle to mineral layering plane ($135^o - 315^o$).

6.3.2.2 Coal-S-CO_2 treatment

The interaction between S-CO_2 and coal core sample was carried out in a high-pressure reaction chamber *(see Figure 6-19)*. The reaction chamber is capable of simulating the conditions for CO_2 sequestration in coal seams with maximum CO_2 pressure and temperature of 20 MPa and 120 ºC, respectively. The sample was initially vacuum saturated with de-ionized water in a vacuum chamber to achieve fully water-saturated condition. Then the sample was transferred into the reaction chamber, and the CO_2 was slowly injected into the sealed cell using a syringe pump until the pressure inside the chamber reached the desired level. A pressure of 10 MPa and a temperature of 40 ºC were applied to the sample and maintained constant throughout the interaction period. The desired pressure and temperature were selected by considering the pressure gradient and geothermal gradient at the sampling location, and to simulate the supercritical-phase of CO_2. The S-CO_2-interacted sample was retrieved after pre-specified interaction periods (i.e. after 14 days and 45 days of S-CO_2 interaction) and the required measurements were taken at each retrieval.

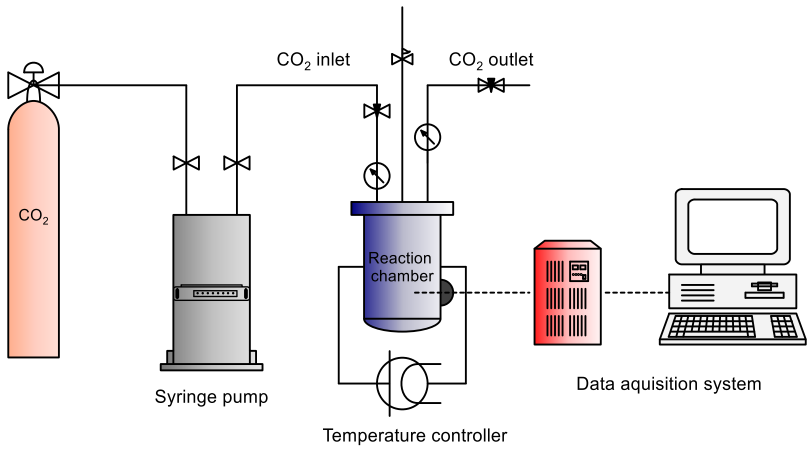

Figure 6-19 - Schematic diagram of the reaction chamber used for the coal-S-CO_2 treatment.

6.3.2.3 Gamma-ray attenuation method (GAM)

Gamma-ray attenuation method (GAM) provides the bulk density measurements of core samples at different orientations and enables the precise evaluation of density anisotropies in heterogeneous coal mass. We used a standard multi-sensor core logger (MSCL-S) to measure the radial rock bulk densities of core sample at four orientations (i.e. at angles of 0^o, 45^o, 90^o and 135^o to the mineral layering) to differentiate the density anisotropies *(see Figure 6-20)*. The radioactive gamma-ray source consists of a 10 milli-curie Caesium-137 capsule, and the detector comprises a 3" thick NaI(TI) crystal and an integral photo-multiplier tube. Since the source and the detector were fixed, the core specimen was rotated around its longitudinal axis to take the radial measurements at four orientations. The obtained densities were incorporated with the ultrasonic wave velocity data to calculate the dynamic moduli at corresponding orientations.

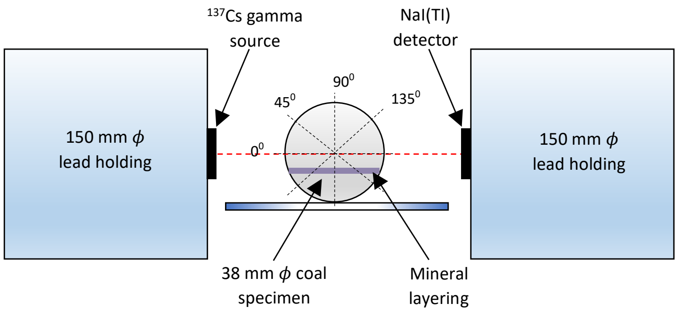

Figure 6-20 - Schematic diagram of the gamma-ray attenuation system *(not to scale)* and the measured orientations of the core specimen.

6.3.2.4 Ultrasonic wave measurements

We used the Pundit Lab+ device to measure the P and S wave velocities at pre-defined orientations of the heterogeneous coal specimen *(see Figure 6-21)*. The device is comprised of 250 Hz transducers, in which the ratio of the P and S wave components is below -30 dB that allows producing both P and S wave motions. The sensor is capable of capturing ultrasonic wave measurements at a time range of 0.1 - 9999 μs with a 0.1 μs precision. The transducers' surfaces were coated with a sonic couplant, and the device was pre-calibrated prior to testing. Transmission amplitude and probe gain must be adjusted according to the particular specimen type to get a legible waveform. We used a pulse amplitude of 500V and probe gains of 500× and 200× for P wave and S wave measurements, respectively. The measurements were taken at three stages of the experiment: 1) natural sample, 2) after 14 days of coal-S-CO_2 interaction and, 3) after 45 days of coal-S-CO_2 interaction. The measured P and S wave delay times, the distance between transmitter and receiver through the specimen and the gamma densities at corresponding orientations were used to calculate the velocities and dynamic moduli. Observed velocity anisotropies and the resultant dynamic moduli alterations of coal specimen due to S-CO_2 interaction were interpreted with the micro-CT image-based 3D-reconstructed data.

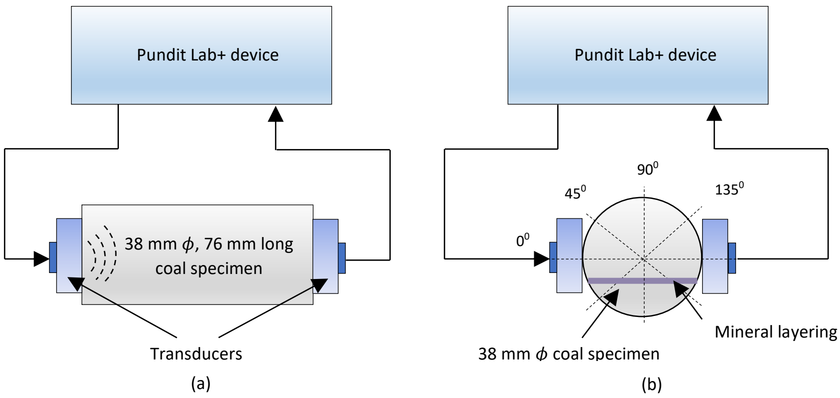

Figure 6-21 - Measurement of ultrasonic wave velocities at: a) axial direction and, b) pre-defined radial orientations of the core specimen *(not to scale)*.

6.3.2.5 Micro-computed tomography (micro-CT)

Micro-computed tomography (micro-CT) is often used to visualize and quantify the characteristics of various geological materials. The 3D-reconstructed results of the full-scale specimen permit visualization of the spatial disposition and geometry of favourable components and their quantification. We scanned the core at the aforementioned three stages by x-ray CT to evaluate the micro-structural alterations induced by S-CO_2 interaction. Scanning was done at Australian Synchrotron imaging and medical beamline (IMBL) facility, in which the scanning parameters were set to enhance both resolution and contrast as much as feasible. We used a mono-chromatic X-ray beam, a Ruby detector with a 150 mm lens and a 20 μm screen filter. The X-ray energy was 50 keV, the voxel size was 16.7 μm, and the acquisition time was 20 min. Obtained images were then 3D-reconstructed using *AVIZO* image analysis software to visualize and quantify the resultant micro-structural alterations.

6.3.3 Results and discussion

6.3.3.1 3D visualization and quantification of micro-structural alterations

Micro-CT image-based coal characterization has been widely used by many researchers to interpret the various features of heterogeneous coal mass (Ramandi et al., 2016; Sampath et al., 2018; Zhang et al., 2016b). Figure 6-22 illustrates the 3D-reconstructed core specimens at the three defined stages of S-CO_2 interaction process. There is an obvious difference between natural and S-CO_2-interacted conditions, in which the latter two cases exhibit a large number of micro-cracks induced during S-CO_2 interaction. For the quantitative interpretation, we calculated the fracture fraction in each case by Eq. 6-6.

$$Fracture\ fraction = \left(\frac{total\ segmented\ fracture\ volume}{total\ sample\ volume}\right) \times 100\% \qquad \text{………… [6-6]}$$

As illustrated in Figure 6-23 (a) the fracture fraction shows an approximate linear increment with S-CO_2 interaction time, in which fracture fractions for natural, after 14 days and after 45 days of S-CO_2-interacted samples were obtained as 0.33%, 0.53% and 0.86%, respectively. Figure 6-23 (b) shows the cumulative fracture volume with respect to fracture geometry (i.e. fracture orientation measured related to mineral layering) that clearly differentiates the orientation-based micro-cracking of the heterogeneous core sample. In fact, it is clearly noticeable that S-CO_2-induced micro-fractures tend to align at favourable orientations, where most of the newborn fractures are oriented parallel to mineral layering. As quantified from segmented fracture networks, the fracture volumes parallel to mineral layering (i.e. $\theta = 0^0$) are 11.9 mm^3, 123 mm^3 and 135.7 mm^3 for natural, 14 days S-CO_2 interacted, and 45 days of S-CO_2 interacted samples, respectively. This observation confirms that most of the alterations are anisotropic, in which S-CO_2 interaction has caused significant alterations at specific orientations, and more alterations have been occurred at heterogeneous mineral-rich areas than comparatively homogeneous maceral-rich regions.

The possibility of anisotropic fracture propagation at more heterogeneous areas (i.e. mineral-rich areas) can be supported with a number of theories: mineral and maceral components have distinct swelling potentials, which lead to swelling of each component at different rates (Karacan, 2003). This can create internal stresses within the coal mass and create fractures at phase-interconnecting boundaries, depending on the coal rank and the mineral types present. Fractures can be preferably propagated along the coal-mineral interface because stress concentrations and localized weaknesses are predominant at grain-grain boundaries due to stiffness contrasts between maceral and mineral phases (Amann et al., 2014; Sampath et al., 2019; Ündül et al., 2015). Moreover, the free-swelling of the coal mass under unconfined condition can extend/widen the existing fractures and induce new fractures within individual components as well. During the two-phase flow interaction process, the injected S-CO_2 molecules may promote desorption of water molecules from the coal micro- and meso-pores (Sun et al., 2016; Sun et al., 2018), resulting in a drying effect in the coal mass that can possibly cause shrinkage cracks (Brenner, 1984). CO_2 adsorption on to crack surfaces may reduce the surface energy, resulting in a reduction of crack initiation stress threshold at crack tips that preferably cause extension of existing fractures (Gibbs, 1879; Griffith, 1921; Viete and Ranjith, 2006). It is evident that there exist a number of concepts and theories that explain the S-CO_2-induced structural alterations of coal mass. These alterations can possibly affect the gamma and ultrasonic wave propagations through the coal mass at each orientation and lead to anisotropic alterations of the resultant densities and dynamic strength parameters.

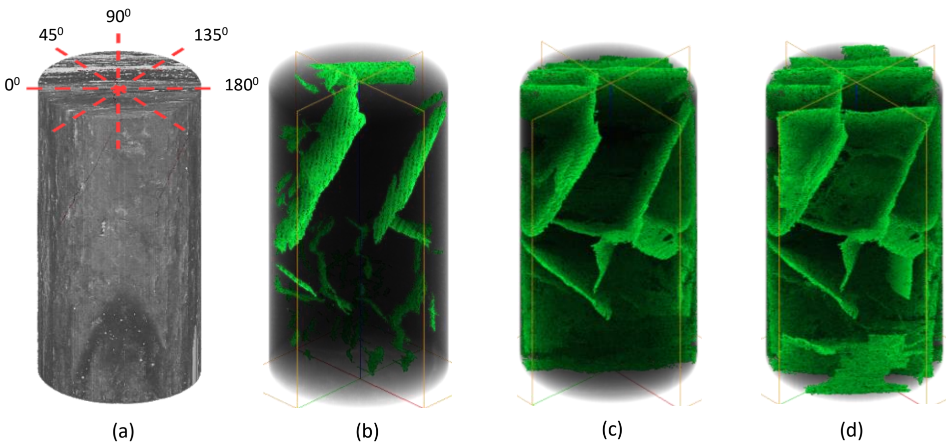

Figure 6-22 - Visualization of full-scale core specimens: a) natural core specimen, indicating the mineral layering and pre-defined orientations. 3D-reconstructed full-scale specimen: b) at natural conditions, c) after 14 days of S-CO_2 interaction and, d) after 45 days of S-CO_2 interaction. Note that the fracture network and coal mass are segmented in green and black colours, respectively, for the visualization.

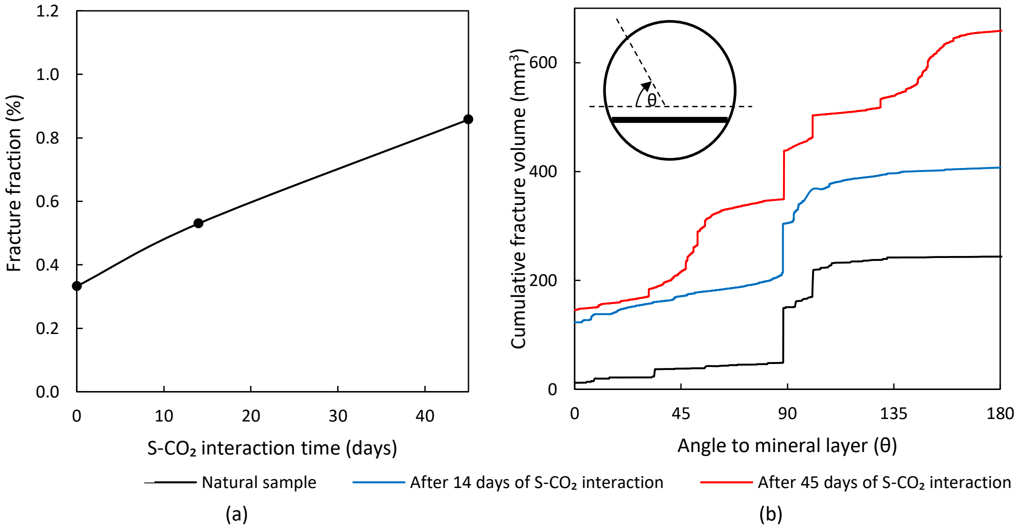

Figure 6-23 – Quantification of induced fracture network: a) variation of fracture fraction with S-CO_2 interaction time and, b) variation of cumulative fracture volume with the angle to mineral layer.

6.3.3.2 Gamma-density anisotropies

Gamma-ray transmission method permits the measurement of a number of parameters in amorphous materials, such as bulk density, porosity, temporal and spatial profiles of moisture, etc. (Bodwadkar and Reis, 1994; Phogat and Aylmore, 1989; Pires et al., 2009). The method was utilized in the current study to evaluate the density anisotropies of the core sample and its alteration with the S-CO_2 interaction time. Evaluation of gamma-density of natural core sample confirms the anisotropies of the bulk density, in which the bulk density increases with the angle to the mineral layering (θ) *(see Figure 6-24)*. It is obvious that densities measured at $0^o - 180^o$ orientation (parallel to mineral layering – i.e. $\theta = 0^o$) give the least values, because waves propagate at particular orientation do not intersect the dense mineral phase, but covers a large portion of more homogenous, less-dense maceral phase (*see Figure 6-17 (b) and Figure 6-20)*, resulting in a low-density value. This is because the mineral layers are not positioned exactly at the centre of the core sample, but have been shifted towards one end. In contrast, the density corresponding to $90^o - 270^o$ orientation gives the highest value, due to wave intersection of a large portion of the dense mineral phase. The difference in natural densities between $0^o - 180^o$ and $90^o - 270^o$ orientations is 2.91%, which depicts the anisotropic nature of the coal mass used.

Moreover, it is noticeable that gamma-density values have been reduced with S-CO_2 interaction time, in which the density values at $0^o - 180^o$ orientation were reduced by 7.4% and 8.5% after S-CO_2 interaction of 14 and 45 days, respectively, whereas that at $90^o - 270^o$ orientation were reduced by 7.5% and 9.1% *(see Table 6-5)*. Initially, the natural sample had less fractures, and most of the fractures and pore spaces were filled with water, due to water-saturated condition, prior to S-CO_2 interaction. Therefore, the resultant gamma-ray attenuation coefficients were high, as the gamma rays predominantly passed through solid and liquid phases, which consequently result in high-density values. During S-CO_2 interaction, the water in the core sample was gradually replaced by CO_2, due to two-phase flow interaction process between water and S-CO_2 in coal. This process may cause water to displace from natural fractures and pore network by replacing them with CO_2, which in turn result in low gamma attenuation coefficients at the latter two cases. Concurrently, the micro-CT images at corresponding stages suggest that core sample has undergone a significant micro-cracking during S-CO_2 interaction due to free- and differential-swelling, which may also affect the gamma attenuation coefficient and resultant densities, as gamma rays passed through a large number of CO_2-filled newborn fractures. As confirmed by Ferraz and Mansell (1979), the attenuation of the beam by the air can be neglected, as it is insignificant as compared with the attenuation by solid and liquid, which may possibly cause the observed low-density values. Thus, gamma-attenuation results confirm the density anisotropies due to the phase distribution of the core specimen and the resultant orientation-based density alterations caused by S-CO_2 interaction that conceivably affects the strength parameters.

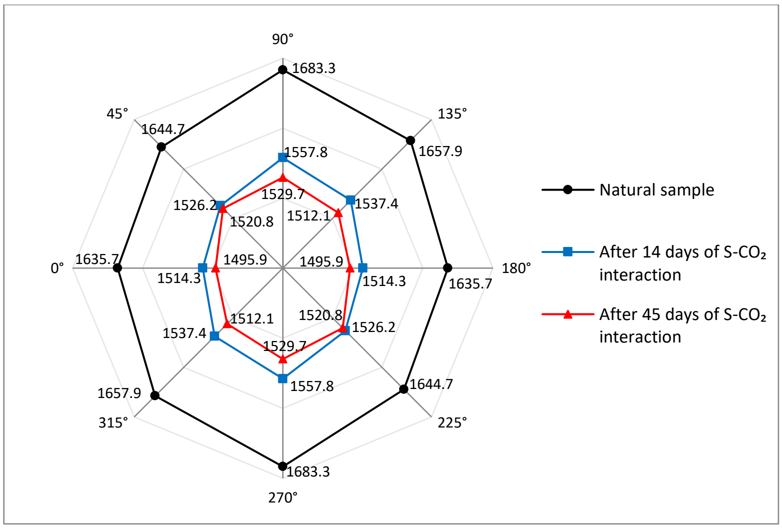

Figure 6-24 – Variation of gamma-density at radial orientations.

Table 6-5 - Results of radially measured gamma-densities at three S-CO_2 interaction periods.

Parameter		Natural sample	After 14 days of S-CO_2 interaction	*Δ_{14} (%)	After 45 days of S-CO_2 interaction	*Δ_{45} (%)
Gamma density (kg/m^3)	0°-180°	1635.7	1514.3	-7.4	1495.9	-8.5
	45°-225°	1644.7	1526.2	-7.2	1520.8	-7.5
	90°-270°	1683.3	1557.8	-7.5	1529.7	-9.1
	135°-315°	1657.9	1537.4	-7.3	1512.1	-8.8

* Δ_{14} and Δ_{45} are reduction percentages after 14 days and 45 days of S-CO_2 interaction, respectively, comped to natural condition.

6.3.3.3 P and S wave delay times and velocities

Velocity measurement of elastic waves propagated through a rock mass is one practical tool of evaluating anisotropic physical and mechanical characteristics of the particular rock. Previous studies on elastic wave propagation in sedimentary rocks show that P and S wave velocities are closely related to density, confining pressure, UCS, pore fluid saturation and type, degree of fracturing and porosity of rocks being considered (Calvet and Margerin, 2016; Matsushima et al., 2016; Parra et al., 2015). Several equations have been established to correlate P and S wave velocities to dynamic strength parameters of rocks. As illustrated in Figure 6-18, we measured P and S wave delay times at both axial and radial directions and computed the corresponding velocities to evaluate the S-CO_2 interaction-induced dynamic strength alterations in coal. The radial measurements obtained at three sections along the longitudinal axis were averaged to attain reliable results.

Figure 6-25 illustrates the variation of P and S wave velocities with respect to the angle to mineral layering. Figure is drawn from 0^o to 180^o due to symmetry, in which values at both 0^o and 180^o are the same. Moreover, the values at 45^o, 90^o and 135^o correspond to the velocities at $45^o - 225^o$, $90^o - 270^o$ and $135 - 315^o$ orientations, respectively. The results suggest that at all three stages, P and S wave velocities decrease with the increasing angle to mineral layering, where waves propagate at $0^o - 180^o$ orientation give the highest values and conversely that of $90^o - 270^o$ orientation give the least values. In fact, compared to $0^o - 180^o$ orientation (i.e. $\theta = 0^o$), the P wave velocities have been decreased by 27.8%, 32.5% and 27.8% at $\theta = 45^o, 90^o$ and 135^o orientations, respectively. This is in agreement with most of the previous studies on foliated rocks, in which studies show that P and S waves mostly tend to propagate at higher velocities parallel to foliation plane. For instance, Vishnu et al. (2010) showed that P wave velocity in quartz is greater in the direction parallel to foliation and lower perpendicular to the same. A similar trend was observed by Esamaldeen et al. (2015) in amphibolite rocks, Kern et al. (1997) in serpentinite rocks and Lo et al. (1986) in granite, shale and sandstone. It is apparent that ultrasonic wave velocities depend on the intensity of rock fabric or the foliation, which could be defined by the preferential orientation of rock minerals (David Suits et al., 2006; Goodman, 1989). Waves propagate perpendicular to mineral layer intersect a large number of rock discontinuities between mineral-maceral interface, which may obviate the obvious and direct wave paths due to geometric spreading, scattering, reflections and intrinsic damping of waves that can possibly disturb the simple wave propagations, and consequently affect the velocities at corresponding orientations.

Moreover, as illustrated in Figure 6-26 and Figure 6-27, the P and S wave delay times, and the corresponding wave velocities have significantly been influenced by S-CO_2 interaction at both axial and radial directions. This is plausible due to change in pore fluid condition and the significant micro-cracking at preferred orientations. At initial water-saturated condition, with a better-interconnected fracture network, water easily accesses the fractures and pores by reducing the free space between water and coal skeleton, which can cause higher P and S wave velocities (Johansen et al., 2002; Liu et al., 2017). However, displacement of water by CO_2 during the interaction may create more free spaces with the coal mass, which can consequently reduce the wave velocities. Concurrently, the increment of fracture fraction *(see Figure 6-23 (a))* and the fracture aperture due to free and differential swelling effect during the interaction may also cause the wave velocity reduction. For instance, as observed by Wang et al. (2015), P wave velocity can be linearly or nonlinearly decreased with the increase of fracture density in coal samples. Moreover, the influence of fracture aperture on wave velocity is more significant than that of fracture density

It is apparent from Figure 6-24 and Figure 6-26 that gamma density and P and S wave velocities have been reduced significantly at the first stage (i.e. from natural condition to 14 days of S-CO_2 saturation condition), but slightly at the latter stage. The sample was initially fully-saturated with water and had fewer fractures, which consequently resulted in higher attenuations and velocities. After 14 days of S-CO_2 interaction, there were new fractures appeared and simultaneously, the moisture filled in pore spaces and fractures has been replaced by CO_2. Combination of these two phenomena may result in a significant velocity reduction in the initial case. In contrast, the velocity reduction at latter stage may only occur due to increased fracture density, as all the pore spaces have already been invaded by CO_2, by replacing moisture during the first stage. Hence, although the fracture fraction increases linearly *(see Figure 6-23 (a))*, the velocity reduction is comparatively significant in the initial stage, as it occurs due to the combination of new fracture initiation and moisture replacement with CO_2.

If the orientation-based alteration is considered, it is noticeable that P wave delay time and velocity have been changed only by 8.7% and -7.7% at $0^o - 180^o$ orientation, whereas that at $90^o - 270^o$ orientation have been changed by 88.7% and -47.0%. The observation is the same for S wave delay times and velocities as well *(see Table 6-6 and Table 6-7)*. Large reduction of wave velocities at $90^o - 270^o$ orientation emphasizes that more structural alterations, including micro-cracking occurred at the mineral-rich area, which in turn significantly affected the waves propagated through that region. The orientation of the induced micro-cracks seems to critically influence the wave propagation. As apparent from Figure 6-22 and Figure 6-23 (b), a large number of micro-cracks were induced parallel to mineral layering or in other terms - perpendicular to $90^o - 270^o$ directional wave propagation. These observations conclude the fact that P and S waves tend to affect significantly, when they propagate perpendicular to the fracture orientation. The results are in line with previous work, where Zhou (2012) observed that P and S wave velocities vary with a minimum and maximum wave velocities perpendicular and parallel to the fracture alignment, respectively. A similar trend was observed by Ding et al. (2014) in synthetic sandstone samples and, Yan (2006) and Guo et al. (1998) in coal. Zhao and Hao (2006) revealed that angle to the fracture and P wave velocity has a periodic relationship, in which P wave velocity drops down from 0^o to 90^o, and then goes up from 90^o to 180^o, with maximum and minimum velocities closer to 0^o and 90^o. Cai et al. (2014) showed that P wave velocity has a decreasing trend with increasing angle between fracture and P wave path, measured from 0^o to 90^o.

Overall, the results conclude that S-CO_2 interaction-induced micro-structural alterations significantly affect the ultrasonic wave propagation through coal mass and that alterations are noticeably anisotropic, as they greatly depend on the spatial distribution of mineral/maceral phases and the natural/induced fracture network. Consequently, the dynamic strength parameters can also be varied an-isotropically, as they generally are based on ultrasonic wave velocities.

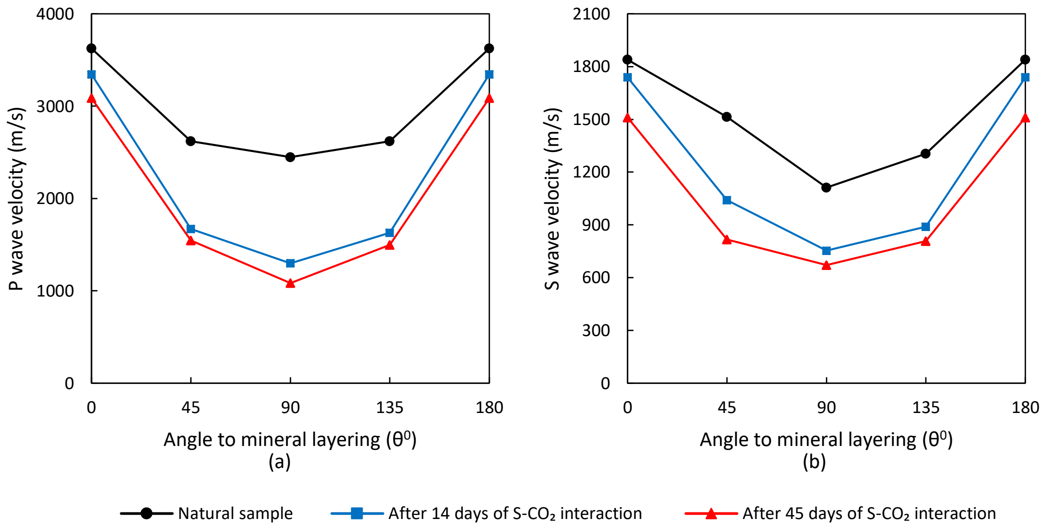

Figure 6-25 – Variation of a) P wave velocities and, b) S wave velocities with angle to mineral layering.

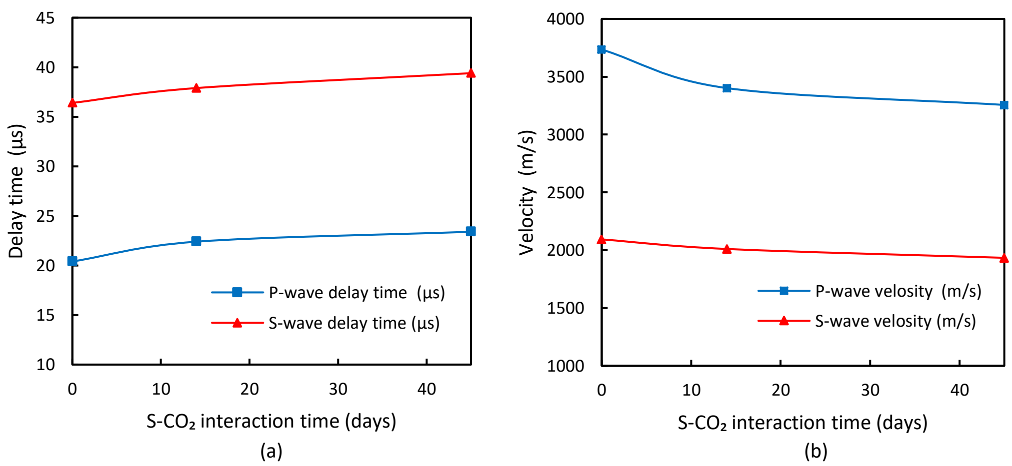

Figure 6-26 – Variation of axial: a) P and S wave delay times and, b) P and S wave velocities with S-CO_2 interaction time.

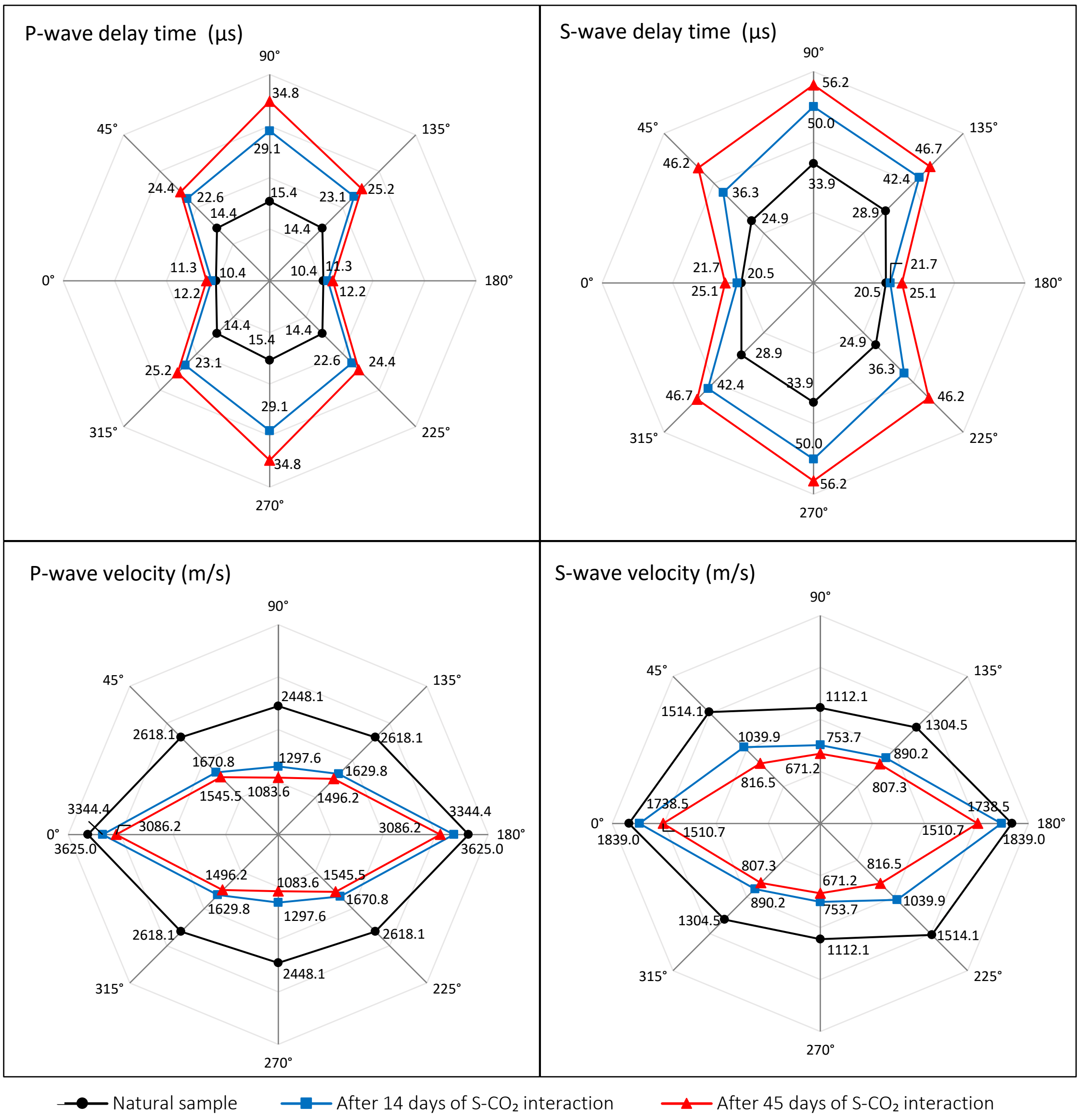

Figure 6-27 – Variation of radially measured P and S wave delay times and velocities.

Table 6-6 - Axially and radially measured P and S wave delay times at three S-CO_2 interaction periods.

Parameter		P wave					S wave				
		Natural sample	After 14 days of S-CO_2 interaction	Δ_{14} (%)	After 45 days of S- CO_2 interaction	Δ_{45} (%)	Natural sample	After 14 days of S- CO_2 interaction	Δ_{14} (%)	After 45 days of S- CO_2 interaction	Δ_{45} (%)
Delay time (us)	Axial	20.4	22.4	9.8	23.4	14.7	36.4	37.9	4.1	39.4	8.2
	0°-180°	10.4	11.3	8.7	12.2	17.6	20.5	21.7	6.0	25.1	22.3
	45°-225°	14.4	22.6	56.7	24.4	69.4	24.9	36.3	45.6	46.2	85.7
	90°-270°	15.4	29.1	88.7	34.8	126.0	33.9	50.0	47.6	56.2	65.8
	135°-315°	14.4	23.1	60.6	25.2	75.0	28.9	42.4	46.6	46.7	61.6

Table 6-7 - Computed axial and radial P and S wave velocities at three S-CO_2 interaction periods.

Parameter		P wave					S wave				
		Natural sample	After 14 days of S-CO_2 interaction	Δ_{14} (%)	After 45 days of S- CO_2 interaction	Δ_{45} (%)	Natural sample	After 14 days of S- CO_2 interaction	Δ_{14} (%)	After 45 days of S- CO_2 interaction	Δ_{45} (%)
Velocity (m/s)	Axial	3735.3	3401.8	-8.9	3256.4	-12.8	2093.4	2010.6	-4.0	1934.0	-7.6
	0°-180°	3625.0	3344.4	-7.7	3086.2	-14.9	1839.0	1738.5	-5.5	1510.7	-17.9
	45°-225°	2618.1	1670.8	-36.2	1545.5	-41.0	1514.1	1039.9	-31.3	816.5	-46.1
	90°-270°	2448.1	1297.6	-47.0	1083.6	-55.7	1112.1	753.7	-32.2	671.2	-39.6
	135°-315°	2618.1	1629.8	-37.7	1496.2	-42.8	1304.5	890.2	-31.8	807.3	-38.1

6.3.3.4 Evaluation of dynamic strength parameters

Dynamic strength parameters are often related to mechanical properties of heterogeneous material, mostly because the anisotropic features significantly influence the sensitive undelaying measured parameters; thus, easily reflect through the resultant moduli. Numerous studies have used this method to define strength parameters to evaluate mechanical competency of anisotropic rock specimens. For instance, Wanniarachchi et al. (2017) characterized the dynamic material properties of different rock types, including siltstone, shale, sandstone and granite. Stan Kłeczek (2016) compared the laboratory-measured dynamic elastic moduli of dolomite and limestone with field measurements. Yun et al. (2016) characterized the elastic properties of six kinds of metamorphic coal under room pressure-temperature conditions. The key benefit is that the technique is non-destructive and extremely sensitive; thus, can be utilized for repetitive and temporal measurements of highly-anisotropic and heterogeneous materials, especially coal.

Based on the directional ultrasonic wave velocities and corresponding gamma densities, we computed six moduli at three stages of the experiment to characterize the dynamic mechanical alterations of S-CO_2-interacted coal. The P wave and S wave propagations through a material depend on the material P wave modulus (M) and the shear modulus (G), respectively. Hence, the said moduli can be correlated to the wave velocities as given in Eqs. 6-7 and 6-8 (Kearey et al., 2013). The latter strength parameters are basically derived from P wave and shear moduli, and can be deduced to express in terms of material density and wave velocities *(see Eqs. 6-9 – 6-12)* (Wanniarachchi et al., 2017).

$$M = \rho v^2{}_p \qquad \text{………… [6-7]}$$

$$G = \rho \mathrm{v}^2{}_s \qquad \text{………… [6-8]}$$

$$E = \frac{\rho v^2{}_s(3v^2{}_p - 4v^2{}_s)}{v^2{}_p - v^2{}_s} \quad \text{………… [6-9]}$$

$$K = \rho\left(v^2{}_p - \frac{4}{3}v^2{}_s\right) \quad \text{………… [6-10]}$$

$$\lambda = \rho\left(v^2{}_p - 2v^2{}_s\right) \quad \text{………… [6-11]}$$

$$\nu = \frac{v^2{}_p - 2v^2{}_s}{2(v^2{}_p - v^2{}_s)} \quad \text{………… [6-12]}$$

where, M is the P wave modulus, G is the dynamic shear modulus, E is the dynamic elastic modulus, K is the dynamic bulk modulus, λ is the Lame's first parameter, ν is the dynamic Poisson's ratio, ρ is the rock density, v_p is the P wave velocity and v_s is the S wave velocity.

The computed dynamic moduli are few of several quantities for measuring the stiffness of materials. Each parameter has a different interpretation for material mechanical properties: P wave modulus is a measure of longitudinal elasticity, shear modulus describes the materials' response to shear stress, bulk modulus represents the volumetric elasticity and Poisson's ratio relates deformation in materials at orthogonal directions.

Table 6-8 summarises the computed dynamic mechanical parameters at both axial and radial directions, including the change percentages after each interaction period, compared to the natural condition. The moduli values and Poisson's ratio values of the natural sample are in the range of 2-23 GPa and 0.25-0.37, respectively, which are in agreement with previous studies done on coal (Morcote et al., 2010; Yun et al., 2016; Zheng et al., 1991). Figure 6-28 illustrates the variation of axially measured dynamic moduli *(see Figure 6-21 (a))* with respect to S-CO_2 interaction time. It is noticeable that a significant reduction of all the moduli values occurred within the initial interaction stage (i.e. within 14 days), but longer interaction with S-CO_2 caused only a gradual strength reduction in the coal mass. For instance, as given in detail in Table 6-8, the reduction of P wave modulus is 23.1% and 30.5% after 14 days and 45 days of S-CO_2 interaction respectively, which depicts that the coal mass has been subjected to only a 9.5% of reduction (compared to 14 days condition) at latter longer interaction period. The axial results are in line with the radially measured values, as can be seen in Figure 6-29, all the dynamic moduli, except dynamic Poisson's ratio, depict a larger reduction of values after 14 days of S-CO_2 interaction. The overlapping of 14 days and 45 days trendlines at most cases confirms the fact that there is no comparatively larger strength reduction occurred at the latter stage. This can be due to the complex CO_2 adsorption behaviour on coal mass. Previous studies suggest that CO_2 adsorb relatively rapidly on to coal matrix and trigger interactions as soon as the adsorption took place (Karacan, 2003). This can alter the mechanical response of coal mass, in which a significant mechanical degradation may occur in the short-term condition. This is in line with the experiment conducted by Ranathunga et al. (2016a), in which they assessed the UCS of low-rank coal saturated with S-CO_2 for different time periods. They found that S-CO_2 adsorption-induced coal mechanical alterations are largely completed with the initial interaction with CO_2, whereas further strength reduction occurs at a slower rate.

Since the strength parameters are generally derived from gamma density values and ultrasonic velocity values, they principally reflect the anisotropic strength alterations of the coal specimen. Consequently, the highest and the least moduli values fall at the directions parallel to and perpendicular to mineral layering, respectively *(see Table 6-8)*, which confirm the anisotropic nature of the coal specimen. For example, the dynamic elastic modulus of natural coal specimen, parallel to mineral layering is computed as 14.7 GPa, whereas that in perpendicular to mineral layering is only 5.7 GPa. Hence the sensitive nature of the technique is capable of evaluating such mechanical anisotropies of heterogeneous coal specimens, which cannot be simply captured from bulk specimen failure by static mechanical testing.

It is clear from Table 6-8 that majority of strength moduli values show a large reduction at $90^o - 270^o$ orientation, compared to that of $0^o - 180^o$. For instance, after 14 days of S-CO_2 interaction, dynamic shear modulus and dynamic elastic modulus show reductions of 17.3% and 18.0% at $0^o - 180^o$ orientation, whereas that at $90^o - 270^o$ orientation show 57.5% and 61.4% reductions, respectively. This is because the micro-cracking occurred at mineral-maceral interconnections significantly influenced the ultrasonic wave propagation at $90^o - 270^o$ orientation, which is reflected by the consequent dynamic moduli values at the particular orientation. Accordingly, this concludes that S-CO_2 interaction-induced coal mechanical property alteration is anisotropic, where the more heterogeneous mineral/maceral distribution causes significant localized mechanical alterations in mineral-rich areas, compared to that of comparatively homogeneous maceral-rich regions. Hence, the results emphasize that for same interaction conditions and same interaction periods, coal mass exhibits mechanical anisotropies and strength alterations at different levels, depending on its spatial distribution of mineral/maceral phases and fracture network. Importantly, the temporal evaluation of strength parameters suggests that a significant strength alteration occurs at the initial stage of the coal-S-CO_2 interaction process and the longer interaction causes only a slight strength alteration.

It should be noted that the results obtained from this study may be specific to this particular coal sample or type. The localized mechanical alterations and their magnitudes can be varied depending on the coal type and spatial disposition of mineral/maceral phases and fracture network. It is difficult to obtain a universal trend for S-CO_2-induced mechanical alterations in coal due to its extreme complexity. Hence, more experimental and theoretical studies are needed to precisely evaluate such alterations. Moreover, in this particular study, the non-destructive techniques are not real-time, where the S-CO_2 pressure was released, and the sample was taken out from the reaction chamber for detection. Although we paid careful attention to minimize the effect of pressure relief, results may still be slightly deviated from the real process of coal-S-CO_2 interaction. Furthermore, it should be noted that the experiment was conducted under the unconfined condition to support most of the lab experiments. Numerous static mechanical testings are conducted under unconfined condition, including UCS tests. Hence, this study more likely represents the static UCS test results, but in a dynamic manner. We recommend more studies to be conducted under the confined condition to represent *in-situ* conditions and to compare with static tri-axial test results.

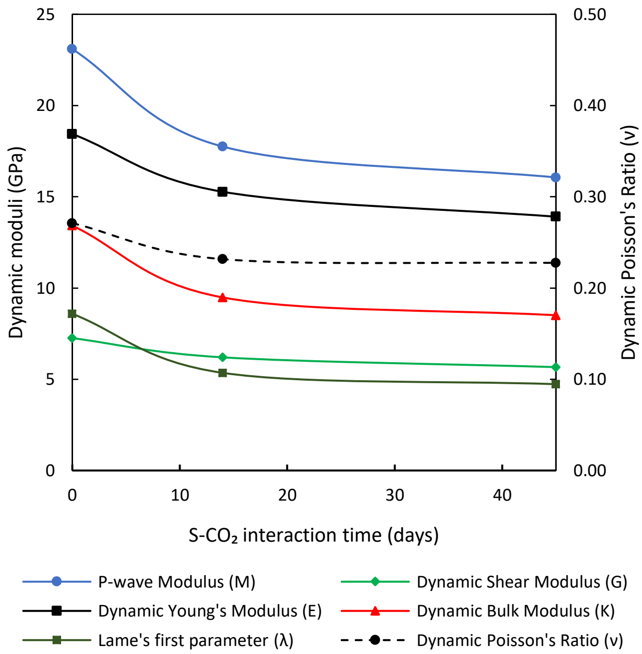

Figure 6-28 – Variation of axially measured dynamic strength parameters with S-CO_2 interaction time.

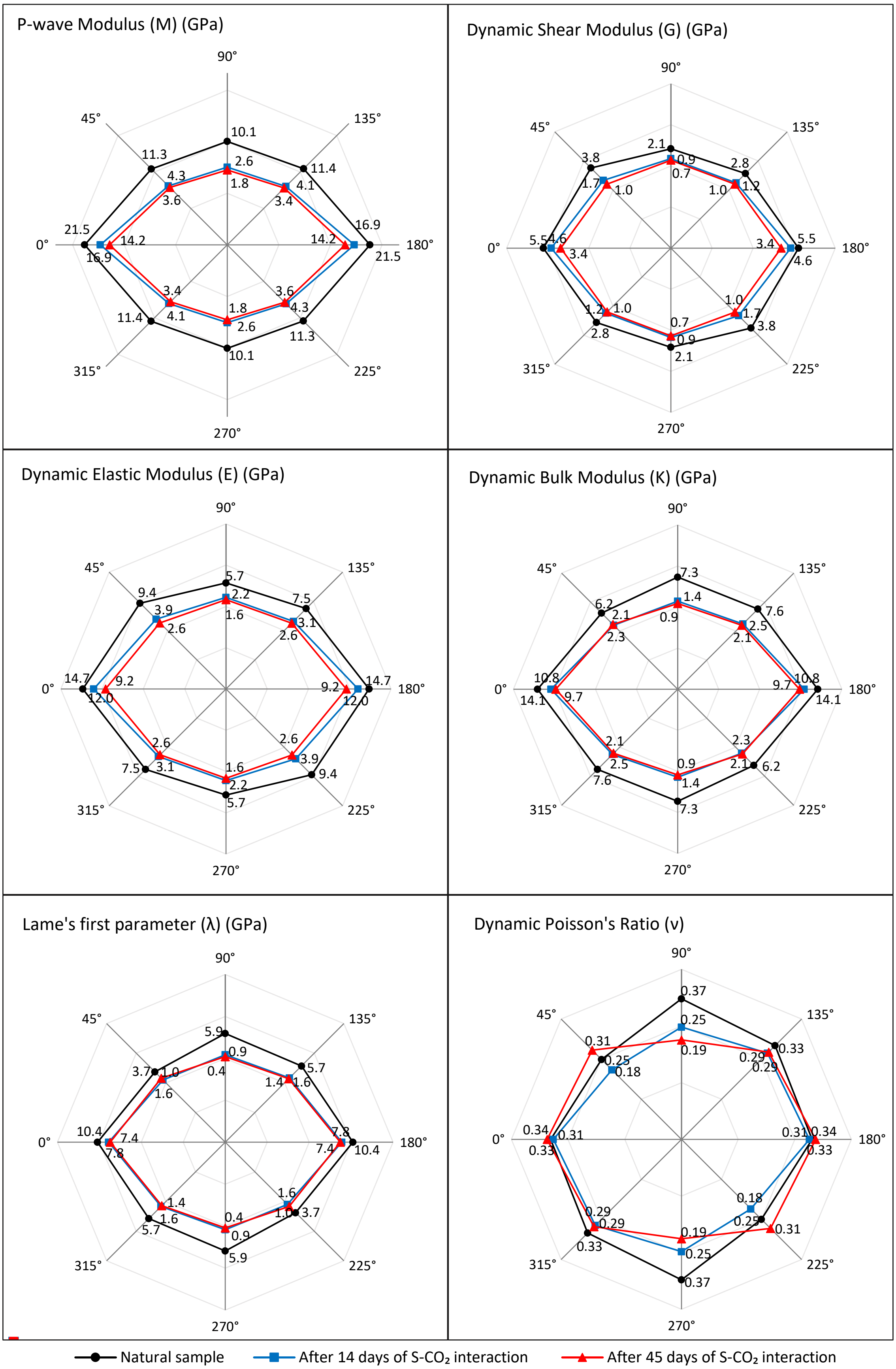

Figure 6-29 – Variation of radially measured dynamic strength parameters.

Table 6-8 – Results of the dynamic strength parameters at three stages of the experiment and the strength reductions with respect to the natural condition.

Parameter	Orientation	Natural sample	After 14 days of S-CO_2 interaction	Δ_{14} (%)	After 45 days of S-CO_2 interaction	Δ_{45} (%)
P-wave Modulus (M) (GPa)	Axial	23.1	17.8	-23.1	16.1	-30.5
	0°-180°	21.5	16.9	-21.2	14.2	-33.7
	45°-225°	11.3	4.3	-62.2	3.6	-67.8
	90°-270°	10.1	2.6	-74.0	1.8	-82.2
	135°-315°	11.4	4.1	-64.1	3.4	-70.2
Dynamic Shear Modulus (G) (GPa)	Axial	7.3	6.2	-14.5	5.7	-21.9
	0°-180°	5.5	4.6	-17.3	3.4	-38.3
	45°-225°	3.8	1.7	-56.2	1.0	-73.1
	90°-270°	2.1	0.9	-57.5	0.7	-66.9
	135°-315°	2.8	1.2	-56.8	1.0	-65.1
Dynamic Elastic Modulus (E) (GPa)	Axial	18.4	15.3	-17.2	13.9	-24.6
	0°-180°	14.7	12.0	-18.0	9.2	-37.6
	45°-225°	9.4	3.9	-58.5	2.6	-71.9
	90°-270°	5.7	2.2	-61.4	1.6	-71.3
	135°-315°	7.5	3.1	-58.4	2.6	-66.1
Dynamic Bulk Modulus (K) (GPa)	Axial	13.4	9.5	-29.4	8.5	-36.6
	0°-180°	14.1	10.8	-23.3	9.7	-31.3
	45°-225°	6.2	2.1	-67.0	2.3	-63.5
	90°-270°	7.3	1.4	-80.3	0.9	-88.0
	135°-315°	7.6	2.5	-67.6	2.1	-72.8
Lame's first parameter (λ) (GPa)	Axial	8.6	5.3	-37.7	4.7	-44.9
	0°-180°	10.4	7.8	-25.4	7.4	-28.9
	45°-225°	3.7	1.0	-74.3	1.6	-57.0
	90°-270°	5.9	0.9	-85.6	0.4	-92.9
	135°-315°	5.7	1.6	-71.2	1.4	-75.3
Dynamic Poisson's Ratio (ν)	Axial	0.27	0.23	-14.6	0.23	-16.1
	0°-180°	0.33	0.31	-3.6	0.34	4.8
	45°-225°	0.25	0.18	-26.1	0.31	23.2
	90°-270°	0.37	0.25	-33.7	0.19	-49.0
	135°-315°	0.33	0.29	-14.2	0.29	-12.0

6.3.4 Conclusions

Three non-destructive techniques were combined to evaluate the anisotropic dynamic mechanical alterations of a S-CO_2-interacted heterogeneous coal specimen at three stages of the interaction process (i.e. natural sample, after 14 days and 45 days of S-CO_2 interaction). Ultrasonic wave measurements and gamma density values were used to precisely compute the dynamic moduli at axial and radial directions, and micro-CT 3D-reconstructed data were used to interpret the resultant alterations. The selected core specimen consists of spatially distributed mineral layers that induce a heterogeneity into the coal mass. Resultant anisotropies were discussed based on the angle to these mineral layers. Based on the experimental results, the following conclusions were made:

- 3D-reconstructed data show that S-CO_2 interaction has caused a significant micro-cracking in the core specimen and most of the micro-cracks tend to align at favourable orientations (i.e. parallel to the mineral layering). This may occur due to differential and free swelling of mineral/maceral phases, existing weak mineral-maceral interconnecting boundaries, drying-induced shrinkage effect and S-CO_2 adsorption-induced surface energy reduction at crack tips.

- Evaluation of gamma-density of core sample confirms the anisotropies of the bulk density, in which the bulk density increases with the angle to the mineral layering (θ). The density values have been reduced with S-CO_2 interaction time, due to replacement of water in pores and fractures by S-CO_2 and the large number of S-CO_2-filled newborn fractures.

- P and S wave velocities decrease with the angle to mineral layering because waves propagate through mineral layer intersect a large number of rock discontinuities between mineral-maceral interface, which may obviate simple wave paths. Moreover, the wave velocities have significantly been reduced by S-CO_2 interaction at both axial and radial directions, possibly due to change in pore fluid condition and significant micro-cracking at preferred orientations.

- Computation of dynamic moduli at each orientation confirms the mechanical anisotropies of S-CO_2-interacted coal mass, where the more heterogeneous mineral/maceral distribution cause significant localized mechanical alterations in mineral-rich areas, compared to that of comparatively homogeneous maceral-rich regions. Temporal assessment of moduli highlights that a significant strength alteration occurs at the initial stage of the coal-S-CO_2 interaction process and the longer interaction causes a minor strength alteration.

Overall, the combined results from three techniques emphasize that S-CO_2 interaction-induced mechanical property alteration is extremely complex in heterogeneous coal; thus, more sensitive techniques like inversion of ultrasonic wave velocities should be utilized to precisely evaluate localized and anisotropic mechanical alterations.

Reference

Amann, F., Ündül, Ö., & Kaiser, P. K. (2014). Crack initiation and crack propagation in heterogeneous sulfate-rich clay rocks. *Rock Mechanics and Rock Engineering, 47*(5), 1849-1865.

Bodwadkar, S. V., & Reis, J. C. (1994). Porosity measurements of core samples using gamma-ray attenuation. *Nuclear Geophysics, 8*(1), 61-78.

Brenner, D. (1984). Microscopic in-situ studies of the solvent-induced swelling of thin sections of coal. *Fuel (Guildford), 63*(9), 1324-1328.

Cai, Y., Liu, D., Mathews, J. P., Pan, Z., Elsworth, D., Yao, Y., Li, J., & Guo, X. (2014). Permeability evolution in fractured coal—combining triaxial confinement with X-ray computed tomography, acoustic emission and ultrasonic techniques. *International Journal of Coal Geology, 122*, 91-104.

Calvet, M., & Margerin, L. (2016). Impact of grain shape on seismic attenuation and phase velocity in cubic polycrystalline materials. *Wave Motion, 65*, 29-43.

David Suits, L., Sheahan, T. C., Basu, A., & Aydin, A. (2006). Evaluation of Ultrasonic Testing in Rock Material Characterization. *Geotechnical testing journal, 29*(2), 12652.

Ding, P., Di, B., Wang, D., Wei, J., & Li, X. (2014). P and S wave anisotropy in fractured media: Experimental research using synthetic samples. *Journal of Applied Geophysics, 109*, 1-6.

Esamaldeen, A., Wu, G., & Nuha, M. (2015). Assessments of Elastic Anisotropy of Banded Amphibolite as a Function of Cleavage Orientation Using S- and P-Wave Velocity. *Natsional'nyi Universytet Bioresursiv i Pryrodokorystuvannya Ukrainy. Naukovyi Visnyk. Seriya: Ahronomiya, 03*(05), 62-71.

Ferraz, E. S. B., & Mansell, R. S. (1979). Determining water content and bulk density of soil by gamma ray attenuation methods. *Technical Bulletin 807 IFAS. Institute of Food and Agricultural Sciences, University of Florida*, 51.

Gibbs, J. W. (1879). On the equilibrium of heterogeneous substances. 300-320.

Goodman, R. E. (1989). *Introduction to rock mechanics* (Vol. 2): John Wiley & Sons, New York.

Griffith, A. A. (1921). The phenomena of rupture and flow in solids. *Philosophical transactions of the royal society of london. Series A, 221*, 163-198.

Guo, D., Han, D., & Feng, Z. (1998). Experimental research on wave velocity of deformed coal characteristics under the ambient pressure. *Coal Science and Technology, 26*(4), 21-23.

Johansen, T., Drottning, A., Lecomte, I., & Gjoystdal, H. (2002). An approach to combined rock physics and seismic modelling of fluid substitution effects. *Geophysical Prospecting, 50*(2), 119-137.

Karacan, C. Ö. (2003). Heterogeneous Sorption and Swelling in a Confined and Stressed Coal during CO_2 Injection. *Energy & Fuels, 17*(6), 1595-1608.

Kearey, P., Brooks, M., & Hill, I. (2013). *An introduction to geophysical exploration*: John Wiley & Sons.

Kern, H., Liu, B., & Popp, T. (1997). Relationship between anisotropy of P and S wave velocities and anisotropy of attenuation in serpentinite and amphibolite. *Journal of Geophysical Research, 102*(B2), 3051-3065.

Liu, J., Liua, D., Cai, Y., Gan, Q., & Yao, Y. (2017). Effects of water saturation on P-wave propagation in fractured coals: An experimental perspective. *Journal of Applied Geophysics, 144*, 94–103.

Lo, T., Coyner, K., & Toksöz, M. N. (1986). Experimental determination of elastic anisotropy of Berea sandstone, Chicopee shale, and Chelmsford granite. *Geophysics, 51*(1), 164-171.

Matsushima, J., Suzuki, M., Kato, Y., & Rokugawa, S. (2016). Ultrasonic measurements of attenuation and velocity of compressional and shear waves in partially frozen unconsolidated sediment and synthetic porous rock. *Geophysics, 81*(2), D141-D153.

Morcote, A., Mavko, G., & Prasad, M. (2010). Dynamic elastic properties of coal. *Geophysics, 75*(6), E227-E234.

Pal, P. K., Paul, S., & Chatterjee, R. (2015). Estimation of in-situ stress and coal bed methane potential of coal seams from analysis of well logs, ground mapping and laboratory data in central part of Jharia coalfield—An overview *Petroleum Geosciences: Indian Contexts* (pp. 143-173): Springer.

Parra, J. O., Iturrarán-Viveros, U., Parra, J., & Xu, P.-C. (2015). Attenuation and velocity estimation using rock physics and neural network methods for calibrating reflection seismograms. *Interpretation: A Journal of Political Philosophy, 3*(1), SA121-SA133.

Perera, M. S. A., Ranjith, P. G., & Peter, M. (2011). Effects of saturation medium and pressure on strength parameters of Latrobe Valley brown coal: Carbon dioxide, water and nitrogen saturations. *Energy, 36*, 6941-6947.

Phogat, V. K., & Aylmore, L. A. G. (1989). Evaluation of soil structure by using computer-assisted tomography. *Australian Journal of Soil Research, 27*(2), 313.

Pires, L. F., Rosa, J. A., Pereira, A. B., Arthur, R. C. J., & Bacchi, O. O. S. (2009). Gamma-ray attenuation method as an efficient tool to investigate soil bulk density spatial variability. *Annals of Nuclear Energy, 36*(11-12), 1734-1739.

Ramandi, H. L., Mostaghimi, P., & Armstrong, R. T. (2017). Digital rock analysis for accurate prediction of fractured media permeability. *Journal of Hydrology, 554*, 817-826.

Ramandi, H. L., Mostaghimi, P., Armstrong, R. T., Saadatfar, M., & Pinczewski, W. V. (2016). Porosity and permeability characterization of coal: a micro-computed tomography study. *International Journal of Coal Geology, 154*, 57-68.

Ranathunga, A. S., Perera, M. S. A., & Ranjith, P. G. (2016a). Influence of CO_2 adsorption on the strength and elastic modulus of low rank Australian coal under confining pressure. *International Journal of Coal Geology, 167*, 148-156.

Ranathunga, A. S., Perera, M. S. A., Ranjith, P. G., & Bui, H. (2016b). Super-critical CO_2 saturation-induced mechanical property alterations in low rank coal: An experimental study. *The Journal of supercritical fluids, 109*, 134-140.

Sampath, K. H. S. M., Perera, M. S. A., Elsworth, D., Ranjith, P. G., Matthai, S. K., & Rathnaweera, T. (2018). Experimental Investigation on the Mechanical Behavior of Victorian Brown Coal under Brine Saturation. *Energy & Fuels, 32*(5), 5799-5811.

Sampath, K. H. S. M., Perera, M. S. A., Elsworth, D., Ranjith, P. G., Matthai, S. K., Rathnaweera, T., & Zhang, G. (2019). Effect of coal maturity on CO_2-based hydraulic fracturing process in coal seam gas reservoirs. *Fuel, 236*, 179-189.

Stan Kłeczek, I. (2016). The study of the elastic properties of carbonate rocks on a base of laboratory and field measurement. *Acta Montanistica Slovaca, 21*(1), 76.

Sun, X., Yao, Y., Liu, D., Elsworth, D., & Pan, Z. (2016). Interactions and exchange of CO_2 and H_2O in coals: an investigation by low-field NMR relaxation. *Scientific Reports, 6*(1), 19919.

Sun, X., Yao, Y., Liu, D., & Zhou, Y. (2018). Investigations of CO_2 -water wettability of coal: NMR relaxation method. *International Journal of Coal Geology, 188*, 38-50.

Ündül, Ö., Amann, F., Aysal, N., & Plötze, M. L. (2015). Micro-textural effects on crack initiation and crack propagation of andesitic rocks. *Engineering Geology, 193*, 267-275.

Viete, D. R., & Ranjith, P. G. (2006). The effect of CO_2 on the geomechanical and permeability behaviour of brown coal: Implications for coal seam CO_2 sequestration. *International Journal of Coal Geology, 66*, 204 – 216.

Vishnu, C. S., Mamtani, M., & Basu, A. (2010). AMS, ultrasonic P-wave velocity and rock strength analysis in quartzites devoid of mesoscopic foliations – implications for rock mechanics studies. *Tectonophysics (Amsterdam. Online), 494*(3-4), 191-200.

Wang, H., Pan, J., Wang, S., & Zhu, H. (2015). Relationship between macro-fracture density, P-wave velocity, and permeability of coal. *Journal of Applied Geophysics, 117*, 111-117.

Wang, Y., Xu, X., & Yang, D. (2014). Ultrasonic elastic characteristics of five kinds of metamorphic deformed coals under room temperature and pressure conditions. *Science China Earth Sciences, 57*(9), 2208-2216.

Wanniarachchi, W. A. M., Ranjith, P. G., Perera, M. S. A., Rathnaweera, T. D., Lyu, Q., & Mahanta, B. (2017). Assessment of dynamic material properties of intact rocks using seismic wave attenuation: an experimental study. *Royal Society Open Science, 4*(10), 170896.

Yan, L. (2006). Relationship study between characteristics and strength of coal and rock wave velocity in Yangzhuang Mine. *Coal Science and Technology, 34*(6), 57-60.

Yun, W., Xiao Kai, X. U., & Yu Gui, Z. (2016). Ultrasonic elastic characteristics of six kinds of metamorphic coals in china under room temperature and pressure conditions. *Chinese Journal of Geophysics, 59*(4), 350-363.

Zhang, Y., Lebedev, M., Sarmadivaleh, M., Barifcani, A., & Iglauer, S. (2016a). Swelling-induced changes in coal microstructure due to supercritical CO_2 injection. *Geophysical Research Letters, 43*(17), 9077-9083.

Zhang, Y., Sarmadivaleh, M., Barifcani, A., Lebedev, M., & Iglauer, S. (2016b). Coal microstructure changes due to water absorption and CO_2 injection. *The APPEA Journal, 56*(2), 593-593.

Zhao, Q., & Hao, S. (2006). Anisotropy test instance of ultrasonic velocity and attenuation of coal sample. *Prog. Geophys, 21*(2), 531-534.

Zheng, Z., Khodaverdian, M., & McLennan, J. (1991). *Static and dynamic testing of coal specimens.* Paper presented at the 1991 SCA Conference.

Zhou, F. (2012). Experiment of influence of fractures on coal/rock acoustic velocity: with Carboniferous seams of Qinshui basin as example. *Coal Geol. Explor, 40*(2), 71-74.

6.4 Chapter summary

The CO_2 interaction can cause severe mechanical degradation in coal, affecting the coal seam integrity and the safety of the CO_2 sequestration process. Even though there exist several experimental studies that investigate the mechanical alterations, the complexity of the material and coal-CO_2 interaction process triggers the necessity of conducting more focused and systematic experiments, targeting the definite coal type, specifically considering the supercritical-phase of CO_2. Chapter 6 provides a detailed experimental study of the mechanical alterations in CO_2-interacted coal, in the sense of static and dynamic mechanical properties.

In general, the current experimental study conducted with static mechanical testing concludes that the pore fluid condition or the fluid chemistry of the targeted reservoir has a substantial impact on the ultimate mechanical alterations in coal, and therefore the effect of the pore fluid+CO_2 interaction should be considered in-depth when planning the CO_2 injectivity into the seam. Further, the temporal behaviour of mechanical degradation shows a complex trend, in which the short term interaction causes a rapid strength reduction, while latter longer interaction causes a gradual but continuous strength alteration. The dynamic mechanical testing study concludes that the CO_2 interaction causes localized mechanical alterations in heterogeneous and anisotropic coal specimens and the localization depends on the spatial disposition of macerals, minerals, cleat system and the pore network. The temporal analysis shows a similar degradation trend as in the static mechanical testing study, confirming that CO_2 interaction time has a significant impact on all the mechanical parameters, irrespective of the testing method.

It should be noted that static mechanical testings were conducted under unconfined conditions, in order to compare with common lab-scale experimental results. Also, there were no experimental facilities available to test the dynamic mechanical testings under confined condition, because the transducers could not be connected to the sample directly, while the confining pressure was applied on the sample. However, the sample behaviour can be different when the CO_2 interactions are occurred under confined condition due to different swelling mechanisms. For instance, the existing fracture network can be closed due to CO_2 adsorption-induced matrix-swelling under confined condition (as explained in chapter 5), rather than developing more micro-cracks due to free-swelling. Therefore, it is recommended to conduct more experimental studies to evaluate the effect of confining pressure as well. Overall, the experimental studies confirm the complex nature of the CO_2-induced mechanical property alterations, where the observed results are largely dependent on the tested coal rank and the testing conditions. The science and the conclusions gathered from the experimental observations can be utilized in developing numerical models. Comprehensive numerical analyses, supported with pertinent theories and validated with experimental results are vital in understanding the underlying multi-physics, and to precisely simulate the mechanical alterations in general – which is the motivation of the next chapter.

CHAPTER 7

Numerical analysis of free and adsorbed CO_2-induced mechanical property alterations in coal

7 Numerical analysis of free and adsorbed CO_2-induced mechanical property alterations in coal

7.1 Chapter overview and structure

The experimental analyses are important to accurately evaluate the CO_2 interaction-induced mechanical property alterations and various trends in coal under specific reservoir conditions. The results and the conclusions obtained from experimental studies are useful in postulating and validating underlying theories – that can be further used for modelling studies. Essentially, the numerical models that consider the underlying multi-physics of the complex processes and validated with experimental results are imperative to analyse the general mechanical alterations in CO_2-interacted coal. Therefore, this chapter presents a numerical study carried out to investigate the free and the adsorbed CO_2-induced mechanical property alterations in coal – both under confined and unconfined conditions.

In fact, among multiple factors that influence the coal mechanical degradation upon CO_2 injection, the interaction of CO_2 as free gas and adsorbed gas phases plays a significant role. The coal compressive strength is one of the critical parameters, widely utilized by scholars to interpret the mechanical competency of coal. Hence, this particular study aims to develop a numerical model to assess the effects of both free and adsorbed CO_2 on the alterations of coal compressive strength. The modelling procedure consists of two phases, i.e. 1) CO_2 saturation phase and, 2) mechanical loading phase – that represents an entire lab-scale strength measurement test of a CO_2-interacted coal specimen. The compressive strength alteration was modelled using the Mohr-Coulomb failure criterion, where the adjusted failure envelope of CO_2-saturated coal was defined by a theoretically-extended cohesion model, integrated with effective stress and the adsorption-induced surface energy change. The model was validated with experimental data under both confined and unconfined conditions, and finally, a sensitivity analysis was conducted to assess the strength sensitivity on various influential modelling parameters, such as Biot's coefficient and Langmuir constants. The chapter comprehensively describes the entire study, including introduction, theoretical approach, model validation and the sensitivity analysis, which is presented as a peer-reviewed journal paper.

7.2 Journal paper: Free and adsorbed CO_2-induced mechanical alterations in coal

This section is presented as the author-accepted manuscript of a peer-reviewed article published in "The International Journal of Coal Geology". The journal is a Q1 journal with impact factor of 5.33.

Citation:

- Perera M. S. A., Sampath K. H. S. M., (2019). *Modelling of free and adsorbed CO_2-induced mechanical property alterations in coal*. International Journal of Coal Geology, 217, 103348.

Journal paper title: Modelling of free and adsorbed CO_2-induced mechanical property alterations in coal

Authors' names: *M.S.A. Perera[1,2], K.H.S.M. Sampath[1]

[1]Department of Infrastructure Engineering, Engineering Block B, Grattan Street, Parkville, The University of Melbourne, Victoria 3010, Australia.

[2]Department of Civil Engineering, Monash University, Clayton Campus, Victoria 3800, Australia.

Abstract

CO_2 interaction-induced mechanical alteration in coal is imperative in the context of CO_2 geo-sequestration, as it governs the project safety, in general. Accurate estimations of mechanical characteristics are thus essential prior to the implementation of field projects. Through this study, we numerically model the alterations in coal compressive strength, caused by CO_2 interaction. The combined effect of both free and adsorbed CO_2 on coal strength is evaluated based on the Mohr-Coulomb failure criterion, in which a modified-cohesion model is derived to define the adjusted-failure envelope, by integrating the CO_2 adsorption-induced surface energy change. The model is initially validated with two experimental studies conducted under confined- and unconfined-stress conditions. The validation results confirm that the model is capable of successfully simulating the effect of confining stress, and the effect of free and adsorbed CO_2 on the alterations of coal compressive strength. The calibrated model is used to estimate the strength alterations at relatively large confining stresses (i.e. $P_b \approx 25\, MPa$) and at incremental pore pressures (i.e. $0.1\, MPa < P_{CO_2} < 24\, MPa$), in which a sensitivity analysis is carried out to evaluate the model's sensitivity on different influential parameters. The results show that coal compressive strength decreases substantially with CO_2 pore pressure and starts to slightly increase beyond a certain pore pressure (i.e. $P_{CO_2} > 12\, MPa$) due to the matrix-compression, caused by the elevated pore pressure, and the developed modified-cohesion model is capable of capturing this behaviour. The model is highly-sensitive to the Biot's coefficient, as it defines the fraction of

pore pressure that contributes to the effective stress, and ultimately to both free and adsorbed CO_2-induced strength alteration. The sensitivity analysis highlights the significance of the Langmuir constants, as they play a critical role in modelling the fully-coupled process; thus, should be precisely determined for a given coal type, in order to accurately simulate the overall strength alterations.

Keywords: *coal seam, free and adsorbed CO_2, mechanical alterations*

7.2.1 Introduction

The increase in anthropogenic greenhouse gas concentration in the atmosphere significantly contributes to global warming, compelling the researchers to find solutions on alleviating the issue. The CO_2 geo-sequestration in deep un-minable coal seams has gained increasing attention due to its economic viability, and importantly due to the coupled-process with enhanced coalbed methane (ECBM) extraction. However, the successful implementation of sequestration projects has been greatly barriered by the unforeseeable behaviour of coal seams, caused by the CO_2 interaction-induced hydro-mechanical alterations. For instance, the CO_2 adsorption-induced coal swelling causes a notable mechanical degradation, rendering the sequestration efforts ineffective and risky (Vandamme et al., 2010; White et al., 2005).

Previous efforts on characterising the coal mechanical parameters have identified a number of factors that can possibly cause the CO_2 interaction-induced coal mechanical alterations (Ates and Barron, 1988; Perera et al., 2011; Perera et al., 2013; Sampath et al., 2019a; Sampath et al., 2019b). These include: 1) the increase in pore pressure due to free gas phase, causing a reduced-effective stress (Van Eeckhout, 1976), 2) the CO_2 adsorption-induced surface energy reduction, which is known as the 'Rehbinder effect', that can cause easy propagation and extension of cracks (da C Andrade et al., 1950), 3) the CO_2 adsorption-induced plasticization of coal structure, that transforms the coal structure from a glassy material to a rubbery material (Larsen, 2004), 4) shrinkage-, free and differential swelling-induced micro-cracking in the coal structure (Karacan, 2003; Sampath et al., 2019c), 5) swelling-induced volume expansion and the consequent reduction in cohesion and particle bonding strength (Lu et al., 2019), 6) formation of a gas membrane on the fracture surfaces by the adsorbed CO_2, which has a lubricating effect reducing the frictional resistance (Lu et al., 2019), and 7) dissolution of pore-filling minerals affecting the grain-to-grain contact, due to carbonic acids formed by the dissolved CO_2 in the formation water (Guo et al., 2018).

It is apparent that the CO_2 interaction-induced coal strength alteration is a highly-complex process that depends on numerous parameters, including coal rank and composition, heterogeneity and anisotropy, stress environment, temperature, interaction time, pore fluid chemistry, etc. Several experimental studies have been carried out to evaluate the effect of each parameter on the alterations of coal mechanical properties, often in terms of its compressive strength, under uni-axial and tri-axial conditions. For instance, Masoudian et al. (2014) studied the effect of confining pressure and CO_2 pore pressure, Perera et al. (2013) investigated the effect of CO_2 phase change from subcritical to supercritical, Sampath et al. (2019a) studied the effect of heterogeneity caused by the spatial distribution of minerals and macerals on the localized damage of coal structure, and Ranathunga et al. (2016) evaluated the effect of CO_2 interaction time on the mechanical degradation. However, due to complex heterogeneity and sensitivity of coal, the obtained results are highly-specific to the tested coal type and the adopted experimental conditions that question the applicability of the results in general. Analytical and numerical approaches that couple the complex underlying physics are thus essential to accurately capture and predict the CO_2-induced mechanical degradation in coal.

In this study, we develop a numerical model to simulate the CO_2 interaction-induced mechanical alterations in coal. The complete process is coupled through the mechanical property models including cohesion, Young's modulus and the compressive strength. Both effects from free and adsorbed CO_2 are considered on the mechanical alterations, in which the theoretical approach based on the Mohr-Coulomb failure criterion is extended to model the compressive strength alterations, under uni-axial and tri-axial conditions. The model is validated with two published experimental studies to confirm the model's reliability on simulating the strength alterations under uni-axial and tri-axial loading conditions, and finally, a sensitivity analysis is conducted using the validated model.

7.2.2 The theoretical approach of modelling the coal strength alterations

The governing equations used for mechanical alteration modelling is explained in this section. This includes the theory for coal deformation, pore pressure development, CO_2 adsorption-induced surface energy change, cohesion and Young's modulus evolution and the Mohr-Coulomb failure criterion-based compressive strength alteration. The derivations are based on the following assumptions: 1) coal is an isotropic and homogeneous continuum, 2) gas contained in coal is ideal, and 3) the system is isothermal.

7.2.2.1 Governing equation for coal deformation

The strain-displacement relationship for an elastic, isotropic and homogeneous medium is given as,

$$\varepsilon_{ij} = \frac{1}{2}(u_{i,j} + u_{j,i}) \qquad \text{………… [7-1]}$$

where, ε_{ij} and u_i are the components of the total-strain tensor and the displacement, respectively.

The stress equilibrium equation is defined as,

$$\sigma_{ij,j} + f_i = 0 \qquad \ldots\ldots\ldots\ldots [7\text{-}2]$$

where, σ_{ij} and f_i are the components of the total-stress tensor and the body force, respectively.

Free and adsorbed gas cause a substantial deformation in coal, which is expressed by a Navier-type equation for linear poro-elastic medium, that includes adsorption-induced strain (ε_s) and gas pore pressure (p) as additional body forces. The ε_s is considered analogously to thermal expansion in porous media and is assumed to cause isotropic normal-strains only (Palmer and Mansoori, 1996). Thus, the constitutive equation for deformed-coal is given as,

$$\varepsilon_{ij} = \frac{1}{2G}\sigma_{ij} - \left(\frac{1}{6G} - \frac{1}{9K}\right)\sigma_{kk}\delta_{ij} + \frac{\alpha}{3K}p\delta_{ij} + \frac{\varepsilon_s}{3}\delta_{ij} \qquad \ldots\ldots\ldots\ldots [7\text{-}3]$$

where, G is the shear modulus, K is the bulk modulus, and α is the Biot's coefficient, as given in Eqs. 7-4, 7-5 and 7-6, respectively. δ_{ij} is the Kronecker delta and $\sigma_{kk} = \sigma_{11} + \sigma_{22} + \sigma_{33}$.

$$G = \frac{E}{2(1+\upsilon)} \qquad \ldots\ldots\ldots\ldots [7\text{-}4]$$

$$K = \frac{E}{3(1-2\upsilon)} \qquad \ldots\ldots\ldots\ldots [7\text{-}5]$$

$$\alpha = 1 - \frac{K}{K_s} \qquad \ldots\ldots\ldots\ldots [7\text{-}6]$$

where, E is the Young's modulus, υ is the Poisson's ratio and K_s is the bulk modulus of coal grains.

The adsorption-induced strain (ε_s) is modelled with a Langmuir-type equation (Harpalani and Mitra, 2010), and is given as,

$$\varepsilon_s = \frac{\varepsilon_L p}{p + P_L} \qquad \ldots\ldots\ldots\ldots [7\text{-}7]$$

where, ε_L is the Langmuir volumetric strain constant and P_L is the Langmuir pressure constant.

Combination of Eqs. 7-1 to 7-3 yields the Navier-type equation, expressed as,

$$Gu_{i,kk} + \frac{G}{1-2\upsilon}u_{k,ki} - \alpha p_{,i} - K\varepsilon_{s,i} + f_i = 0 \qquad \ldots\ldots\ldots\ldots [7\text{-}8]$$

Eq. 7-8 defines the governing equation for coal deformation, which accounts for the CO_2 adsorption-induced deformation and the CO_2 pore pressure.

7.2.2.2 Governing equation for CO_2 pore pressure development in coal

Injection of CO_2 causes the development of CO_2 pore pressure in coal, resulting in the mechanical property alterations due to the combined effect of free and adsorbed CO_2. The balance equation for gas transport and pressure development in coal is established based on the principle of mass conservation.

$$\frac{\partial m}{\partial t} + \nabla.(\rho_g \vec{v}) = Q_s \qquad \text{........... [7-9]}$$

where, m is the total gas content, ρ_g is the gas density, $\vec{v}$ is the Darcy velocity vector and Q_s is the gas source or sink.

The total gas content that includes free gas phase (m_f) and adsorbed gas phase (m_{ad}) can be expressed as:

$$m = \frac{M_g}{RT}\left[\phi + (1-\phi)P_a\rho_c\frac{V_L}{p+P_L}\right]p \qquad \text{........... [7-10]}$$

where, M_g is the molar mass of gas, T is the temperature, R is the universal gas constant, ϕ is the coal porosity, P_a is the atmospheric pressure, ρ_c is the density of coal and V_L is the Langmuir sorption constant.

Assuming that the effect of gravity is negligible, the Darcy velocity vector is defined as,

$$\vec{v} = -\frac{k}{\mu}\nabla p \qquad \text{........... [7-11]}$$

where, k is the coal permeability, and μ is the dynamic viscosity of the gas.

By adding Eqs. 7-10 and 7-11 into Eq. 7-9, the governing equation for CO_2 pore pressure development in coal can be derived and simplified as,

$$\left[\phi + (1-\phi)P_a\rho_c\frac{V_L P_L}{(p+P_L)^2}\right]\frac{\partial p}{\partial t} + \left(p - P_a\rho_c\frac{V_L p}{p+P_L}\right)\frac{\partial \emptyset}{\partial t} - \nabla\left(\frac{k}{\mu}p\nabla p\right) = Q_s \qquad \text{........... [7-12]}$$

In Eq. 7-12, the k and ϕ are considered as functions of CO_2 adsorption-induced strain and are dependent on the gas pore pressure. The current study considers general porosity and permeability models that account for variable stress conditions (Zhang et al., 2008) and the relationship between the porosity and the permeability is defined by a cubic law (Chilingar, 1964). The detailed derivation is given elsewhere (Zhang et al., 2008). Hence, the general porosity and permeability models that are incorporated in the current study are given by Eqs. 7-13 and 7-14, respectively.

$$\phi = \phi_0\left\{1 + \frac{\alpha}{\phi_0}\left[\varepsilon_V + \frac{p-P_0}{K_s} - \frac{\varepsilon_L P_L(p-P_0)}{(P_0+P_L)(p+P_L)}\right]\right\} \qquad \text{........... [7-13]}$$

$$\frac{k}{k_0} = \left(\frac{\phi}{\phi_0}\right)^3 = \left\{1 + \frac{\alpha}{\phi_0}\left[\varepsilon_V + \frac{p-P_0}{K_s} - \frac{\varepsilon_L P_L (p-P_0)}{(P_0+P_L)(p+P_L)}\right]\right\}^3 \qquad \text{………… [7-14]}$$

where, ϕ_0 and k_0 are the initial porosity and permeability of coal, respectively, ε_V is the total matrix volumetric strain and P_0 is the initial pore pressure.

Eq. 7-12 defines the CO_2 pore pressure development in coal that causes the coal deformation and modifies the strength parameters. This process is coupled through the free and adsorbed gas-induced mechanical property alterations, as explained in the following section.

7.2.2.3 Theory of modelling the free and adsorbed CO_2 -induced mechanical property alterations

The current study evaluates the coal mechanical property alterations through the Young's modulus, cohesion and the coal strength. The coal strength is characterised in terms of compressive strength and is modelled incorporating the Mohr-Coulomb model as the failure criterion, due to its concise and practical characteristics (Lu et al., 2017). The model includes the hydrostatic pore pressure in the failure criterion, which is essential for modelling the CO_2 interaction-induced strength alterations. In general, the Mohr-Coulomb failure criterion states that the failure occurs, when the effective normal stress and the shear stress acting on a material satisfy the following condition (Handin, 1969);

$$\tau = C_u + \sigma' tan\varphi \qquad \text{………… [7-15]}$$

where, τ is the shear stress, σ' is the effective normal stress, C_u and φ denote the cohesion and the angle of internal friction, respectively.

In terms of Mohr's circle representation, this criterion can be expressed as,

$$\sigma'_1 = \frac{1+sin\varphi}{1-sin\varphi}\sigma'_3 + 2C_u\sqrt{\frac{1+sin\varphi}{1-sin\varphi}} \qquad \text{………… [7-16]}$$

Moreover, the criterion may be re-formed in terms of the invariants I_1 and J_2 and the lode angle $0 \le \theta \le \pi/3$, in which the effective principal stresses are sorted as $\sigma'_1 \ge \sigma'_2 \ge \sigma'_3$. Then, the yield function may be expressed as,

$$F_y = \sqrt{J_2}m(\theta) + \alpha' I_1 - k' = 0 \qquad \text{………… [7-17]}$$

where,

$$m(\theta) = \cos\left(\theta - \frac{\pi}{6}\right) - \sqrt{\frac{1}{3}} sin\varphi . sin\left(\theta - \frac{\pi}{6}\right) \qquad \text{………… [7-18]}$$

and, $\alpha' = \sin\left(\frac{\varphi}{3}\right)$ and $k' = C_u cos\varphi$.

The effect of CO_2 interaction on coal compressive strength mainly includes two aspects: 1) the effect of the free gas phase, and 2) the effect of the adsorbed gas phase (Lu et al., 2019). The effective stress change due to the effect of free gas can be determined according to the Biot's effective law (Biot, 1941);

$$\sigma' = \sigma - \alpha p \quad \text{........... [7-19]}$$

where, σ is the total normal stress.

Combining Eqs. 7-16 and 7-19, the failure criterion for CO_2-interacted coal, considering only the effect of free gas can be expressed as,

$$\begin{cases} \left[\sigma' - \frac{(\sigma_1+\sigma_3-2\alpha p)}{2}\right]^2 + \tau^2 = \left[\frac{(\sigma_1-\sigma_3)}{2}\right]^2 \\ \tau = C_u + \sigma' tan\varphi \end{cases} \quad \text{........... [7-20]}$$

In addition, the free and adsorbed CO_2 cause the volume of coal to be relaxed and expanded (Sampath et al., 2018; Zhang et al., 2016), resulting in a change in the cohesion of the coal mass, altering the compressive strength. In order to model this behaviour, the following conditions for a CO_2 saturation experiment, conducted under a typical tri-axial configuration are assumed: confining stress $(\sigma_3) = P_b$, initial pore pressure (i.e. corresponds to natural sample) is P_o, pore pressure after CO_2 injection is P_{CO_2}. Hence, the effective minor principal stresses (σ'_3) for natural and CO_2-interacted samples under the same confining stress of P_b are given by Eqs. 7-21 and 7-22, respectively;

$$\sigma'_{3_0} = P_b - \alpha P_o \quad \text{........... [7-21]}$$

$$\sigma'_{3_{CO_2}} = P_b - \alpha P_{CO_2} \quad \text{........... [7-22]}$$

Let us denote the compressive strength of natural and CO_2-interacted coal (at P_{CO_2} pore pressure) as σ'_{c_0} and $\sigma'_{c_{CO_2}}$, respectively, and the cohesion of natural and CO_2-interacted coal as C_{u_0} and $C_{u_{CO_2}}$, respectively. Also, the change in friction angle due to CO_2 interaction is assumed to be negligible (Hu et al., 2016; Xueqiu et al., 1996).

Hence, by combining Eqs. 7-16, 7-21 and 7-22, the Mohr-Coulomb failure criterion for natural and CO_2-interacted coal can be expressed in terms of Mohr's circle parameters as,

$$\sigma'_{c_0} = \psi(P_b - \alpha P_o) + 2C_{u_0}\sqrt{\psi} \quad \text{........... [7-23]}$$

$$\sigma'_{c_{CO_2}} = \psi(P_b - \alpha P_{CO_2}) + 2C_{u_{CO_2}}\sqrt{\psi} \quad \text{........... [7-24]}$$

where, $\psi = \frac{1+sin\varphi}{1-sin\varphi}$.

From material properties, it is found that the compressive strength of coal is proportional to its Young's modulus and surface energy (Fairhurst, 1973; Roy and Gouda, 1973);

$$\sigma'_c \propto (E.\gamma)^{1/2} \quad \text{........... [7-25]}$$

where, γ is the surface energy.

By combining Eqs. 7-23 to 7-25, the ratio of the compressive strength of natural and CO_2-interacted coal can be expressed as,

$$\frac{\sigma'_{cCO_2}}{\sigma'_{c_0}} = \frac{\psi(P_b-\alpha P_{CO_2})+2C_{u_{CO_2}}\sqrt{\psi}}{\psi(P_b-\alpha P_o)+2C_{u_0}\sqrt{\psi}} = \sqrt{\frac{E_{CO_2}\gamma_{CO_2}}{E_0\gamma_0}} \quad \text{........... [7-26]}$$

where, E_0 and E_{CO_2} are the Young's moduli of natural and CO_2-interacted coal, respectively, and γ_0 and $\gamma_{CO_2}(= \gamma_0 - \Delta\gamma)$ are the surface energy of natural and CO_2-interacted coal, and $\Delta\gamma$ is the change of surface energy due to CO_2 adsorption.

By simplifying Eq. 7-26, the solution for the cohesion of the CO_2-interacted coal can be expressed as;

$$C_{u_{CO_2}} = \beta C_{u_0} + 0.5\sqrt{\psi}\left[\beta(P_b - \alpha P_o) - (P_b - \alpha P_{CO_2})\right] \quad \text{........... [7-27]}$$

where,

$$\beta = \sqrt{\frac{E_{CO_2}\gamma_{CO_2}}{E_0\gamma_0}} = \sqrt{\frac{E_{CO_2}}{E_0}\left(1 - \frac{\Delta\gamma}{\gamma_0}\right)} \quad \text{........... [7-28]}$$

Eq. 7-27 defines the modified-cohesion model for CO_2-interacted coal that accounts for the effects of both free and adsorbed CO_2, under confined-stress condition. In Eq. 7-27, the first term in RHS is due to initial cohesion of coal and the second term yields from the effect of the confining stress and pore pressure. It is apparent that the change in the cohesion of coal with the CO_2 interaction is a function of the surface energy change ($\Delta\gamma$). The surface energy of coal can be diminished due to the replacement of an existing adsorbate with a more reactive adsorbate or an uncompensated increment of the concentration of an existing adsorbate (Ates and Barron, 1988; Sampath et al., 2019b; Viete and Ranjith, 2006). In accordance with the theory of surface physico-chemistry, decrease in surface energy of a solid results in a reduction of its strength (Gibbs, 1879; Griffith, 1921). The decrease in the coal surface energy can be given as,

$$-d_\gamma = RT\Gamma d(lnp) \quad \text{........... [7-29]}$$

where, d_γ is the surface free energy increment and Γ is the constant of an irreversible reaction process.

Thus, the change in the solid surface energy due to CO_2 adsorption is expressed as (Boyd and Livingston, 1942),

$$\Delta\gamma = \frac{RT}{S_E V_M}\int_0^{P_{CO_2}} \frac{V_{ad}}{p}\, dp \qquad \text{........... [7-30]}$$

where, V_M is the molar volume of gas, S_E is the coal surface area and V_{ad} is the adsorbed gas volume, which can be expressed according to a Langmuir-type equation as,

$$V_{ad} = (1-\phi)\frac{V_L p}{p+P_L} \qquad \text{........... [7-31]}$$

By combining Eqs. 7-30 and 7-31, the change in the coal surface energy due to CO_2 adsorption can be expressed as,

$$\Delta\gamma = \frac{RT}{S_E V_M}\int_0^{P_{CO_2}} (1-\phi)\frac{V_L}{p+P_L}\, dp \qquad \text{........... [7-32]}$$

It should be noted that the porosity ϕ is a function of pore pressure and acts as a variable in the integral, according to the porosity evolution model defined in section 7.2.2.2. By combining Eqs. 7-28 and 7-32, the parameter β may be expressed as,

$$\beta = \sqrt{\frac{E_{CO_2}}{E_0}\left(1 - \frac{RT}{\gamma_0 S_E V_M}\int_0^{P_{CO_2}} (1-\phi)\frac{V_L}{p+p_L}\, dp\right)} \qquad \text{........... [7-33]}$$

Hence, by considering the effects of both free gas phase and adsorbed gas phase, the failure criterion for CO_2-interacted coal can be expressed as,

$$\begin{cases} \left[\sigma' - \frac{(\sigma_1+\sigma_3-2\alpha P_{CO_2})}{2}\right]^2 + \tau^2 = \left[\frac{(\sigma_1-\sigma_3)}{2}\right]^2 \\ \tau = \beta C_{u_0} + 0.5\sqrt{\psi}\,\left[\beta(P_b-\alpha P_o) - (P_b - \alpha P_{CO_2})\right] + \sigma' tan\varphi \end{cases} \qquad \text{........... [7-34]}$$

The complete expression of the modified-cohesion model for CO_2-interacted coal may be expressed as,

$$C_{u_{CO_2}} = C_{u_0}\sqrt{\frac{E_{CO_2}}{E_0}\left(1 - \frac{RT}{\gamma_0 S_E V_M}\int_0^{P_{CO_2}} (1-\phi)\frac{V_L}{p+P_L}\, dp\right)} + 0.5\sqrt{\frac{1+sin\varphi}{1-sin\varphi}}\left[(P_b-\alpha P_o)\sqrt{\frac{E_{CO_2}}{E_0}\left(1 - \frac{RT}{\gamma_0 S_E V_M}\int_0^{P_{CO_2}} (1-\phi)\frac{V_L}{p+P_L}\, dp\right)} - (P_b - \alpha P_{CO_2})\right]$$

.... [7-35]

According to the modified strength modelling criterion, the free gas phase predominantly affects the effective stress of coal, in which the abscissa of the centre of effective stress Mohr's circle reduces with the increasing gas pore pressure, that causes the stress circle to move towards the Mohr-Coulomb failure envelope. Concurrently, the free and adsorbed gas phases increase with the CO_2 pore pressure and alter the coal internal-structure, reducing the cohesion parameter, that causes the Mohr-Coulomb failure envelope to move towards the effective stress circle. Both effects simultaneously contribute to the CO_2 interaction-induced coal compressive strength alteration. A detailed diagram depicting both phenomena is illustrated in Figure 7-1.

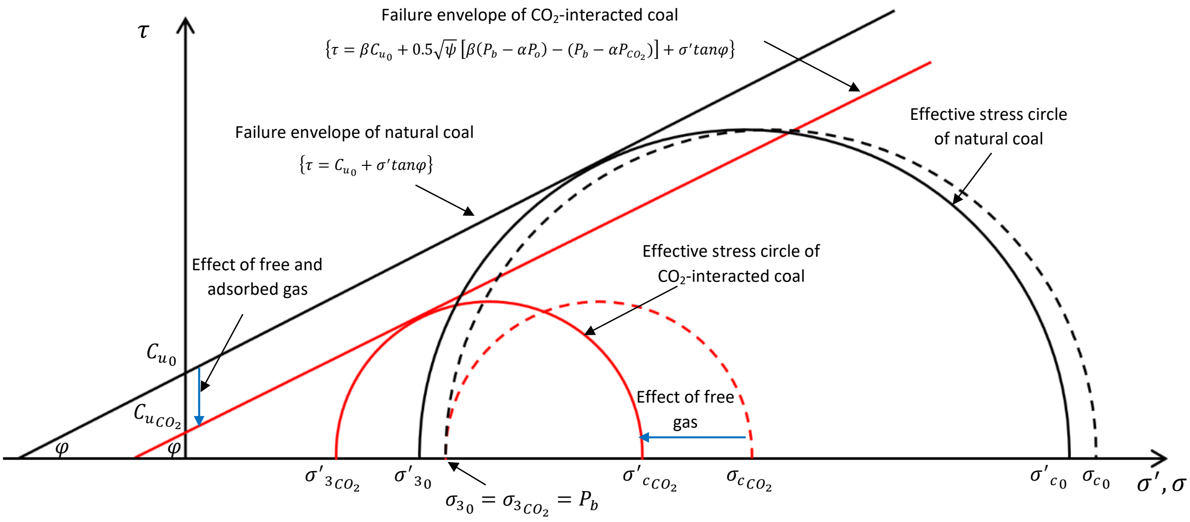

Figure 7-1 – Effect of free and adsorbed gas phases on the alteration of compressive strength of CO_2-interacted coal based on the Mohr-Coulomb failure criterion.

Apart from the compressive strength alteration, when CO_2 is adsorbed on to coal, it alters the coal bond structure and reduces the coal stiffness significantly (Kuvaev and Panchenko, 1975; Perera et al., 2011), affecting the coal Young's modulus. According to experimental observations, the alteration in Young's modulus typically shows a Langmuir-type variation with CO_2 interaction pressure (Masoudian et al., 2014; Ranathunga et al., 2016). Hence, the change in the Young's modulus is expressed as,

$$\Delta E = \frac{E_L \cdot p}{p + P_E} \qquad \text{........... [7-36]}$$

where, ΔE is the change in the Young's modulus after CO_2 interaction, E_L and P_E are the Langmuir fitting parameters.

The Young's modulus of CO_2-interacted coal can be expressed as,

$$E_{CO_2} = E_0 - \Delta E = E_0 - \frac{E_L \cdot p}{p + P_E} \qquad \text{........... [7-37]}$$

The Langmuir fitting parameters can be found from experimental data for a given coal type and given experimental conditions and can be incorporated to accurately model the CO_2 interaction-induced coal strength variation.

7.2.3 Simulation procedure to model the mechanical property alterations

The complete simulation procedure consists of two simulation phases *(see Figure 7-2)*. As the first simulation phase, a geometric model representing the lab-scale test is developed, and the initial and boundary conditions are applied considering the experimental configuration. A defined CO_2 injection pressure is then applied as a Dirichlet boundary condition (P_{CO_2}) and allows to develop the pore pressure through the sample. The time-dependent simulation is run until the model reaches its pressure and swelling equilibriums. During this process, the CO_2 pore pressure development, adsorption and the consequent swelling are modelled. The adsorbed amount of CO_2 and the swelling strains are dependent on the CO_2 pore pressure, that is equivalent to the CO_2 injection pressure at the final equilibrium. The change in the effective stresses, surface energy, and the mechanical parameters, including cohesion and the Young's modulus at the pressure equilibrium are determined simultaneously, during this simulation phase. The modified parameters of the equilibrated model are then transferred to the second simulation phase to determine the compressive strength at failure, according to Mohr-Coulomb failure criterion. In the second simulation phase, a prescribed vertical displacement is applied on the top boundary at a constant displacement rate to simulate the axial loading, without changing the other boundary conditions. In order to determine the axial loading stress caused by the prescribed top displacement, the z component of the reaction force over the top surface is integrated with;

$$F_{res} = \int \sigma_z 2\pi r \, dr \qquad \text{………… [7-38]}$$

where, F_{res} is the total reaction force and $2\pi r$ is the factor calculated from the integration in cylindrical coordinates.

Hence, the axial loading stress due to prescribed displacement is calculated as,

$$\sigma_a = \frac{F_{res}}{\pi {R_0}^2} \qquad \text{………… [7-39]}$$

where, σ_a is the axial stress and R_0 is the sample radius.

The axial stress at the failure is determined from the stress-strain curves, based on the Mohr-Coulomb failure criterion, in which the modified model parameters, effective stresses and the failure envelop combinedly result in various compressive strength values, depending on the initial CO_2 injection pressure *(see Figure 7-1)*.

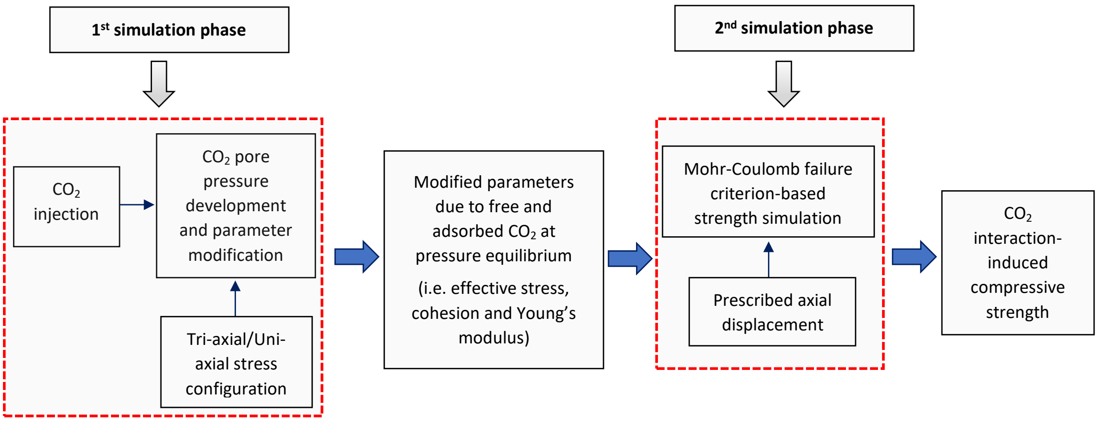

Figure 7-2 – Complete simulation procedure to model the mechanical property alterations.

7.2.4 Validation of the model with experimental results

Initially, the model is validated with the strength results from laboratory experiments obtained under confined- and unconfined-stress conditions.

7.2.4.1 Compressive strength under confined-stress condition

7.2.4.1.1 Model description and geometry

The experimental data extracted from Masoudian et al. (2014) are used to validate the compressive strength results of CO_2-interacted coal core samples (25 mm diameter × 50 mm height), under tri-axial stress condition. A 2D-axi-symmetric geometric model is considered assuming a homogeneous coal mass, as illustrated in Figure 7-3. The coal properties and modelling parameters obtained from experimental data and supplementary sources (Kang et al., 2019; Masoudian et al., 2014; Mazumder et al., 2008; Robertson and Christiansen, 2005) are given in Table 7-1. The fully-couped numerical model is designed to simulate the actual laboratory experimental procedure, as explained in the particular study. In fact, in the tri-axial stress conditions, the bottom boundary is constrained at all directions, the confining stress (P_b) is applied on side and top boundaries and initial stress (σ_0), displacement (u_0) and pressure (P_0) are set in the domain *(see Figure 7-3)*. The simulations are conducted, as explained in section 7.2.3.

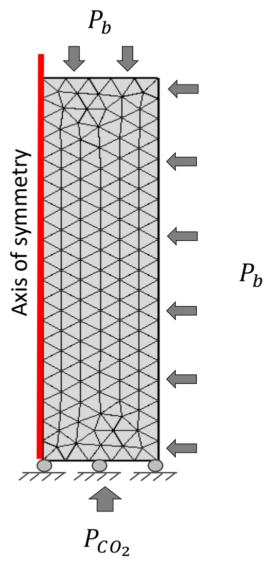

Figure 7-3 – Geometry and the boundary conditions for the confined-stress condition.

Table 7-1 – Parameters used for validation of the model under confined-stress condition.

Parameter	Value
Coal density ($\boldsymbol{\rho_c}$) ($\boldsymbol{kg/m^3}$)	1331
Initial porosity ($\boldsymbol{\phi_0}$)	0.1491
Initial permeability ($\boldsymbol{k_0}$) ($\boldsymbol{mD}$)	0.001
Poisson's ratio ($\boldsymbol{\upsilon}$)	0.226
Surface area of coal per unit mass ($\boldsymbol{S_E}$) ($\boldsymbol{m^2/g}$)	230.7
Surface energy of natural coal ($\boldsymbol{\gamma_0}$) ($\boldsymbol{mJ/m^2}$)	25
Cohesion of natural coal ($\boldsymbol{C_{u_0}}$) ($\boldsymbol{MPa}$)	6.549
Friction angle ($\boldsymbol{\varphi}$) (°)	45.46
Langmuir sorption constant ($\boldsymbol{V_L}$) ($\boldsymbol{m^3/kg}$)	0.05
Langmuir pressure constant ($\boldsymbol{P_L}$) ($\boldsymbol{MPa}$)	4.44
Langmuir volumetric strain constant ($\boldsymbol{\varepsilon_L}$)	0.023
Langmuir constant for Young's modulus ($\boldsymbol{E_L}$) ($\boldsymbol{GPa}$)	0.65
Langmuir pressure constant for Young's modulus ($\boldsymbol{P_E}$) ($\boldsymbol{MPa}$)	1.519
Biot's coefficient ($\boldsymbol{\alpha}$)	0.6
Temperature ($\boldsymbol{T}$) (°$\boldsymbol{C}$)	22
Molar mass of CO_2 ($\boldsymbol{M_g}$) ($\boldsymbol{g/mol}$)	44.01
Molar volume of CO_2 ($\boldsymbol{V_M}$) ($\boldsymbol{l/mol}$)	22.4
Dynamic viscosity ($\boldsymbol{\mu}$) ($\boldsymbol{Pa.s}$)	1.84×10^{-5}
Initial pore pressure ($\boldsymbol{P_0}$) ($\boldsymbol{MPa}$)	0.01
Atmospheric pressure ($\boldsymbol{P_a}$) (k$\boldsymbol{Pa}$)	101.325
Universal gas constant ($\boldsymbol{R}$) ($\boldsymbol{J/mol.K}$)	8.314

7.2.4.1.2 Modelling results

Initially, the model is calibrated to simulate the strength variation of natural coal with the confining pressure, in which the values of friction angle and the cohesion of the natural coal are defined according to given experimental data. Figure 7-4 depicts the variation of experimental and modelled results of maximum compressive strength of natural coal with the confining pressure. It is apparent that the compressive strength increases with the increasing confining pressure due to restrained lateral movement that makes the material stronger and hard to fail (Gentzis et al., 2007). As illustrated in Figure 7-4, the model results show a good fit with the experimental data, that confirms the model's capability of simulating the variation of natural coal strength with the confining pressure.

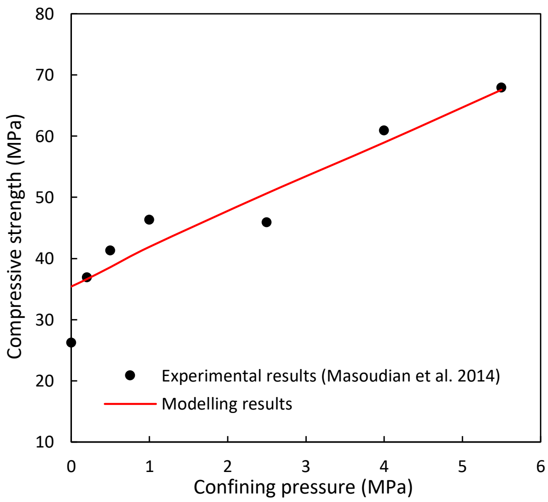

Figure 7-4 – Variation of natural coal strength with confining pressure (fitted with the data from Masoudian et al. (2014)).

In the next phase, the strength variation of coal after CO_2 interaction at different injection and confining pressures is modelled and fitted with the experimental data. According to the experimental description, the CO_2 injection pressure was maintained approximately similar to the confining pressure (i.e. $P_{CO_2} \approx P_b$), which is exactly simulated in the numerical model. Figure 7-5 illustrates the temporal and spatial distribution of CO_2 pore pressure and the consequent swelling deformation of the sample, simulated at 5.5 MPa confining and injection pressures. Since CO_2 is injected at the bottom of the sample, the pressure develops upwards, resulting in coal swelling during the first simulation phase. The temporal variation of average pore pressure and the volumetric strain of the sample are illustrated in Figure 7-6 (a) and (b), respectively. Both parameters increase with the CO_2 interaction time until the model reaches the pressure and swelling equilibriums. It is noticeable that although the volumetric strain at the beginning is negative due to the shrinkage of the sample caused by the applied confining stress, the CO_2 adsorption-induced swelling gradually overcomes it, resulting in a positive volumetric strain at the equilibrium *(see Figure 7-6 (b))*.

As explained in section 7.2.2 and 7.2.3, a number of model parameters are modified during CO_2 interaction phase and are contributed to the consequent strength alterations, namely, porosity, surface energy, cohesion and Young's modulus. The porosity and permeability are varied with CO_2 pore pressure according to the corresponding evolution models, and each variation with the CO_2 pore pressure are given in Figure 7-6 (c) and (d), respectively. It is apparent from the figures that both parameters decrease with the increasing CO_2 pore pressure, which reflects the alterations in the CO_2 migration through a coal seam, due to the adsorption-induced coal matrix swelling, under confined-stress condition. As the next varying parameters, the adsorption-induced surface energy reduction and the consequent change in the cohesion are calibrated to model the CO_2 interaction-induced strength alteration. Figure 7-6 (e) and (f) illustrate the calibrated variations of said parameters with the CO_2 pore pressure. The surface energy change (i.e. reduction) increases with the increasing CO_2 pore pressure, and consequently, the corresponding cohesion of the coal mass decreases. This reduction in the cohesion modifies the Mohr-Coulomb failure envelope in the second simulation phase, resulting in different compressive strength values. The change in Young's modulus is modelled by fitting the experimental data with a Langmuir-type model as given in Eq. 7-36. Figure 7-7 depicts the variation of the change in Young's modulus with CO_2 pore pressure. It is apparent that the Young's modulus reduces with the increasing CO_2 pore pressure, that reflects the coal mechanical degradation at elevated CO_2 pore pressure. The fitted Langmuir constants are used in the simulation to incorporate this behaviour on compressive strength modelling.

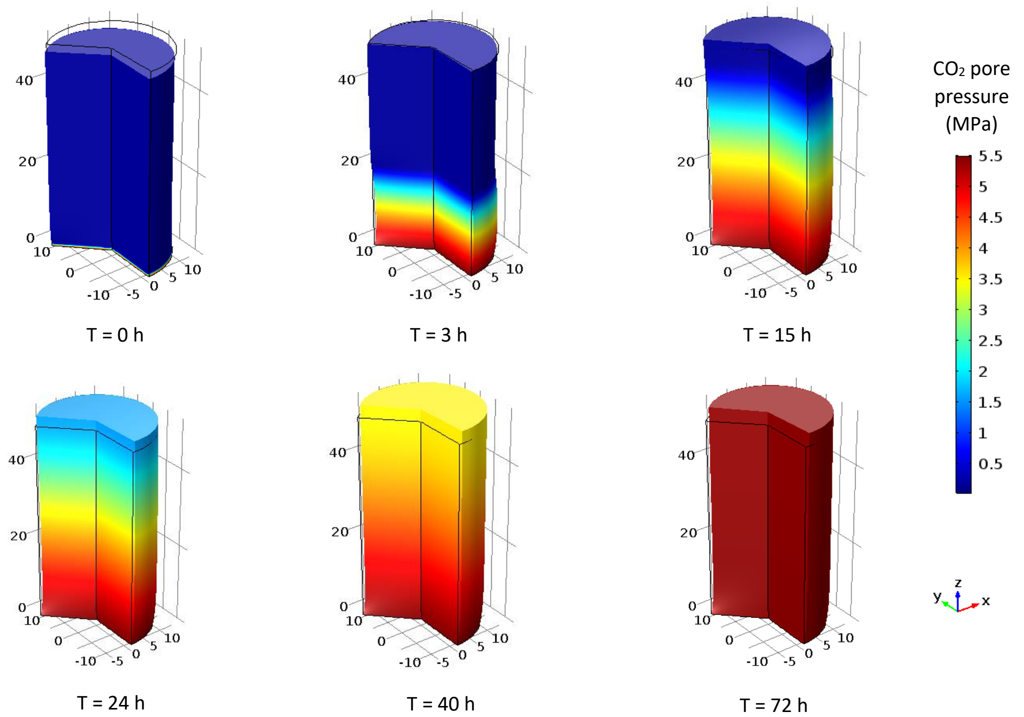

Figure 7-5 – Temporal and spatial distribution of CO_2 pore pressure and the consequent swelling deformation of the sample, under confined-stress condition – simulated at $P_b = P_{CO_2}$= 5.5 MPa.

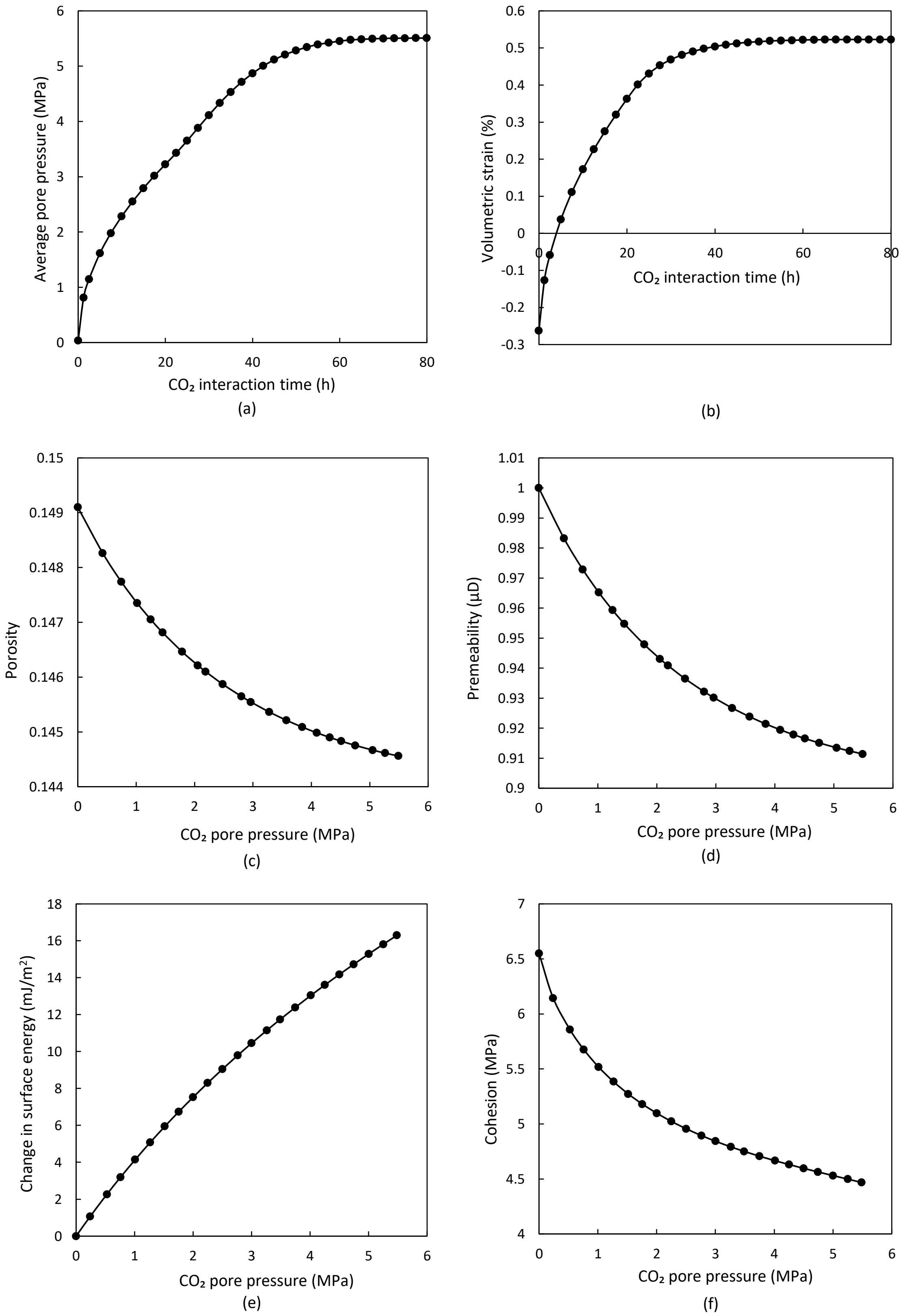

Figure 7-6 – Simulation results under confined-stress condition: a) variation of average pore pressure and, b) variation of volumetric strain with CO_2 interaction time. c) variation of porosity, d) variation of permeability, e) change in adsorption-induced surface energy ($\Delta\gamma$) *(refer Eq. 7-32)* and, f) variation of cohesion *(refer Eq. 7-35)* with the CO_2 pore pressure – simulated at $P_b = P_{CO_2}$= 5.5 MPa.

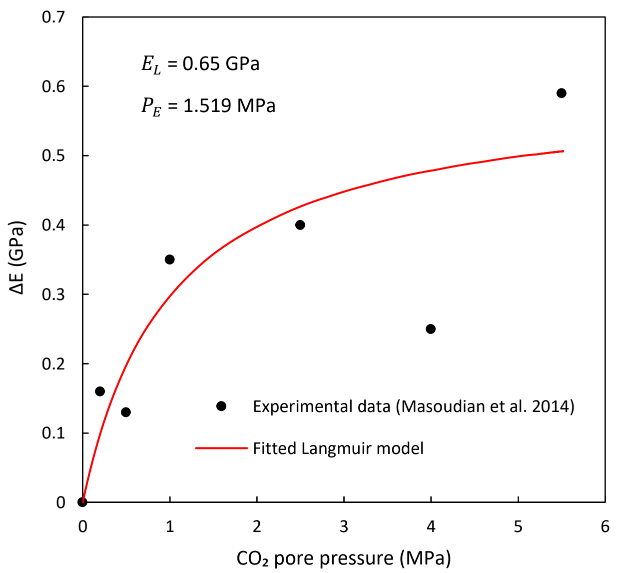

Figure 7-7 – The experimental data fitted with the Langmuir-type model, illustrating the change in the Young's modulus with the CO_2 pore pressure *(refer Eq. 7-36)* (modified after Masoudian et al. (2014)).

Figure 7-8 is produced with experimental and modelling results to compare the variation of compressive strength of natural and CO_2-interacted coal with confining pressure. Similar to natural coal strength variation, the CO_2-interacted coal strength also increases with the increasing confining pressure, regardless of the CO_2 interaction – due to the confining pressure applied on the samples. However, since the CO_2 injection pressure is also increased with the increasing confining pressure, as per the experimental procedure, a significant strength reduction can be observed with increasing confining pressures, due to the moderately elevated CO_2 pore pressure. For instance, according to the simulation results, the reduction in coal strength at 0.2 MPa and 5.5 MPa pore pressures are 3.8% and 20.1%, respectively, which confirms the higher strength reductions at higher CO_2 interaction pressures. This is because, the higher the pore pressure, the higher the reduction in effective stress, that moves the effective stress Mohr's circle towards the failure envelop. Simultaneously, cohesion reduction is higher at this particular CO_2 pore pressure that causes large modifications in the failure envelope. The associated Young's modulus reduction also contributes to mechanical degradation. Combination of all these effects in modelling causes a significant reduction in the resultant compressive strength, which is in line with the experimental results. This is further evident from Figure 7-9, that shows the modelled stress-strain curves of natural and CO_2-interacted samples at four selected confining pressures. It is clear that both gradient and the yielding point of curves vary with the confining pressure and CO_2 pore pressure, which confirms the successful modelling of CO_2 interaction-induced Young's modulus reduction and the compressive strength alteration, respectively.

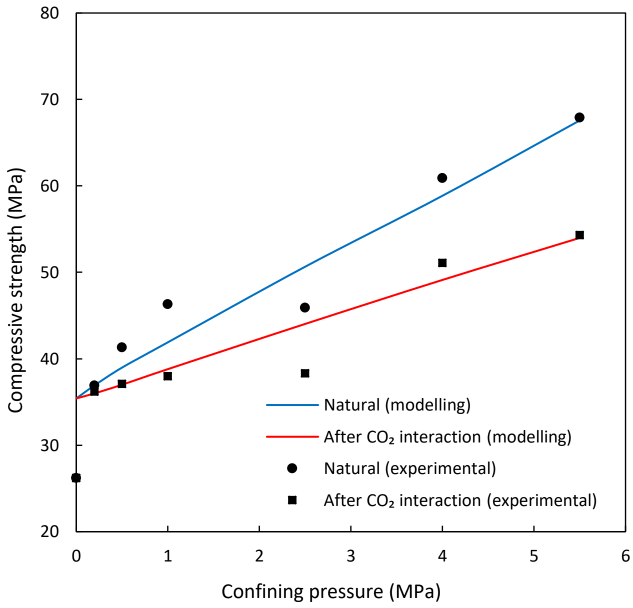

Figure 7-8 – Comparison of strength variation between natural and CO_2-interacted coal, which indicates the effect of confining pressure and CO_2 injection pressure on the strength alteration (fitted with the data from Masoudian et al. (2014)).

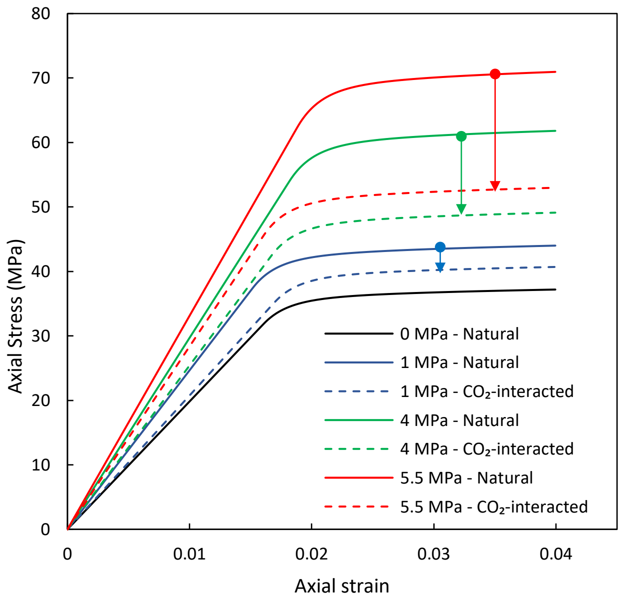

Figure 7-9 - Modelled stress-strain curves for selected confining pressures that depict the variation of Young's modulus and compressive strength.

7.2.4.2 Compressive strength under unconfined-stress condition

7.2.4.2.1 Model description and geometry

Under this section, the model is validated with an experimental study, conducted by Perera et al. (2013) on bituminous coal core samples (38 mm diameter × 80 mm height), under unconfined-stress condition. The geometric and boundary conditions are shown in Figure 7-10. Model parameters corresponding to particular coal type and experimental condition are listed in Table 7-2, and the rest is similar to that given in Table 7-1.

As per the experimental methodology, the samples were initially interacted with CO_2 in reaction chambers and tested for UCS. During the interaction period, the samples were exposed to CO_2 at given pressure (P_{CO_2}) and temperature conditions without applying a confining stress on the sample body. Hence, CO_2 migrated into the samples from all the directions and allowed the samples to freely swell under unconfined-stress condition, altering strength properties. The samples were then retrieved from the reaction chambers prior to testing, by slowly releasing the applied CO_2 pressure. This causes the free gas phase to be reduced to the initial pore pressure (P_0), resulting in a negligible effect from the free gas on the strength reduction. Under this particular condition, only the effect of adsorbed gas phase is considered, and it is assumed that the change in influential parameters, including Young's modulus, surface energy and cohesion due to initial CO_2 adsorption are irreversible. Assuming the effect from initial pore pressure (P_0) is negligible, the confining stress (P_b) is zero, and the maximum pre-exposed CO_2 interaction pressure is P_{CO_2}, the change in the cohesion, considering only the effect of adsorbed gas can be expressed by simplifying the Eq. 7-35 as,

$$C_{u_{CO_2}} = C_{u_0}\sqrt{\frac{E_{CO_2}}{E_0}\left(1 - \frac{RT}{\gamma_0 S_E V_M}\int_0^{P_{CO_2}}(1-\phi)\frac{V_L}{p+p_L}dp\right)} \qquad \text{........... [7-40]}$$

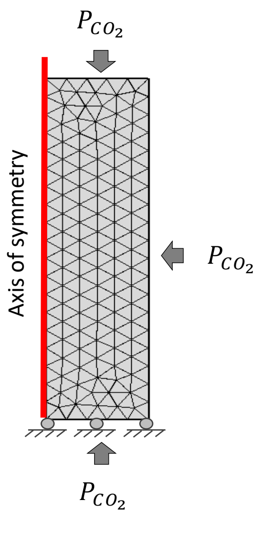

Figure 7-10 – Geometry and the boundary conditions for the unconfined-stress condition.

Table 7-2 –Parameters used for validation of the model under unconfined-stress condition.

Parameter	Value
Coal density ($\boldsymbol{\rho_c}$) ($\boldsymbol{kg/m^3}$)	1450
Initial permeability ($\boldsymbol{k_0}$) ($\boldsymbol{mD}$)	0.0005
Surface area of coal per unit mass ($\boldsymbol{S_E}$) ($\boldsymbol{m^2/g}$)	275.7
Cohesion of natural coal ($\boldsymbol{C_{u_0}}$) ($\boldsymbol{MPa}$)	7.8
Friction angle ($\boldsymbol{\varphi}$) (°)	35
Langmuir volumetric strain constant ($\boldsymbol{\varepsilon_L}$)	0.019
Langmuir constant for Young's modulus ($\boldsymbol{E_L}$) ($\boldsymbol{GPa}$)	48.31
Langmuir pressure constant for Young's modulus ($\boldsymbol{P_E}$) ($\boldsymbol{MPa}$)	209.11
Biot's coefficient ($\boldsymbol{\alpha}$)	0.8
Temperature ($\boldsymbol{T}$) ($^o\boldsymbol{C}$)	33
Initial pore pressure ($\boldsymbol{P_0}$) ($\boldsymbol{MPa}$)	0

7.2.4.2.2 Modelling results

Figure 7-11 illustrates the distribution of CO_2 pore pressure in the sample during the CO_2 interaction phase at 8 MPa injection pressure, and the resultant swelling deformation of the coal mass. Unlike the previous case, since the whole sample is exposed to CO_2, the gas migrates into the sample from all boundaries due to induced pressure gradient and the sample subjects to free and outward swelling under unconfined-stress condition, which is exactly similar to the process occurring in a reaction chamber. The change in cohesion as defined in Eq. 7-40 is illustrated in Figure 7-12 (a). The cohesion shows a decreasing trend with the increasing CO_2 interaction pressure, due to CO_2 adsorption-induced surface energy reduction, and ultimately modifies the Mohr-Coulomb failure envelop. However, the variation shows approximately a linear reduction, compared to that in the confined case *(see Figure 7-6 (f))*, possibly due to the absence of the effect of free gas and the confining stress. Moreover, the reduction in Young's modulus is modelled by fitting the experimental data with the Langmuir-type model, as shown in Figure 7-12 (b). These modifications in the initial model parameters are incorporated in the second simulation phase to model the UCS alterations at given CO_2 interaction pressures.

Figure 7-13 (a) shows the variation of UCS with CO_2 interaction pressure. The UCS reduces with the increasing interaction pressure and the model results show a good fit with the experimental results. It is noticeable that although the effect of free gas is not contributed to the strength alterations, the effect of adsorbed gas itself causes a significant strength reduction, through the modification of failure envelope. This partly reflects the CO_2 adsorption-induced modifications in coal internal structure, that consequently lead to coal mechanical degradation. Figure 7-13 (b) further shows the modelled stress-strain curves for the natural sample and CO_2-interacted samples under different CO_2 injection pressures. The stress-strain curves depict that both UCS and Young's modulus vary with the CO_2 pressure, confirming the model's capability of simulating the CO_2 interaction-induced strength alterations under unconfined-stress condition.

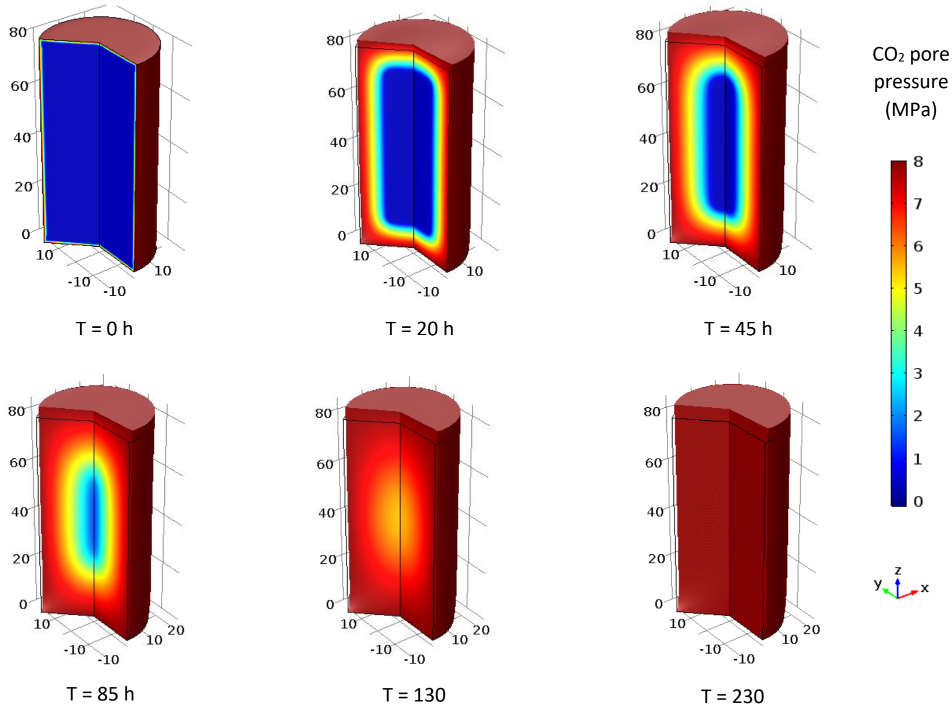

Figure 7-11 – Temporal and spatial distribution of CO_2 pore pressure and the consequent swelling deformation of the sample, under unconfined-stress condition.

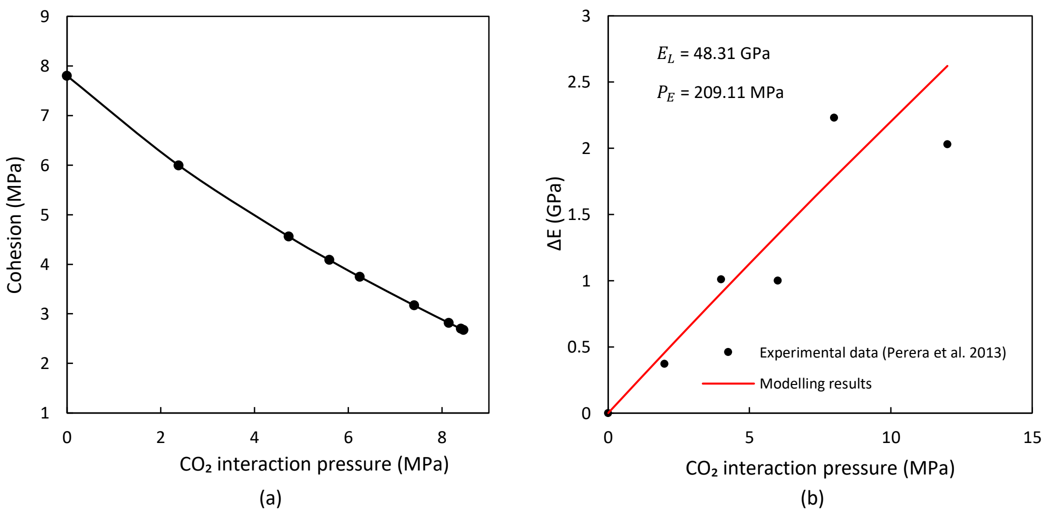

Figure 7-12 – a) Variation of cohesion with CO_2 interaction pressure *(refer Eq.7-40)* and, b) the experimental data fitted with the Langmuir-type model, illustrating the change in the Young's modulus with the CO_2 interaction pressure *(refer Eq. 7-36)* (modified after Perera et al. (2013))

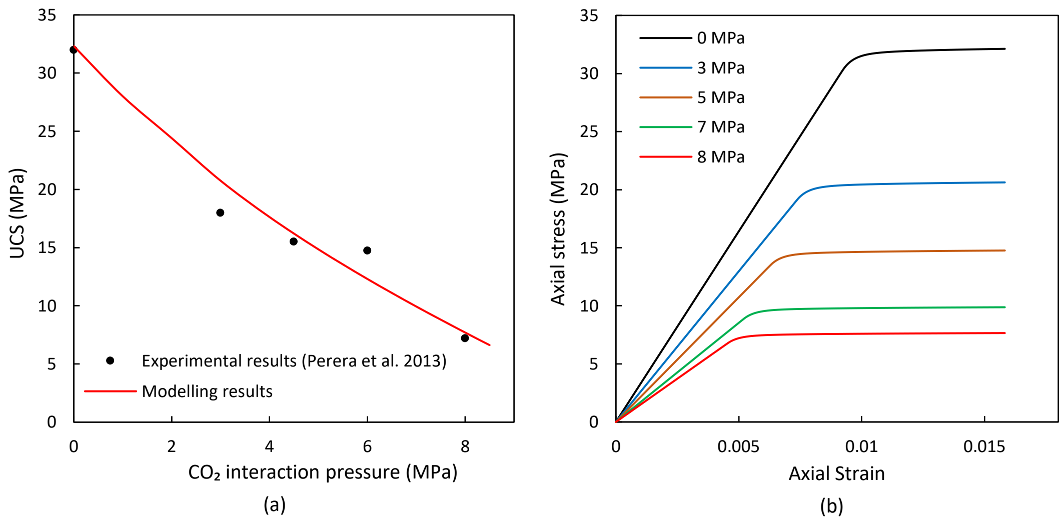

Figure 7-13 – a) Variation of UCS with CO_2 interaction pressure (fitted with the data from Perera et al. (2013)) and, b) modelled stress-strain curves that depict the variation of Young's modulus and compressive strength at different CO_2 interaction pressures.

7.2.5 Model performance-based sensitivity analysis

In this phase, the calibrated model from section 7.2.4.1 has been used to evaluate the effect of different influential parameters on coal strength, through a sensitivity analysis. The experimental study conducted in section 7.2.4.1 is only up to 5.5 MPa confining and injection pressures, which are not adequate to interpret the field conditions. Hence, in this section, we estimate the strength alterations of coal subjected to 25 MPa confining pressure and to incremental CO_2 injection pressures (i.e. $0.1\ MPa < P_{CO_2} < 24\ MPa$).

7.2.5.1 Effect of Biot's coefficient on the strength alteration

The effective stress law is vital in the process of modelling coupled-solid-fluid problems. As outlined by Biot (1941), the Biot's coefficient defines what is the fraction of pore pressure that contributes to the effective stress of the solid, which in turn critical in material strength modelling. Based on the theoretical approach of the current study, the Biot's coefficient is an important parameter, as it appears in both equations of free and adsorbed gas-induced mechanical alterations *(see Eq. 7-34)*, and ultimately governs the overall mechanical alteration.

Since the Biot's coefficient directly contributes to the free and adsorbed gas-induced mechanical alterations though the modified-cohesion model, the variation of cohesion with CO_2 pore pressure is initially plotted for different values of Biot's coefficient *(see Figure 7-14 (a))*. It can be seen that the Biot's coefficient has a significant impact on the cohesion at higher pore pressures than at relatively lower pore pressures. Next, the variation of compressive strength is plotted with increasing CO_2 pore pressure for the same values of Biot's coefficient *(see Figure 7-14 (b))*. Interestingly, the extended analysis up to a relatively large pore pressure of 24 MPa depicts that compressive strength initially decreases but starts to slightly increase beyond 12 MPa CO_2 pore pressure. This is in line with Perera et al. (2013) and Yin et al. (2017), who observed that the compressive strengths of CO_2-interacted coal and shale slightly increase from 12 MPa to 16 MPa pore pressures. As explained by Pan and Connell (2007), the largely elevated CO_2 pore pressure can cause a net contraction rather than a swelling, due to increased-matrix compression, resulting in a slight strength increment. This behaviour is well-reflected in the model through the variation of cohesion, that depicts an increment in cohesion at largely elevated pore pressures due to matrix compression, causing the strength increment. This is further confirmed with the Biot's coefficient-based sensitivity analysis, as the larger the Biot's coefficient, the higher the contribution of pore pressure, which consequently results in large increments of cohesion and compressive strength *(see Figure 7-14)*. This conveys the capability of the derived cohesion model *(see Eq. 7-35)* on predicting strength alterations of CO_2-interacted coal over a wide range of CO_2 pore pressures. Moreover, it is apparent that the effect of Biot's coefficient on the coal strength alteration is not as significant as that on cohesion. For instance, the change in cohesion when Biot's coefficient increases from 0.55 to 0.65 at 24 MPa injection pressure is 87.1%, whereas that in strength variation is only 8.9%. This is because the overall strength alteration is governed by the movement of effective stress Mohr's circle and the adjusted failure envelope, both of which are combinedly dependent on the free and adsorbed gas-induced effects.

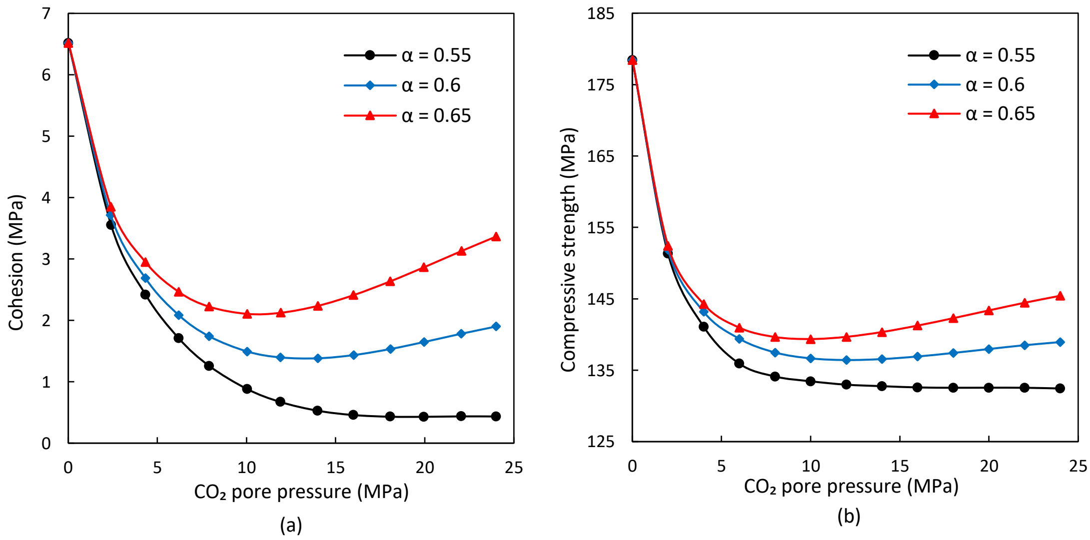

Figure 7-14 – Variation of a) cohesion and, b) peak compressive strength with CO_2 pore pressure, for different Biot's coefficient values (Note: $P_b = 25\ MPa$).

7.2.5.2 Effect of Langmuir constants on the strength alteration

Langmuir-type empirical models have been defined in the coupled-process at several occasions, including the modellings of CO_2 adsorption, adsorption-induced swelling and the Young's modulus alteration. Although numerous experimental studies confirm the validity of Langmuir-type models on simulating these processes, it is important to evaluate the effect of Langmuir constants on each process and subsequently on the compressive strength, through a sensitivity analysis.

Figure 7-15 (a) shows the variation of volumetric strain with pore pressure, that is basically governed by the Langmuir volumetric strain constant (ε_L), which reflects the swelling potential of a particular coal type. The higher the value of ε_L, the higher the volumetric strain at a given pore pressure. Noticeably, the volumetric strain depicts a decreasing trend at largely elevated pore pressures (i.e. $P_{CO_2} > 10\ MPa$) for large ε_L values. This is in line with Pan and Connell (2007), who showed that the ratio of coal swelling reaches a maximum, and then decreases at elevated pore pressures, due to matrix compression. Moreover. the compressive strength decreases with the increasing ε_L value, indicating the adverse effect of swelling potential on the coal mechanical degradation *(see Figure 7-15 (b))*. In fact, the compressive strength at 10 MPa pore pressure has been reduced by 11.9% and 23.8%, when ε_L value increased from 0.023 to 0.053 and 0.083, respectively. The Langmuir sorption constant (V_L) defines the amount of adsorbed CO_2 on coal and subsequently the surface energy reduction that contributes to the adsorbed gas-induced strength alteration. Figure 7-15 (c) illustrates the variation of the adsorbed amount of CO_2 with pore pressure for different V_L values, representing the adsorption potential of different coal types. Clearly, a higher V_L value outcomes a higher adsorbed amount of CO_2 at a certain pore pressure, resulting in lower compressive strength values *(see Figure 7-15 (d))*. Theoretically, this is due to the larger adsorption-induced surface energy reduction that alters the cohesion of the coal and the resultant Mohr-Coulomb failure envelope. Young's modulus is an imperative parameter in the context of modelling mechanical degradation. Since we assume the alteration in Young's modulus fits in a Langmuir-type empirical model, the said alteration significantly depends on the coal type, which is represented by the Langmuir constant - E_L. Figure 7-15 (e) shows the decrease of Young's modulus with increasing pore pressure for different E_L values. It is apparent that Young's modulus decreases with the increasing E_L value for all CO_2 pore pressures. For instance, the Young's moduli at 24 MPa CO_2 pore pressure have been decreased by 4.7% and 9.4%, at $E_L = 0.65$ and 1 respectively, when compared to $E_L = 0.3$, and consequently, the peak compressive strengths at 24 MPa have been reduced by 1.9% and 4.2% *(see Figure 7-15 (f))*. Although this is not significant, the analysis conveys that the CO_2 interaction-induced compressive strength alteration is moderately sensitive to E_L value.

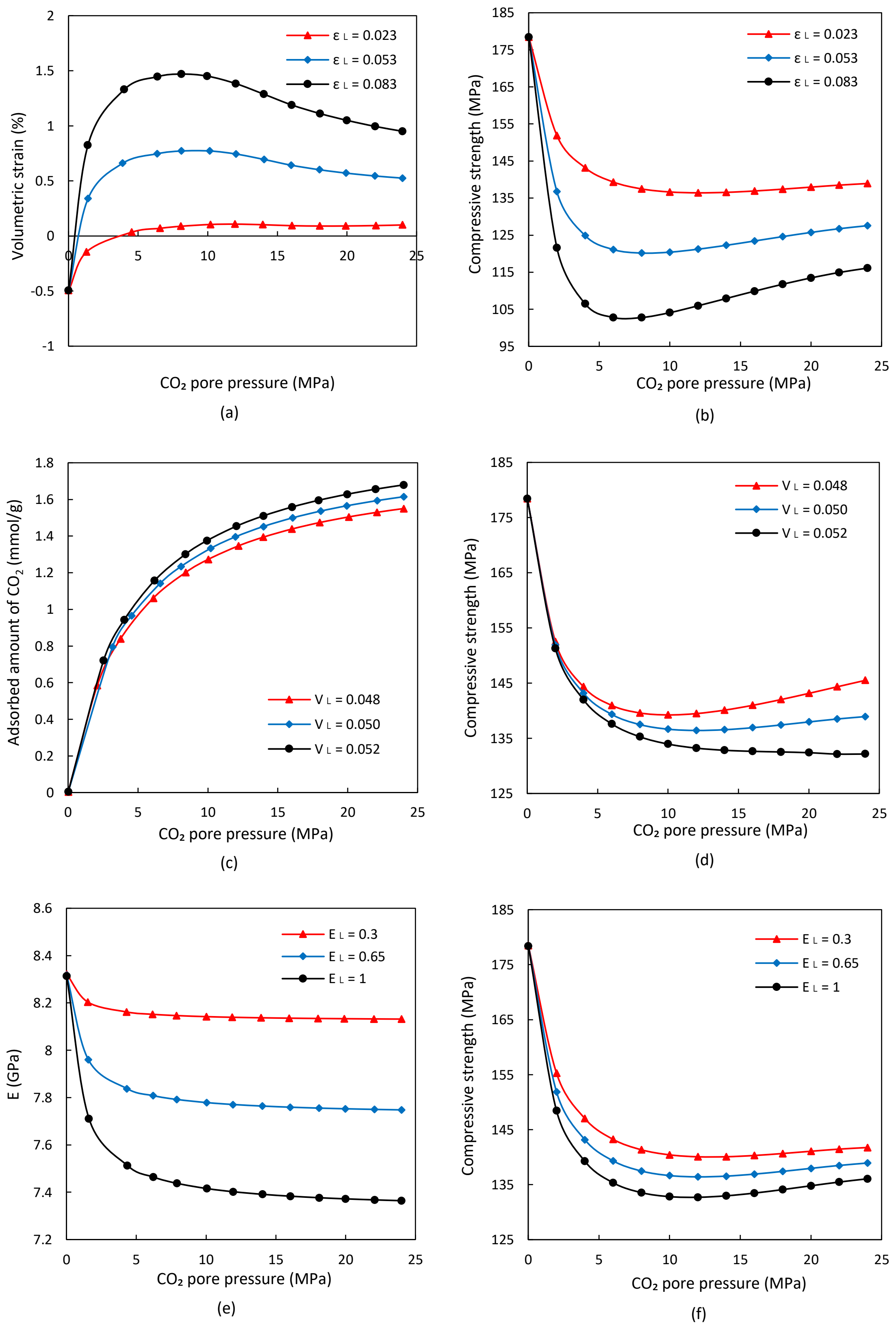

Figure 7-15 – Sensitivity analysis based on Langmuir constants: Variation of a) volumetric strain and b) peak compressive strength for different ε_L values. Variation of c) adsorbed amount of CO_2 and d) peak compressive strength for different V_L values. Variation of e) Young's modulus and f) peak compressive strength for different E_L values. (Note: $P_b = 25\ MPa$).

Overall, the sensitivity analysis confirms that Langmuir constants play a vital role at different levels in modelling the fully-coupled process. Since the Langmuir constants greatly depend on the coal type, they should be precisely determined for a given coal type, in order to accurately model the ultimate mechanical alterations.

The results of the current study confirm that coal compressive strength alters with the free and adsorbed CO_2 and the developed model is capable of simulating this behaviour, coupling through the effective stresses, cohesion and Young's modulus, under both confined- and unconfined-stress conditions. However, the theoretical approach relies on a number of parameters, which are highly-sensitive to the final outcome. Moreover, the strength alterations in coal is a highly-complex and localized process due to the heterogeneity and anisotropy induced by the spatial disposition of minerals and the cleat system. The moisture content and the chemistry of the existing pore fluid infers the necessity of adopting multi-phase flow behaviour that makes the coupled-process rather complex. Hence, we recommend considering these effects, when extending the further analysis on CO_2 interaction-induced strength alterations in coal.

7.2.6 Conclusions

A model is developed to simulate the CO_2 interaction-induced compressive strength alterations in coal by combining the CO_2 pore pressure and the change in multiple mechanical parameters, including cohesion and Young's modulus. Following conclusions are made, based on the simulation results.

- The model results of the spatial and temporal distribution of CO_2 pore pressure and the resultant swelling depict that the CO_2 adsorption-induced coal deformation depends on the boundary stress conditions, in which unlike confined-stress condition, the coal mass subjects to free and outward swelling under unconfined-stress condition.
- The calibrated model is capable of successfully simulating the effect of confining pressure, and the effect of free and adsorbed gas on the alterations of the coal compressive strength, under both confined- and unconfined-stress conditions.
- The estimations from the calibrated model confirm that coal compressive strength can be decreased and then slightly increased at relatively high pore pressures (i.e. $P_{CO_2} > 12\ MPa$) due to the matrix-compression induced by the elevated pore pressure and the developed cohesion model is capable of capturing this behaviour.
- The overall mechanical alterations are highly-sensitive to the Biot's coefficient, as it governs the fraction of the pore pressure that contributes in determining the effective

stresses, which is vital in modelling the mechanical properties of coupled fluid-solid problems.

- The Langmuir constants play a critical role in modelling the fully-coupled process, where the sensitivity analysis highlights the importance of determining the constants precisely for a given coal type, in order to accurately simulate the overall strength alterations.

Reference

Ates, Y., & Barron, K. (1988). The effect of gas sorption on the strength of coal. *Mining Science and Technology, 6*(3), 291-300.

Biot, M. (1941). General Theory of Three-Dimensional Consolidation. *Journal of Applied Physics, 12*(2), 155-164.

Boyd, G., & Livingston, H. (1942). Adsorption and the Energy Changes1 at Crystalline Solid Surfaces. *Journal of the American Chemical Society, 64*(10), 2383-2388.

Chilingar, G. V. (1964). Relationship between porosity, permeability, and grain-size distribution of sands and sandstones *Developments in Sedimentology* (Vol. 1, pp. 71-75): Elsevier.

da C Andrade, E., Randall, R., & Makin, M. (1950). The rehbinder effect. *Proceedings of the Physical Society. Section B, 63*(12), 990.

Fairhurst, C. (1973). *Estimation of the mechanical properties of rock masses*. Retrieved from

Gentzis, T., Deisman, N., & Chalaturnyk, R. J. (2007). Geomechanical properties and permeability of coals from the Foothills and Mountain regions of western Canada. *International Journal of Coal Geology, 69*(3), 153-164.

Gibbs, J. W. (1879). On the equilibrium of heterogeneous substances. 300-320.

Griffith, A. A. (1921). The phenomena of rupture and flow in solids. *Philosophical transactions of the royal society of london. Series A, 221*, 163-198.

Guo, H., Ni, X., Wang, Y., Du, X., Yu, T., & Feng, R. (2018). Experimental Study of CO_2-Water-Mineral Interactions and Their Influence on the Permeability of Coking Coal and Implications for CO_2-ECBM. *Minerals, 8*(3), 117.

Handin, J. (1969). On the Coulomb-Mohr failure criterion. *Journal of Geophysical Research, 74*(22), 5343-5348.

Harpalani, S., & Mitra, A. (2010). Impact of CO_2 Injection on Flow Behavior of Coalbed Methane Reservoirs. *Transport in Porous Media, 82*(1), 141-156.

Hu, S., Wang, E., Li, X., & Bai, B. (2016). Effects of gas adsorption on mechanical properties and erosion mechanism of coal. *Journal of Natural Gas Science and Engineering, 30*, 531-538.

Kang, J., Zhang, B., Wang, J., Wu, J., Wang, L., Yin, B., & Kang, T. (2019). Mechanical testing of anthracite to assess its surface energy and temperature dependence. *Fuel, 239*, 76-86.

Karacan, C. Ö. (2003). Heterogeneous Sorption and Swelling in a Confined and Stressed Coal during CO_2 Injection. *Energy & Fuels, 17*(6), 1595-1608.

Kuvaev, N., & Panchenko, D. (1975). Effect of moisture on the dynamic strength of brown coals. *Journal of Mining Science, 11*(3), 220-222.

Larsen, J. W. (2004). The effects of dissolved CO_2 on coal structure and properties. *International Journal of Coal Geology, 57*(1), 63– 70.

Lu, S., Li, L., Cheng, Y., Sa, Z., Zhang, Y., & Yang, N. (2017). Mechanical failure mechanisms and forms of normal and deformed coal combination containing gas: Model development and analysis. *Engineering Failure Analysis, 80*, 241-252.

Lu, S., Zhang, Y., Sa, Z., & Si, S. (2019). Evaluation of the effect of adsorbed gas and free gas on mechanical properties of coal. *Environmental Earth Sciences, 78*(6), 218.

Masoudian, M. S., Airey, D. W., & El-Zein, A. (2014). Experimental investigations on the effect of CO_2 on mechanics of coal. *International Journal of Coal Geology, 128*, 12-23.

Mazumder, S., Wolf, K., Van Hemert, P., & Busch, A. (2008). Laboratory experiments on environmental friendly means to improve coalbed methane production by carbon dioxide/flue gas injection. *Transport in Porous Media, 75*(1), 63-92.

Palmer, I., & Mansoori, J. (1996). *How permeability depends on stress and pore pressure in coalbeds: a new model.* Paper presented at the SPE annual technical conference and exhibition.

Pan, Z., & Connell, L. D. (2007). A theoretical model for gas adsorption-induced coal swelling. *International Journal of Coal Geology, 69*(4), 243-252.

Perera, M., Ranjith, P., Airey, D., & Choi, S.-K. (2011). Sub-and super-critical carbon dioxide flow behavior in naturally fractured black coal: An experimental study. *Fuel, 90*(11), 3390-3397.

Perera, M. S. A., Ranjith, P. G., & Viete, D. R. (2013). Effects of gaseous and super-critical carbon dioxide saturation on the mechanical properties of bituminous coal from the Southern Sydney Basin. *Applied Energy, 110*, 73-81.

Ranathunga, A. S., Perera, M. S. A., & Ranjith, P. G. (2016). Influence of CO_2 adsorption on the strength and elastic modulus of low rank Australian coal under confining pressure. *International Journal of Coal Geology, 167*, 148-156.

Robertson, E. P., & Christiansen, R. L. (2005). *Modeling permeability in coal using sorption-induced strain data*. Retrieved from

Roy, D. M., & Gouda, G. R. (1973). Porosity-strength relation in cementitious materials with very high strengths. *Journal of the American Ceramic Society, 56*(10), 549-550.

Sampath, K. H. S. M., Perera, M., Li, D. Y., Ranjith, P., & Matthai, S. (2019a). Characterization of dynamic mechanical alterations of supercritical CO_2-interacted coal through gamma-ray attenuation, ultrasonic and X-ray computed tomography techniques. *Journal of Petroleum Science and Engineering, 174*, 268-280.

Sampath, K. H. S. M., Perera, M. S. A., Elsworth, D., Ranjith, P. G., Matthai, S. K., & Rathnaweera, T. (2018). Experimental Investigation on the Mechanical Behavior of Victorian Brown Coal under Brine Saturation. *Energy & Fuels, 32*(5), 5799-5811.

Sampath, K. H. S. M., Perera, M. S. A., Ranjith, P. G., & Matthai, S. K. (2019b). CO_2 interaction induced mechanical characteristics alterations in coal: A review. *International Journal of Coal Geology, 204*, 113-129.

Sampath, K. H. S. M., Perera, M. S. A., Ranjith, P. G., Matthai, S. K., & Dong yin, L. (2019c). Qualitative and quantitative evaluation of the alteration of micro-fracture characteristics of supercritical CO_2-interacted coal. *The Journal of supercritical fluids, 147*, 90-101.

Van Eeckhout, E. M. (1976). The mechanisms of strength reduction due to moisture in coal mine shales. *International Journal of Rock Mechanics and Mining Sciences & Geomechanics Abstracts, 13*(2), 61-67.

Vandamme, M., Brochard, L., Lecampion, B., & Coussy, O. (2010). Adsorption and strain: the CO2-induced swelling of coal. *Journal of the Mechanics and Physics of Solids, 58*(10), 1489-1505.

Viete, D. R., & Ranjith, P. G. (2006). The effect of CO_2 on the geomechanical and permeability behaviour of brown coal: Implications for coal seam CO_2 sequestration. *International Journal of Coal Geology, 66*, 204 – 216.

White, C. M., Smith, D. H., Jones, K. L., Goodman, A. L., Jikich, S. A., LaCount, R. B., DuBose, S. B., Ozdemir, E., Morsi, B. I., & Schroeder., K. T. (2005). Sequestration of carbon dioxide in coal with enhanced coalbed methane recovery a review. *Energy & Fuels, 19*(3), 659-724.

Xueqiu, H., Enyuan, W., & Haiyan, L. (1996). Coal deformation and fracture mechanism under pore gas action. *Journal of china university of mining & technology, 1*.

Yin, H., Zhou, J., Xian, X., Jiang, Y., Lu, Z., Tan, J., & Liu, G. (2017). Experimental study of the effects of sub-and super-critical CO2 saturation on the mechanical characteristics of organic-rich shales. *Energy, 132*, 84-95.

Zhang, H., Liu, J., & Elsworth, D. (2008). How sorption-induced matrix deformation affects gas flow in coal seams: a new FE model. *International Journal of Rock Mechanics and Mining Sciences, 45*(8), 1226-1236.

Zhang, Y., Lebedev, M., Sarmadivaleh, M., Barifcani, A., & Iglauer, S. (2016). Swelling-induced changes in coal microstructure due to supercritical CO_2 injection. *Geophysical Research Letters, 43*(17), 9077-9083.

7.3 Chapter summary

Although there exist numerous experimental studies that investigate the CO_2-induced coal mechanical property alterations, those results are useful only for the tested coal type or the experimental condition, that questions the applicability of experimental data in general CO_2 sequestration process. The best way to overcome this setback is to understand the underlying physics and coupled processes and implement them in a numerical model. Based on this argument, this study presents a numerical study that analyses the effect of the free and the adsorbed CO_2 on the coal mechanical property alterations, where the mechanical property alteration is interpreted in terms of compressive strength – an important mechanical parameter widely used in the rock mechanics field.

The compressive strength variation is modelled with the Mohr-Coulomb failure criterion, where the strength variation of saturated samples was defined by appropriately adjusting the failure envelope; by taking the effects of free and adsorbed CO_2 into account. The change in cohesion was modelled by developing a theoretically-modified cohesion model that integrates the effective stress and the adsorbed CO_2-induced surface energy reduction. In general, the study models a CO_2 saturation and mechanical testing experiment on a lab-scale coal core sample, where the complete simulation procedure consists of two main phases: 1) CO_2 saturation phase and, 2) mechanical loading phase upon sample saturation. In the first phase, CO_2 injection, pore pressure development and the consequent changes in the influential parameters were modelled, where the simulation was run until the full-pressure equilibrium to reflect the fully-saturated condition of the sample. Then the adjusted parameters were transferred to the next simulation phase, in which the mechanical load was applied, and the compressive strength was determined at the failure. This model was validated with experimental results conducted under confined and unconfined conditions, in which only the irreversible changes occur due to adsorbed gas phase were considered for the validation under unconfined condition. A sensitivity analysis was finally conducted to analyse the influence of various parameters on the ultimate strength alterations.

In summary, the results conclude that the developed mechanical model can successfully simulate the effect of free and the adsorbed CO_2 on the coal compressive strength alterations, under both confined and unconfined conditions. The CO_2 injection pressure or the pore pressure at full pressure equilibrium, and the model parameters such as Biot's coefficient and the Langmuir parameters have a significant impact on the overall strength alteration; thus, should be defined precisely when setting up the model parameters – targeting the specific coal type and the reservoir conditions. The study provides a good initiative for the numerical modelling of CO_2-induced strength alterations in coal; thus, can be used to generally evaluate the mechanical competency of coal seams during the CO_2 sequestration process.

CHAPTER 8

Statistical analysis with machine learning techniques to predict the CO_2-induced mechanical property alterations in coal

8 Statistical analysis with machine learning techniques to predict the CO_2-induced mechanical property alterations in coal

8.1 Chapter overview and structure

Similar to experimental and numerical analyses presented in chapters 6 and 7, statistical analyses have also been widely used by researchers to evaluate the CO_2 interaction-induced mechanical property alterations in coal. The technique has become popular because numerous experimental data related to coal-CO_2-induced mechanical modifications are readily available in the literature, that can be effectively used in statistical models to predict the strength modifications. Rather than using traditional statistical tools like regression analyses, the use of machine learning techniques has become prominent in recent years, as the techniques have the capability of capturing the complex interrelationship among the influential parameters and accurately determining the output values. Hence, this study is focused on utilizing advanced statistical tools to predict the mechanical property alterations in CO_2-interacted coal – that can be used to expedite the related analyses and to assist in precisely predicting the mechanical modifications in coal under specific interaction environments.

Current study adopts two well-known machine learning techniques: i.e. 1) the artificial neural networks (ANN) and 2) the adaptive neuro-fuzzy inference systems (ANFIS) to predict the coal strength alterations based on three independent parameters, *viz*. the natural coal strength, the CO_2 saturation pressure and the CO_2 interaction time. Altogether, 96 data sets were utilized in developing the statistical models, including own experimental data, in which most coal types used in the models (i.e. coal from Gippsland and Sydney Basins, Australia, and Jharia and Korba coalfields, India) are related to the upper and lower Gondwana coal groups. The model performances were compared with conventional linear and non-linear regression analyses by using 5 statistical indices. Finally, the trained models were used to predict the mechanical alterations under long-term CO_2 saturation conditions successfully. The chapter comprises of a basic background of the coal-related statistical modelling, selection of input parameters, modelling approach with machine learning techniques, comparison with conventional regression analyses, model performance evaluation and strength prediction with trained models. Following section comprehensively describes the entire study, which is presented as a peer-reviewed journal paper.

8.2 Journal paper: Intelligent prediction of CO_2-induced mechanical property alterations in coal

This section is presented as the author-accepted manuscript of a peer-reviewed article published in "Measurement". The journal is a Q2 journal with impact factor of 2.79.

Citation:

- Sampath K. H. S. M., Perera M. S. A., Ranjith P. G., Matthai S. K., Tao X., Wu B. K. (2019). *Application of neural networks and fuzzy systems for the intelligent prediction of CO_2-induced strength alteration of coal*. Measurement (London. Print), 135, 47-60.

Journal paper title: Application of neural networks and fuzzy systems for the intelligent prediction of CO_2-induced strength alteration of coal

Authors' names: K.H.S.M. Sampath[1], *M.S.A. Perera[1], P.G. Ranjith[2], S.K. Matthai[1], X. Tao[3], B. Wu[4]

[1]Department of Infrastructure Engineering, Engineering Block B, Grattan Street, Parkville, The University of Melbourne, Victoria 3010, Australia.

[2]Department of Civil Engineering, Monash University, Clayton Campus, Victoria 3800, Australia.

[3]School of Resources and Civil Engineering, North-Eastern University, Shenyang 110819, China.

[4]Commonwealth Scientific and Industrial Research Organization (CSIRO), Ian Wark Laboratory, Clayton, Victoria 3168, Australia

Abstract

CO_2 sequestration and enhanced coal bed methane (ECBM) extraction necessitate CO_2 injection into coal reservoirs that affect the coal strength properties and long-term integrity of the seam. Evaluation of CO_2-induced coal strength alterations is essential to minimize the reservoir damage. Advanced soft computing models have become prevalent in rock mechanics field, as they are capable of learning trends from complex data sets, preserving the experience and using it for predictions. We present two models *viz.* artificial neural network (ANN) and adaptive neuro-fuzzy inference system (ANFIS) to predict the strength alterations of coal, under various CO_2 saturation conditions. Model performances are compared with linear and non-linear multivariate regression analyses (L-MRA and NL-MRA). We consider three effective input parameters (i.e. coal type, CO_2 saturation pressure and CO_2 interaction time) and one output parameter (i.e. unconfined compressive strength (UCS)) in the models. ANN consists of a three-layer feed-forward back-propagation network with a 3-5-1 architecture, and ANFIS consists of [4 4 4] Gaussian type membership functions. Model results confirm that ANFIS has the highest prediction capacity, followed by ANN, with R^2 equal to 0.9954 and 0.9933, respectively. Both L-MRA and NL-MRA prediction performances are not satisfactory, as R^2 values are only 0.7854 and 0.7821 for two models, respectively. Thus, general statistical models like MRA fail to precisely predict the complex strength alterations. From the verified models, we show that well-trained ANN and

ANFIS models can successfully fit and forecast the experimental data, and are able to predict the long-term CO_2 saturation effect on coal strength.

Keywords: *Unconfined compressive strength (UCS), Coal rank, CO_2 saturation pressure, CO_2 interaction time, Artificial neural network (ANN), Adaptive neuro-fuzzy inference system (ANFIS)*

8.2.1 Introduction

The rapid increment of CO_2 level in the atmosphere has become one of the main drivers of global warming, triggering the necessity of searching for appropriate greenhouse gas mitigation techniques. CO_2 sequestration in geological media has gained increasing attention as a part of the carbon capture and storage within a portfolio of options targeted at mitigating anthropogenic greenhouse gas emissions. The International Energy Agency (IEA) predicts that 94 Gt of CO_2 will be captured and sequestrated between 2013 and 2050, and the contribution of CO_2 sequestration to reduce greenhouse gas level would reach 12% of the cumulative emission reduction by 2050 (IEA, 2016). Among multiple geological mediums, coal seams have been identified as one of the most potential storage mediums, as it can adsorb a large quantity of CO_2 due to large surface area and is coupled with enhanced coal bed methane recovery (ECBM) to minimize the operational cost (Shi and Durucan, 2005; Stevens et al., 2001).

Despite the advantages, CO_2 sequestration in coal seams causes significant alterations in its chemical and mechanical properties, which in turn affect the coal seam integrity in the long-run. The mechanical degradation may cause irreversible damage to the host rock and pose a great threat of CO_2 back-migration into the atmosphere, rendering storage efforts ineffective and risky (White et al., 2005). The polymer-like coal structure readily undergoes volumetric swelling and shrinkage due to CO_2 adsorption on to coal matrix, creating micro-cracks under regional and localised *in-situ* stresses (Wang et al., 2013). According to Karacan (2007), strength reduction significantly occurs in the vitrinite component of the coal mass. Moreover, CO_2 may dissolve pore filling minerals in the coal seam and create a secondary porosity system within the primary pores, resulting in a strength reduction (Marbler et al., 2013). The strength alteration can be varied due to a number of effective parameters: coal type, CO_2 saturation pressure, coal-CO_2 interaction time, CO_2 phase, etc. (Aziz and Ming Li, 1999; Czapliński and Hołda, 1982; Ettinger, 1957). Ranathunga et al. (2016b) observed a 21.3% and 46% reduction of UCS of Australian brown coal specimens, due to the adsorption of gaseous and supercritical CO_2, respectively. Bagga et al. (2015) showed that UCS of CO_2 adsorbed Indian coal could be reduced by 65%. Moreover, Ettinger (1957), Czapliński and Hołda (1982), Viete and Ranjith (2006), Jasinge et al. (2011) and Perera et al. (2011b) observed coal strength reductions due to subcritical CO_2 adsorption, and Perera et al. (2013) observed a significant strength reduction of supercritical CO_2-adsorbed coal over subcritical CO_2-adsorbed coal.

Measurement of UCS of CO_2-treated coal samples is widely used to characterize the strength alterations of coal (Ettinger, 1957; Perera et al., 2011b; Ranathunga et al., 2016b; Vishal et al., 2015). The technique is rapid, inexpensive, easy to conduct, and meaningful relationships between coal strength and CO_2 saturation conditions have been developed based on UCS measurements. However, the standard procedure for the determination of UCS is destructive, and the standard sample preparation is difficult, time-consuming and requires careful handling, especially due to the softer nature of coal. Moreover, CO_2-induced coal strength alteration depends on many effective parameters; thus, it is difficult to evaluate the effect of all in a single test series. A comprehensive and controlled experimental methodology associated with a significant number of sample testings is required to understand the complexity behind the alterations. Development of alternate indirect methods to estimate the strength alterations is thus essential to substitute the difficult experimental procedures and to accelerate the analysis, which in fact is the motivation of the present study.

Studies have proposed empirical relationships to predict the UCS in terms of various rock index parameters, such as slake durability, Brazilian tensile strength (Nazir et al., 2013), point-load index (Basu and Aydin, 2006), ultrasonic velocity (Çobanoğlu and Çelik, 2008). In addition, researchers have used general statistical models like multiple regression models, independent component analysis (ICA), etc. to predict the UCS. However, most of the models are specific to the tested rock type and consider a limited number of effective parameters; thus, often unable to provide reliable general relationships. Application of soft-computing techniques such as artificial neural network (ANN) and adaptive neuro-fuzzy inference system (ANFIS) are being recently emphasized for the caption of complicated interrelationships among multiple parameters (Armaghani et al., 2016; Armaghani et al., 2015; Momeni et al., 2015a; Momeni et al., 2015b). The techniques are rapidly gaining popularity in every aspect, as they have a high prediction capacity in multivariable, non-linear and complex engineering problems. Since the mathematical algorithms adopted in the techniques are capable of rapid-learning from the patterns acquainted before, they can successfully capture the complex interrelationships among multiple variables and precisely predict output parameters. Moreover, the techniques are highly-advantageous, as they consist of characteristics such as generalization, mapping capability, robustness and high-speed information processing.

In this paper, we present two advanced soft computing techniques, *viz.* ANN and ANFIS to forecast the strength alteration of coal, under various CO_2 saturation conditions. Three index parameters: coal rank, CO_2 saturation pressure and CO_2 interaction time were considered as effective input parameters. UCS measurements were obtained for CO_2-treated Australian brown coal samples under different saturation conditions, and the current results were combined with data sets collected from 9 previous studies (Bagga et al., 2015; Perera et al., 2011b; Perera et al., 2013; Ranathunga et al., 2016a; Ranathunga et al., 2016b; Ranjith et al., 2010; Ranjith and Perera, 2012; Viete and Ranjith, 2006; Vishal et al., 2015) to accurately train the models. The prediction performances of the models were compared with the traditional statistical methods of linear and non-linear multivariate regression analyses, using five statistical indices. The verified models were fitted with the current experimental data, and the results were forecasted to evaluate the long-term CO_2 interaction effect on coal. From the model results, we show that there exists a good correlation between the index parameters and corresponding coal strength, and the developed machine learning techniques can successfully predict the strength alterations of CO_2-saturated coal masses under various saturation conditions.

8.2.2 Experimental methodology

UCS tests were carried out on Australian brown coal samples, obtained from Loy-Yang mine, Latrobe Valley, Victoria, Australia. The samples were cored, cut, and ground (length of 76 mm and diameter of 38 mm) at deep earth engineering research laboratory (DEERL) of Monash University. The prepared samples were treated with CO_2 for different time periods (i.e. 1 day, 14 days and 45 days) under 10 MPa saturation pressure and 40 ºC temperature to simulate the supercritical CO_2 conditions. Congruent with ASTM standards (ASTM-D.2938), UCS tests were conducted for both natural and treated samples using Shimadzu AG9 uniaxial compression machine. The load was applied at a rate of 0.2 mm/min, and the applied load and displacement were recorded with an advanced data acquisition system.

The obtained results confirm a strength reduction in the coal samples due to CO_2 interaction *(see Figure 8-1)*. It is noticeable that a large strength reduction occurs soon after CO_2 interaction. However, UCS reduction is not completed by short-term (1-day) CO_2 saturation, in which further saturation of CO_2 has caused a further strength reduction, but at a slower rate *(see Figure 8-1 (b))*. In fact, the strength reductions after 1-day and 45-days of CO_2 saturation are 13.9% and 23.5%, respectively. The rates of strength reduction are 12.1% and 0.19% in 0–1-day CO_2 saturation and 1–45-days CO_2 saturation, which confirms the significant difference of strength reduction rates in short-term and long-term saturation conditions, and the consequent complexity of the strength behaviour. The only sensitive parameter varied in the current study is the CO_2 interaction time, as other effective parameters (i.e. coal type and CO_2 saturation pressure) were controlled throughout the experiment. However, previous studies conclude that the strength reduction depends on many other parameters; thus, the soft computing models should contemplate all the possible effective parameters to precisely predict the strength alterations. Also, the bigger the number of input data sets, the accurate the model predictions. Therefore, the current results were combined with 9 previous studies, which take other effective parameters into account as well.

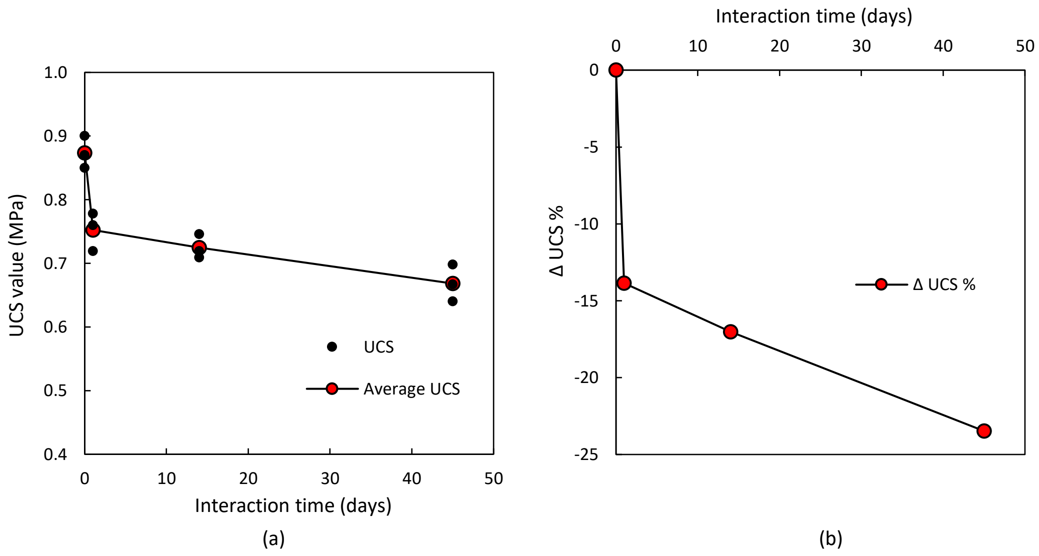

Figure 8-1 - Strength results from the current experimental study: a) variation of UCS with CO_2 interaction time and, b) reduction of UCS with CO_2 interaction time.

8.2.3 Selection of input parameters

The regression analyses and the machine learning techniques utilize three input parameters: 1) coal rank, 2) CO_2 saturation pressure and 3) CO_2 interaction time to predict the consequent UCS value. The latter two parameters are obvious, as confirmed from the current study and from a number of previous studies (Perera; Perera et al., 2011a; Ranathunga et al., 2016a; Ranathunga et al., 2016b). However, each study considered in this paper has used different coal types, acquired from several coal basins with diverse geological settings. For instance, the current study, Ranathunga et al. (2016b), Perera et al. (2011b), Viete and Ranjith (2006), Ranathunga et al. (2016a) used the coal specimens obtained from Latrobe Valley, Victoria, Australia. Perera et al. (2013), Ranjith and Perera (2012), Ranjith et al. (2010) used coal specimens obtained from Southern Sydney Basin, Australia, Vishal et al. (2015) used Gondwana coal from Jharia coalfield, India and Bagga et al. (2015) used specimens from Korba coalfield, Madhya Pradesh, India. The coal specimens belong to different coal ranks and depict largely varied strength results, even with same saturation conditions. For example, the UCS values for bituminous coal specimens are in the range of 20-33 MPa (Perera et al., 2013), whereas the UCS for Lignite samples are in the range of 0.6-3 MPa (Ranathunga et al., 2016b), under same saturation conditions. Thus, a general trend cannot be established by combining all the studies, without considering another effective parameter that coalesces the coal types or their natural strengths. Although, density is one effective parameter that represents the rank or the natural coal strength, the CO_2 saturation affects the sample bulk density due to micro-structural alterations and micro-cracking. Consequently, it cannot be used as an effective independent input parameter, without knowing the actual densities of the CO_2-saturated samples tested for strengths. Alternatively, fixed carbon content directly relates to the coal rank and its natural strength (Zhu, 2014), and does not significantly vary with the CO_2 saturation. Figure 8-2 exhibits a positive correlation between natural coal strength and fixed carbon content with a R^2 of 0.9905, which is produced with the experimental data of unsaturated (i.e. natural) samples from the selected studies. Based on this argument, we selected three independent, effective input parameters namely, coal type (i.e. fixed carbon content) that represents the natural coal strength, CO_2 saturation pressure and CO_2 interaction time, and one output parameter: UCS.

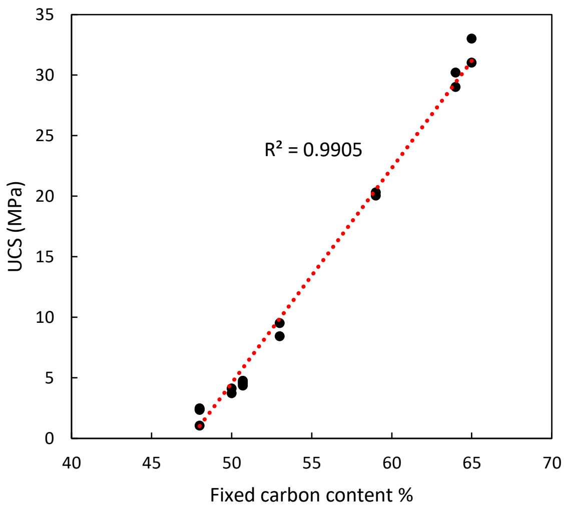

Figure 8-2 - Relationship between natural coal strength and fixed carbon content (developed with data from (Bagga et al., 2015; Perera; Perera et al., 2011b; Perera et al., 2013; Ranathunga et al., 2016a; Ranathunga et al., 2016b; Viete and Ranjith, 2006; Vishal et al., 2015)).

It should be noted that besides these three parameters, there exist many other effective parameters that affect the CO_2-induced coal mechanical alteration. For instance, CO_2 affects coal mechanical properties in many ways due to its unique characteristics, such as adsorption capacity, diffusivity, viscosity, phase change etc. CO_2 adsorption on to coal seams can alter coal micro-structure due to adsorption-induced swelling, mineral dissolution, hydrocarbon mobilization. In soft computing models, we address the effect of CO_2 by considering saturation time and pressure. Depending on these two parameters, CO_2 affect coal structure and alter mechanical strength at different levels. For instance, the incremental variation of saturation pressure may replicate the effect of CO_2 phase change from subcritical to supercritical region. Hence, we are able to capture the effect of CO_2 on coal mechanical strength to some extent. However, other parameters cannot be reliably utilized in models, due to lack of published data in considered studies. Input data should be reliable and consistent throughout the whole data sets to successfully utilize them in the models. Since this study was initiated by combining a number of previous studies, aforementioned three parameters were the consistent and reliable parameters that could be collected from published data; thus, the current study is focused on those three input parameters.

The input and output parameter ranges are defined in Table 8-1. Totally, 96 data sets were used for the study, including the current experimental results and data obtained from the literature. There is no ideal ratio between training and testing data sets, where previous studies have often used 50:50 (Taghavifar and Mardani, 2014), 70:30 (Sharma et al., 2017a; Singh et al., 2013), 80:20 (Ranjith and Khandelwal, 2012; Sharma et al., 2017b) split ratios. Hence, we selected 70:30 ratio for training/validation and testing of the models. From the total data sets, 66 sets were used to train the models, and two separate sets of 15 data were used to validate the models and to test the model performance.

Table 8-1 - Ranges of the parameters used for regression analysis and machine learning techniques.

Parameter		**Range**
Input	CO_2 interaction time (days)	0 - 365
	CO_2 saturation pressure (MPa)	0 - 16
	Fixed carbon content (coal type) (%)	45 - 65
output	Measured UCS (MPa)	0.639 - 33

8.2.4 Multivariate Regression Analysis (MRA)

Multivariate or multiple regression analysis is a simple but powerful statistical tool that allows to assess the association between two or more independent variables (or predictors) and a single dependent variable. Linear multiple regression analysis (L-MRA) provides linear relationships between input and output parameters, whereas non-linear multiple regression analysis (NL-MRA) provides non-linear relationships. L-MRA performs least-square fit to solve the data sets by forming a regression matrix to solve the simultaneous equations and to determine the coefficients using the backslash operator. The generalized equation between independent and dependent variables for L-MRA is in the form of Eq. 8-1.

$$y = \alpha + \beta_1 x_1 + \beta_2 x_2 + \cdots + \beta_n x_n \qquad \text{[8-1]}$$

where, y is the dependent/output variable and $x_1, x_2, ..., x_n$ are the independent/input variables.

Both L-MRA and NL-MRA methods have been widely used in the field of rock mechanics to build predictive models. For instance, a number of studies were conducted to analyse *in-situ* deformation modulus of rocks using various parameters namely, elastic modulus, compressive strength, disturbance factor, degree of weathering etc. (Barton, 2002; Hoek and Diederichs, 2006; Kayabasi et al., 2003; Zhang and Einstein, 2004). Thermal damage of sandstone was calculated by Gautam et al. (2016) using compressive strength, failure strain, temperature and elastic modulus as input parameters. Salimi et al. (2016) used joint quality rating, rock quality designation and compressive strength to determine the field penetration index of basalt and pyroclastic rocks. The compressive strength of jet grouted column was predicted by Akan et al. (2015) using grout and water pressure, cement water ratio, lifting-rotate speed and eater flow. In the current study, we execute both L-MRA and NL-MRA using fixed carbon content, CO_2 saturation pressure and CO_2 interaction time as input parameters to predict the consequent UCS of coal. Same data sets were used for MRA analyses, which are used to train/test the ANN and ANFIS models, and the outcomes were incorporated to assess the prediction performance of the soft computing models.

8.2.5 Artificial Neural Network (ANN)

Artificial neural networks (ANN) are a form of the machine learning algorithm, which is constructed on artificial intelligence and approximation algorithms. The structure is roughly based on that of a human brain and is capable of learning from their environment, without being explicitly programmed with rules to follow. The ANN techniques are advantageous than statistical data classification methods, as they do not require a priori knowledge on statistical distributions of classes in original data sources to categorize them (Ranjith and Khandelwal, 2012). The algorithm is capable of learning trends from large data sets, preserving the experience and using it for predictions.

ANN has been successfully used in multiple geo-mechanics problems to predict the desired property from a number of given input parameters. For instance, the compressive strengths of sedimentary and crystalline rocks were estimated by means of P and S wave velocities, point load index, porosity, grain size parameters, density, water saturation, etc. (Ceryan et al., 2013; Meulenkamp and Grima, 1999; Singh et al., 2001; Zorlu et al., 2008). Roy et al. (2018) used CO_2 saturation pressure, UCS to predict the young’s modulus of coal. Ranjith and Khandelwal (2012) predicted the airflow rate in fractured rock using cell pressure, air inlet and outlet pressures. The shearing behaviour of rock joints was predicted by Neto et al. (2017). Shi et al. (2016) used ANN-based extreme learning method to evaluate the organic content of shale.

An ANN structure is basically composed of three layers: an input layer, a hidden layer and an output layer. The number of hidden layers depend on the performance of the model and the available data sets but should be kept minimum to reduce computational burden (Ham and Kostanic, 2000). Each layer contains multiple processing units called ‘neurons’. The selection of the number of neurons is critical because too less or too many neurons can cause underfitting or overfitting the data, respectively. Hence, the optimized model is developed through trial and error method. ANN utilizes three types of learning paradigms: 1) supervised learning, 2) unsupervised (self-organized) learning and, 3) reinforcement learning. The supervised learning technique is used in this study, as it adopts the multilayer back-propagation algorithm for the training, which is considered as the most robust and versatile technique (Simpson, 1990). The back-propagation algorithm is based on the model weights, biases and the selected error function. At the learning stage, input data are processed forward through the network to the output layer (forward pass) and the resultant output is compared with the corresponding measured value. The error is processed back through the network (backward pass), updating the weights and biases of each neuron (Khandelwal and Singh, 2006). The whole process is called a 'feed-forward back-propagation algorithm' and is repeated for the entire data set until the network error converged to a threshold minimum, which is determined by the defined error function. The network architecture is defined in Figure 8-3, and the process is described below.

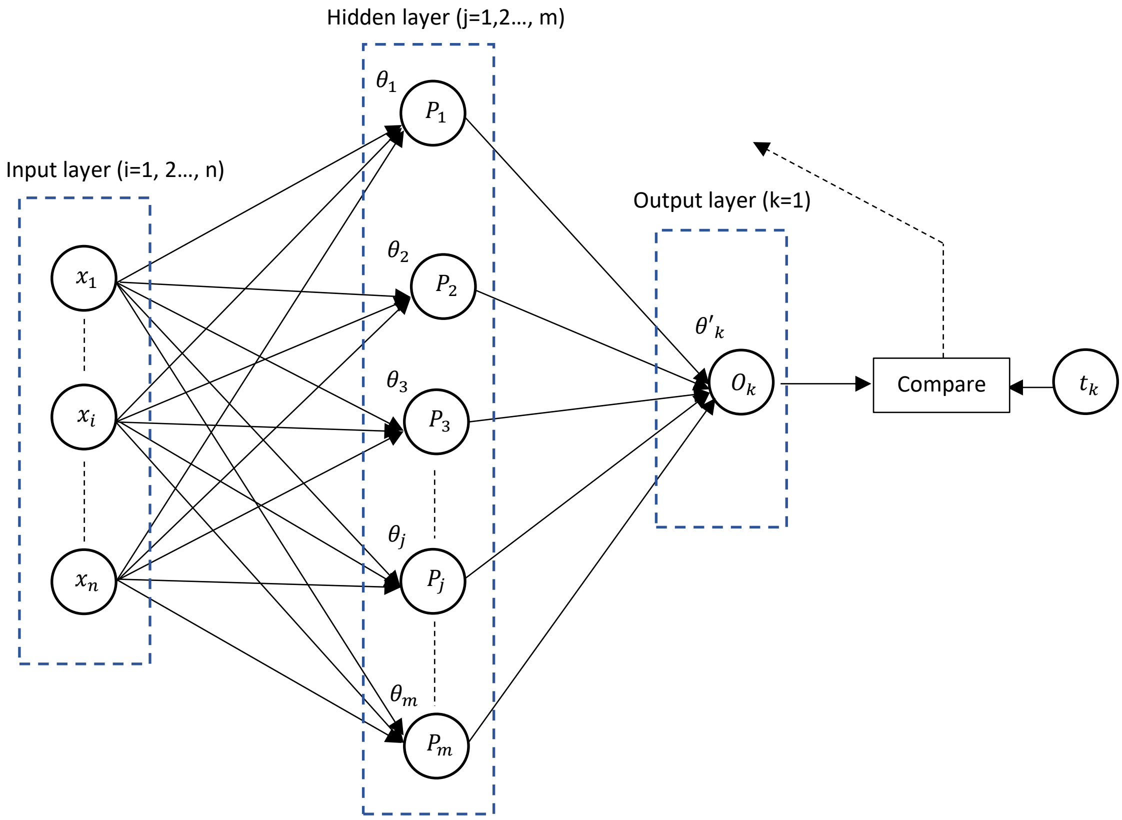

Figure 8-3 - Network architecture of ANN structure with feed-forward back-propagation network.

In Figure 8-3, the structure is fed with 'n' number of input parameters *(see Eq.8-2)* and the j^{th} neuron in the hidden layer is connected with the 'n' number of inputs.

$$x_i = (x_1, x_2, x_3 \ldots, x_n) \qquad \ldots\ldots\ldots\ldots [8\text{-}2]$$

The net input values in the hidden layer will be:

$$Net_j = \sum_{i=1}^{n} x_i w_{ij} + \theta_j \qquad \text{……….. [8-3]}$$

where x_i is input unit, w_{ij} is weight on the connection of i^{th} input and j^{th} neuron and θ_j is bias in the j^{th} neuron.

An activation function ($f(n)$) is used to calculate the net output from the hidden layer, as given in Eq. 8-4. We use 'hyperbolic tangent sigmoid transfer function (tansig)' as the activation or the transfer function, as given in Eq. 8-5.

$$P_j = f(Net_j) \qquad \text{……….. [8-4]}$$

$$f(n) = \frac{2}{1+e^{-2n}} - 1 \qquad \text{……….. [8-5]}$$

The net input for the output layer (3rd layer) is:

$$Net_k = \sum_{j=1}^{m} P_j w_{jk} + \theta'_k \qquad \text{……….. [8-6]}$$

Again, the output from the output layer (predicted value from ANN model) is:

$$O_k = f(Net_k) \qquad \text{……….. [8-7]}$$

Now, the predicted output is compared with the desired output. The error at k^{th}output in the output layer is:

$$e_k = t_k - O_k \qquad \text{……….. [8-8]}$$

where, t_k is desired output and O_k is ANN predicted output.

The total error function (performance) is given by the mean squared error (MSE):

$$E = \frac{1}{n}\sum_{k=1}^{n}(t_k - O_k)^2 \qquad \text{……….. [8-9]}$$

Once the error is calculated for a forward pass, the training of the network is basically a process of determining the optimum weights and biases through minimizing the error. The descent down error surface is made using the TRAINGDX function, which combines adaptive learning rate with momentum training. LEARNGDM is used as the adaptive learning function to calculate the weight (or bias) change (∇w_{jk}) for a given neuron *(see Eq. 8-10)*.

$$\nabla w_{jk} = m_c \delta w_{jk(prev)} - \eta m_c (\delta E / \delta w_{jk}) \qquad \text{……….. [8-10]}$$

where, m_c is momentum coefficient, $w_{jk(prev)}$ is previous change to the weight, η is learning rate parameter and E is error function or performance.

The update of weights for the $(n+1)^{th}$ pattern is given as:

$$w_{jk(n+1)} = w_{jk(n)} + \nabla w_{jk(n)} \quad \text{........... [8-11]}$$

Each pass through all the training patterns is called an epoch. This procedure is repeated with each data set assigned for the network training for a user-specified number of epochs until the error becomes minimal. The model parameters used in the current study are given in Table 8-2.

Table 8-2 - Model parameters and the network architecture of the ANN model.

Parameter	Value
Number of input neurons	3
Number of output neurons	1
Number of hidden layers	1
Number of hidden neurons	5
Number of training epochs	1000
Number of total datasets	96
Number of training datasets	66
Number of validation datasets	15
Number of testing datasets	15
Network type	Feed-forward back-propagation
Transfer function	TANSIG
Error (Performance) function	MSE
Training function	TRAINGDX
Adaptation learning function	LEARNGDM

8.2.6 Adaptive neuro-fuzzy inference system (ANFIS)

Adaptive neuro-fuzzy inference system (ANFIS) often provides better prediction models, as it has both the learning capability of ANN and reasoning capability of fuzzy inference system (FIS), using the if-then rule. The fundamental structure is a superset of neural network paradigms with the capability of supervised learning. ANFIS structure is typically composed of five layers: 1) fuzzification layer, 2) rule antecedent layer, 3) rule strength normalization layer, 4) rule consequent layer, and 5) rule inference layer (Mohammadi and Montazeri Gh, 2015) *(see Figure 8-4)*. The configuration of the multilayer adaptive feed-forward network generates a single-node output by performing a static-node function on its incoming signals. A learning algorithm is adopted in ANFIS to determine the optimum parameters of the equivalent fuzzy inference system. The parameter optimization is done at the training stage by minimizing the error between actual and target output.

The method is widely used in the field of rock mechanics to build predictive models to evaluate rock mechanics parameters. For instance, Sharma et al. (2017a) used neural network and fuzzy systems to predict UCS of 13 types of rock samples, using P wave velocity, density and slake durability index as input parameters. Sharma et al. (2017b) used effective stress and injection pressure to predict the permeability of bituminous coal. Singh et al. (2013) predicted the UCS of rock samples using P and S wave velocities and the density of rock.

We use a Sugeno-type fuzzy inference system (Takagi and Sugeno, 1985) with the hybrid learning algorithm to tune the membership function parameters. The hybrid learning algorithm applies a combination of gradient descent algorithm and least-squares algorithm to search for the optimal parameters (Rezaei et al., 2014). Since the hybrid approach reduces the search space dimensions of the back-propagation method, it converges much faster (Hamdan and Garibaldi, 2010). Four Gaussian-type membership functions are used for each input. The optimum number of membership functions were determined by a trial and error method, in which the number of functions per each input was incrementally varied until the model outputs satisfactory results with a minimum complexity. Figure 8-4 illustrates the architecture of the 5-layer ANFIS model. The equations that govern the five layers may be expressed in the following manner *(see Eqs. 8-12 to 8-17).*

$$(O_1)_{ij} = \mu_{A_{ij}}\left(x_{j,}\overline{x}_{ij}, \sigma_{ij}\right) \quad ; i = 1, \dots, n, \quad j = 1, \dots, m \qquad \text{[8-12]}$$

$$\mu_{A_{ij}}\left(x_{j,}\overline{x}_{ij}, \sigma_{ij}\right) = e^{-\left(x_j - \overline{x}_{ij}\right)^2/2\sigma_{ij}{}^2} \qquad \text{[8-13]}$$

$$(O_2)_k = w_k = \prod_{i=1}^{m} \mu_{A_{ik}}(x_i) \quad ; k = 1, \dots, r \qquad \text{[8-14]}$$

$$(O_3)_k = \overline{w}_k = \frac{w_k}{\sum_{i=1}^{r} w_i} \qquad \text{[8-15]}$$

$$(O_4)_k = \overline{w}_k f_k = \overline{w}_k\left(p_{k0} + \sum_{j=1}^{m} p_{kj} x_j\right) \qquad \text{[8-16]}$$

$$O_5 = y = \sum_{i=1}^{r} \overline{w}_i f_i \qquad \text{[8-17]}$$

where, O_i is the output of the i^{th} layer, m, r, and n are the number of inputs, number of rules, and the number of membership functions for each input, respectively. $\mu_{A_{ij}}$ is the Gaussian membership function *(see Eq. 8-13)*, $\overline{x}_{ij}$ and σ_{ij} are the mean value and variance of each membership function, respectively. y is the ANFIS predicted output, t is the actual output of the corresponding input data set. f_k is the consequent part function in the k^{th} rule and p_{kj} is the scalar coefficients of function "f" (Mohammadi and Montazeri Gh, 2015). The model parameters used for the ANFIS are summarized in Table 8-3.

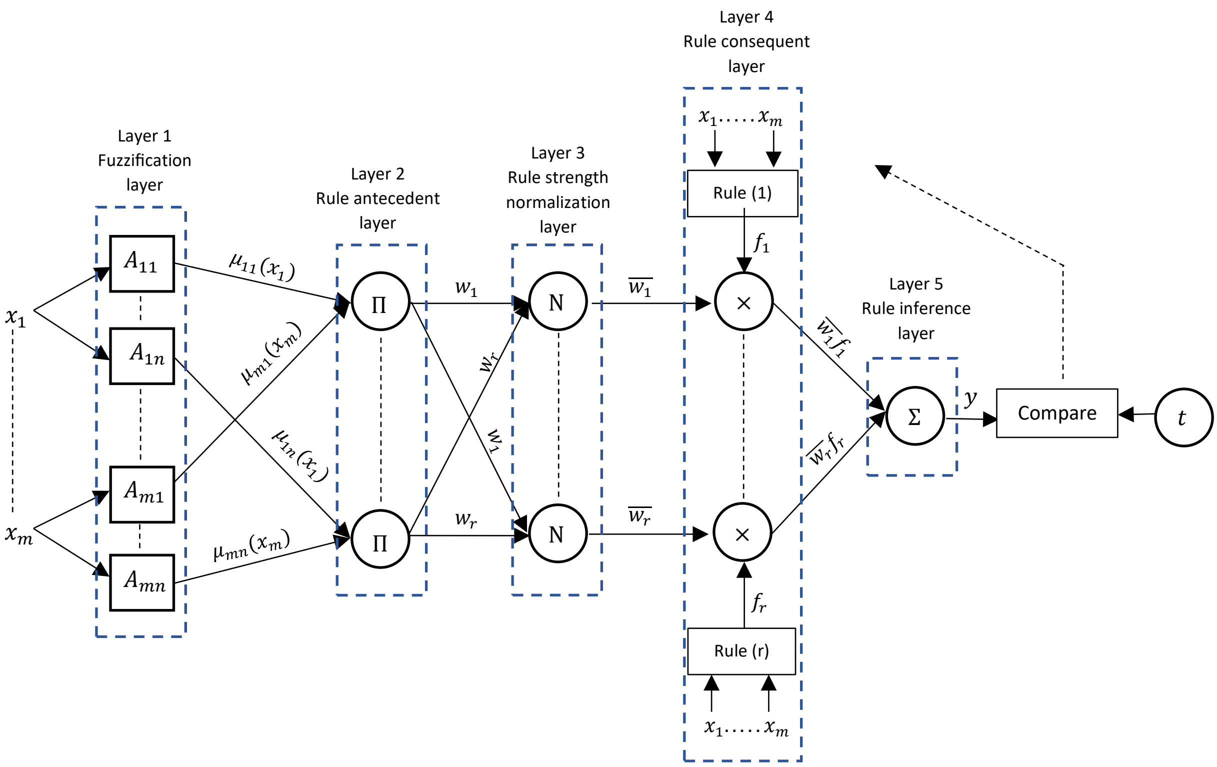

Figure 8-4 - Network architecture of ANFIS with m inputs and one output, equivalent to Sugeno-type fuzzy inference structure.

Table 8-3 - Model parameters and the network architecture of the ANFIS model

Parameter	Value
Number of training epochs	500
Number of total datasets	96
Number of training datasets	81
Number of testing datasets	15
Number of membership functions	4 for each input [4 4 4]
Input membership function type	GAUSSMF
Output type	Constant
Parameter tuning method	Hybrid

8.2.7 Results and Discussion

8.2.7.1 Multivariate Regression Analysis (MRA) results

Both L-MRA and NL-MRA were executed with 81 data sets at a 95% confidence level. The statistical parameters of the L-MRA analysis are tabulated in Table 8-4. Based on the developed model, the linear relationship between UCS and the input parameters can be presented in the form of Eq. 8-18. Referred to Eq. 8-18, 15 different data sets were used for the testing of the accuracy of the developed model. Figure 8-5 shows the relationship between L-MRA predicted and the actual UCS values of both training and testing stages. It is apparent from the statistical parameters *(see Table 8-4)* and correlation figures *(see Figure 8-5)* that L-MRA does not provide an acceptable model to predict the consequent strength alterations of coal using the particular input parameters.

The simple non-linear relationships between the output and each individual input parameter have depicted that fixed carbon content has the best relationship with UCS in the form of a power law, whereas that of CO_2 saturation pressure and CO_2 interaction time are in the form of exponential functions. Based on this observation, we performed an NL-MRA using similar functions for input parameters and obtained a non-linear relationship between multiple input values and the UCS, as given in Eq. 8-19. Figure 8-6 was constructed to illustrate the relationship between NL-MRA predicted and actual UCS values for both training and testing stages. It is found that the R^2 value is around 0.78 in both cases, which is approximately similar to the results of L-MRA analysis. Thus, it is concluded that both L-MRA and NL-MRA analyses fail to produce satisfactory models for the given conditions; thus, more advanced tools like machine learning techniques are required to accurately model the strength alterations of CO_2-saturated coal masses.

$$UCS = -45.75 + 1.024\,(FC) - 0.4339\,(P_i) + 0.00476\,(t_i) \qquad \text{[8-18]}$$

$$UCS = 0.032\,(FC)^{1.725} - 1.443e^{-0.264\,P_i} + 5.178e^{-130.01t_i} - 24.273 \qquad \text{[8-19]}$$

where, FC is the fixed carbon content (%), P_i is the saturation pressure (MPa), and t_i is the interaction time (days).

Table 8-4 - Statistical information of L-MRA

Statistical parameter	Value
Multiple R	0.886873
R Squared	0.786544
Adjusted R Squared	0.778119
Standard Error	3.862389

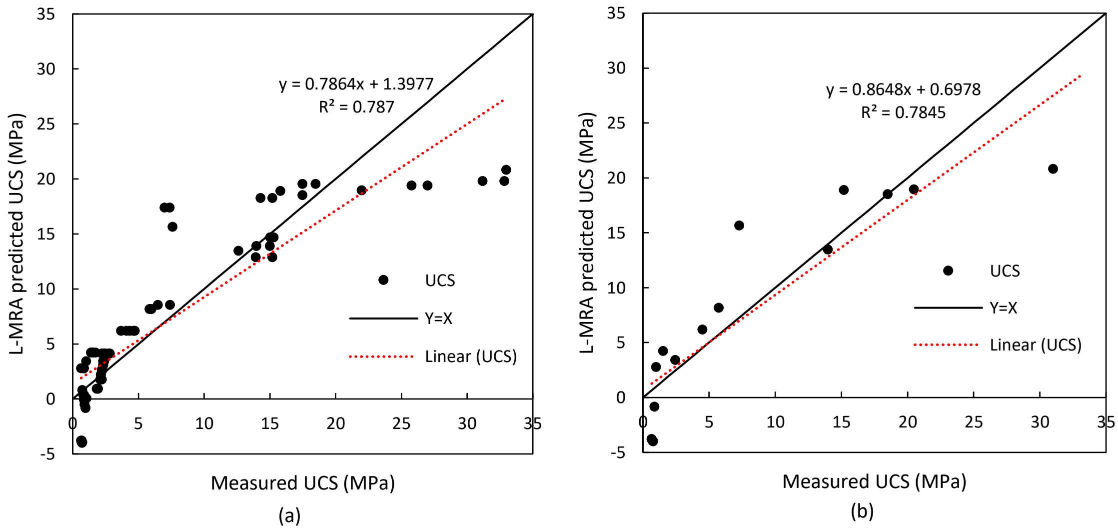

Figure 8-5 - The correlation between L-MRA predicted UCS values and the measured UCS values at a) training stage and, b) testing stage.

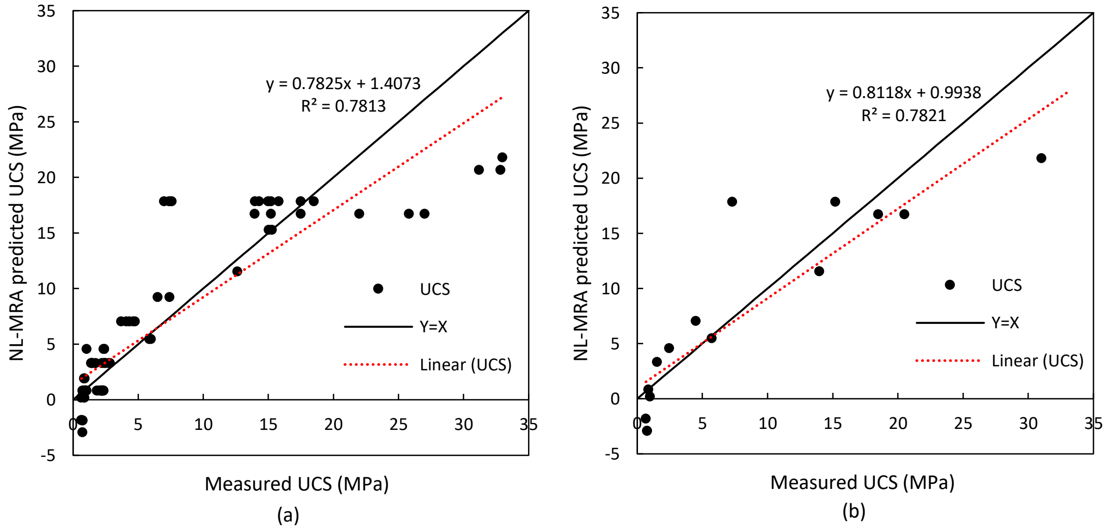

Figure 8-6 - The correlation between NL-MRA predicted UCS values and the measured UCS values at a) training stage and, b) testing stage.

8.2.7.2 Artificial Neural Network (ANN) results

The optimum ANN structure was selected by a trial and error method, in which a number of ANN structures were executed with the data sets to get the optimum model with the simplest structure. The optimum model parameters are illustrated in Table 8-2. Figure 8-7 displays the validation curve of the model, in which the mean squared error (MSE) for the training, validation, and testing stages decrease with increasing epoch number and the best validation performance is registered at epoch 988. The correlation between the ANN predicted and measured UCS for both training, and testing stages are shown in Figure 8-8. The scatter plots reveal that for the output parameters at both stages, the predictability was satisfactory and data points were well-concentrated along the 1:1 slope line and the linear trendline, with R^2 equal to 0.985 and 0.993 for training and testing stages, respectively.

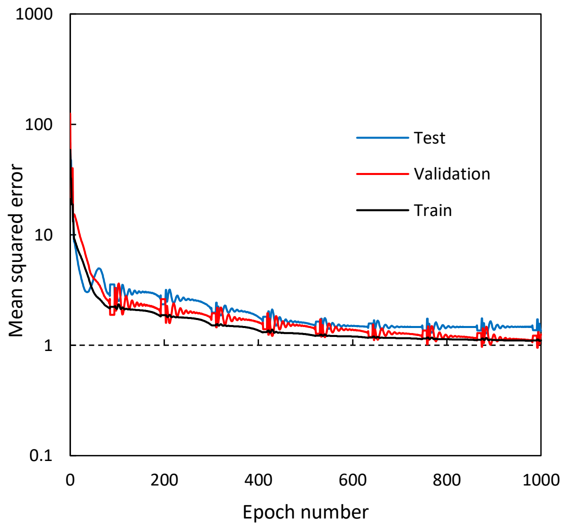

Figure 8-7 - Validation curve for the ANN model.

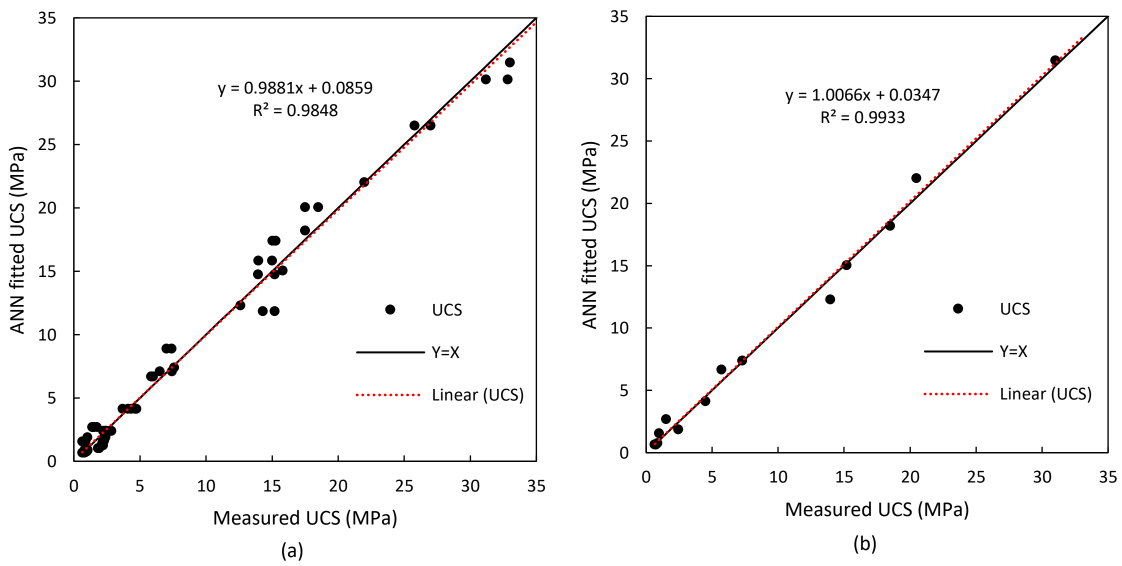

Figure 8-8 - The correlation between ANN predicted UCS values and the measured UCS values at a) training stage and, b) testing stage.

8.2.7.3 Adaptive neuro-fuzzy inference system (ANFIS) results

Same data sets as used for MRA and ANN were used to train and test the ANFIS model. Similar to ANN model, the optimum ANFIS structure was obtained with a trial and error method, by changing the number of membership functions and their types in each input. The optimum model parameters that give the highest correlation with the simplest structure for the used data sets are summarized in Table 8-3. The model was trained with 500 epochs, and the training error has reached to a minimum of 0.303 after 224 epochs *(see Figure 8-9)*. Figure 8-10 illustrates the correlation between ANFIS predicted and measured UCS values at both training and testing stages. The scatter plot confirms the positive correlation between the output values at both stages, as the R^2 values equal to 0.9986 and 0.9954 for training and testing data sets, respectively. In fact, from the four models developed in this study, ANFIS model depicts the best correlation between two values, which confirms that proposed ANFIS model can precisely predict the coal UCS alterations, using the coal type, CO_2 saturation pressure and CO_2 interaction time as input parameters.

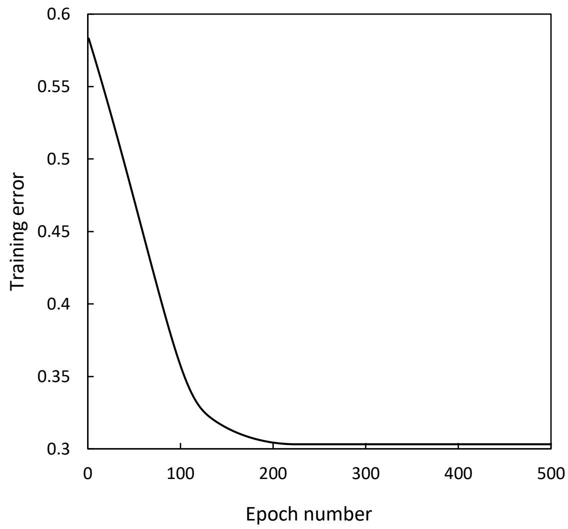

Figure 8-9 - Training error minimization in the ANFIS model.

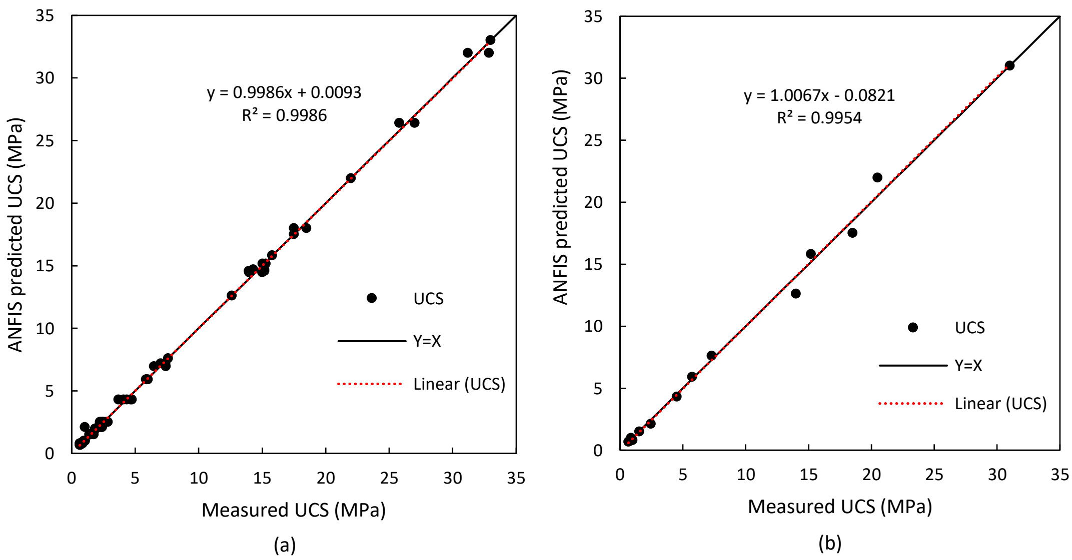

Figure 8-10 - The correlation between ANFIS predicted UCS values and the measured UCS values at a) training stage and, b) testing stage.

8.2.7.4 Model performance evaluation

The input parameters, measured (actual) UCS, predicted UCS and the residual error for tested 15 data sets are summarized in Table 8-5. The measured UCS and the predicted UCS by four models for the tested 15 samples are plotted in Figure 8-11 (a). Figure illustrates that both ANN and ANFIS predicted UCS values follow the same trend as measured UCS values, which confirms the satisfactory predictability of the two models. However, the L-MRA and NL-MRA predicted UCS values significantly deviate from the measured values, indicating that MRA models fail to provide accurate predictions for coal UCS alterations, considering given input parameters.

The discrepancy between MRA predicted values and the measured UCS values can be clearly seen in Figure 8-11 (b), which is plotted with the residual errors between measured and predicted values. The residual error of both ANN and ANFIS predicted values are closer to zero, whereas that of L-MRA and NL-MRA reach up to about 10.5 MPa in some cases. Such relatively large errors are not acceptable, as the UCS for coal specimens varies only between 0.639 – 33 MPa, *(see Table 8-1)* for a range of coal types and CO_2 saturation conditions.

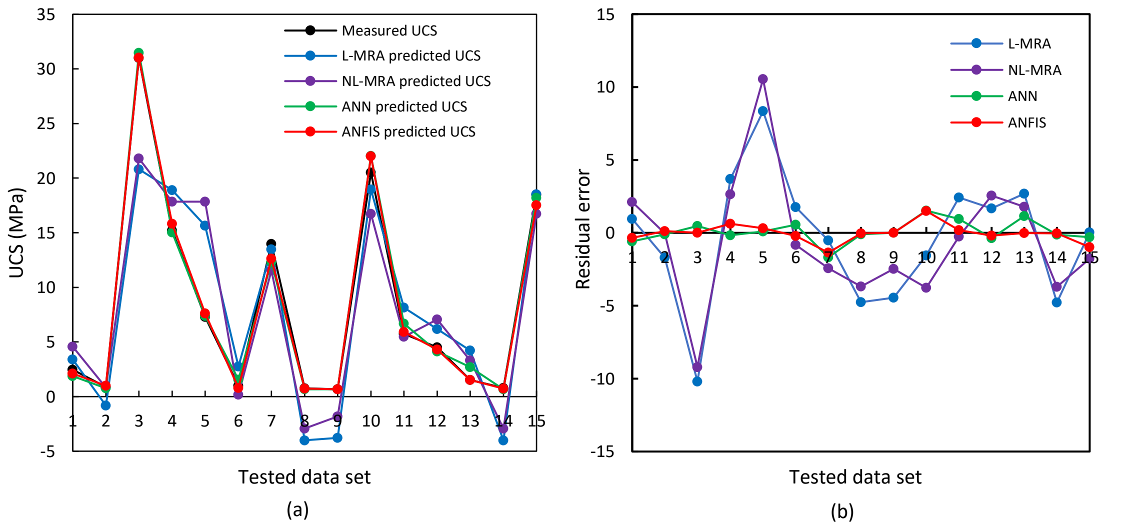

Figure 8-11 – a) Measured UCS and predicted UCS by L-MRA, NL-MRA, ANN and ANFIS models for the tested 15 data sets and, b) residual error of L-MRA, NL-MRA, ANN and ANFIS predicted UCS values for the tested 15 data sets.

Table 8-5 - Testing data set with measured UCS values and predicted UCS values by L-MRA, NL-MRA, ANN and ANFIS models.

Testing data set	**Input parameters**			**Measured UCS (MPa)**	**Predicted UCS (MPa)**				**Residual error (MPa)**			
	FC content (%)	**CO_2 saturation pressure (MPa)**	**CO_2 interaction time (days)**		**L-MRA**	**NL-MRA**	**ANN**	**ANFIS**	**L-MRA**	**NL-MRA**	**ANN**	**ANFIS**
1	48	0	0	2.46	3.40	4.56	1.88	2.11	0.94	2.10	-0.58	-0.35
2	48	10	21	0.87	-0.83	0.82	0.77	0.99	-1.70	-0.05	-0.10	0.12
3	65	0	0	31.01	20.81	21.80	31.48	31.02	-10.2	-9.21	0.47	0.01
4	65	4.5	7	15.2	18.90	17.84	15.04	15.83	3.70	2.64	-0.16	0.63
5	65	12	7	7.3	15.64	17.84	7.39	7.61	8.34	10.5	0.09	0.31
6	48	1.5	3	1	2.77	0.17	1.56	0.80	1.77	-0.83	0.56	-0.20
7	59	3	21	13.98	13.47	11.55	12.30	12.62	-0.51	-2.43	-1.68	-1.36
8	45	10	1	0.76	-4.00	-2.92	0.66	0.73	-4.76	-3.68	-0.10	-0.03
9	45	10	45	0.667	-3.79	-1.82	0.67	0.67	-4.46	-2.48	0.00	0.00
10	64	2	7	20.5	18.96	16.72	22.02	22.00	-1.54	-3.78	1.52	1.50
11	53	1	14	5.73	8.16	5.47	6.68	5.92	2.43	-0.26	0.95	0.19
12	50.7	0	0	4.5	6.17	7.05	4.13	4.31	1.67	2.55	-0.37	-0.19
13	50.7	5	45	1.53	4.21	3.31	2.69	1.52	2.68	1.78	1.16	-0.01
14	45	10	1	0.778	-4.00	-2.92	0.66	0.73	-4.78	-3.70	-0.11	-0.05
15	64	3	7	18.5	18.52	16.72	18.20	17.53	0.02	-1.78	-0.30	-0.97

Except for R^2 value, there are numerous advanced methods to statistically evaluate the model performance. In order to validate the prediction performance of the four models, we consider a number of statistical parameters that assess the correlation between measured and predicted UCS values and their associated errors. The performance indices were selected to assess model performance in various aspects, especially covering the goodness of fit, error and variance. In fact, we use five statistical parameters: 1) coefficient of determination (R^2), 2) Nash–Sutcliffe model efficiency coefficient (E_f), 3) variance accounted for (VAF), 4) root mean square error (RMSE), and 5) mean absolute percentage error (MAPE) to assess the model performance. The first three parameters assess the goodness of fit between measured and predicted values, whereas the latter two parameters evaluate the associated error.

Coefficient of determination (R^2) is a statistical measure of how close the data are to the fitted regression line. As given in Eq. 8-20, the parameter essentially is the ratio between the explained sum squares to the total sum squares of the data. R^2 is an excellent indicator of the scatter data that varies between 0 to 1, depending on how well the data fit the regression line. A coefficient closer to 1 is an indicator of better goodness of fit for the observations. As illustrated in Table 8-6, ANN and ANFIS give R^2 values closer to 1, which in turn confirms the good fit between the measured and predicted UCS values. Nash–Sutcliffe model efficiency coefficient (E_f) is a normalized statistical parameter that determines the relative magnitude of the residual variance, compared to measured (actual) data variance (Nash and Sutcliffe, 1970) *(see Eq. 8-21)*. E_f indicates how well the plot of measured and model-predicted data fits the 1:1 line. The value of E_f varies between $-\infty$ and 1, with $E_f = 1$ being the optimal value. Similar to R^2 values, the ANFIS model gives the optimum E_f value, confirming the higher accuracy of the model *(see Table 8-6)*. Variance accounted for (VAF) is a statistical index that measures the model fit in terms of variance *(see Eq. 8-22)*. Statistically, a predictive model with VAF of 100% is considered to be excellent. Table 8-6 illustrates that VAF values for both ANN and ANFIS are greater than 99% that confirms the models' superior performance compared to both MRA models.

The root mean square error (RMSE) is frequently used to measure the difference between measured values and the predicted values by a model *(see Eq. 8-23)*. Simply, RMSE is the standard deviation of the residuals/prediction errors and indicates how concentrated the data is around the best fit line. The larger errors have a disproportionately large effect on RMSE because the effect of each error on RMSE is proportional to the size of the squared error. Consequently, RMSE is sensitive to outliers (Pontius et al., 2008). In general, an RMSE value closer to 0 indicates a good fit to the data. ANFIS model gives the least RMSE value for the used data set, followed by ANN, NL-MRA and L-MRA. It is noticeable that both ANN and ANFIS show relatively smaller RMSE values, compared to that of L-MRA and NL-MRA *(see Table 8-6)*, which confirms that ANN and ANFIS give relatively small errors than MRA for the executed data set. Mean absolute percentage error (MAPE), which is defined as in Eq. 8-24, measures the error size or the model accuracy as a percentage. MAPE is often used as an excellent statistical parameter to analyse the prediction performance of multiple models. The smaller the MAPE, the better the forecast. As given in Table 8-6, ANFIS model depicts the least MAPE value verifying the better prediction capability of the model. However, the MAPE values corresponding to both MRA models are greater than 100%, which confirms the poor performance of the conventional statistical models.

$$Coefficient\ of\ determination\ (R^2) = \left(\frac{\sum_{i=1}^{n}(t_i-\bar{t})(o_i-\bar{o})}{\sqrt{\sum_{i=1}^{n}(t_i-\bar{t})^2\sum_{i=1}^{n}(o_i-\bar{o})^2}}\right)^2 \qquad \text{………… [8-20]}$$

$$Nash–Sutcliffe\ model\ effciency\ coeffcient\ (E_f) = 1 - \frac{\sum_{i=1}^{n}(t_i-o_i)^2}{\sum_{i=1}^{n}(t_i-\bar{t})^2} \quad \text{........... [8-21]}$$

$$Variance\ accounted\ for\ (VAF) = \left(1 - \frac{var(t_i-o_i)}{var(t_i)}\right) \times 100\% \quad \text{........... [8-22]}$$

$$Root\ mean\ square\ error\ (RMSE) = \sqrt{\frac{\sum_{i=1}^{n}(t_i-o_i)^2}{n}} \quad \text{........... [8-23]}$$

$$Mean\ absolute\ percentage\ error\ (MAPE) = \frac{1}{n}\sum_{i=1}^{n}\left|\frac{t_i-o_i}{t_i}\right| \times 100 \quad \text{........... [8-24]}$$

where, t_i and o_i are the measured (actual) and model predicted values, respectively. $\bar{t}$ and $\bar{o}$ are the corresponding mean values and n is the number of tested data.

Table 8-6 - Statistical parameters used to assess the prediction performance of models

Parameter	Model			
	L-MRA	NL-MRA	ANN	ANFIS
Coefficient of determination (R^2)	0.7845	0.7821	0.9933	0.9954
Nash–Sutcliffe model efficiency coefficient (E_f)	0.7741	0.7769	0.9931	0.9953
Variance accounted for (VAF)	77.629	78.098	99.315	99.531
Root mean square error (RMSE)	4.305	4.277	0.755	0.621
Mean absolute percentage error (MAPE)	183.89	128.07	16.23	6.50

Overall, based on the results of the tested data sets and the determined statistical indices, it can be concluded that ANFIS model shows the highest prediction performance, followed by ANN and MRA models. Although, the prediction performance of ANN is quite similar to that of ANFIS and provide statistical parameters that are in acceptable ranges, L-MRA and NL-MRA prediction performances are not satisfactory in terms of all the statistical indices, which in turn concludes that general statistical models like MRA fail to precisely predict the complex strength alterations of different types of coal, saturated with CO_2 under various conditions. Advanced machine learning techniques are thus essential for precise prediction of CO_2-induced complex alterations of coal mass strength.

8.2.7.5 Forecasting the experimental results with the validated models

After the performance evaluation of the prediction models, we use ANN and ANFIS models to fit and forecast the current experimental data. Statistical indices summarized in Table 8-6 suggest that both MRA models fail to provide accurate UCS results for a given CO_2 saturation condition; thus, cannot be used as an effective prediction model. The current experiment was conducted with

Australian brown coal samples under fixed CO_2 saturation pressure. Therefore, the first two input parameters are fixed, and the consequent strength alterations occur only due to CO_2 interaction time. As illustrated in Figure 8-12 (a), the ANN and ANFIS models can successfully fit the experimental data with acceptable accuracy. Since the experimental data are limited only up to 45 days of CO_2 interaction time, the validated models are used to forecast the results for longer CO_2 interaction time *(see Figure 8-12 (b))*. The models are expected to provide accurate results within the data range that are used to train the models *(see Table 8-1)*. Results depict that CO_2 interaction causes a plummet and a gradual decrement of consequent UCS at short-term and, follows a level-off in the long-term interaction. Thus, it is evident that a significant strength alteration occurs soon after CO_2 interaction with coal mass and longer interaction causes only a gradual strength reduction, and the well-trained machine learning techniques can successfully capture this complex behaviour.

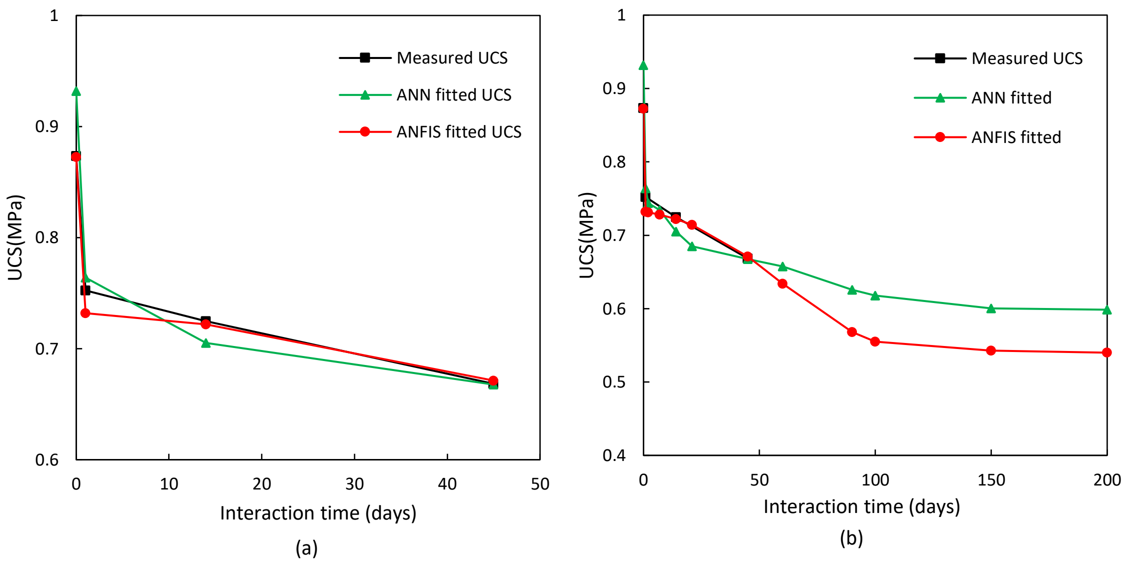

Figure 8-12 – a) ANN and ANFIS predicted results fitted with the experimental data from current study and, b) variation of coal UCS due to long-term CO_2 interaction, forecasted with ANN and ANFIS models.

The results of the present study are in line with most of the previous studies, which show that advanced machine learning techniques are essential to address most of the complex geo- and rock-mechanical problems. For instance, Armaghani et al. (2016) showed that ANN related models can reliably predict the UCS of sandstone in terms of Schmidt hammer porosity, P wave velocity and point load index, but L-MRA and NL-MRA fail to provide models with high accuracy. Sharma et al. (2017a) showed that UCS prediction of ANFIS is much better than MRA and ANN for 13 types of rocks. Roy et al. (2018) revealed that over MRA model, ANN and ANFIS models have a better capability to capture the variation of Young's modulus of coal in terms of UCS and CO_2 saturation pressure. Ranjith and Khandelwal (2012) predicted the airflow rate in rocks and found that prediction by ANN is very closer to the measured values, whereas prediction by MRA has a wide variation.

Overall, the current study reveals that CO_2-induced coal mechanical alteration is complicated and cannot be successfully predicted without utilizing advanced soft computing models. However, the study is based on experimental results collected from Australian and Indian coal samples; thus, is restricted to a limited number of data sets and range. Coal seams are extremely heterogeneous in nature and can render unpredictable behaviour depending on its geological environment. Moreover, besides all benefits of soft computing techniques, they are often faced with limitations due to a limited number of data sets used to train and validate the models. A model tuned with smaller data sets may depict increased errors if they are trained with considerably large data sets with the same model parameters. Models can always be improved by adding more data sets to cover a wide range. Although we consider totally 96 data sets and only three variables due to limited published data, there exists a number of effective parameters that possibly affect CO_2-induced coal mechanical behaviour. Hence, the study can be further improved and generalized by taking more effective input variables into account through more laboratory experiments and data collections. Furthermore, it is possible that most of the input parameters are strongly correlated, and their analysis may become unnecessarily complex and time-consuming. Thus, statistical methods like principal component analysis (PCA) may be useful to determine the most important parameters and to reduce the number of input parameters without affecting the variance of original data. PCA achieves dimension reduction by creating principal components, which are linear combinations of original variables. Hence, the conversion of collected data sets into principal components that are linearly uncorrelated to each other may reduce the unnecessary burden of data analysis, especially for the present type of studies, which are dealing with largely correlated input variables.

8.2.8 Conclusions

We present two advanced machine learning techniques: ANN and ANFIS to model and forecast the strength alteration of coal, under various CO_2 saturation conditions. Coal rank, CO_2 saturation pressure and CO_2 interaction time were used as input parameters, and the consequent UCS was considered as the corresponding output.

- Model results confirm that ANFIS and ANN have the best prediction capability with R^2 equal to 0.9954 and 0.9933, respectively. This was further confirmed with model performance indices. Both models have VAF > 99% and RMSE < 1, which confirm the models' higher accuracy in terms of goodness of fit and error. Thus, we conclude that both ANFIS and ANN models are able to successfully predict the CO_2-induced coal strength alterations.

- Both L-MRA and NL-MRA prediction performances are not satisfactory, as the R^2 values are only 0.7845 and 0.7821 for two models, respectively. For both cases, MAPE > 100%, which reveal the significant error associated with the model predictions. Thus, it is concluded that general statistical models fail to precisely predict the complex strength alterations.

- Experimental results, ANN and ANFIS model predictions confirm that although a significant coal strength reduction occurs soon after CO_2 interaction, longer interaction causes only a gradual strength reduction. In fact, the CO_2-induced coal strength reduction occurs at a higher rate of 12.1% in short-term (i.e. 0-1 day), whereas that in long-term (i.e.1-200 days) is approximately 0.08%, which reveals the complexity of the CO_2-induced coal strength alteration.

Overall, the study concludes that advanced soft computing models can be utilized as alternate indirect methods to estimate the CO_2-induced coal strength alterations. More optimized and well-trained models with large data sets are capable of precisely predicting the consequent strength alterations; thus, essential to at least partially replace the experimental procedure and to expedite the analysis.

Reference

Akan, R., Keskin, S. N., & Uzundurukan, S. (2015). Multiple Regression Model for the Prediction of Unconfined Compressive Strength of Jet Grout Columns. *Procedia Earth and Planetary Science, 15*, 299-303.

Armaghani, D. J., Amin, M. F. M., Yagiz, S., Faradonbeh, R. S., & Abdullah, R. A. (2016). Prediction of the uniaxial compressive strength of sandstone using various modeling techniques. *International Journal of Rock Mechanics and Mining Sciences, 85*, 174-186.

Armaghani, D. J., Mohamad, E. T., Momeni, E., & Narayanasamy, M. S. (2015). An adaptive neuro-fuzzy inference system for predicting unconfined compressive strength and Young's modulus: a study on Main Range granite. *Bulletin of Engineering Geology and the Environment, 74*(4), 1301-1319.

ASTM-D.2938. Standard Test Method for Unconfined Compressive Strength of Intact Rock Core Specimens. ASTM International, West Conshohocken, PA.

Aziz, N. I., & Ming Li, W. (1999). The effect of sorbed gas on the strength of coal–an experimental study. *Geotechnical and geological engineering, 17*(3/4), 387-402.

Bagga, P., Roy, D. G., & Singh, T. N. (2015). *Effect of carbon dioxide sequestration on the mechanical properties of Indian coal*. Paper presented at the ISRM Regional Symposium-EUROCK 2015. International Society for Rock Mechanics and Rock Engineering.

Barton, N. (2002). Some new Q-value correlations to assist in site characterisation and tunnel design. *International journal of rock mechanics and mining sciences (1997), 39*(2), 185-216.

Basu, A., & Aydin, A. (2006). Predicting uniaxial compressive strength by point load test: significance of cone penetration. *Rock Mechanics and Rock Engineering, 39*(5), 483-490.

Ceryan, N., Okkan, U., & Kesimal, A. (2013). Prediction of unconfined compressive strength of carbonate rocks using artificial neural networks. *Environmental Earth Sciences, 68*(3), 807-819.

Çobanoğlu, İ., & Çelik, S. B. (2008). Estimation of uniaxial compressive strength from point load strength, Schmidt hardness and P-wave velocity. *Bulletin of Engineering Geology and the Environment, 67*(4), 491-498.

Czapliński, A., & Hołda, S. (1982). Changes in mechanical properties of coal due to sorption of carbon dioxide vapour. *Fuel (Guildford), 61*(12), 1281-1282.

Ettinger, I. L. (1957). Gas medium in coal-breaking processes. *Fuel (Guildford), 36*(3), 298.

Gautam, P. K., Verma, A. K., Maheshwar, S., & Singh, T. N. (2016). Thermomechanical Analysis of Different Types of Sandstone at Elevated Temperature. *Rock Mechanics and Rock Engineering, 49*(5), 1985-1993.

Ham, F. M., & Kostanic, I. (2000). *Principles of Neurocomputing for Science and Engineering*: McGraw-Hill Higher Education.

Hamdan, H., & Garibaldi, J. M. (2010). Adaptive neuro-fuzzy inference system (ANFIS) in modelling breast cancer survival. *In FUZZ-IEEE*, 1-8.

Hoek, E., & Diederichs, M. S. (2006). Empirical estimation of rock mass modulus. *International journal of rock mechanics and mining sciences (1997), 43*(2), 203-215.

IEA. (2016). International Energy Agency. *Energy Technology Perspectives, OECD/IEA: Paris, France, 2016;ISBN 978-92-64-25234-9*.

Jasinge, D., Ranjith, P. G., & Choi, S. K. (2011). Effects of effective stress changes on permeability of latrobe valley brown coal. *Fuel (Guildford), 90*(3), 1292-1300.

Karacan, C. Ö. (2007). Swelling-induced volumetric strains internal to a stressed coal associated with CO2 sorption. *International Journal of Coal Geology, 72*(3-4), 209-220.

Kayabasi, A., Gokceoglu, C., & Ercanoglu, M. (2003). Estimating the deformation modulus of rock masses: a comparative study. *International journal of rock mechanics and mining sciences (1997), 40*(1), 55-63.

Khandelwal, M., & Singh, T. N. (2006). Prediction of blast induced ground vibrations and frequency in opencast mine: A neural network approach. *Journal of Sound and Vibration, 289*(4-5), 711-725.

Marbler, H., Erickson, K. P., Schmidt, M., Lempp, C., & Pöllmann., H. (2013). Geomechanical and geochemical effects on sandstones caused by the reaction with supercritical CO_2: an experimental approach to in situ conditions in deep geological reservoirs. *Environmental Earth Sciences, 69*(6), 1981-1998.

Meulenkamp, F., & Grima, M. A. (1999). Application of neural networks for the prediction of the unconfined compressive strength (UCS) from Equotip hardness. *International journal of rock mechanics and mining sciences (1997), 36*(1), 29-39.

Mohammadi, E., & Montazeri Gh, M. (2015). A New Approach to the Gray-Box Identification of Wiener Models With the Application of Gas Turbine Engine Modeling. *Journal of Engineering for Gas Turbines and Power, 137*(7), 071202.

Momeni, E., Armaghani, D. J., Hajihassani, M., & Amin, M. F. M. (2015a). Prediction of uniaxial compressive strength of rock samples using hybrid particle swarm optimization-based artificial neural networks. *Measurement, 60*, 50-63.

Momeni, E., Nazir, R., Armaghani, D. J., & Mohamad, E. (2015b). Prediction of unconfined compressive strength of rocks: a review paper. *Jurnal Teknologi, 77*(11), 43-50.

Nash, J. E., & Sutcliffe, J. V. (1970). River flow forecasting through conceptual models. Part1: A discussion of principles. *Journal of hydrology (Amsterdam), 10*(3), 282.

Nazir, R., Momeni, E., Armaghani, D. J., & Amin, M. M. (2013). Correlation between unconfined compressive strength and indirect tensile strength of limestone rock samples. *Electronic Journal of Geotechnical Engineering, 18*(1), 1737-1746.

Neto, S. A. D., Dantas Neto, S., Indraratna, B., Oliveira, D. A. F., & de Assis, A. (2017). Modelling the Shear Behaviour of Clean Rock Discontinuities Using Artificial Neural Networks. *Rock Mechanics and Rock Engineering, 50*(7), 1817-1831.

Perera, M. S. A. Effects of sub-critical and super-critical carbon dioxide saturation on the mechanical properties of Southern Sydney basin bituminous coal. *Applied Energy*.

Perera, M. S. A., Ranjith, P. G., Choi, S. K., & Airey, D. (2011a). The effects of sub-critical and super-critical carbon dioxide adsorption-induced coal matrix swelling on the permeability of naturally fractured black coal. *Energy, 36*(11), 6442-6450.

Perera, M. S. A., Ranjith, P. G., & Peter, M. (2011b). Effects of saturation medium and pressure on strength parameters of Latrobe Valley brown coal: Carbon dioxide, water and nitrogen saturations. *Energy, 36*, 6941-6947.

Perera, M. S. A., Ranjith, P. G., & Viete, D. R. (2013). Effects of gaseous and super-critical carbon dioxide saturation on the mechanical properties of bituminous coal from the Southern Sydney Basin. *Applied Energy, 110*, 73-81.

Pontius, R., Thontteh, O., & Chen, H. (2008). Components of information for multiple resolution comparison between maps that share a real variable. *Environmental and Ecological Statistics, 15*(2), 111-142.

Ranathunga, A. S., Perera, M. S. A., & Ranjith, P. G. (2016a). Influence of CO_2 adsorption on the strength and elastic modulus of low rank Australian coal under confining pressure. *International Journal of Coal Geology, 167*, 148-156.

Ranathunga, A. S., Perera, M. S. A., Ranjith, P. G., & Bui, H. (2016b). Super-critical CO_2 saturation-induced mechanical property alterations in low rank coal: An experimental study. *The Journal of supercritical fluids, 109*, 134-140.

Ranjith, P. G., Jasinge, D., Choi, S. K., Mehic, M., & Shannon, B. (2010). The effect of CO2 saturation on mechanical properties of Australian black coal using acoustic emission. *Fuel (Guildford), 89*(8), 2110-2117.

Ranjith, P. G., & Khandelwal, M. (2012). Artificial neural network for prediction of air flow in a single rock joint. *Neural computing & applications, 21*(6), 1413-1422.

Ranjith, P. G., & Perera, M. S. A. (2012). Effects of cleat performance on strength reduction of coal in CO_2 sequestration. *Energy (Oxford), 45*(1), 1069-1075.

Rezaei, K., Hosseini, R., & Mazinani, M. (2014). A Fuzzy Inference System for Assessment of the Severity of the peptic ulcers. *Computer Science & Information Technology, 10*, 263-271.

Roy, D. G., Guha Roy, D., & Singh, T. N. (2018). Regression and soft computing models to estimate young's modulus of CO 2 saturated coals. *Measurement (London. Print), 129*, 91-101.

Salimi, A., Rostami, J., & Moormann, C. (2016). TBM performance prediction in Basalt and Pyroclastic rocks of Deacn traps, A case study of Maroshi-Ruparel water supply tunnel. . *Rock Mechanics and Rock Engineering: From the Past to the Future, Taylor & Francis Group, London*, 975-980.

Sharma, L. K., Vishal, V., & Singh, T. N. (2017a). Developing novel models using neural networks and fuzzy systems for the prediction of strength of rocks from key geomechanical properties. *Measurement (London. Print), 102*, 158-169.

Sharma, L. K., Vishal, V., & Singh, T. N. (2017b). Predicting CO 2 permeability of bituminous coal using statistical and adaptive neuro-fuzzy analysis. *Journal of Natural Gas Science and Engineering, 42*, 216-225.

Shi, J., & Durucan, S. (2005). CO_2 storage in deep unminable coal seams. *Oil & Gas Science and Technology, 60*(3), 547-558.

Shi, X., Wang, J., Liu, G., Yang, L., Ge, X., & Jiang, S. (2016). Application of extreme learning machine and neural networks in total organic carbon content prediction in organic shale with wire line logs. *Journal of Natural Gas Science and Engineering, 33*, 687-702.

Simpson, P. K. (1990). *Artificial neural systems: foundations, paradigms, applications, and implementations*. Pergamon Press, New York.

Singh, R., Vishal, V., Singh, T. N., & Ranjith, P. G. (2013). A comparative study of generalized regression neural network approach and adaptive neuro-fuzzy inference systems for prediction of unconfined compressive strength of rocks. *Neural computing & applications, 23*(2), 499-506.

Singh, V. K., Singh, D., & Singh, T. N. (2001). Prediction of strength properties of some schistose rocks from petrographic properties using artificial neural networks. *International journal of rock mechanics and mining sciences (1997), 38*(2), 269-284.

Stevens, S., Kuuskraa, V., Gale, J., & Beecy, D. (2001). CO_2 Injection and Sequestration in Depleted Oil and Gas Fields and Deep Coal Seams: Worldwide Potential and Costs. *Environmental Geosciences, 8*(1), 200-209.

Taghavifar, H., & Mardani, A. (2014). Application of artificial neural networks for the prediction of traction performance parameters. *Journal of the Saudi Society of Agricultural Sciences, 13*(1), 35-43.

Takagi, T., & Sugeno, M. (1985). Fuzzy identification of systems and its applications to modeling and control. *IEEE Transactions on Systems, Man, and Cybernetics, SMC-15*(1), 116-132.

Viete, D. R., & Ranjith, P. G. (2006). The effect of CO_2 on the geomechanical and permeability behaviour of brown coal: Implications for coal seam CO_2 sequestration. *International Journal of Coal Geology, 66*, 204 – 216.

Vishal, V., Ranjith, P. G., & Singh, T. N. (2015). An experimental investigation on behaviour of coal under fluid saturation, using acoustic emission. *Journal of Natural Gas Science and Engineering, 22*, 428-436.

Wang, S., Elsworth, D., & Liu, J. (2013). Permeability evolution during progressive deformation of intact coal and implications for instability in underground coal seams. *International journal of rock mechanics and mining sciences (1997), 58*, 34-45.

White, C. M., Smith, D. H., Jones, K. L., Goodman, A. L., Jikich, S. A., LaCount, R. B., DuBose, S. B., Ozdemir, E., Morsi, B. I., & Schroeder., K. T. (2005). Sequestration of carbon dioxide in coal with enhanced coalbed methane recovery a review. *Energy & Fuels, 19*(3), 659-724.

Zhang, L., & Einstein, H. H. (2004). Using RQD to estimate the deformation modulus of rock masses. *International journal of rock mechanics and mining sciences (1997), 41*(2), 337-341.

Zhu, Q. (2014). Coal sampling and analysis standards. *IEA Clean Coal Centre, London, United Kingdom*.

Zorlu, K., Gokceoglu, C., Ocakoglu, F., Nefeslioglu, H. A., & Acikalin, S. (2008). Prediction of uniaxial compressive strength of sandstones using petrography-based models. *Engineering Geology, 96*(3-4), 141-158.

8.3 Chapter summary

This chapter presents a statistical analysis, developed using two machine learning techniques to predict the CO_2 interaction-induced strength modifications in coal. Except for experimental and numerical analyses, statistical modelling has proven to be another viable way of predicting the strength alterations in coal. Since the history of coal+CO_2 related experimental studies runs back to 1980s, there are plenty of experimental data available in the literature that can be used to develop statistical models under given reservoir conditions. The statistical data that capture the interrelationships between various influential parameters and the consequent strength alterations have been revealed in many of those studies; thus, can be utilized in developing and training the statistical models, based on machine learning techniques.

In summary, the study presents two machine learning techniques (i.e. ANN and ANFIS) to predict the mechanical property alterations in coal due to CO_2 interaction. The coal strength was defined in terms of UCS and the alterations were assessed with the combined effect of three influential parameters, that are the natural coal strength defined by fixed carbon content, the CO_2 interaction time and the CO_2 pore pressure. 96 data sets were used to train, validate and test the models, where modelling procedure and the parameters of the trained models are given in the methodology section. Apart from that, the same data sets were used in linear and non-linear regression analyses, and the results were compared with the outcomes of the machine learning techniques. The model results conclude that although the traditional regression analyses failed to capture the complex interrelationships between the input and the output parameters, the machine learning techniques accurately capture these relations, as they are capable of learning trends from multifaceted data sets, conserving the experiences and utilizing them for predictions. The 5 statistical indices used in the study confirms the superiority of model performance, concluding that the machine learning techniques can be utilized in predicting the CO_2 interaction-induced mechanical property alterations, with an acceptable accuracy. Finally, the intelligent prediction with well-trained models confirms that the adopted techniques are capable of accurately predicting the mechanical property alterations at long-term CO_2 interaction conditions, within the range of the used input and output parameters.

Overall, the collective conclusions from all the analyses presented in chapters 6, 7 and 8 confirm that the experimental, numerical and statistical analyses can be combinedly used to examine the complex mechanical degradation trends comprehensively in CO_2-interacted coal. Since the level of degradation depends on several influential parameters, further investigations, combining all the analyses are essential to attain definite conclusions and to precisely predict the mechanical modifications of targeted coal reservoirs under different CO_2 interaction conditions. The introduced numerical/statistical modelling approaches in the current research provide a better initiative and insights into the study area, except for the existing general material testing methods.

Part 4:

Concluding remarks

(Chapter 9)

CHAPTER 9

Conclusions, suggestions for future research and an insight into field-applications

9 Conclusions, suggestions for future research and insight into field-applications

This chapter provides the concluding remarks of the doctoral research, suggestions for future research that are inspired by the current work and an insight into field-application of the technique based on the findings of the research. In general, this research provides an understanding of the CO_2 sequestration process in coal reservoirs, by comprehensively investigating structural alterations occur in coal, upon CO_2 interaction. A systematic experimental analysis integrated with numerical and statistical modellings was conducted to improve the current understanding of the fully-coupled hydro-mechanical alterations. The investigation specifically focused on evaluating the CO_2 flow behaviour in coal cleat system and the coal matrices, the adsorption and the swelling processes, the alterations in local fracture aperture and concurrently the fracture permeability and the modifications of various mechanical parameters such as compressive strength, Young's modulus, brittleness index and dynamic moduli.

The motivation for the current research was enthused due to the complications faced by the current CO_2 sequestration process in coal. In fact, it was well-observed that the project efficiency and the safety are declined substantially in the long-run, due to the complex physico-chemical interactions occur in coal, upon CO_2 injection. A detailed understanding of the alterations in the influential parameters is essential to alleviate such issues. Although experimental analyses are really important to bring science into the field and to identify underlying physics and variation trends, a precise understanding of this complicated process cannot be guaranteed only with experimental findings, as the experimental observations are highly-specific to the coal type being tested and the testing conditions. Therefore, the underpinning multi-physics have to be studied in detail and grasped accurately; then the process should be numerically simulated by integrating the experimental results. Based on this notion, the current study evaluates the complex structural alterations occur in CO_2-interacted coal and addresses some of the important issues in the context of CO_2 sequestration through combined experimental, numerical and statistical analyses. The whole research question is divided into two main parts, according to the two defined research objectives, and are presented in parts 2 and 3 of the dissertation body. A number of conclusions pertinent to the CO_2 geo-sequestration process in coal seams are made, based on the findings of the study, and are provided in the subsequent section. Appropriate suggestions for the extension of the current research work in future are given in section 9.2, that can be further considered when addressing the in-depth matters associated with the CO_2 sequestration in coal. Finally, an insight into the field-application of the CO_2 sequestration technique is given in section 9.3, by discussing the possibility of utilizing the current findings for an effective and safer sequestration process in the field.

9.1 Conclusions

9.1.1 Conclusions drawn from objective 1 of the research

The first objective of the research is to evaluate the CO_2 flow behaviour and the subsequent coal seam response and the alterations, which was covered by developing numerical models, validated with experimental results. As the first phase, a rigorous numerical analysis was conducted on a single coal matrix block, in which the complete CO_2 diffusion–adsorption–swelling process was simulated by considering multiple CO_2 diffusion mechanisms in nano-scale coal pores.

- The validated model's results conclude that the coal matrix starts to swell immediately after the coal-CO_2 interaction takes place, where a substantial portion of the matrix swelling occurs long before the respective matrix reaches the pressure equilibrium state. This finding is quite important in determining the design parameters of the CO_2 sequestration process, as the swelling-induced permeability reduction is one of the major drawbacks, related to the project efficiency.

- In terms of accurately simulating the entire process, the sensitivity analysis infers that the model results are largely sensitive to Langmuir parameters that are used to model the CO_2 adsorption and the swelling processes. Since the particular parameters depend on the coal type being considered, they should be accurately determined for the targeted coal reservoir by appropriate experimental studies. Otherwise, the model predictions may be significantly deviated from the actual reservoir behaviour, causing numerous unforeseen issues during the CO_2 sequestration process.

- Further, the theoretically-extended diffusion approach concludes that the CO_2 diffusion in coal pores consists of multiple diffusion mechanisms, that are dependent on the pore attributes and the pore pressure. Since the total flow conductance and contribution of each diffusion mechanism to the total conductance are dependent on pore attributes and the pore pressure, it is important to incorporate such theoretically-extended diffusion mechanisms in the simulations – as it provides in-depth details of the realistic flow behaviours in nano-scale pores in coal matrices.

- In fact, identifying the dominating diffusion mechanisms and the contribution of each diffusion mechanism at a given reservoir condition is vital, as the diffusion process is the major transport mechanism in coal matrices, that controls the transference of the injected CO_2 from fractures to the potential adsorption sites. This, in turn, governs the stored CO_2 quantity in a particular coal reservoir and therefore, the efficiency and the productivity of the sequestration process.

As the second phase, the numerical simulation was extended on a fractured coal geometry through a DFM modelling approach, by considering multiple matrix block interactions. The model developed using an actual coal fracture network is particularly useful in simulating the realistic fully-coupled hydro-mechanical alterations in CO_2-interacted coal, as the simulation combines most of the underlying multi-physics associated with the process, such as the CO_2 flow in fractures, diffusion in matrices, adsorption, matrix swelling, modification of local fracture aperture and permeability, contact and frictional forces developed at fully-fracture closure, and ultimately the complete CO_2 flow behaviour. This phase includes two model scenarios for single-phase and two-phase flow behaviours, under *in-situ* reservoir conditions.

- The outcomes of the study conclude that the natural cleat system predominantly controls the CO_2 flow behaviour in coal, in which the rapid CO_2 flow through the fractures provides easy pathways for CO_2 to access the coal matrices. The distribution of fracture network affects the temporal and spatial saturation of corresponding coal matrices – with different sizes and shapes in a complex fracture-matrix geometry. This is imperative for the CO_2 geo-sequestration process in fractured rocks in general because the fracture pathways basically enhance the CO_2 storage quantity by easily transporting the CO_2 from injection wells to the matrices that contain the potential adsorption sites.

- However, the fully-coupled simulation affirms that the CO_2 adsorption-induced swelling of coal matrices adversely affects the CO_2 flow behaviour in the reservoir, as the volume expansion of the matrices reduces the local fracture aperture and therefore the fracture permeability. As introduced in the study, the real-time evaluation of the fracture aperture and the consequent fracture permeability from the deformed model geometry is important when simulating the fully-coupled time-dependent processes – rather than incorporating stationary solvers with theoretical scalar porosity and permeability variables.

- Importantly, the fully-closure of some fractures due to initial small apertures and the swelling behaviour of bounding matrices can substantially affect the CO_2 flow behaviour in the subsequent injection phases, especially in the vicinity of the respective fractures. This can be the most disadvantageous modification occur in coal, as it may significantly reduce the process efficiency by declining the further CO_2 injectivity into the reservoir. Further, model concludes that a certain fracture closure significantly depends on the localized mechanical deformation of bounding matrices, rather than the overall deformation of the entire reservoir.

- The introduced equi-dimensional DFM modelling approach incorporated with the contact pressure modelling provides evidence of the locations and the points of fully-closure of certain fractures during the CO_2 injection – that is imperative in deciding the CO_2

injection parameters in a fractured coal mass with a complex fracture geometry such as CO_2 injection rate, etc.

- Moreover, the two-phase flow model confirms that the existence of pore fluid in the reservoir may completely change the modelling approach and the CO_2 flow behaviour in water-wet fractures during the drainage process, depending on the saturation degree, relative permeabilities, capillary effect, etc. It is important to consider multi-phase flow behaviour because most coal seams are saturated with pore fluids with various chemistries and saturation degrees, and can affect the overall CO_2 transportation through the seam.
- Importantly, the model results conclude that the effect of the cleat system is quite dominant in the CO_2 sequestration process in coal, where the hydro-mechanical alterations occur in CO_2-interacted coal are highly-localized due to the spatial disposition of the cleat network. Therefore, the complete process should be resolved accurately through a fully-coupled DFM modelling approach with an explicit representation of the fracture network – in order to model realistic CO_2 sequestration processes, occur in fractured coal reservoirs.

9.1.2 Conclusions drawn from objective 2 of the research

The second objective of the research covers the modifications in coal mechanical properties due to CO_2 interaction, which was studied through a combination of experimental, numerical and statistical analyses. Initially, experimental analysis was conducted to evaluate the effect of CO_2+pore fluid, the effect of CO_2 interaction time and the effect of coal heterogeneity on the alterations of static and dynamic mechanical characteristics of coal.

- Results conclude that presence of moisture substantially reduces the static mechanical parameters such as compressive strength, Young's modulus and brittleness index due to moisture adsorption-induced softening effect. The CO_2 interaction causes further mechanical degradation due to multiple causative factors such as corrosive chemical interactions, adsorption-induced surface energy reduction and the plasticization. Hence, any mechanical property evaluation should be carried out considering the pore fluid saturation as well, rather than just conducting the experiments on dry coal specimens.
- The direct comparison of FTIR spectrums affirms that the CO_2 interaction causes severe modifications in coal macro-molecular structure, resulting in mechanical degradation in low-rank coal like Lignite. The experimental evidence provided by the current study confirms that the alterations in the coal macro-molecular structure is the major reason for

the mechanical property changes in CO_2-interacted low-rank coal, as the material is lack of a significant mineral component, unlike high-rank coal.

- Importantly, the temporal analysis infers that a noteworthy strength reduction occurs at short-term interaction periods, whereas the latter, longer interactions cause only slight but continuous strength decrements, due to the fact that the CO_2 adsorption is a rapid process – this is in line with the conclusions attained in objective 1 as well. The complex mechanical degradation trend should be considered carefully, as the short-term mechanical degradation may cause sudden failures in the reservoir, causing CO_2 back-migration into the atmosphere or adjacent aquifers, rendering numerous social and environmental hazards.

- Further, the dynamic mechanical property evaluation through sensitive measurement techniques confirms that the heterogeneity and the anisotropy, induced by the complex spatial distribution of the mineral and maceral phases and, the fracture network cause localized damages in a bulk coal mass. The damages are high in mineral-rich regions than homogenous maceral-rich regions, and are specifically localized at mineral-maceral interfaces, due to the weaker interconnections exist at the corresponding regions and the distinct swelling potentials/mechanisms. The conclusions are quite important in evaluating the complicated structural alterations – possibly occurred in a complex heterogeneous material like coal, upon CO_2 interaction.

The numerical analysis validated with experimental results provides good initiative for the modelling of CO_2 interaction-induced mechanical property alterations in coal, which is the next important step to improve the understanding of the complex underlying process. It evaluates the effect of the free and the adsorbed CO_2 on the mechanical property alterations of coal, in which the model specifically simulates the compressive strength alterations, using the Mohr-Coulomb failure criterion. This is quite important because the mechanical property alterations in a coal seam is occurred due to the combined effect of both free and adsorbed CO_2.

- The validated model results conclude that the simulation procedure is particularly capable of modelling the mechanical alterations with varying CO_2 pore pressure, under both confined and unconfined stress conditions, in different coal types. The introduced theoretically-extended cohesion model – incorporated with the effective stress change and the adsorption-induced surface energy change is capable of simulating the strength alterations over a wide range of pore pressures at different confining pressures, which agrees with several experimental observations.

- This, in turn, furnishes the understanding of the underlying physical process and provides a great initiative in numerically simulating the CO_2-induced mechanical degradation in coal, rather than just conducting tests on random coal specimens.

- The model sensitivity analysis further concludes that the mechanical alterations are greatly dependent on the specific coal properties, such as adsorption capacity and the swelling potential, that are primarily defined by the Langmuir sorption and swelling constants in the model. Therefore, the specific parameters of the targeted coal reservoir should be determined accurately prior to the implementation of sequestration projects.

- The CO_2 pore pressure plays a critical role in coal strength modifications, due to the change in both effective stress and sorption-induced surface energy. In fact, the compressive strength variation follows a 'U-shaped' trend with the increasing CO_2 pore pressure, where the strength is reduced continuously up to a certain moderate pore pressure, and then starts to slightly increase with further pore pressure increment, due to coal matrix compression – caused by the elevated pore pressures. This may provide an insight into deciding the CO_2 storage and targeted CO_2 pore pressure at the end-stage of the sequestration process, in terms of preserving the mechanical competency of the reservoir, while sequestrating a maximum amount of CO_2.

Moreover, the statistical models are another set of tools that can be successfully utilized to predict the CO_2 interaction-induced mechanical property alterations in coal. The last phase of the objective was carried out by conducting a statistical analysis using two well-known machine learning techniques, i.e. ANN and ANFIS.

- The model results conclude that the readily available experimental data can be successfully utilized in developing statistical relationships between influential parameters and the mechanical alterations in CO_2-interacted coal. The technique is quite important in this field of research because there are plenty of experimental data available in the literature that have investigated the coal strength modifications under various reservoir conditions.

- The introduction of the fixed carbon content as an effective input parameter overcomes a huge barrier in combining the results of different coal ranks. Therefore, it is able to successfully combine several experimental results readily available in the literature, and utilize them to determine general statistical trends for predicting strength alteration in different kinds of coal under various interaction environments. Further, most of the experimental data used for the statistical modelling are related to the coal types from upper and lower Gondwana coal formation; thus, the results of this study may be directly applicable to other investigations where, Gondwana formations are exposed/present, and coal being mined.

- Unlike traditional regression analyses, the machine learning techniques adopted in this study are capable of capturing the complex interrelationships between input and output variables with acceptable accuracy; thus, can be used to replace the conventional regression analyses. In general, the study infers that these statistical evaluation tools can be used as indirect and alternative methods to estimate the mechanical modifications occur in CO_2-interacted coal. The precise predictions with well-trained models may provide additional backing to assess the mechanical competency of coal reservoirs, during CO_2 sequestration.

Overall, the results and the conclusions of the research project confirm that the CO_2 interaction causes significant structural modifications in coal, affecting the hydro-mechanical parameters of coal that are pertinent to CO_2 sequestration process – particularly coal seam permeability and mechanical parameters. There are numerous methods, techniques and tools to evaluate such complex alterations as introduced and explained in current study and, one should consider the possibility of utilizing most of them when examining the complex alterations. In fact, as concluded from the current research project, it is crucial to obtain an in-depth understanding of the fully-coupled process – appraised with combined experimental, numerical and statistical analyses in order to design an efficient and safer CO_2 sequestration process in a particular coal reservoir.

9.2 Suggestions for future research

CO_2 sequestration in a coal seam is a vast research area, where most complex processes and mechanisms still remain unexplored; thus, require further investigations. Although current research findings provide useful insights into many aspects of the process by combining experimental, numerical and statistical analyses, further improvements and extensions are essential to advance towards an effective and safer sequestration process. This section provides suggestions for the advancement of future research, which may support in extending the current research work, eliminating some of the assumptions and overcoming the limitations of the evaluation procedures.

9.2.1 Suggestions for extending the work carried out in objective 1 of the research

- In objective 1, when modelling CO_2 diffusion–adsorption–swelling process, it was assumed that the coal matrix is generally a homogeneous material, and an equivalent pore size was theoretically derived when modelling the multiple diffusion mechanisms. However, an actual coal matrix contains an intricate pore network with complicated pore characteristics, including multiple pore sizes, pore channels and a complex pore connectivity. Therefore, the CO_2 diffusion may be localized and spatially varied, depending on the respective pore attributes and the pore pressure. It is therefore recommended to focus on analysing the localized flow regimes by considering 3D-geometric models of the actual nano-scale pore network, using high-resolution imaging techniques, like focused-ion beam and scanning electron microscopy (FIB-SEM).

- Further, the study only considers two diffusion mechanisms, i.e. slip flow and Knudsen diffusion. Nevertheless, there exist several other diffusion mechanisms such as no-slip flow, surface diffusion and free-molecular flow, that can be considered for the precise modelling of the entire diffusion process.

- In the DFM modelling approach of the fractured coal mass, the geometric model was developed with a stochastically simplified DFM model, due to the intricacy of the actual fracture network. However, the geometric model represents the fracture network of a typical coal reservoir that incudes orthogonal face cleats and butt cleats with appropriate fracture apertures and the unique fracture interconnectivity. Although the results provide a better understanding of the fully-coupled process in the fractured coal seam, some of the important attributes of the original fracture network such as fracture roughness may be lost due to the simplification. Therefore, it is recommended to adopt geometric models with preserving the original fracture attributes to the fullest extent, irrespective of the computational complexity.

- Coal being a brittle material can easily induce new cracks during CO_2 interaction, that can affect the structural and topological aspects of the fracture network, and therefore the entire hydro-mechanical alteration process. Hence, it is suggested to consider the formation of new cracks and extension of existing cracks in future DFM modelling studies.
- Moreover, since most CO_2 sequestration processes are combined with the CBM extraction, it is important to consider the effect of methane in DFM modelling approach as well, by considering competitive adsorption and the methane desorption processes to assess the CBM production during CO_2 sequestration.
- Although the current DFM model simulates the fully-coupled process at the coal constituent-scale (i.e. fractures and matrices) and analysed the localized hydro-mechanical alterations, the model was implemented on a lab-scale geometry, due to the excessive computational cost. It is worthwhile to extend and upscale current theoretical approach on a reservoir-scale geometric model with the spatial mapping of actual fracture networks, that further replicates the CO_2 sequestration in the field – regardless of the required large computational powers.

9.2.2 Suggestions for extending the work carried out in objective 2 of the research

- In objective 2, the experimental analyses were carried out on selected two coal ranks, i.e. Lignite and high-volatile bituminous coal, representing both low- and high-rank coal. There are several coal ranks available, and their characteristics vary depending on the coalification process, composition and the spatial disposition of each component. Consequently, the observed experimental outcomes may also vary with the coal rank, and they are largely specific to the tested coal samples and the experimental environment. Further, the sample properties can be affected during the transportation, storage and preparation due to moisture loss. Hence, further experimental studies with more controlled techniques on different coal ranks are obviously essential in the context of experimental analyses to understand the complex structural alterations.
- Further, the static mechanical property evaluations were conducted under unconfined condition to compare with common lab-scale testing techniques, such as UCS tests. The dynamic mechanical property evaluations were also conducted under unconfined

condition due to lack of experimental facilities. Since the effect of confining pressure has a great influence on sample behaviour and alterations in fracture network due to different swelling mechanisms, it is recommended to conduct more experiments under confined condition, mimicking different *in-situ* stress environments.

- Although the current temporal analyses successfully capture the complex strength alteration trends with the increasing CO_2 interaction time, they were conducted only up to a maximum of three months due to the limited time frame of the research. It is therefore recommended to extend the temporal analyses for longer CO_2 interaction periods because the injected CO_2 is expected to be stored in coal reservoirs for a significant geological period, that may trigger unexpected structural alterations with the long-term interactions.
- The numerical analysis provides a great initiative in modelling the CO_2 interaction-induced mechanical alterations, by combining the effects of both the free and the adsorbed CO_2, under both confined and unconfined conditions. Since mechanical degradation is a complex process, the model can be further improved by including the effect of other influential parameters, such as the coal heterogeneity, physico-chemical interactions, effect of moisture, etc.
- Further, it is recommended to extend the current single-continuum model to a DFM model through the inclusion of an explicit fracture network, that can further evaluate the effect of natural cleat system on the mechanical alterations.
- The current statistical analysis with machine learning techniques introduces a novel method to estimate the CO_2-induced mechanical modifications in coal, that can be easily utilized in predicting the strength alterations under specific reservoir conditions. The well-trained models demonstrate a higher accuracy in predicting the complex strength alterations, upon CO_2 interaction. It is acknowledged that the current models adopted 96 data sets with 3 input variables and 1 output variable, due to the limited experimental data available in the literature. However, models can be easily improved and generalized by conducting further experiments under different conditions and collecting data, and including them in the models to capture the alterations in a wide range.
- Also, it is recommended to adopt statistical methods like principal-component analysis (PCA) to minimize the number of independent variables, without disturbing the variance of original data, in order to minimize the complexity of the models.

9.3 An insight into the field-application of the CO_2 sequestration technique

Carbon capture and storage (CCS) technique has a great potential of reducing the atmospheric CO_2 level. The current research is specifically assessing the storage or the sequestration part, which focuses on determining new measures for an effective and safer process – through the evaluation of CO_2-induced structural alterations in the reservoir. The CO_2 sequestration in geological reservoirs – particularly in coal seams has been implemented worldwide at field-scale due to its proven efficiency. Numerous successful pilot projects have already been implemented in several coal basins in various countries, such as San Juan basin in the United States, Ishikari coalfield in Japan, Upper Silesian basin in Poland, Fenn-Big Valley in Canada and Qinshui basin in China. Literature shows that the viability of sequestrating a maximum quantity of CO_2 in a certain coal reservoir depends on multiple factors including, tectonic setting, geology, depth, size, hydrology, maturity, sensitivity of the coal reservoir, infrastructure, accessibility, climate, CO_2 source, etc. Among them, the reservoir reaction upon CO_2 interaction is a critical factor that should be investigated prior to the implementation of field-scale CO_2-sequestration projects, particularly in sensitive reservoirs like coal.

The current findings of the combined experimental, numerical and statistical analyses strongly suggest that the efficiency in terms of CO_2 injectivity and flow behaviour and, the safety in terms of mechanical competency are highly-dependent on the coal type and its intricate characteristics. Although a potential coal reservoir spreads in a vast area, the complex diffusion processes in nano-scale pores in coal matrices and the CO_2 flow behaviour in micro-scale fracture network play huge roles in the entire sequestration process – that emphasize the necessity of investigating such process at the coal constituent-scale. Further, the bulk coal specimens tested at lab-scale and the integrated numerical and statistical analyses provide conclusive evidence on how the mechanical degradation occurs due to CO_2 interaction. The decisive conclusions obtained from the current study and the numerical approaches adopted in modelling the fully-coupled process can be successfully utilized in modelling the field-scale reservoir behaviour through an appropriate up-scaling process.

In addition, the interest of flied-scale CO_2 sequestration in coal is greatly increased due to the possibility of combining the technique with the CBM extraction. There are two conceivable ways of enhancing the CBM extraction during CO_2 sequestration at field-scale: 1) CO_2 flooding and 2) CO_2-based hydraulic fracturing. As evident from several previous studies, CO_2 flooding can concomitantly boost the desorption of methane from coal pores due to the higher adsorption capacity of CO_2, enhancing the overall CBM production. However, the second technique, i.e. CO_2-based hydraulic fracturing is a novel technique in the industry that needs further attention and improvement at field-scale. The technique can be feasible because, instead of simply injecting CO_2 into coal reservoirs during CO_2 sequestration, the injection of CO_2 with a high pressure to create an artificial fracture network may enhance the CBM production, that can facilitate easy pathways for the desorbed in-built methane to reach the production wells. The successful implementation of this method would indeed offset the sequestration cost significantly. Although this technique has been proven efficient in other geological reservoirs like shale, granite and sandstone, the applicability in coal seams has not been sufficiently studied yet. Hence, as an initiative for implementing this technique, an additional experimental analysis was conducted during the doctoral research to evaluate the applicability of CO_2 as an alternative and non-aqueous fracturing fluid for the hydraulic fracturing of coal reservoirs.

In fact, the analysis comprehensively evaluates the CO_2-based fracking process in different coal ranks through three important factors, i.e. break-down pressure, resultant fracture properties and the complete fracture propagation process. The outcomes of the study conclude that all three parameters are significantly dependent on the coal rank. In fact, the break-down pressure rises with the increasing coal rank or the coal maturity due to the higher fixed carbon content that possibly imparts a higher strength. Further, the fracture propagation process also depends on the coal rank, in which low-rank coal demonstrates a sudden an unstable fracture propagation, upon CO_2 injection. The extensive fracking may lead to possible damages in the particular coal seam, rendering CO_2 outbursts and leakages, low-level earthquakes, etc. Similar to localized damages observed in objective 2, the fracking process induces more localized fractures at mineral-maceral interfaces due to the weaker areas available in those regions. This is important in selecting a coal reservoir for CO_2-based fracking because the project efficiency and the CBM productivity are greatly dependent on the attributes of the induced fracture network. In general, the overall results of the study provide an understanding of deciding the targeted coal reservoir and the design parameter of the fracking process, such as the injection pressure and the pressurization rate. Use of accurate design parameters on the targeted coal reservoir may enhance the productivity of the process while minimizing the reservoir damage. The outcomes of the study are presented in a peer-reviewed journal paper, published in “Fuel”. The journal is a Q1 journal with impact factor of 5.13. The publication details are as follows.

- Sampath K. H. S. M., Perera M. S. A., Elsworth D., Ranjith P. G., Matthai S. K., Rathnaweera T., Zhang G. (2019). *Effect of coal maturity on CO_2-based hydraulic fracturing process in coal seam gas reservoirs*. Fuel, 236, 179-189.

Overall, it is acknowledged that the CO_2-sequestration in coal reservoir is a viable technique that has a noteworthy influence on minimizing atmospheric CO_2 level. The efficiency and feasibility of field-scale processes can be enhanced by combining it with the CBM extraction, especially with the CO_2-based fracking process. However, a great attention should be paid towards the CO_2 interaction-induced structural alterations in coal, as it can substantially affect the process efficiency while damaging the mechanical competency of the reservoir.

Page intentionally left blank

Reference

IEA. (2016). International Energy Agency. *Energy Technology Perspectives, OECD/IEA: Paris, France, 2016;ISBN 978-92-64-25234-9*.

IPCC. (2014). Climate Change 2014: Synthesis Report. Contribution of Working Groups I, II and III to the Fifth Assessment Report of the Intergovernmental Panel on Climate Change. Geneva, Switzerland, . 151.

Sampath, K. H. S. M., Perera, M. S. A., Ranjith, P. G., Matthai, S. K., & Dong yin, L. (2019). Qualitative and quantitative evaluation of the alteration of micro-fracture characteristics of supercritical CO_2-interacted coal. *The Journal of supercritical fluids, 147*, 90-101.

Van Alphen, K., Van Ruijven, J., Kasa, S., Hekkert, M., & Turkenburg, W. (2009). The performance of the Norwegian carbon dioxide, capture and storage innovation system. *Energy Policy, 37*(1), 43-55.

Agheshlui, H., Sedaghat, M. H., & Matthai, S. (2018). Stress influence on fracture aperture and permeability of fragmented rocks. *Journal of Geophysical Research: Solid Earth, 123*(5), 3578-3592.

Apps, J., Zheng, L., Zhang, Y., Xu, T., & Birkholzer, J. (2010). Evaluation of potential changes in groundwater quality in response to CO2 leakage from deep geologic storage. *Transport in Porous Media, 82*(1), 215-246.

Arbogast, T., Douglas, J., Jim, & Hornung, U. (1990). Derivation of the double porosity model of single phase flow via homogenization theory. *SIAM Journal on Mathematical Analysis, 21*(4), 823-836.

Ateş, Y. (1987). *The effect of sorption on strength of coal and its influence on coal outbursts.* (M.Sc), The University of Alberta, Edmonton, Canada.

Ates, Y., & Barron, K. (1988). The effect of gas sorption on the strength of coal. *Mining science & technology, 6*(3), 291-300.

Bae, J.-S., & Bhatia, S. K. (2006). High-pressure adsorption of methane and carbon dioxide on coal. *Energy & Fuels, 20*(6), 2599-2607.

Bagga, P., Roy, D. G., & Singh, T. N. (2015). *Effect of carbon dioxide sequestration on the mechanical properties of Indian coal*. Paper presented at the ISRM Regional Symposium-EUROCK 2015. International Society for Rock Mechanics and Rock Engineering.

Berre, I., Doster, F., & Keilegavlen, E. (2019). Flow in fractured porous media: A review of conceptual models and discretization approaches. *Transport in Porous Media, 130*(1), 215-236.

Botnen, L. S., Fisher, D. W., Dobroskok, A. A., Bratton, T. R., Greaves, K. H., McLendon, T. R., Steiner, G., Sorensen, J. A., Steadman, E. N., & Harju, J. A. (2009). Field test of CO_2 injection and storage in lignite coal seam in North Dakota. *Energy Procedia, 1*(1), 2013-2019.

Brenner, D. (1984). Microscopic in-situ studies of the solvent-induced swelling of thin sections of coal. *Fuel (Guildford), 63*(9), 1324-1328.

Coulomb, C. A. (1773). Sur une application des regles de maximums et minimums a quelques problemes de statistique relatifs a larchitesture. *Académie Royale de Science Memorie Mechanics and Mining Sciences, 7*, 343–382.

Crank, J. (1979). *The mathematics of diffusion*: Oxford university press.

Cui, X., & Bustin, R. M. (2005). Volumetric strain associated with methane desorption and its impact on coalbed gas production from deep coal seams. *Aapg Bulletin, 89*(9), 1181-1202.

Czapliński, A., & Hołda, S. (1982). Changes in mechanical properties of coal due to sorption of carbon dioxide vapour. *Fuel (Guildford), 61*(12), 1281-1282.

da C Andrade, E., Randall, R., & Makin, M. (1950). The rehbinder effect. *Proceedings of the Physical Society. Section B, 63*(12), 990.

Darcy, H. P. G. (1856). *Les Fontaines publiques de la ville de Dijon. Exposition et application des principes à suivre et des formules à employer dans les questions de distribution d'eau, etc*: V. Dalamont.

Ertekin, T. (1995). Coalbed methane recovery modeling: what we know and what we need to learn. *Turkish Journal of Oil and Gas, 1*(1), 7-18.

Ettinger, I., & Lamba, E. (1957). Gas medium in coal-breaking processes. *Fuel, 36*(3), 298-306.

Farquhar, S., Pearce, J., Dawson, G., Golab, A., Sommacal, S., Kirste, D., Biddle, D., & Golding, S. (2015). A fresh approach to investigating CO_2 storage: Experimental CO_2–water–rock interactions in a low-salinity reservoir system. *Chemical Geology, 399*, 98-122.

Feucht, L. J., & Logan, J. M. (1990). Effects of chemically active solutions on shear behaviour of a sandstone. *Tectonophysics, 175*, 156–176.

Gathitu, B. B., Chen, W. Y., & McClure, M. (2009). Effects of coal interaction with supercritical CO_2: physical structure. *Industrial & Engineering Chemistry Research, 48*(10), 5024-5034.

Gentzis, T., Deisman, N., & Chalaturnyk, R. J. (2007). Geomechanical properties and permeability of coals from the Foothills and Mountain regions of western Canada. *International Journal of Coal Geology, 69*(3), 153-164.

Gibbs, J. W. (1879). On the equilibrium of heterogeneous substances. 300-320.

Goodman, A. L., Campus, L. M., & Schroeder, K. T. (2005). Direct Evidence of Carbon Dioxide Sorption on Argonne Premium Coals Using Attenuated Total Reflectance−Fourier Transform Infrared Spectroscopy. *Energy & Fuels, 19*(2), 471-476.

Green, T. K., Pan, W.-P., & Clark, M. (1991). Glass transition temperature of modified coals. *Papers of the American Chemical Society. Fuel, 201*, 110.

Griffith, A. A. (1921). The phenomena of rupture and flow in solids. *Philosophical transactions of the royal society of london. Series A, 221*, 163-198.

Guo, H., Ni, X., Wang, Y., Du, X., Yu, T., & Feng, R. (2018). Experimental Study of CO_2-Water-Mineral Interactions and Their Influence on the Permeability of Coking Coal and Implications for CO_2-ECBM. *Minerals, 8*(3), 117.

Gustkiewicz, J. (1985). Deformation and failure of the Nowa Ruda sandstone in a three-axial state of stress with gas under pressure in the pores. *Archiwum Górnictwa, 30*(3), 401-424.

Harpalani, S., & Schraufnagel, R. A. (1990). Shrinkage of coal matrix with release of gas and its impact on permeability of coal. *Fuel, 69*(5), 551-556.

He, Q., Mohaghegh, S. D., & Gholami, V. (2013). A field study on simulation of CO_2 injection and ECBM production and prediction of CO_2 storage capacity in unmineable coal seam. *Journal of Petroleum Engineering, 2013*.

Hiramatsu, Y., Saito, T., & Oda, N. (1983). *Studies On The Mechanism Of Gas And Coal Bursts In Japanese Coal Mines.* Paper presented at the 5th ISRM Congress.

Holda, S. (1986). Investigation of adsorption, dilatometry and strength of low rank coal. *Archiwum Górnictwa, 31*, 599-608.

Jackson, L. J. (1984). *Outbursts in coal mines* (Vol. No. ICTIS/TR25): IEA Coal Research Londin report.

Jasinge, D. (2010). *An investigation of the effect of carbon dioxide sequestration on the behaviour of brown coal.* (PhD degree), (PhD thesis), Monash University.

Kendall, J. L., Canelas, D. A., Young, J. L., & DeSimone, J. M. (1999). Polymerizations in supercritical carbon dioxide. *Chemical Reviews, 99*(2), 543-564.

Langmuir, D. (1997). Aqueous environmental geochemistry. *No. 551.48 L3*.

Larsen, J. W. (2004). The effects of dissolved CO_2 on coal structure and properties. *International Journal of Coal Geology, 57*(1), 63– 70.

Laubach, S. E., Marrett, R. A., Olson, E., & Scott, A. R. (1998). Characteristics and origins of coal cleat: A review. *International Journal of Coal Geology, 35*(1-4), 175-207.

Lepillier, B., Daniilidis, A., Gholizadeh, N. D., Bruna, P.-O., Kummerow, J., & Bruhn, D. (2019). A fracture flow permeability and stress dependency simulation applied to multi-reservoirs, multi-production scenarios analysis. *Geothermal Energy, 7*(1), 24.

Lucht, L. M., Larson, J. M., & Peppas, N. A. (1987). Macromolecular structure of coals. 9. Molecular structure and glass transition temperature. *Energy & Fuels, 1*(1), 56-58.

Ma, Q., Harpalani, S., & Liu, S. (2011). A simplified permeability model for coalbed methane reservoirs based on matchstick strain and constant volume theory. *International Journal of Coal Geology, 85*(1), 43-48.

Marbler, H., Erickson, K. P., Schmidt, M., Lempp, C., & Pöllmann., H. (2013). Geomechanical and geochemical effects on sandstones caused by the reaction with supercritical CO_2: an experimental approach to in situ conditions in deep geological reservoirs. *Environmental Earth Sciences, 69*(6), 1981-1998.

Masoudian, M. S., Airey, D. W., & El-Zein, A. (2014). Experimental investigations on the effect of CO_2 on mechanics of coal. *International Journal of Coal Geology, 128*, 12-23.

Meng, M., & Qiu, Z. (2018). Experiment study of mechanical properties and microstructures of bituminous coals influenced by supercritical carbon dioxide. *Fuel, 219*, 223-238.

Oudinot, A. Y., Koperna, G. J., Philip, Z. G., Liu, N., Heath, J. E., Wells, A., Young, G. B., & Wilson, T. (2011). CO_2 injection performance in the Fruitland coal fairway, San Juan Basin: results of a field pilot. *Spe Journal, 16*(04), 864-879.

Ozdemir, E. (2009). Modeling of coal bed methane (CBM) production and CO_2 sequestration in coal seams. *International Journal of Coal Geology, 77*(1-2), 145-152.

Perera, M. S. A., Ranjith, P. G., Choi, S. K., & Airey, D. (2011). The effects of sub-critical and super-critical carbon dioxide adsorption-induced coal matrix swelling on the permeability of naturally fractured black coal. *Energy, 36*(11), 6442-6450.

Perera, M. S. A., Ranjith, P. G., & Viete, D. R. (2013). Effects of gaseous and super-critical carbon dioxide saturation on the mechanical properties of bituminous coal from the Southern Sydney Basin. *Applied Energy, 110*, 73-81.

Pini, R., Ottiger, S., Burlini, L., Storti, G., & Mazzotti, M. (2009). CO_2 storage through ECBM recovery: An experimental and modeling study. *Energy Procedia, 1*(1), 1711-1717.

Ranathunga, A. S., Perera, M. S. A., Ranjith, P. G., & Bui, H. (2016). Super-critical CO_2 saturation-induced mechanical property alterations in low rank coal: An experimental study. *The Journal of supercritical fluids, 109*, 134-140.

Ranjith, P. G., Jasinge, D., Choi, S. K., Mehic, M., & Shannon, B. (2010). The effect of CO2 saturation on mechanical properties of Australian black coal using acoustic emission. *Fuel (Guildford), 89*(8), 2110-2117.

Ranjith, P. G., & Perera, M. S. A. (2012). Effects of cleat performance on strength reduction of coal in CO_2 sequestration. *Energy (Oxford), 45*(1), 1069-1075.

Saghafi, A., Faiz, M., & Roberts, D. (2007). CO_2 storage and gas diffusivity properties of coals from Sydney Basin, Australia. *International Journal of Coal Geology, 70*(1-3), 240-254.

Sampath, K. H. S. M., Perera, M. S. A., Ranjith, P. G., & Matthai, S. K. (2019). CO_2 interaction induced mechanical characteristics alterations in coal: A review. *International Journal of Coal Geology, 204*, 113-129.

Sampath, K. H. S. M., Perera, M. S. A., Ranjith, P. G., Matthai, S. K., Rathnaweera, T., Zhang, G., & Tao, X. (2017). CH_4-CO_2 gas exchange and supercritical CO_2 based hydraulic fracturing as CBM production-accelerating techniques: A review. *Journal of CO2 Utilization, 22*, 212-230.

Shi, J., & Durucan, S. (2005). CO_2 storage in deep unminable coal seams. *Oil & Gas Science and Technology, 60*(3), 547-558.

Sun, X., Yao, Y., Liu, D., Elsworth, D., & Pan, Z. (2016). Interactions and exchange of CO_2 and H_2O in coals: an investigation by low-field NMR relaxation. *Scientific Reports, 6*(1), 19919.

Tunc, X., Faille, I., Gallouët, T., Cacas, M. C., & Havé, P. (2012). A model for conductive faults with non-matching grids. *Computational Geosciences, 16*(2), 277-296.

Viete, D. R., & Ranjith, P. G. (2006). The effect of CO_2 on the geomechanical and permeability behaviour of brown coal: Implications for coal seam CO_2 sequestration. *International Journal of Coal Geology, 66*, 204 – 216.

Vinokurova, E., Bogomolova, L., Ketslakh, A., & Kontorovich, S. (1988). Crushing of gas-saturated anthracites. *Colloid J. USSR (Engl. Transl.);(United States), 50*(1).

Vishal, V., Ranjith, P. G., & Singh, T. N. (2015). An experimental investigation on behaviour of coal under fluid saturation, using acoustic emission. *Journal of Natural Gas Science and Engineering, 22*, 428-436.

Wen, H., Li, Z., Deng, J., Shu, C.-M., Laiwang, B., Wang, Q., & Ma, L. (2017). Influence on coal pore structure during liquid CO 2-ECBM process for CO_2 utilization. *Journal of CO2 Utilization, 21*, 543-552.

Witherspoon, P. A., Wang, J. S., Iwai, K., & Gale, J. E. (1980). Validity of cubic law for fluid flow in a deformable rock fracture. *Water Resources Research, 16*(6), 1016-1024.

Wu, K., Chen, Z., Li, X., Guo, C., & Wei, M. (2016). A model for multiple transport mechanisms through nanopores of shale gas reservoirs with real gas effect–adsorption-mechanic coupling. *International Journal of Heat and Mass Transfer, 93*, 408-426.

Zhang, Y., Lebedev, M., Sarmadivaleh, M., Barifcani, A., & Iglauer, S. (2016). Swelling-induced changes in coal microstructure due to supercritical CO_2 injection. *Geophysical Research Letters, 43*(17), 9077-9083.

Zhang, Y., Lebedev, M., Yu, H., & Iglauer, S. (2018). Experimental Study of Supercritical CO_2 Injected into Water Saturated Medium Rank Coal by X-ray MicroCT. *Energy Procedia, 154*, 131-138.

ASTM-D.2938. Standard Test Method for Unconfined Compressive Strength of Intact Rock Core Specimens. ASTM International, West Conshohocken, PA.

Bishop, M. G. (2000). *Petroleum system of the Gippsland Basin, Australia* (2331-1258). Retrieved from

Durie, R. A. (1991). *The Science of Victorian Brown Coal: Structure, Properties and Consequences from Utilization*: Butterworth, Heinemann, Oxford.

Grigore, M., & Sakurovs, R. (2016). Inorganic matter in Victorian brown coals. *International Journal of Coal Geology, 154*(257-264).

Holda, S. (1986). Investigation of adsorption, dilatometry and strength of low rank coal. *Archiwum Górnictwa, 31*, 599-608.

Holdgate, G., Kershaw, A., & Sluiter, I. (1995). Sequence stratigraphic analysis and the origins of Tertiary brown coal lithotypes, Latrobe Valley, Gippsland Basin, Australia. *International Journal of Coal Geology, 28*(2-4), 249-275.

Holdgate, G. R. (2005). Geological processes that control lateral and vertical variability in coal seam moisture contents—Latrobe Valley (Gippsland Basin) Australia. *International Journal of Coal Geology, 63*(1-2), 130-155.

Li, Z., Zhang, X., Sugai, Y., Wang, J., & Sasaki, K. (2012). Properties and developments of combustion and gasification of coal and char in a CO_2-rich and recycled flue gases atmosphere by rapid heating. *Journal of Combustion, 2012*.

Sampath, K. H. S. M., Perera, M. S. A., Elsworth, D., Ranjith, P. G., Matthai, S. K., & Rathnaweera, T. (2018). Experimental Investigation on the Mechanical Behavior of Victorian Brown Coal under Brine Saturation. *Energy & Fuels, 32*(5), 5799-5811.

Stevenson, A. W., Hall, C. J., Mayo, S. C., Häusermann, D., Maksimenko, A., Gureyev, T. E., Nesterets, Y. I., Wilkins, S. W., & Lewis, R. A. (2012). Analysis and interpretation of the first monochromatic X-ray tomography data collected at the Australian Synchrotron Imaging and Medical beamline. *Journal of synchrotron radiation, 19*(5), 728-750.

Wang, B., Qin, Y., Shen, J., Zhang, Q., & Wang, G. (2018). Pore structure characteristics of low-and medium-rank coals and their differential adsorption and desorption effects. *Journal of Petroleum Science and Engineering, 165*, 1-12.

Wu, Q., Zhao, D., Wang, Y., Shen, J., Mu, W., & Liu, H. (2017). Method for assessing coal-floor water-inrush risk based on the variable-weight model and unascertained measure theory. *Hydrogeology Journal, 25*(7), 2089-2103.

Yu, B., & Zhao, J. (2011). *Study on transport rules and fully mechanized mining with top coal caving technology of coal seam with huge thickness in Tashan mine.* Paper presented at the Applied Mechanics and Materials.

Zhang, Z., Zhang, R., Li, G., Li, H., & Liu, J. (2014). The effect of bedding structure on mechanical property of coal. *Advances in Materials Science and Engineering, 2014*.

Zhu, C.-j., & Lin, B.-q. (2015). Effect of igneous intrusions and normal faults on coalbed methane storage and migration in coal seams near the outcrop. *Natural Hazards, 77*(1), 17-38.

Bertrand, F., Buzzi, O., & Collin, F. (2019). Cleat-scale modelling of the coal permeability evolution due to sorption-induced strain. *International Journal of Coal Geology, 216*, 103320.

Darcy, H. P. G. (1856). *Les Fontaines publiques de la ville de Dijon. Exposition et application des principes à suivre et des formules à employer dans les questions de distribution d'eau, etc*: V. Dalamont.

Fan, C., Elsworth, D., Li, S., Zhou, L., Yang, Z., & Song, Y. (2019). Thermo-hydro-mechanical-chemical couplings controlling CH_4 production and CO_2 sequestration in enhanced coalbed methane recovery. *Energy, 173*, 1054-1077.

Fourar, M., & Lenormand, R. (1998). *A viscous coupling model for relative permeabilities in fractures.* Paper presented at the SPE Annual Technical Conference and Exhibition.

Hadi, S.-J. (2016). Analytical estimation of water-oil relative permeabilities through fractures. *Oil & Gas Science and Technology–Revue d'IFP Energies nouvelles, 71*(3), 31.

Liu, G., & Smirnov, A. V. (2008). Modeling of carbon sequestration in coal-beds: A variable saturated simulation. *Energy Conversion and Management, 49*(10), 2849-2858.

Masoudian, M. S., Airey, D. W., & El-Zein, A. (2014). Experimental investigations on the effect of CO_2 on mechanics of coal. *International Journal of Coal Geology, 128*, 12-23.

Robertson, E. P., & Christiansen, R. L. (2005). *Modeling permeability in coal using sorption-induced strain data*. Retrieved from

Romm, E. (1966). Flow characteristics of fractured rocks. *Nedra, Moscow, 283*.

Tunc, X., Faille, I., Gallouët, T., Cacas, M. C., & Havé, P. (2012). A model for conductive faults with non-matching grids. *Computational Geosciences, 16*(2), 277-296.

Van Voast, W. A. (2003). Geochemical signature of formation waters associated with coalbed methane. *Aapg Bulletin, 87*(4), 667–676.

Wang, J., & Narasimhan, T. N. (1985). Hydrologic mechanisms governing fluid flow in a partially saturated, fractured, porous medium. *Water Resources Research, 21*(12), 1861-1874.

Yang, R., Ma, T., Xu, H., Liu, W., Hu, Y., & Sang, S. (2019). A model of fully coupled two-phase flow and coal deformation under dynamic diffusion for coalbed methane extraction. *Journal of Natural Gas Science and Engineering, 72*, 103010.

Page intentionally left blank